

**CHARACTERIZATION OF METALLOENZYMES INVOLVED IN THE BACTERIAL
CATABOLISM OF LIGNIN-DERIVED BIARYLS**

by

Eugene Kuatsjah

B.Sc., The University of British Columbia, 2010

A THESIS SUBMITTED IN PARTIAL FULFILLMENT OF
THE REQUIREMENTS FOR THE DEGREE OF

DOCTOR OF PHILOSOPHY

in

THE FACULTY OF GRADUATE AND POSTDOCTORAL STUDIES
(Genome Sciences and Technology)

THE UNIVERSITY OF BRITISH COLUMBIA
(Vancouver)

February 2019

© Eugene Kuatsjah, 2019

The following individuals certify that they have read, and recommend to the Faculty of Graduate and Postdoctoral Studies for acceptance, the dissertation entitled:

Characterization of metalloenzymes involved in the bacterial catabolism of lignin-derived biaryls

submitted by Eugene Kuatsjah in partial fulfillment of the requirements for

the degree of Doctor of Philosophy

in The Faculty of Graduate and Postdoctoral Studies (GSAT)

Examining Committee:

Prof. Andrew Riseman

Chair

Prof. Lindsay D. Eltis

Supervisor

Prof. Stephen G. Withers

Supervisory Committee Member

Prof. Michael E. P. Murphy

Supervisory Committee Member

Prof. Martin Tanner

University Examiner

Prof. Harry Brumer

University Examiner

Prof. Christian P. Whitman

External Examiner

Additional Supervisory Committee:

Prof. Nobukaho Tokuriki

Supervisory Committee Member

Abstract

Bacteria play a central role in degrading aromatic compounds, including those derived from lignin, a heterogeneous aromatic polymer and a major component of woody biomass. These catabolic pathways and enzymes play a critical role in the global carbon cycle and have biocatalytic potential in the valorization of biomass. Nevertheless, many of these pathways and enzymes remain poorly understood. This thesis describes the characterization of three such catabolic enzymes, LsdA, LigZ and LigY, each of which has a metal cofactor. LsdA from *Sphingomonas paucimobilis* TMY1009 is an Fe²⁺-dependent oxygenase that catalyzes the cleavage of stilbenoids into aldehydes. In kinetic analyses, LsdA only transformed 4-hydroxystilbenes and was inhibited by phenylazophenol. Crystallographic and mutagenesis analyses established that Lys-134 is essential for catalysis, consistent with a role in deprotonating the stilbene's 4-hydroxyl. LigZ and LigY catalyze successive reactions in 2,2'-dihydroxy-3,3'-dimethoxy-5,5'-dicarboxy-biphenyl (DDVA) catabolism by *Sphingobium* sp. SYK-6. In this study, highly active preparations of LigZ, an Fe²⁺-dependent extradiol dioxygenase, afforded an accurate description of the enzyme's substrate specificity and mechanism-based inactivation. 4,11-Dicarboxy-8-hydroxy-9-methoxy-2-hydroxy-6-oxo-6-phenyl-hexa-2,4-dienoate (DCHM-HOPDA) was identified as the *meta*-cleavage product (MCP) of the LigZ reaction and was shown to undergo a rapid, reversible non-enzymatic transformation under physiological conditions ($t_{1/2} \sim 5$ min). The enolate form of the MCP is the substrate of LigY, which catalyzed the hydrolysis of DCHM-HOPDA to 5-carboxyvanillate (5CVA) and 4-carboxy-2-hydroxpenta-2,4-dienoate (CHPD). Phylogenetic, biochemical and structural analyses identified LigY as a Zn²⁺-dependent amidohydrolase, in contrast to all known MCP hydrolases, which are serine-dependent enzymes. Nevertheless, transient-state kinetic analyses revealed a catalytic intermediate, ES^{red}, with a red-shifted spectrum similar to that observed in serine-dependent MCP hydrolases. Further, 4-methyl HOPDA inhibited LigY and yielded a complex with a spectrum similar to that of ES^{red}. Crystallographic analyses of this complex revealed the MCP binds the Zn²⁺ in a bidentate manner. Together, the data support a mechanism in which the nucleophile is activated in the same substrate-assisted manner as in the serine-dependent enzymes, but that in LigY, the nucleophile is water, such that C-C fission is preceded by a *gem*-diol intermediate. Overall, this thesis provides important insights into several lignin-degrading enzymes and the superfamilies to which they belong.

Lay Summary

The degradation of lignin, a major component of wood, is carried out by microorganisms. Many aspects of this degradation are poorly understood, even though it is essential to the global carbon cycle and has great potential for sustainably transforming plant biomass into commodity chemicals and fuels. This thesis describes the characterization of three enzymes that microorganisms use to degrade lignin. A variety of methodologies were used to determine what each enzyme does and how each enzyme works. The results provide fundamental insights into enzymes that catalyze an important biological process as well as into related enzymes involved in other processes.

Preface

This thesis, together with the manuscripts that comprised it, are original intellectual products of the author, Eugene Kuatsjah, under the guidance and mentorship of Prof. Lindsay D. Eltis. Parts of this thesis have been published in, or are in preparation for submission to, peer-reviewed journals. Three of these manuscripts are the result of collaborations with the laboratory of Prof. Michael E.P. Murphy at The University of British Columbia. In each, the Murphy lab was responsible for aspects of the x-ray crystallography. Key contributions were also made by the laboratories of Prof. Stephen G. Withers at The University of British Columbia and Prof. Victor Snieckus at Queen's University in the area of organic synthesis. All of the experiments were performed at The University of British Columbia, unless stated otherwise.

Chapter 1 and 6 contain parts of the four manuscripts described for Chapters 2-5 as well as elements from the literature as cited in the text. Sections on the non-heme iron oxygenases, MCP hydrolases, and the amidohydrolases are inspired by the doctoral works of Drs. Frédéric H. Vaillancourt, Pascal D. Fortin, Geoff P. Horsman, Antonio C. Ruzzini, Richard S. Hall, and Anna V. Vladimirova, respectively.

A version of Chapter 2: Characterization of lignostilbene- α,β -dioxygenase – LsdA is prepared for submission as: 'Kuatsjah E., Verstraete M.M, Kobylarz M.J., Liu A.K.N., Murphy M.E.P., and Eltis L.D. Identification of molecular determinants for substrate specificity in lignostilbene- α,β -dioxygenase'. In this study, I was responsible for the purification and the *in vitro* characterization of LsdA and its variants. The kinetic analysis was assisted by Alvin Ka Nok Liu, an undergraduate student from the Eltis lab working under my supervision. Drs. Meghan M. Verstraete and Marek J. Kobylarz from the laboratory of Prof. Michael E.P. Murphy were responsible for the structural refinements. The collection of inductively coupled plasma mass spectrometry (ICP-MS) data was assisted by Mariko Ikehata from the laboratory of Prof. Michael E.P. Murphy. Lignostilbene was synthesized by Dr. Timothy E. Hurst from the laboratory of Prof. Victor Snieckus.

The contents of Chapter 3 were published as: 'Kuatsjah E., Chen H.M., Withers S.G., and Eltis L.D. (2017) Characterization of an extradiol dioxygenase involved in the catabolism of lignin-derived biphenyl. *FEBS Letter.* **591**, 1001-1009' (1). Characterization of an extradiol dioxygenase involved in the catabolism of lignin-derived biphenyl. *FEBS Letter.* **591**, 1001-1009'. In this study, I was responsible for the purification and the *in vitro* characterization of LigZ and its cleavage product.

The kinetic characterization extends to evaluation of the mechanism-based inactivation. 2,2',3-Trihydroxy-3'-methoxy-5,5'-dicarboxybiphenyl (OH-DDVA) was synthesized by Dr. Hong-Ming Chen from the laboratory of Prof. Stephen G. Withers. The collection of nuclear magnetic resonance (NMR) spectroscopy data was assisted by Dr. Mark Okon from the laboratory of Prof. Lawrence P. McIntosh at The University of British Columbia. The high-resolution mass spectrometry (MS) data was collected by Drs. Israël Casabon and Jason C. Rogalski from the laboratory of Prof. Leonard J. Foster at The University of British Columbia. The ICP-MS data was collected by Mariko Ikehata. The strain SYK-6 (NBRC 103272) was procured from the National Institute of Technology and Evaluation Biological Resource Center (NBRC).

A version of Chapter 4: Characterization of DCHM-HOPDA hydrolase – LigY was published as: 'Kuatsjah E., Chan A.C.K., Kobylarz M.J., Murphy M.E.P., and Eltis, L.D. (2017) The bacterial *meta*-cleavage hydrolase LigY belongs to the amidohydrolase superfamily, not to the alpha/beta-hydrolase superfamily. *Journal of Biological Chemistry.* **292**, 18290-18302 (2). In this study, I was responsible for the purification and the *in vitro* characterization of LigY, its variants and hydrolysis products. Structural refinement and docking experiment were performed by Drs. Anson C. K. Chan and Marek J. Kobylarz from laboratory of Prof. Michael E. P. Murphy. The collection of ICP-MS data was assisted by Mariko Ikehata.

A version of Chapter 5 is reproduced with permission from *ACS Catalysis*, and is published as: Kuatsjah E., Chan A.C.K., Hurst T.E., Snieckus V., Murphy M.E.P., and Eltis L.D. (2018) Metal- and serine-dependent *meta*-cleavage product hydrolases utilize similar nucleophile-activation strategies (3). In this study, I was responsible for the transient-state kinetic analyses of the LigY-catalyzed reaction and the evaluation of substrate analogs. Dr. Anson C.K. Chan was responsible for the structural refinement and for producing Figures 5.10, 5.11, and 5.14. 5-Carboxy DHB and 5-methyl DHB were synthesized by Dr. Timothy E. Hurst. The properties of 4-methyl HOPDA were previously published in *ChemBioChem* in 2018 (4).

Table of Contents

Abstract.....	iii
Lay Summary.....	iv
Preface	v
Table of Contents	vii
List of Tables	xi
List of Figures.....	xii
List of Abbreviations	xv
Acknowledgements	xviii
Dedication	xix
Chapter 1: Introduction	1
1.1 Aromatic compounds.....	1
1.1.1 Lignin	1
1.1.1.1 Lignin valorization – the final frontiers in biomass processing	3
1.2 Catabolism of aromatic compounds by bacteria.....	4
1.2.1 <i>meta</i> vs. <i>ortho</i> cleavage	4
1.2.2 Peripheral vs. central aromatic pathway.....	6
1.2.3 Microbial lignin degradation	6
1.2.3.1 DDVA catabolism	9
1.2.3.2 DCA catabolism	9
1.2.3.3 GGE catabolism	10
1.2.3.4 Catabolism of other lignin-derived biaryls	10
1.3 Oxygenases	11
1.3.1 Non-heme iron oxygenases	12
1.3.1.1 Extradiol dioxygenases	12
1.3.1.1.1 Type-II extradiol dioxygenases	15
1.3.1.2 Carotenoid cleavage oxygenases	17
1.3.1.2.1 Stilbene-cleaving oxygenases.....	18
1.4 <i>meta</i> -Cleavage product hydrolases	20
1.4.1 Classification of MCP hydrolases	20
1.4.2 Mechanistic aspect of MCP hydrolases.....	21
1.4.2.1 Hydrolytic mechanism.....	23
1.4.2.2 Substrate ketonization	24
1.4.2.3 Characterization of ES ^{red}	25
1.4.3 Amidohydrolase superfamily	26
1.4.3.1 COG2159	28
1.5 Aims and scope of the dissertation	33
Chapter 2: Characterization of LsdA, a lignostilbene-α,β-dioxygenase.....	35
2.1 Introduction.....	35

2.2	Material and Methods	36
2.2.1	Chemical and reagents.....	36
2.2.2	DNA manipulation	36
2.2.3	Protein production and purification.....	36
2.2.4	Protein analytical methods.....	37
2.2.5	Steady-state kinetics	37
2.2.6	HPLC resolution of LsdA-catalyzed reaction.....	38
2.2.7	Protein structure determination	38
2.3	Results	41
2.3.1	Purification of LsdA	41
2.3.2	Substrate specificity.....	42
2.3.3	Structure of LsdA.....	44
2.1.1	Metal-binding site.....	47
2.1.2	Structure of the LsdA·phenylazophenol complex	47
2.1.3	Active-site variants	48
2.2	Discussion.....	50
Chapter 3: Characterization of LigZ, OH-DDVA dioxygenase.....	52	
3.1	Introduction.....	52
3.2	Material and Methods	53
3.2.1	Chemical and reagents.....	53
3.2.2	Cloning of <i>ligZ</i>	53
3.2.3	Production and purification of LigZ.....	53
3.2.4	Protein analysis method	54
3.2.5	Steady-state kinetics	54
3.2.6	Inactivation kinetics	55
3.3	Results & Discussion.....	57
3.3.1	Purification of LigZ	57
3.3.2	Substrate specificity.....	57
3.3.3	Inactivation of LigZ.....	58
3.3.4	Product identification	61
3.3.5	Non-enzymatic transformation of DCHM-HOPDA.....	64
Chapter 4: Characterization of LigY, DCHM-HOPDA hydrolase	66	
4.1	Introduction.....	66
4.2	Material and Methods	67
4.2.1	Chemicals and reagents	67
4.2.2	Cloning and mutagenesis	67
4.2.3	Protein production and purification.....	67
4.2.4	Protein analytical methods.....	68
4.2.5	SEC-MALS	69
4.2.6	CD spectroscopy	69

4.2.7	Steady-state kinetic analysis	69
4.2.8	Metal chelation and reconstitution	70
4.2.9	CHPD characterization	70
4.2.10	Protein structure determination	70
4.3	Results	72
4.3.1	LigY is an amidohydrolase.....	72
4.3.2	Purified LigY contains zinc.....	72
4.3.3	LigY hydrolyzes DCHM-HOPDA to 5CVA and CHPD	73
4.3.4	Steady-state kinetic analyses of LigY	75
4.3.5	Metal dependence of LigY activity	76
4.3.6	Structure of LigY	77
4.3.7	LigY metal-binding site	80
4.3.8	Inhibition of LigY activity by chloride.....	83
4.3.9	Methanolysis	83
4.3.10	Active-site variants	84
4.3.11	Modeling substrate-binding.....	86
4.4	Discussion.....	89
Chapter 5: Substrate activation strategy in a metal-dependent MCP hydrolase	92
5.1	Introduction.....	92
5.2	Material and Methods	93
5.2.1	Chemicals, reagents and enzymes.....	93
5.2.2	Production and characterization of 4-carboxy HOPDA and its cleavage products.....	93
5.2.3	Steady-State kinetic analyses	94
5.2.4	K_d determination for 4-methyl HOPDA	94
5.2.5	Transient-state kinetic analyses	95
5.2.6	Protein structure determination	95
5.2.7	Single crystal spectrophotometry.....	96
5.3	Results	97
5.3.1	Single turnover stopped-flow kinetic analysis.....	97
5.3.2	Reactivity of LigY with substrate analogs.....	99
5.3.3	Structure of LigY·4-methyl HOPDA complex	104
5.3.4	Optical spectroscopy with single crystals	109
5.4	Discussion.....	110
Chapter 6: Conclusion and future outlook	115
6.1	Overview.....	115
6.2	Catalytic mechanism of LSDs.....	115
6.3	Stability of the type-II extradiol dioxygenases and its MCP.....	115
6.4	Divergence in MCP hydrolysis	116
6.5	The development of biocatalysts for lignin valorization.....	117
Bibliography	119

Appendices	134
Appendix A Sequences of the synthesized DNA.....	134
A.1 Lignostilbene- α , β -dioxygenase LsdA (locus tag: 1917171A).....	134
A.2 DCHM-HOPDA hydrolase LigY (locus tag: SLG_07750).....	135
Appendix B Oligonucleotides used in this study.....	136
B.1 LsdA Primers	136
B.2 LigY Primers	137
Appendix C Fluorescence spectra of 5CVA	138
Appendix D Additional publications not included in this thesis	139

List of Tables

Table 2.1. Apparent steady-state kinetic parameters of LsdA for different substrates.....	43
Table 2.2. X-ray diffraction data collection and refinement statistics for LsdA structures . .	46
Table 2.3. Apparent steady-state kinetic parameters of LsdA and select variants.	49
Table 3.1. Apparent steady-state kinetic and inactivation parameters of LigZ	59
Table 4.1. LigY data collection and refinement statistics	76
Table 4.2. Relative activity of LigY variants.....	85
Table 4.3. Steady-state kinetic parameters of LigY and select variants.	85
Table 5.1. Reciprocal relaxation times and amplitudes for single-turnover reactions	99
Table 5.2. LigY·4-methyl HOPDA data collection and refinement statistics.....	106

List of Figures

Figure 1.1. Representation of linkages found in lignin and lignin biological depolymerization products.....	2
Figure 1.2. The convergent nature of bacterial aromatic catabolism.	5
Figure 1.3. Proposed DDVA and DCA catabolic pathways in SYK-6.....	8
Figure 1.4. The proposed catalytic mechanisms of homoprotocatechuate 2,3-dioxygenase. 13	
Figure 1.5. Crystal structure of protocatechuate-4,5-dioxygenase (LigAB) from SYK-6.....	16
Figure 1.6. Crystal structure of resveratrol-cleaving dioxygenase (CAO1) from <i>N. crassa</i>	18
Figure 1.7. Possible pathways for MCP hydrolysis.	21
Figure 1.8. Proposed catalytic mechanism of serine-dependent MCP hydrolase.	22
Figure 1.9. BphD _{LB400} ·HOPDA binary complexes.....	23
Figure 1.10. Representative stopped-flow experiment illustrating the formation of ES ^{red} in the BphD-catalyzed single turnover of HOPDA and commensurate decay of ESred and HPD formation.	24
Figure 1.11. Proposed catalytic mechanism of the subtype III amidohydrolase.	27
Figure 1.12. Active site architecture of 5CVA decarboxylase (LigW) from SYK-6.....	29
Figure 1.13. The proposed catalytic mechanism of LigW, a COG2159 decarboxylase.....	30
Figure 1.14. The proposed catalytic mechanism of LigJ, a COG2159 hydratase.	31
Figure 2.1. Reaction catalyzed by LsdA.	35
Figure 2.2. LsdA substrates and analogs.....	41
Figure 2.3. pH-dependent activity profile.	42
Figure 2.4. HPLC resolution of LsdA-catalyzed reaction.....	42
Figure 2.5. Steady-state kinetic analyses of the LsdA-catalyzed reaction.	43
Figure 2.6. Dixon plot of the inhibition of LsdA-catalyzed lignostilbene cleavage by phenylazophenol.....	44
Figure 2.7. Crystal structure of LsdA dimer and protomer.	45
Figure 2.8. The surface electrostatic analyses of LsdA.	45
Figure 2.9. The active site of LsdA.....	47
Figure 3.1. Proposed reaction catalyzed by LigZ of SYK-6.	52

Figure 3.2. Potential modes of inactivation in extradiol dioxygenases during steady-state turnover.....	55
Figure 3.3. pH-dependence of LigZ activity.....	57
Figure 3.4. Steady-state kinetic analyses of the LigZ-catalyzed reaction.....	58
Figure 3.5. Inactivation of LigZ.	59
Figure 3.6. Decay of DCHM-HOPDA.....	60
Figure 3.7. Derivatization of DCHM-HOPDA with ammonia.	61
Figure 3.8. High-resolution MS spectrum of ammonia derivatized DCHM-HOPDA.....	62
Figure 3.9. NMR analyses of ammonia-derivatized DCHM-HOPDA.	63
Figure 3.10. HPLC chromatograms of the pyridine derivatives of PCA cleavage products....	63
Figure 3.11. UV-visible absorption spectra of DCHM-HOPDA.	64
Figure 3.12. Discontinuous measurement of DCHM-HOPDA stability.....	65
Figure 4.1. Proposed reaction catalyzed by LigY of SYK-6.	66
Figure 4.2. Biophysical properties of LigY.	73
Figure 4.3. HPLC resolution of LigY-catalyzed DCHM-HOPDA hydrolysis products and MS analysis of CHPD.....	74
Figure 4.4. HPLC and MS analyses of DNPH-derivatized α -ketoacids.	74
Figure 4.5. Steady-state kinetic hydrolysis of DCHM-HOPDA by LigY.....	75
Figure 4.6. Structures of the LigY hexamer and protomer.	78
Figure 4.7. The amino acid conservation and surface electrostatic analyses of the inter-protomer interactions.	79
Figure 4.8. Topology diagram of LigY.....	79
Figure 4.9. The anomalous density map of LigY active site.....	81
Figure 4.10. The Zn ²⁺ -binding site of LigY.....	82
Figure 4.11. The effect of chloride on LigY activity.	83
Figure 4.12. LigY-catalyzed hydrolysis of DCHM-HOPDA in presence of methanol.....	84
Figure 4.13. Models of the LigY·DCHM-HOPDA complex.	87
Figure 4.14. Proposed mechanism of LigY.	88
Figure 5.1. Substrate analog used in this study and the putative lactone of HOPDA.	97
Figure 5.2. The single turnover of DCHM-HOPDA by LigY.	98

Figure 5.3. Apparent pK_a of 4-carboxy HOPDA	100
Figure 5.4. MS analysis of ammonium-derivatized 4-carboxy HOPDA	100
Figure 5.5. NMR analyses of ammonium-derivatized 4-carboxy HOPDA.....	101
Figure 5.6. HPLC resolution of 4-carboxy HOPDA hydrolysis products.	102
Figure 5.7. The steady-state hydrolysis of 4-carboxy HOPDA by LigY.....	103
Figure 5.8. Dixon plot of the inhibition of LigY-catalyzed DCHM-HOPDA hydrolysis by 4-methyl HOPDA.	103
Figure 5.9. Binding of 4-methyl HOPDA to LigY.	104
Figure 5.10. Structure of the LigY·4-methyl HOPDA complex.....	105
Figure 5.11. The configuration of 4-methyl HOPDA and DCHM HOPDA in the LigY active site.....	107
Figure 5.12. The Zn^{2+} coordination sphere of LigY in the presence of different ligands....	108
Figure 5.13. An updated mechanism for LigY.	110
Figure 5.14. An active site overlay of the LigY·4-methyl HOPDA and ligand-free LigY structures.	113
Figure 6.1. Fluorescence spectra of 5CVA.....	138

List of Abbreviations

β -KA	2-oxoadipate
γ -RSD	gamma-resorcylate decarboxylase
3CM	3-carboxymuconate
5CVA	5-carboxyvanillate
ACMSD	α -amino- β -carboxymuconate- ϵ -semialdehyde decarboxylase
ADA	adenosine deaminase
ADH	alcohol dehydrogenases
ALDH	aldehyde dehydrogenases
CAO1	carotenoid oxygenase 1
CCO	carotenoid cleavage oxygenase
CD	circular dichroism
CDA	cytosine deaminase
CHA	4-carboxy-4-hydroxy-2-oxoadipate
CHES	N-cyclohexyl-2-aminoethanesulfonic acid
CHMS	4-carboxy-2-hydroxymuconate-6-semialdehyde
CHPD	4-carboxy-2-hydroxypenta-2,4-dienoate
CLS	Canadian Light Source
COGs	clusters of orthologous groups
DCA	dehydroniconiferyl alcohol
DCA-C	3-(2-(4-hydroxy-3-methoxyphenyl)-3-(hydroxymethyl)-7-methoxy-2,3-dihydrobenzofuran-5-yl)acrylic acid
DCA-CC	5-(2-carboxyvinyl)-2-(4-hydroxy-3-methoxyphenyl)-7-methoxy-2,3-dihydrobenzofuran-3-carboxylic acid
DCA-S	3-(4-hydroxy-3-(4-hydroxy-3-methoxystyryl)-5-methoxyphenyl)-acrylate
DCHM-HOPDA	4,11-dicarboxy-8-hydroxy-9-methoxy-2-hydroxy-6-oxo-6-phenyl-hexa-2,4-dienoate
DDVA	5,5'-dehydronivanillate / 2,2'-dihydroxy-3,3'-dimethoxy-5,5'-dicarboxy-biphenyl
DHB	dihydroxybiphenyl
DMF	dimethylformamide
DMSO	dimethyl sulfoxide
DTT	dithiothreitol
EDTA	ethylenediaminetetraacetic acid
EPR	electron paramagnetic resonance
GGE	guaiacylglycerol- β -guaiacyl ether
GMC	glucose-methanol-choline
GS-HPV	α -glutathionyl- β -hydroxy-propiovanillone

HEPES	4-(2-hydroxyethyl)-1-piperazineethanesulfonic acid
HEPPS	4-(2-hydroxyethyl)-1-piperazinepropanesulfonic acid
HMPPD	1,2-bis(4-hydroxy-3-methoxyphehyl)-1,3-propanediol.
HOPDA	2-hydroxy-6-oxo-6-phenyl-hexa-2,4-dienoate
HPD	2-hydroxypenta-2,4-dienoate
HPLC	high performance liquid chromatography
HPV	β -hydroxy-propiovanillone
ICP-MS	inductively coupled plasma mass spectrometry
IDCase	iso-orotate decarboxylase
IPTG	isopropyl β -D-thiogalactopyranoside
k_{cat}	turnover number
k_{cat}/K_M	specific activity
KCH	(3Z)-2-keto-4-carboxy-3-hexenedioate
K_{ic}	competitive inhibition constant
K_{iu}	uncompetitive inhibition constant
K_M	Michaeles constant
LC	liquid chromatography
LSD	lignostilbene- α,β -dioxygenases
MCP	<i>meta</i> -Cleavage product
MES	2-(N-morpholino)ethanesulfonic acid
MOPS	3-(N-morpholino)propanesulfonic acid
MPHPV	α -(2-methoxyphenoxy)- β -hydroxypiovanillone
MS	mass spectrometry
NBRC	National Institute of Technology and Evaluation Biological Resource Center
NMR	nuclear magnetic resonance
OH-DDVA	2,2',3-trihydroxy-3'-methoxy-5,5'-dicarboxybiphenyl
OMA	4-oxalomesaconate
PAGE	polyacrylamide gel electrophoresis
PAR	4-(2-pyridylazo)-resorcinol
PCA	protocatechuate
PCD	protocatechuate-4,5-dioxygenase
PDB	Protein Data Bank
PDA	photodiode array
PDC	2-pyrone-4,6-dicarboxylate
Pfam	protein families
PIPES	piperazine-N,N'-bis(2-ethanesulfonic acid)
ppm	parts per million
RHA1	<i>Rhodococcus jostii</i> RHA1
RMSD	root-mean-square deviation

SEC-MALS	size exclusion chromatography-multi-angle light scattering
sKIE	solvent kinetic isotope effect
SSRL	Stanford Synchrotron Radiation Lightsource
SYK-6	<i>Sphingomonas paucimobilis</i> SYK-6
$t_{1/2}$	half-life
TAPS	<i>N</i> -[tris(hydroxymethyl)methyl]-3-aminopropanesulfonic acid
TCEP	tris(2-carboxyethyl)phosphine hydrochloride
TEV	tobacco-etch virus
TMY1009	<i>Sphingomonas paucimobilis</i> TMY1009
t_R	retention time
Tris	2-amino-2-(hydroxymethyl)propane-1,3-diol
WT	wild-type
XAS	x-ray absorption spectroscopy

Acknowledgements

First and foremost, I would like to thank my family, especially my mother, Liana Agus and my father, Agus Kuatsjah. It is their enduring love and support that made all things possible.

I am thankful for my supervisor Prof. Lindsay D. Eltis for the opportunity, guidance, patience, and continuing support over the years. I am also grateful to past and present colleagues of the Eltis lab for their tutelage and friendship, as well as for sharing numerous cups of coffee: Drs. Rahul Singh, Antonio C. Ruzzini, Nicolas Seghezzi, Sawsan Amara, Hiroshi Otani, among others.

Next, I want to thank my supervisory committee members: Stephen G. Withers, Michael E. P. Murphy, and Nobuhiko Tokuriki for their scientific insights. I also want to thank the Microbiology and Immunology department at UBC which acted as my surrogate home department.

I am indebted to all the collaborators without whom this endeavour would be impossible. I would like to thank Drs. Hong-Ming Chen and Timothy E. Hurst, from the Withers and Snieckus labs, respectively for the provision of the chemical reagents. Drs. Anson C. K. Chan, Meghan M. Verstraete, Marek J. Kobylarz from the Murphy lab are thanked for all aspects regarding x-ray crystallography. In addition, Drs. Mark Okon from the McIntosh lab is thanked for continual assistance in NMR analysis.

I'd also like to thank friends, old and new, that I have made along this journey for each of them truly enrich my life experience. I am thankful for the LSI community, in particular working in proximity with these groups: Beatty, Bromme, McIntosh, Mauk, Mohn, and Murphy. I'd like to acknowledge these fine individuals: Dr. Federico I. Rosell, Dr. Hao Ding, Shinako Takimoto, fellow 3rd GSAT cohorts: Dr. Cecilia Perez-Borrajero and Andrew K.O. Wong, Pavneet K. Kalsi, Angelé Arrieta, the aforementioned members of the Murphy groups, and many others for their help along the way. I also want to thank people outside the research community; in particular are Lucianne Galang, the Seraphim choir group, and the Indonesian Catholic Society (UKIBC) for providing a home away from home.

Finally, I would like to thank the Genome Science and Technology graduate program for the funding, support, and opportunity to learn the wonderful craft of protein biochemistry.

To my grandmothers, Hie Fon Moy and Lim Joeng Sim.

Chapter 1:

Introduction

1.1 Aromatic compounds

Aromatic compounds are ubiquitous in Nature and play many essential biological functions. They range in size from small molecules such as amino acids, to large polymers such as lignin (Figure 1.1). As used in the common vernacular, some of these compounds are volatile and act as olfactory sensitizers; compounds such as vanillin, benzaldehyde, and eugenol are partly responsible for the scent of vanilla, almond, and clove, respectively. From a chemistry perspective, aromaticity is a property of planar cyclic molecules bearing fully conjugated π systems that obey Hückel's rule ($4n+2$ π -electrons). The resulting resonance from π -electron delocalization lowers the overall energy of the system thereby imparting additional stability on these molecules. In the case of benzene, the resulting resonance adds ~ 150 kJ/mol of stability relative to the sum of the individual double bonds in cyclohexene (5). Additionally, aromatic moieties may interact with one another through $\pi - \pi$ stacking. This is important in biological processes such as nucleobase stacking, protein folding, and protein ligand recognition.

1.1.1 Lignin

Lignin is a heterogeneous aromatic polymer naturally found in complex with cellulose and hemicellulose to form the woody material of plants. Lignin is the second most abundant polymer in the biosphere after cellulose (6). With 1.5×10^{10} tons yearly influx coming from atmospheric carbon, it has been estimated that $\sim 30\%$ of non-fossil organic carbon in the biosphere is sequestered as lignin (7,8). Plants and some species of algae synthesize lignin through radical coupling of monolignol precursors, the most common ones being: *p*-coumaryl, coniferyl, and sinapyl alcohols (9). The ratio of these precursors varies between species and partly defines the polymer's nature. For example, softwood lignin (e.g., pine and spruce) consists primarily of coniferyl units and thus contains higher degree of branching relative to hardwood lignin (e.g., maple and oak) which contains both coniferyl and sinapyl units. Despite limited number of precursors, the inherent stochasticity of radical polymerization results in the complex structure of lignin. In contrast to the regular $\beta(1,4)$ glycosidic

linkage found in cellulose, lignin is joined together through various ether and C-C bond linkages including β -aryl ether, di-aryl propane, biphenyl, diaryl ether, phenylcoumarane, spirodienone, and pinoresinol linkages to name a few (Figure 1.1) (10). This heterogeneity is by design as it contributes to the recalcitrance of plant cell wall. This same heterogeneity poses a tremendous challenge for breaking down lignin and lignocellulose in the biorefinery.

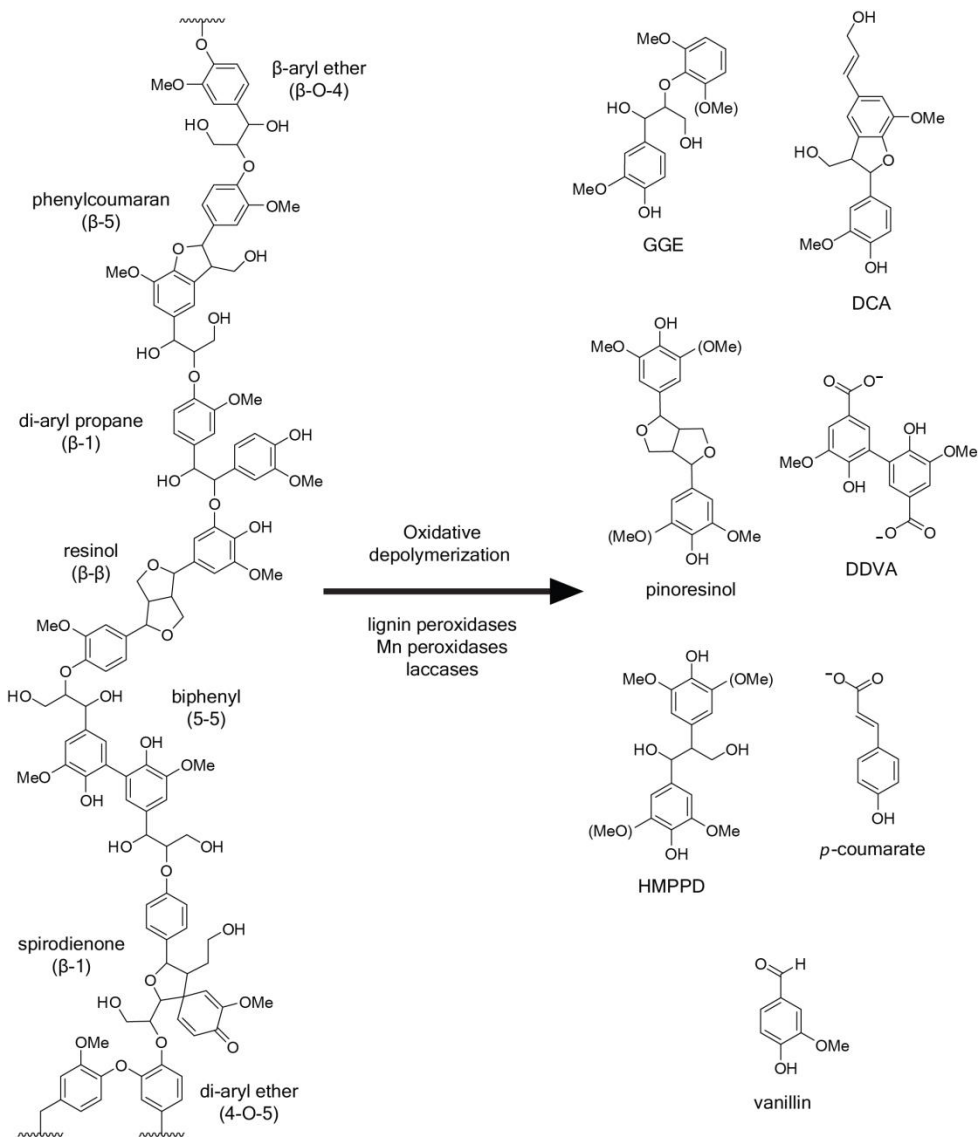


Figure 1.1. Representation of linkages found in lignin and lignin biological depolymerization products.

Abbreviations: GGE, guaiacylglycerol- β -guaiacyl ether; DCA, dehydrodiconiferyl alcohol; DDVA, 5,5'-dehydrodivanillate; HMPPD, 1,2-bis(4-hydroxy-3-methoxyphehyl)-1,3-propanediol.

1.1.1.1 Lignin valorization – the final frontiers in biomass processing

Lignocellulosic biomass offers a renewable source of second-generation biofuels, high-value aromatic compounds and other biomass-derived products (11). Thus, the degradation products of lignin and cellulose are of considerable interest both as a potential solution to curb the world's dependency on petrochemicals, and to address the dwindling reserve and adverse environmental effects from the use of fossil fuels. In industrial applications, such as pulp mills and bioethanol refineries, lignin is produced as a by-product and traditionally burned off as fuel. Raw lignocellulosic biomass (e.g., wood chips) undergoes a pulping process to remove lignin and hemicellulose and only the purified cellulose fiber typically enters downstream processing. Indeed, lignin production is so vast, it often exceeds the requirement for internal energy use by its combustion (12). More importantly, technoeconomic analyses indicate that lignin must be better valorized to make bioethanol economically sustainable (11,13). With the expected increase in bioethanol output in the near future, combined with the steady stream of raw material from both agriculture and forestry sources, it is imperative to find new means to generate value-added product from lignin (11).

Despite its considerable potential, there remain significant challenges in efficient lignin deconstruction and valorization. Biological pretreatment and processes offer a potentially more sustainable method of lignocellulose deconstruction. Recent advances in the field include the addition of enzymatic pretreatment targeting lignin linkages which improve the separation process and glucose yield from poplar biomass (14). Moreover, genetic screening and engineering efforts have been utilized *in planta* with the goal to reduce the recalcitrance of the cell wall which in turn facilitates bioconversion and recovery. More specifically, plant strains are being engineered with monolignols that resist polymerization (15,16). Overall, increasing the processing capacity and efficiency of lignin valorization are critical steps for a viable bioeconomy.

1.2 Catabolism of aromatic compounds by bacteria

Microorganisms play an integral role in the global carbon cycle (17). While the different microbial processes that contribute to this cycle remains an active field of research; their importance is well established. This is illustrated by microbial photosynthesis, which sequesters atmospheric carbon, and microbial catabolic processes that break down biomass, allowing carbon re-assimilation. Indeed, microorganisms are able to degrade and grow on compounds that are not degraded by other organisms, including many aromatic compounds.

Microorganisms have evolved numerous aerobic and anaerobic strategies for catabolizing aromatic compounds (18,19). Despite their diversity, these strategies share a common catabolic logic: the aromatic ring is activated then subsequently cleaved. Activation involves various substitutions on the benzene ring to provide a reactive site to overcome the aforementioned resonance-induced stabilization. In anaerobic catabolism, a typical substitution is carboxylation to eventually form benzoyl-coenzyme A, which is subject to reductive dearomatization and hydrolytic ring opening (19). In aerobic catabolism, ring activation and cleavage are typically catalyzed by oxygenases (20). For example, flavin-dependent monooxygenases and Rieske non-heme iron dioxygenases catalyze mono- and dihydroxylation, respectively, to generate a catechol which is cleaved by an extradiol or intradiol dioxygenase, as described below (Figure 1.2) (21,22). In “hybrid” pathways, O₂ is utilized in ring activation or cleavage, but not in both steps (23). Iterations of these processes are used to catabolize polycyclic aromatic hydrocarbons. The catabolism of the side-chain often takes precedence over the aromatic nucleus. The overall efficiency of the strategy is highlighted by the aerobic catabolism of steroids, which proceeds via the aromatization of a steroid ring followed by its extradiol cleavage (24).

1.2.1 *meta* vs. *ortho* cleavage

The ring fission of catechols, including protocatechuate, may occur in either *meta*- or *ortho*-fashion, as defined by the position of the cleaved C-C bond relative to the hydroxyl groups (18,25). *meta*- and *ortho*-cleavage are catalyzed by extradiol and intradiol dioxygenases, respectively (Figure 1.2). Despite the minor apparent distinction between these two reactions, they are catalyzed by different enzyme classes with distinct catalytic mechanisms (26). For example, extradiol and intradiol dioxygenases typically contain non-heme Fe²⁺ and Fe³⁺, respectively.

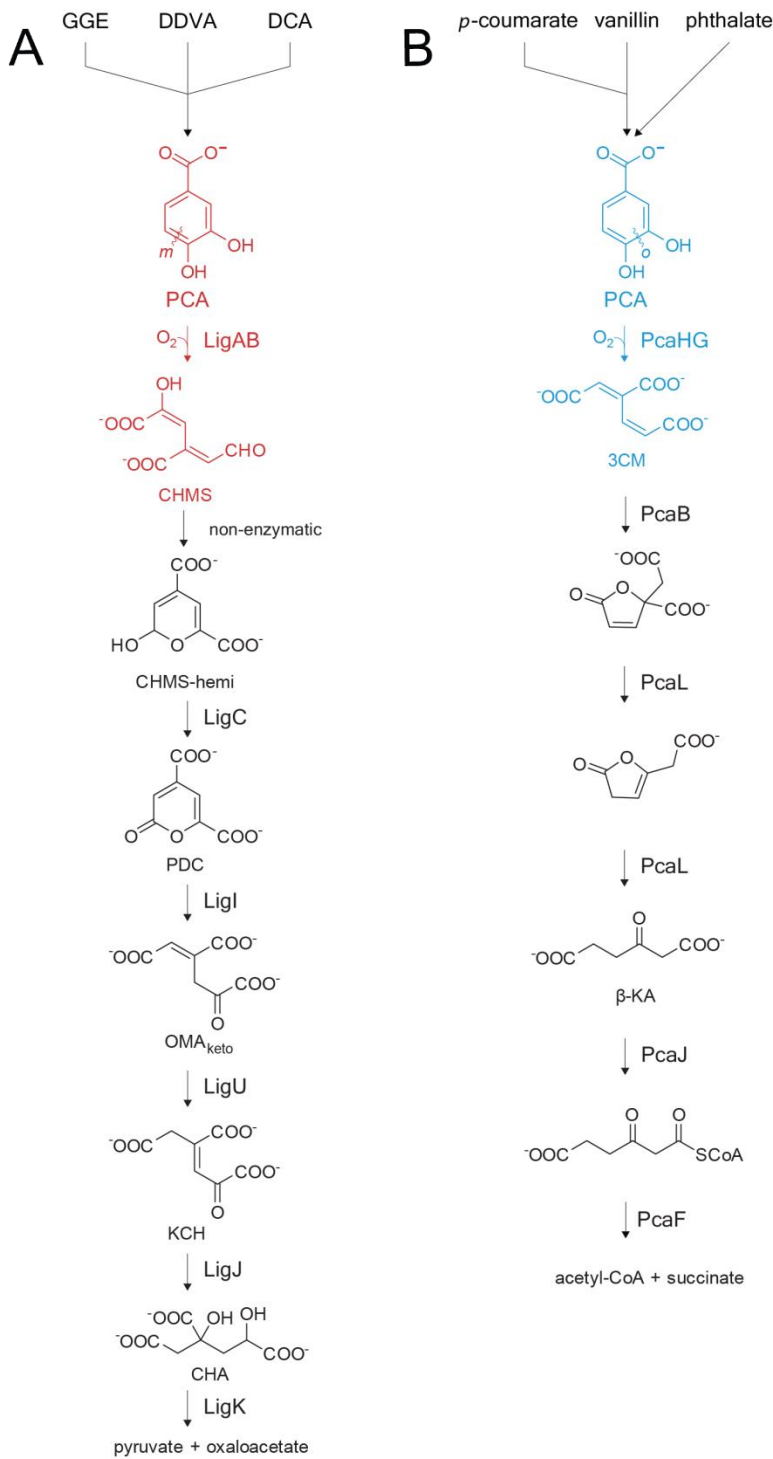


Figure 1.2. The convergent nature of bacterial aromatic catabolism.

(A) In SYK-6, lignin-derived compounds including GGE, DDVA, and DCA are funneled via peripheral pathways into a *meta*-cleavage central aromatic pathway. In this pathway, LigAB, protocatechuate 4,5-dioxygenase, catalyzes extradiol ring cleavage (red). (B) In RHA1, *p*-coumarate, vanillin, and phthalate are funneled via the peripheral Cou, Van and Pad pathways, respectively, into the

β -ketoadipate pathway, a central aromatic pathway. In this pathway, PcaHG, protocatechuate 3,4-dioxygenase, catalyzes intradiol ring cleavage (blue). Abbreviations: PCA, protocatechuate; CHMS, 4-carboxy-2-hydroxymuconate-6-semialdehyde; PDC, 2-pyrone-4,6-dicarboxylate; OMA, 4-oxalomesaconate; KCH, (3Z)-2-keto-4-carboxy-3-hexenedioate; CHA, 4-carboxy-4-hydroxy-2-oxoadipate; 3CM, 3-carboxymuconate; β -KA, 2-oxoadipate. Adapted from Eltis and Singh (27).

1.2.2 Peripheral vs. central aromatic pathway

Studies have revealed that genera such as *Sphingomonas*, *Pseudomonas*, and *Rhodococcus* catabolize a wide range of aromatic compounds, and that the pathways responsible for these processes are organized in a modular, convergent fashion (28,29). More specifically, growth substrates are initially transformed via peripheral aromatic pathways which converge to a limited number of shared intermediates which are then transformed to central metabolites via central aromatics pathway (Figure 1.2). For example, in *Rhodococcus jostii* RHA1 (RHA1 hereafter), vanillate and phthalate are transformed via the Van and Pad peripheral pathways, respectively, to protocatechuate, which is then transformed to central metabolites via the β -ketoadipate pathway (30,31). The convergence is further illustrated by the catabolism of benzoate, which is catabolized to catechol by the Ben pathway, which is also further transformed to central metabolites via the β -ketoadipate pathway (30). This modular and convergent nature can be exploited in engineering biocatalysts by funneling mixtures of aromatic compounds, such as those generated through the depolymerization of lignin, to target metabolites (32).

1.2.3 Microbial lignin degradation

Microorganisms are the only organisms known to degrade lignin. This degradation occurs in two stages: depolymerization of the lignin polymer followed by the catabolism of the generated smaller aromatic compounds (Figure 1.1) (33). The initial depolymerization involves secreted enzymes acting with diffusible intermediates. This process has been primarily attributed to fungi, of which the white-rot and brown-rot basidiomycetes have been most extensively studied (34). White-rot basidiomycetes, exemplified by *Phanerochaete chrysosporium*, employ an arsenal of extracellular laccases and peroxidases for their lignolytic activity, and often form white, cellulose-enriched biomass. Laccases and peroxidases utilize redox mediators, such as Mn^{2+} and veratryl alcohol, as diffusible oxidants to penetrate the lignin (35). Brown-rot basidiomycetes use Fenton chemistry for its lignolytic activity. Lignin degradation is less complete relative to the white-rot, as reflected by the brown-colored, oxidized lignin associated with brown-rot degraded biomass (36,37). Despite tremendous

insight into fungal lignin degradation, this process has not been translated into applications, due in part to the challenges of producing and manipulating lignolytic fungi and their gene products at an industrial scale. Importantly, fungi do not appear to grow on lignin depolymerization products. Instead, their lignolytic activity appears to primarily increase the bioavailability of cellulose and hemicellulose as growth substrates.

Bacteria are generally thought to play second fiddle in lignin depolymerization. By contrast, they play a major role in degrading the small aromatic compounds liberated by the fungal depolymerization. This catabolism occurs as described above. Nevertheless, there is a growing body of literature describing the lignolytic properties of bacteria, including the ability to mineralize isotopically labelled lignin (38,39). Several genera of bacteria, including *Streptomyces*, *Amycolatopsis*, *Pseudomonas*, *Sphingobium*, *Nocardia*, and *Rhodococcus*, have been shown to at least partly modify native and industrial lignins. It remains unclear how much bacteria contribute to the depolymerization of lignin in Nature. Nevertheless, bacteria possess several properties which make them an attractive platform for biocatalyst development.

Recent advances in culture-independent and “omics” approaches have greatly facilitated bioprospecting efforts for novel bacterial ligninases (40). For example, bioinformatic analyses complemented with genetic and biochemical studies of bacterial soil isolates led into the identification of two lignolytic dye-decolorizing peroxidases, DypB from RHA1 and DypP2 from *Amycolatopsis* sp.75iv2 (41,42). Furthermore, metagenomic analyses have enabled access to the tremendous genetic potential of the unculturable members of the population. One particular application is in the high-throughput screening of environmental libraries. These screening efforts have benefitted from the development and miniaturization of various spectroscopic techniques which includes the use of engineered fluorescent-reporter strain equipped with promotor sensitive towards small aromatics (40,43). Fruits of these endeavors include the identification of a lignin-active bacterial multicopper oxidase from a coal bed metagenomic library (40). The native function of these oxidases remains unknown; however, their properties are analogous to those of their fungal counterpart, and thus appropriated for lignin oxidation.

The discovery that bacteria are able to at least partially deconstruct lignin has accelerated the study of enzymes and pathways involved in lignin depolymerization and the catabolism of the resulting products (33,38). Among bacterial strains able to grow on lignin-derived aromatic compounds, *Sphingobium* sp. strain SYK-6 (SYK-6 hereafter) is one of the best characterized, with pathways hav-

ing been identified for the catabolism of β -aryl ethers, pinoresinol, diaryl propane, phenylcoumarane and 2,2'-dihydroxy-3,3'-dimethoxy-5,5'-dicarboxybibhenyl (5,5'-dehydrodivanillate; DDVA) (44,45). The catabolism of these lignin-derived aromatics is effected by peripheral pathways which converge into central aromatic pathways, as described in Section 1.2.2.

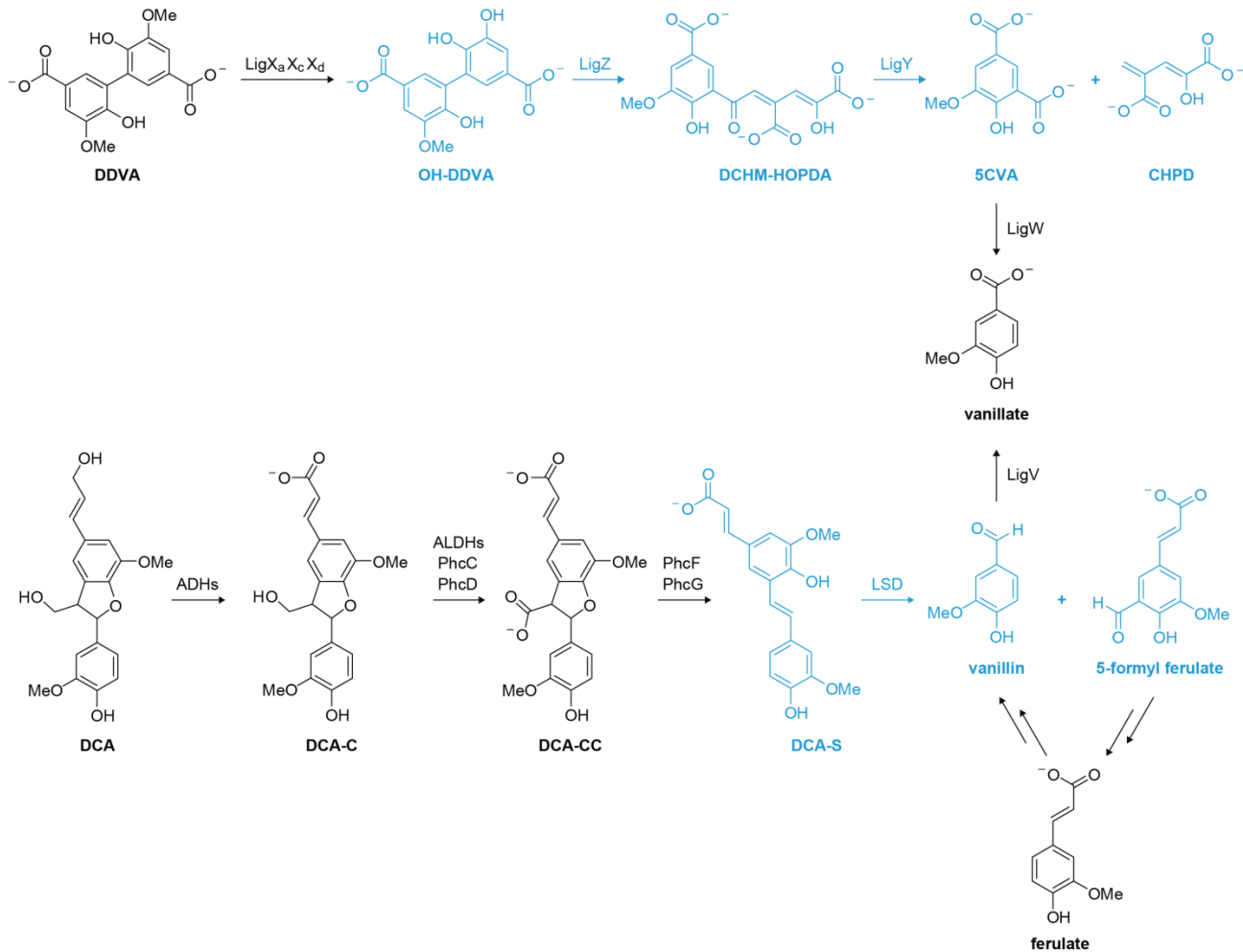


Figure 1.3. Proposed DDVA and DCA catabolic pathways in SYK-6.

The pathways are discussed in 1.2.3.1 and 1.2.3.2, respectively. The pathways converge at vanillate, which is catabolized via a *meta*-cleavage pathway (Fig. 1.2). The LigZ, LigY, and LSD reactions are coloured blue. Adapted from Kamimura *et al.* (29).

1.2.3.1 DDVA catabolism

The bacterial catabolism of lignin-derived biphenyl is exemplified by DDVA catabolism in SYK-6 (Figure 1.3) (29). The 5,5'-bond constitutes up to 25% and 9% of the inter-subunit linkages in softwood and hardwood lignin, respectively (10,46). The catabolism of DDVA has been genetically elucidated and most of the enzymes have been characterized (29). This pathway appears to be similar to the aerobic catabolism of biphenyl in bacteria in which a catechol is formed, cleaved by an extradiol dioxygenase to yield a *meta*-cleavage product (MCP) that is subsequently hydrolyzed (47). In the case of DDVA, the substrate is demethylated by a three-component Rieske-type oxygenase, LigX_a, LigX_c and LigX_d, to yield 2,2',3-trihydroxy-3'-methoxy-5,5'-dicarboxybiphenyl (OH-DDVA) (48,49). The extradiol dioxygenase that cleaves this catechol is LigZ (1,50). The resulting MCP, 4,11-dicarboxy-8-hydroxy-9-methoxy-2-hydroxy-6-oxo-6-phenyl-hexa-2,4-dienoate (DCHM-HOPDA), is transformed by LigY (2,51). However, LigY does not share significant amino acid sequence identity with known MCP hydrolases and of the two proposed hydrolysis products, 5-carboxyvanillate (5CVA) and 4-carboxy-2-hydroxypenta-2,4-dienoate (CHPD), only the former has been identified. Finally, 5CVA is decarboxylated by LigW to yield vanillate (52).

1.2.3.2 DCA catabolism

The catabolism of lignin-derived phenylcoumaranes is exemplified by dehydrodiconiferyl alcohol (DCA) catabolism in SYK-6 (Figure 1.3) (53). The β-5-bond constitutes up to 12% and 11% of the linkages in softwood and hardwood lignin, respectively (10,46). In the DCA pathway, the substrate undergoes a series of oxidations by non-specific alcohol dehydrogenases (ADH) and aldehyde dehydrogenases (ALDH) to produce 3-(2-(4-hydroxy-3-methoxyphenyl)-3-(hydroxymethyl)-7-methoxy-2,3-dihydrobenzofuran-5-yl) acrylic acid (DCA-C) (53). Subsequently, DCA-C undergoes successive stereospecific oxidation to 5-(2-carboxyvinyl)-2-(4-hydroxy-3-methoxyphenyl)-7-methoxy-2,3-dihydrobenzofuran-3-carboxylic acid (DCA-CC). These reactions are catalyzed by PhcC and PhcD, membrane-associated members of the glucose-methanol-choline (GMC) oxidoreductase family (54). Finally, stereoisomers DCA-CC are decarboxylated by PhcF and PhcG, respectively to 3-(4-hydroxy-3-(4-hydroxy-3-methoxystyryl)-5-methoxyphenyl)-acrylate (DCA-S) (55). The resulting stilbene, DCA-S, is thought to be cleaved by a lignostilbene-α,β-dioxygenase (LSD), of which SYK-6 has eight homologs (55).

1.2.3.3 GGE catabolism

The β -O-4 bond is the most abundant linkage in lignin, constituting up to half of the inter-subunit linkages (46). The bacterial catabolism of lignin-derived β -aryl ethers is best described for the catabolism of GGE in SYK-6 (56). The four stereoisomers of GGE are oxidized to form the two enantiomers of α -(2-methoxyphenoxy)- β -hydroxypropiovanillone (MPHPV) (57). These reactions are catalyzed by stereospecific NAD⁺-dependent C α -dehydrogenases: LigD and LigO catalyze the oxidation of the α (R) stereoisomer of GGE, while LigL and LigN catalyze the oxidation of the β (R) stereoisomer (58). The two isomers of MPHPV are subsequently cleaved by stereospecific glutathione S-transferases to yield α -glutathionyl- β -hydroxy-propiovanillone (GS-HPV) and guaiacol: the β (S) isomer of MPHPV is cleaved by LigF, and the β (R) isomer is cleaved by LigE and LigP (59,60). The glutathione of GS-HPV is removed by an omega class glutathione transferase to produce β -hydroxy-propiovanillone (HPV) (61). LigG catalyzes the removal of glutathione from β (S)-GS-HPV, and SLG_04120 is proposed to act on β (R)-GS-HPV (58). Finally, the catabolism of HPV to vanillate is proposed to proceed via successive oxidation and thioesterification reactions to produce a 4-hydroxy-3-methoxyphenyl- β -ketopropionyl-CoA intermediate (62). While not all of these enzymes have been characterized, the oxidation of HPV to vanilloyl acetaldehyde is catalyzed by HpvZ, a GMC oxidoreductase (62).

1.2.3.4 Catabolism of other lignin-derived biaryls

The catabolism of other lignin-derived compounds such as the pinoresinol (β - β linkage) and HMPPD (β -1 linkage) remain poorly understood in part due to the low percentage of these linkages in lignin. In SYK-6, PinZ catalyzes a two-step reductive cleavage of the ether linkages of pinoresinol to produce a seco-isolariciresinol (63). However, the subsequent catabolism of the metabolite is unknown as SYK-6 is unable to grow on pinoresinol (63). The catabolism of HMPPD has been previously reported in *Sphingomonas paucimobilis* TMY1009 (TMY1009 hereafter) (64). In this pathway, HMPPD is subject to Cy-deformylation to form a stilbene which is cleaved by an LSD (65). The identity of the enzyme catalyzing this deformylation is unclear as neither the amino acid sequence of the protein nor the nucleotide sequence of the gene have been reported.

1.3 Oxygenases

Oxygenases (EC 1.13 or EC 1.14) catalyze the oxidation of organic substrates by incorporating one or both atoms of O₂ into it (66). Monooxygenases incorporate one atom from O₂ into the substrate while dioxygenases incorporate both atoms into it. Analyses of the product's isotopic distribution upon reaction with isotopically labelled water and O₂ are typically used in this determination. These experiments should be performed with rigor and care as the atom of interest, such as carbonyl in aldehydes, can rapidly exchange with the solvent, thereby obscuring the final tally; moreover, this process may also be exacerbated in the presence of the enzyme. In monooxygenase reactions, the second oxygen atom from O₂ is typically reduced to water. In some monooxygenase reactions, a second atom of oxygen is incorporated into the substrate but originates from a water molecule (67)

Oxygenases activate O₂ for various biochemical transformations with an exquisite spatial and temporal specificity. More specifically, the uncatalyzed reaction between O₂ and organic substrate is thermodynamically favorable, but does not proceed spontaneously as it is kinetically impaired because O₂ exists primarily in the triplet ground state, which is unreactive with organic compounds. Oxygenases activate O₂ from this ground state to the more reactive singlet or doublet species. Indeed, these enzymes typically generate species of even greater reactivity by cleaving the O-O bond. The electrons that are required for oxygenase reactions can originate from reduced pyridine nucleotides, a sacrificial co-substrate (e.g., α -ketoglutarate), ascorbate, or the organic substrate itself (68). In nature, oxygenases are predominantly metalloenzymes and use redox active transition metal ions such as Fe²⁺, Cu⁺, and Mn²⁺ as cofactors to bind and activate the O₂. Copper oxygenases include laccases, some of which are involved in initial lignin depolymerization as described above (69). Iron-containing oxygenases include the extradiol and intradiol dioxygenases and lignostilbene dioxygenase (70,71). In some cases, the metal ion can be incorporated into a prosthetic group, as exemplified by cytochromes P450 and other heme-dependent oxygenases (72). By contrast, metal-independent oxygenases include flavin-containing oxygenases, examples of which are involved in the degradation of xenobiotics, drug metabolites, and steroids (73,74). Further, there exist at least two families of oxygenases without any apparent requirement for cofactors: the quinone-forming monooxygenases involved in the biosynthesis of several aromatic polyketide antibiotics and the bacterial dioxygenases involved in the cleavage of 3-hydroxy-4-quinolones (75).

1.3.1 Non-heme iron oxygenases

Non-heme iron oxygenases are widely distributed throughout biological systems and catalyze an enormous variety of oxygenation reactions. A common motif used by these enzymes to coordinate the metal ion is the “2-His-1-carboxylate facial triad” (Figure 1.4B) (76). The facial triad provides up to three sites to coordinate the substrates and to orchestrate the reaction. This is in contrast to the single open site afforded by the heme cofactor. Further, the three sites are in proximity to each other, allowing the juxtaposition of the reactants to promote catalysis. Non-heme iron oxygenases may use either Fe^{2+} or Fe^{3+} for substrate activation (77). In addition, variation of this facial triad can exist, such as the occurrence of a third histidine ligand in lipoxygenase, (78).

Non-heme iron oxygenases that utilize the 2-His-1-carboxylate facial triad include extradiol dioxygenases, Rieske-type oxygenases, pterin-dependent hydroxylases, and α -ketoglutarate-dependent enzymes. Extradiol dioxygenases are discussed in more detail in 1.3.1.1. Rieske-type oxygenases can be dioxygenases, exemplified by naphthalene and biphenyl dioxygenases, and monooxygenases, such as vanillate O-demethylase (31,79,80). The former catalyze the *cis*-dihydroxylation of aromatic rings to produce diols that are re-aromatized to yield catechols. The reaction product of vanillate O-demethylase is protocatechuate, which is also subject to ring-cleavage (Figure 1.2). Rieske-type oxygenases are multi-component enzymes that minimally require a reductase component to transfer the reducing equivalents from NADH to the oxygenase component. The electrons are first transferred to a Rieske-type [2Fe-2S] cluster in the oxygenase, and then to the mononuclear iron active site where substrate transformation occurs. Pterin-dependent hydroxylases are involved in the biosynthesis of neurotransmitters and amino acids (81). In these enzymes, tetrahydropterin is proposed to supply the electrons required to cleave the O-O bond during the catalysis. The α -ketoglutarate-dependent enzymes represent the largest multifunctional sub-class of O_2 -activating non-heme iron enzymes (76) and catalyze a variety of oxygenase reactions including hydroxylations, epoxidations, and endoperoxidations. In these enzymes, exemplified by TauD, which catalyzes the hydroxylation of taurine, the reducing equivalents are provided by α -ketoglutarate, which is decarboxylated in the process (82).

1.3.1.1 Extradiol dioxygenases

Extradiol dioxygenases (EC 1.13.11) catalyze the oxygenolytic cleavage of catechols adjacent to the vicinal hydroxyl groups via insertion of both atoms of oxygen from O_2 to yield muconic semi-

aldehyde adducts (76) (Figure 1.2A). The enzymes utilize Fe^{2+} or sometimes Mn^{2+} coordinated by a 2-His-1-carboxylate facial triad, as noted above. The cleavage reaction requires no external reductant as the organic substrate supplies the electrons required for the activation of O_2 . In contrast, intradiol dioxygenases utilize Fe^{3+} coordinated by four residues: two histidines and two tyrosines (70).

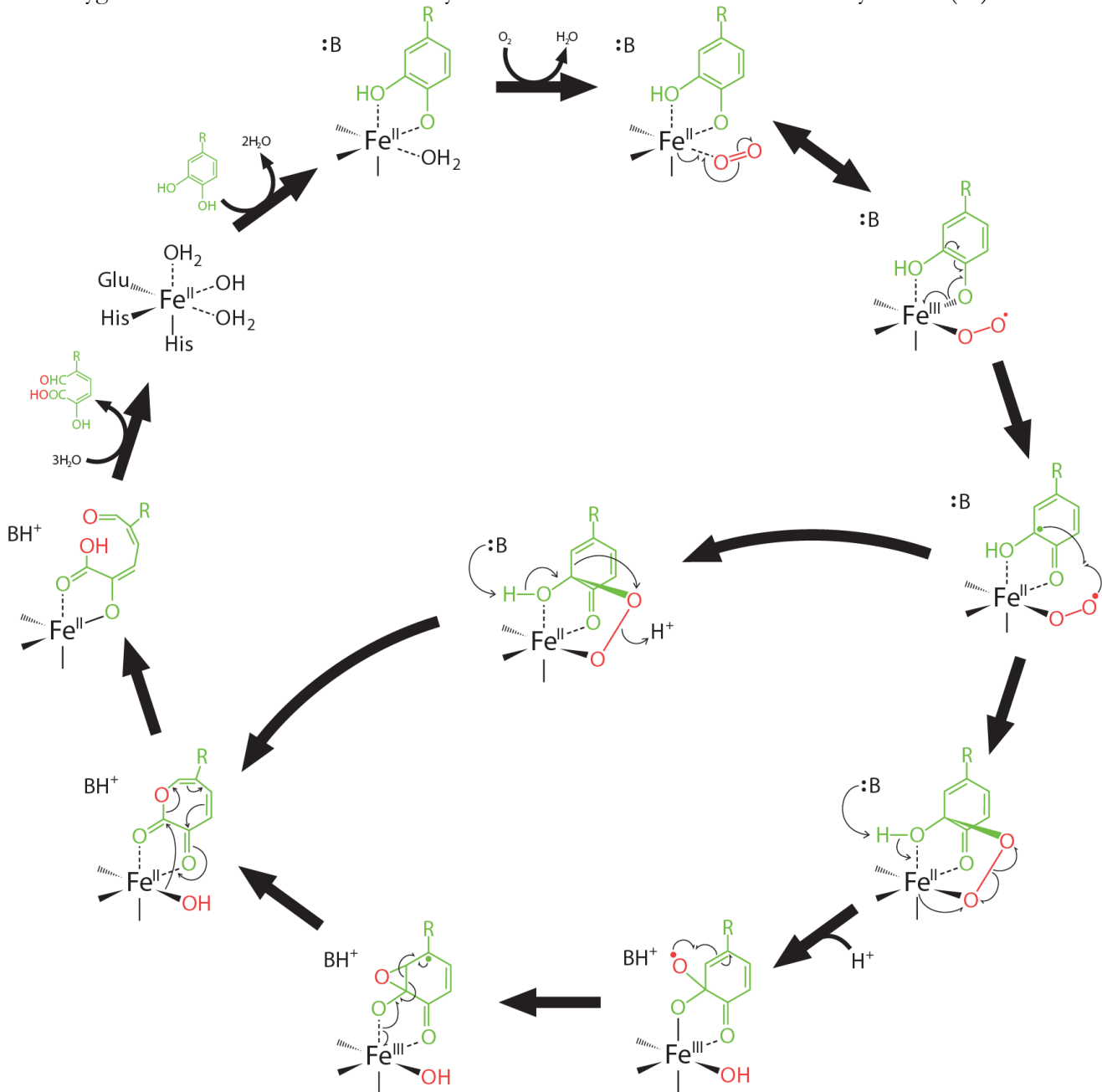


Figure 1.4. The proposed catalytic mechanisms of homoprotocatechuate 2,3-dioxygenase.
The organic substrate and oxygen are in green and red, respectively. Adapted from Wang *et al.* (70)

Three evolutionary independent families of extradiol dioxygenases have been identified based on their structural folds (83-85). Type-I extradiol dioxygenases belong to the vicinal-oxygen-chelate superfamily, and include two- and one-domain enzymes. Phylogenetic analyses revealed that the divergence was due to gene duplication events. The two-domain enzymes are exemplified by 2,3-dihydroxybiphenyl 1,2-dioxygenase (BphC) of *Burkholderia xenovorans* LB400, catechol-2,3-dioxygenase of *Pseudomonas putida* MT-2, and homoprotocatechuate 2,3-dioxygenase of *Brevibacterium fuscum* (86-88). Type-II extradiol dioxygenases, exemplified by the LigAB protocatechuate 4,5-dioxygenase, are discussed in 1.3.1.2. Type-III extradiol dioxygenases belong to the cupin superfamily which includes homogentisate dioxygenase and 3-hydroxyanthranilate dioxygenase in human (89,90). There is no correlation between an enzyme's substrate specificity (e.g., preference towards mono or bicyclic substrates) and its evolutionary origin.

Despite the different structural folds, all extradiol dioxygenases utilize similar catalytic machinery and mechanisms (18,91). The mechanism of extradiol dioxygenases is best elucidated in homoprotocatechuate 2,3-dioxygenase which includes crystallographic evidence of various intermediates during its catalytic cycle (Figure 1.4) (88). In the proposed mechanism, the catecholic substrate binds to the Fe^{2+} in a bidentate manner as a monoanion (92). The second substrate, O_2 , then binds side-on to the Fe^{2+} -catechol chelate complex. Electron transfer within the ternary complex from the catechol to the O_2 via the ferrous ion simultaneously activates both substrates. The recombination of the resulting radicals forms an Fe^{2+} -alkyl-peroxy intermediate. This intermediate breaks down by a concerted Criegee rearrangement to yield a seven-membered lactone, a process facilitated by an acid catalyst. Finally, the lactone is hydrolyzed to yield the ring-open product. There has been no evidence for the iron cofactor changing its redox state during the catalytic cycle. However, a computational study had suggested that the Criegee rearrangement may proceed in a step-wise fashion involving a transient epoxide intermediate and a concomitant formal charge transfer from the iron (93). To address this, preparations of homoprotocatechuate-2,3-dioxygenase bearing iron and manganese, a physiological and a non-physiological metal cofactor, respectively, were evaluated. Kinetic analyses of these two preparations yielded nearly identical values, suggesting a fixed metal oxidation state proposal. However, these transient intermediates are not rate-limiting and would not be discernable through steady-state kinetic analyses.

Extradiol dioxygenases are subject to mechanism-based inactivation and substrate inhibition (86,94). Mechanism-based inactivation had variously been proposed to involve the reversible chela-

tion of the metal ion or covalent modification of the active site (94,95). However, little evidence for these mechanisms has been presented. It is generally accepted that the mechanism-based inactivation of extradiol dioxygenases is due to the adventitious dissociation of superoxide from the E·catechol·O₂ ternary complex, which results in the oxidation of the active site ferrous ion (86,96). *In vitro* studies have demonstrated that this inactivation results in the production of Fe³⁺ and the process is reversed by anaerobically incubating the inactivated enzyme with Fe²⁺ and reducing agent. The mechanism-based inactivation is more prominent for poorer substrates (97), suggesting some mode of active site tuning to maximize substrate cleavage while minimizing inactivation during catalytic turnover. Moreover, some catabolic pathways have evolved a ferredoxin whose gene is cotranscribed with that encoding the extradiol dioxygenase and that functions to reduce inactivated enzyme (98). However, some extradiol dioxygenases are reactivated *in vivo* without an associated ferredoxin, suggesting that non-specific reductases or electron transfer proteins may suffice (86). Extradiol dioxygenases can also be oxidatively inactivated in the absence of their catecholic substrate (86). This inactivation involves the binding of O₂ to the active site metal and subsequent loss of superoxide. To protect against such inactivation, extradiol dioxygenases employ a gating mechanism whereby the E·catechol complex has a much higher affinity for O₂ than the organic substrate-free enzyme (99). For example, catechol 2,3-dioxygenase utilizes a compulsory order, ternary complex mechanism where the binding of catechol precedes that of O₂ (100).

The O₂-labile nature of extradiol dioxygenases complicates their purification and characterization. To minimize such complications, these enzymes should be purified anaerobically with buffers supplemented with reducing agent, ferrous iron and an organic additive such as isopropanol, acetone, *t*-butanol (87,101). These small organic additives bind to and stabilize the active site, protecting the enzyme from oxidation. The ideal stabilizer varies as the different extradiol dioxygenases have different affinities for the different additives. An alternative strategy is to use a chelator to strip the enzyme preparation of all metal ions, and then to reconstitute the purified enzyme with the appropriate metal ion in a protected environment (102). This strategy takes advantage of the relative ease with which extradiol dioxygenases may be stripped of their metal ion and reconstituted.

1.3.1.1 Type-II extradiol dioxygenases

Type-II extradiol dioxygenases belong to the LigB-like superfamily, also referred as protocatechuate 4,5-dioxygenase superfamily (103). LigAB, a protocatechuate 4,5-dioxygenase involved in

lignin catabolism in SYK-6 (Figure 1.2), is a canonical Type-II enzyme in which LigB, the larger subunit, harbors the catalytic machinery and LigA forms a cap above the active site (Figure 1.5) (104). SYK-6 possesses at least four extradiol dioxygenases involved in catabolizing lignin depolymerization products: DesB, a gallate dioxygenase (102,105,106); DesZ, a 3-methylgallate dioxygenase (107); LigAB (103); and LigZ, OH-DDVA dioxygenase (50). DesB, DesZ and LigZ are all homologous to LigB. However, DesB also possesses a cap domain that is homologous to LigA. Dimerization of DesB results in each LigB-like domain being capped with a LigA-like domain of their respective partner. By contrast, DesZ and LigZ are “cap-less” enzymes that lack a domain corresponding to LigA. The role of the LigA-like domain is unclear: it may contribute to determining substrate specificity or to protecting the Fe^{2+} from oxidative inactivation. Studies of DesB have further revealed two possible metal-binding sites and that substrate binding induces displacement of the active site metal ion from the resting-state to the active-state (102). In the resting state, the Fe^{2+} is coordinated by the 2-His-1-carboxylate facial triad, an asparagine, and two solvent molecules. Upon gallate-binding, the Fe^{2+} coordination is shifted into an active (productive) binding with two histidines (from the facial triad) and the gallate’s vicinal hydroxyls. It remains unclear whether this trait is generalizable across all type-II extradiol dioxygenases. Finally, vanillate has been reported to activate LigAB in a rare example of feed-forward activation (108).

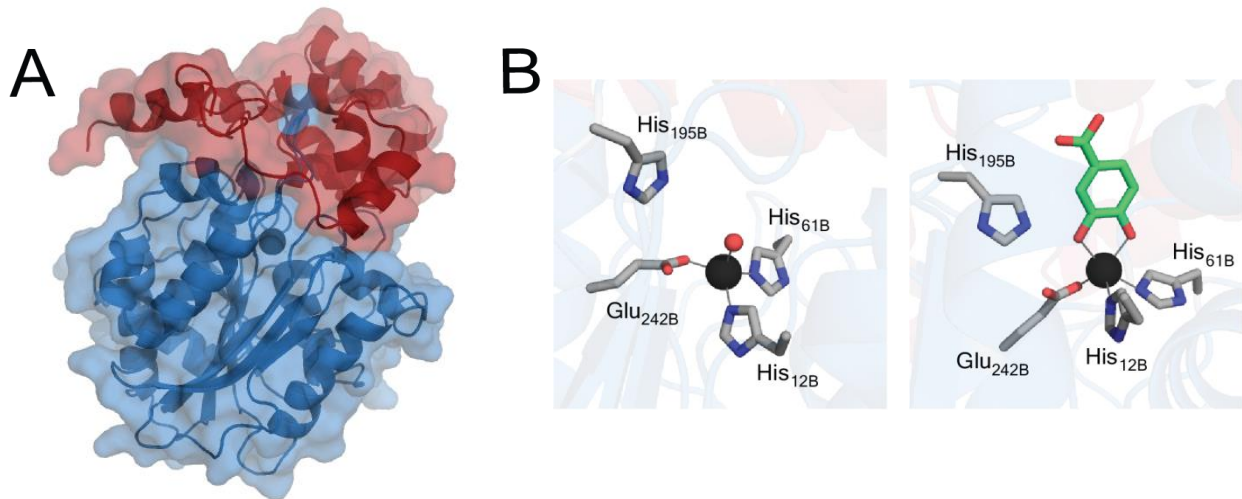


Figure 1.5. Crystal structure of protocatechuate-4,5-dioxygenase (LigAB) from SYK-6.

(A) Ribbon and surface representations of LigA in red and LigB in blue (104). (B) The catalytic centre of LigAB in the resting state (left – Protein Data Bank (PDB) ID: 1BOU) and in complex with PCA, in green, (right – PDB ID: 1B4U). The Fe^{2+} ions and water are represented as black and red spheres, respectively.

1.3.1.2 Carotenoid cleavage oxygenases

Carotenoids are a family of fat-soluble isoprenoid compounds representing the largest class of color pigments synthesized by organisms from all domain of life. These compounds have many important biological functions including photosynthesis, visual pigments, signaling molecules, and antioxidants (109). In photosynthesis, carotenoids are harnessed as accessory pigments in the light harvesting complex to broaden the usable wavelengths, particularly in the blue region of the spectrum. Carotenoids contribute to reproductive success in plants and animals: bright and vivid pigmentation are used by flowering plants to attract pollinators and to increase sexual allure in animals. Carotenoids also serve as antioxidants as its polyene backbone can react with and quench free radicals. Many carotenoids and their breakdown products are precursors to plant hormones. For example, VP14 from *Zea mays* (corn) catalyzes 9-cis-violaxanthin to generate xanthoxin, *en route* to the biosynthesis of abscisic acid which governs plant stress response and seed germination (110). The importance of carotenoids and their derivatives in human health is well documented, most notably in ontogeny and light perception (111). For example, β -carotene is cleaved primarily at the 15,15' site to produce two molecules of retinal. The enzyme that catalyzes this reaction is a carotenoid cleavage oxygenase (CCO).

CCOs cleave a double bond in stilbenoids and carotenoids with high regio- and stereospecificity (71). CCOs are non-heme Fe^{2+} -dependent enzymes characterized by a structural fold comprising a seven-bladed β -propeller (Figure 1.6A) (112). The active site occurs at the center of this propeller, and contains an Fe^{2+} coordinated by four histidines (Figure 1.6B) (112). The four histidines that coordinate the metal ion hydrogen bond with three conserved glutamates found in the second shell of the coordination sphere (112). Four-histidine coordination leaves two open coordination sites for ligands to bind the metal cofactor. However, one of the sites is occluded in most CCOs by a nearby bulky substituent (113,114). In general, CCOs possess hydrophobic active-sites which are tuned to the nature of their substrates.

Recent studies with isotopically labelled H_2O and O_2 conclusively established that these enzymes are dioxygenases (113,115). CCO readily purifies aerobically with an intact Fe^{2+} cofactor and remains active despite prolonged exposure to atmospheric oxygen (112,114,116). However, it is unclear how CCO maintains the redox state of its cofactor; in particular, whether the organic substrate gates the reactivity of the ferrous ion with O_2 to inhibit the oxidation of the metal ion, as is the case for extradiol dioxygenases (see 1.3.1.1) (99). For example, electron paramagnetic resonance (EPR)

spectroscopy analyses have suggested that NO, a surrogate for O₂, binds to the iron center independent of organic substrate (117). By contrast, crystallographic, x-ray absorption spectroscopy, and Mössbauer spectroscopy data indicate that a number of CCOs do not bind O₂ in the absence of the organic substrate (114).

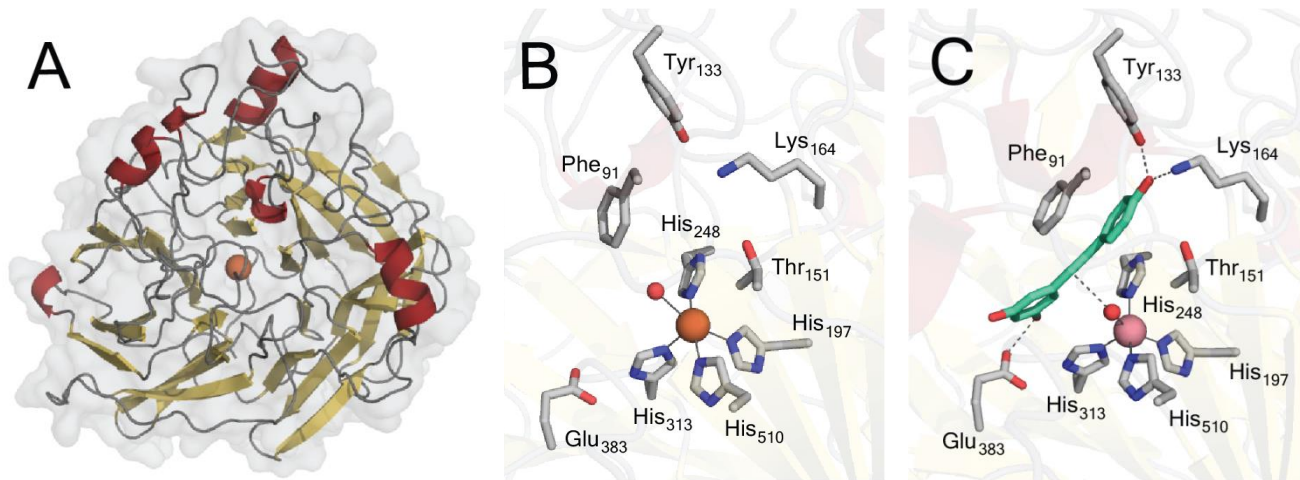


Figure 1.6. Crystal structure of resveratrol-cleaving dioxygenase (CAO1) from *N. crassa*.

(A) Ribbon and surface representations of a seven-bladed β -propeller structure of CAO1, the α -helices are in red and the β -strands are in yellow (114). (B) The active site structure of Fe-CAO1 in the resting-state (PDB ID: 5U8X). (C) The structure of Co-CAO1 in complex with resveratrol, in green, (PDB ID: 5U90). The Fe²⁺ and Co²⁺ ions are represented as orange and pink spheres, respectively; and waters are shown as red spheres.

1.3.1.2.1 Stilbene-cleaving oxygenases

Lignostilbene- α,β -dioxygenases (LSD, EC 1.13.11.43) are homologous to CCOs but catalyze the oxygenolytic fission of lignostilbene to two molecules of vanillin (116). Naturally occurring stilbenoids include resveratrol, a phytoalexin produced by many plants to protect against pathogens or physical damage. Lignin-derived stilbenes are produced in the bacterial catabolism of diaryl propane or phenylcoumarane (Figure 1.3B), which may explain why some bacterial strains contain multiple LSD homologs (29,55,118). Despite their name, lignostilbenoids occur in a very limited number of naturally occurring lignins, but are prevalent in industrial lignins due to condensation reactions (119,120).

LsdA from TMY1009, the first LSD to be described, shares 98% amino acid sequence identity with LSD1 from SYK-6, encoded by SLG_37450, 56% with NOV1 from *Novosphingomonas aro-*

maticivorans, and 40% with carotenoid oxygenase 1 (CAO1) of *Neurospora crassa* (29,121-123). LSDs are dimeric in solution and have different substrate preferences, but can also occur as heterodimers (118,124,125). Among tested stilbenes, LsdA had the highest substrate specificity (k_{cat}/K_M) for lignostilbene as well as a requirement for a 4-hydroxy moiety and a *trans*-configuration of the stilbene (126). Further, substrate analogs bearing substitutions on the C α or C β atoms generally act as inhibitors of LSD (127,128).

Crystal structures of LSD homologs (Figure 1.6) and spectroscopic studies have led to the proposal of two different mechanisms for these oxygenases, both of which proceed via an iron-peroxo-substrate intermediate. In crystal structures of LSD_{NOV1} and CAO1 in complex with stilbenoid substrates, the organic substrate is bound such that the scissile double bond is in close proximity to the ferrous ion (114,117). The ferrous ion also binds O₂ to form a ternary complex. In the mechanism proposed by McAndrew *et al.*, the hydroxystilbenoid is activated via the enzyme-catalyzed deprotonation of the 4-hydroxy group, which allows electron delocalization toward an Fe³⁺-superoxo electrophile (117). In an alternate proposal by Sui *et al.*, π electron density from the scissile double bond is redistributed to the iron-oxy complex to form an Fe²⁺-peroxo-substrate cation intermediate (114). The charge on the hydroxystilbenoid is neutralized via deprotonation of the hydroxyl group to form a dienone intermediate. The mechanisms are further distinguished by the subsequent resolution of the iron-peroxo-substrate intermediate to yield the aldehyde products. In the mechanism proposed by McAndrew *et al.*, this intermediate resolves to a vicinal diol which undergoes homolytic fission (117). By contrast, in the mechanism proposed by Sui *et al.*, the iron-peroxo-substrate intermediate resolves via a Criegee rearrangement, similar to what occurs in extradiol dioxygenases (114). In both mechanisms, deprotonation of the hydroxyl moiety is important and assisted by Lys134 and Tyr101 (LsdA/NOV1 numbering), two active site residues conserved among stilbene-cleaving oxygenases (114,117). The roles of these residues have not been investigated.

1.4 *meta*-Cleavage product hydrolases

meta-Cleavage product (MCP) hydrolases (EC 3.7.1.-) catalyze the hydrolysis of vinylogous 1,5-diketones formed by the dioxygenative *meta*-ring cleavage of catechols (Figure 1.7) (129). This *meta*-cleavage strategy, and therefore MCP hydrolases, are primarily involved in the bacterial catabolism of alkylated aromatic compounds. Thus, BphD from *Burkholderia xenovorans* LB400 and DxnB2 from *Sphingomonas wittichii* RW1 are involved in biphenyl and dibenzofuran catabolism, respectively (130-132). *B. xenovorans* LB400 degrades a range of polychlorinated biphenyls, but BphD is a bottleneck in this process (133). Finally, HsaD is an MCP hydrolase involved in the bacterial catabolism of steroids as one of the steroid rings is aromatized and subject to *meta*-cleavage (134). In *Mycobacterium tuberculosis*, HsaD is essential for growth on cholesterol, which contributes to the survival of pathogen during infection (135,136).

1.4.1 Classification of MCP hydrolases

Members of the α/β hydrolase superfamily catalyze a wide range of reactions, including the hydrolysis of a C-C bond in MCPs. Indeed, the α/β hydrolase superfamily is among the earliest reported cases of evolutionary divergent enzymes, as first identified from a structural comparative study of five different hydrolases (137). The superfamily catalyzes hydrolysis of a wide range of substrates, including esters, peptides, lipids, thioesters, MCPs, epoxides, haloacids, and haloalkanes (138). In addition, members of the superfamily catalyze perhydrolysis, transferase reactions and oxygenations. The wide catalytic repertoire of the α/β hydrolase superfamily stems in part from the scaffold's ability to tolerate a large number of insertions (139). Most α/β hydrolases utilize a nucleophilic mechanism that involves a covalent intermediate (137). However, some superfamily members, exemplified by hydroxynitrile lyase and 1-H-3-hydroxy-4-oxoquinaldine 2,4-dioxygenase, utilize a general base mechanism (140,141). Regardless, the catalytic machinery of these enzymes includes a catalytic triad and an 'oxyanion hole' (137). The nucleophilic residue of the triad may be Ser, Cys, or Asp, and the acidic residue of the triad is Asp or Glu.

All MCP hydrolases characterized to date are α/β hydrolases with a Ser-His-Asp catalytic triad. Structurally, they comprise a core domain and an α -helical lid domain, with the enzyme active site at the interface of the two domains (142). The lid domain is connected to the core domain by a non-conserved flexible loop linker. The linker's architecture has been implicated in contributing to the enzyme's substrate specificity and oligomeric state (143). The active site of MCP hydrolases

comprises polar and nonpolar subsites and reflects the distribution of polarity in the MCP substrates (131).

LigY, which catalyzes the hydrolysis of DCHM-HOPDA in the catabolism of DDVA (Figure 1.3), has also been identified as an MCP hydrolase (51). However, LigY shares no significant amino acid sequence identity with α/β hydrolases and lacks the catalytic triad. Only one of its two reaction products was identified, 5CVA; neither the enzyme's putative substrate, DCHM-HOPDA, nor the second expected product, CHPD, was not. However, under alkaline conditions, the product of the LigZ-catalyzed cleavage of OH-DDVA absorbs strongly (λ_{max} 455 nm), consistent with an MCP dienolate (50). Further, 5CVA was isotopically labeled when the LigY reaction was performed in H_2^{18}O , consistent with a hydrolytic reaction (51).

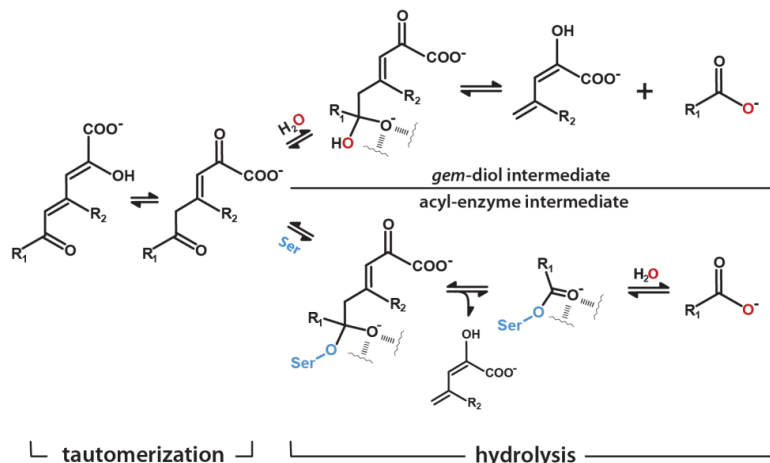


Figure 1.7. Possible pathways for MCP hydrolysis.

The mechanisms of serine-independent and -dependent pathways are distinguished by the key catalytic intermediate: a *gem*-diol and an acyl-enzyme, respectively. In both cases, substrate ketonization precedes formation of the distinguishing intermediate. Adapted from Ruzzini *et al.* (129).

1.4.2 Mechanistic aspect of MCP hydrolases

MCP hydrolases are interesting for their ability to catalyze C-C bond hydrolysis. The enzymatic hydrolysis of C-C bonds presents a particular challenge because, as in all hydrolases, collapse of the tetrahedral oxanion intermediate is assisted by delocalizing the negative charge on the leaving group. In carbon-heteroatom hydrolysis, the charge is typically alleviated by protonating the heteroatom, a strategy that is not available to C-C bond hydrolases. In the latter, Nature has evolved several strategies in providing the requisite electron sink for the leaving carbanion. The first strategy involves a β -di-ketone functionality which is then hydrolyzed through a retro-Claisen reaction (144).

This is exemplified by β -ketolases such as fumarylacetoacetate hydrolase and IpdB (145,146), involved in tyrosine and steroid catabolism, respectively. The second strategy involves the generation of β -ketiminium which then facilitates the bond fission analogous to the β -ketolase. For example, kynurenine uses pyridoxal 5'-phosphate in the hydrolysis of kynurenine (147). The third strategy is provided by MCP hydrolases by catalyzing an enol-to-keto tautomerization of the substrate prior to C–C bond cleavage (130,148). Indeed, the formation of an electron sink in MCP hydrolases exploits a diketone-like functionality spaced by a conjugated system.

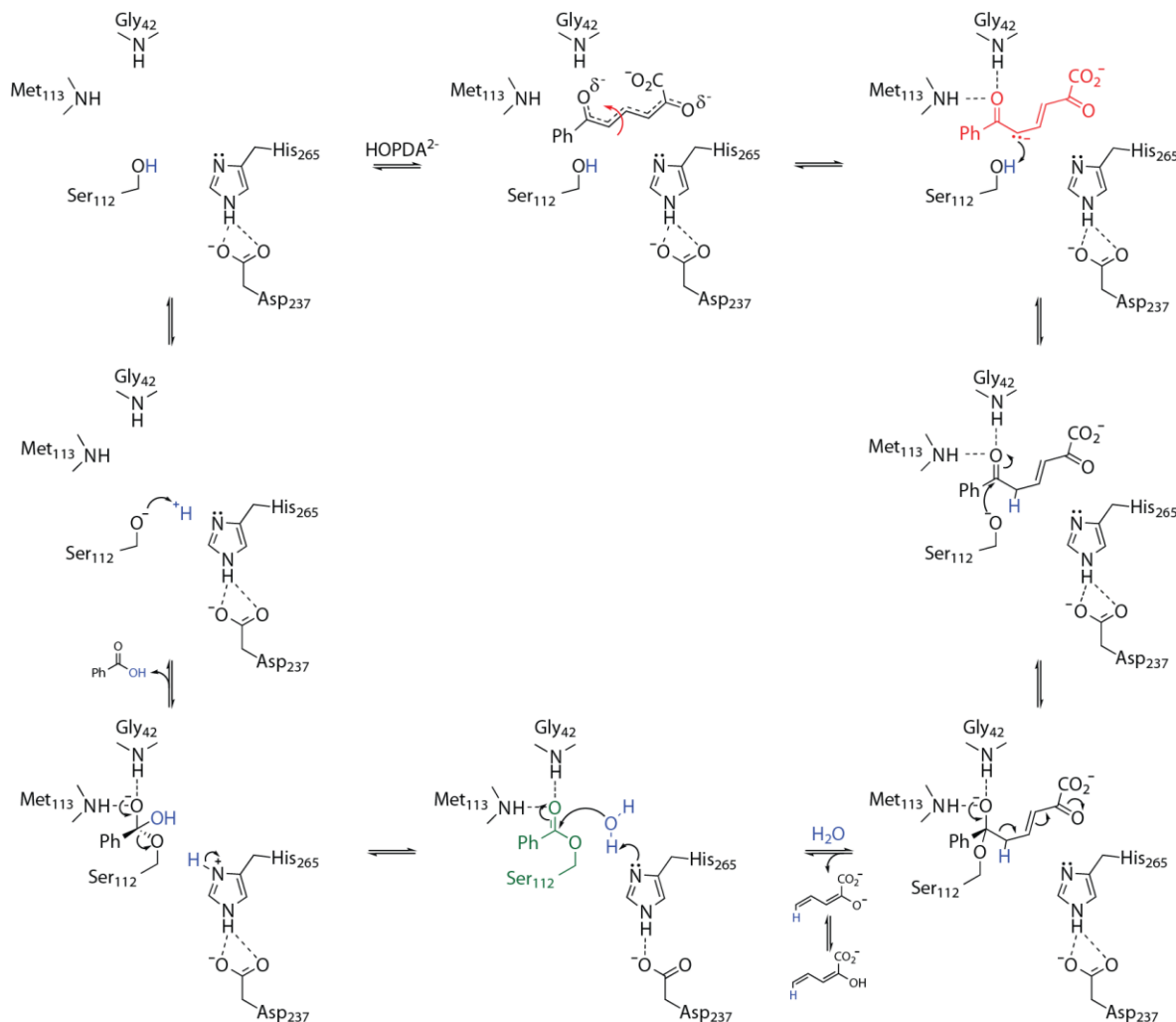


Figure 1.8. Proposed catalytic mechanism of serine-dependent MCP hydrolase.

A complete catalytic cycle of DxnB2-catalyzed hydrolysis of 2-hydroxy-6-oxo-6-phenyl-hexa-2,4-dienoate (HOPDA) to benzoate and 2-hydroxypenta-2,4-dienoate (HPD). The purported C-5 carbanion, the acyl-enzyme intermediate, and the hydrolytic water are colored red, green, and blue, respectively. Taken from Ruzzini *et al.* (129).

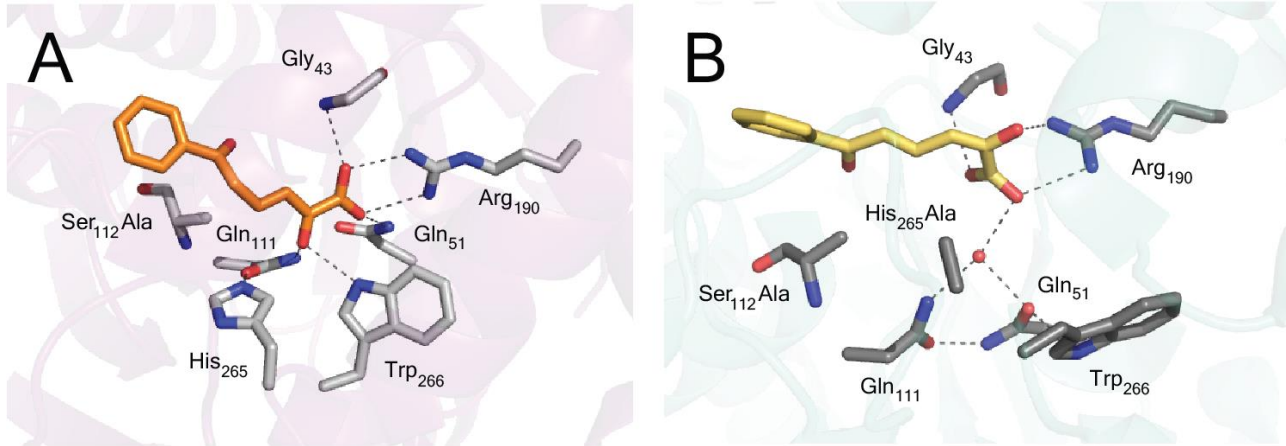


Figure 1.9. $\text{BphD}_{\text{LB}400}$ •HOPDA binary complexes.

Stick representation of (A) $\text{BphD}_{\text{LB}400}$ S112A•HOPDA (PDB ID: 2PUH) and (B) $\text{BphD}_{\text{LB}400}$ S112A/H265A•HOPDA (PDB ID: 2PUJ) (149). Polar interactions ($\leq 3.4 \text{ \AA}$) are indicated using dashed lines. The HOPDAs are colored as orange or yellow to represent their respective spectrum *in crystallo*. Waters are shown as red spheres. The complexes highlight the different binding conformations and interactions with the polar subsite.

1.4.2.1 Hydrolytic mechanism

As first proposed by Bugg, the reaction mechanism involves two half-reactions: an initial enol-keto tautomerization to form a discrete keto intermediate followed by a stereospecific C-C fragmentation reaction (Figures 1.7, 1.8) (130,148). In the first half-reaction, ES^{red} is generated during the course of substrate tautomerization (131). It has been proposed that ES^{red} is protonated at C5 by the active site serine, coupling the formation of the α,β -unsaturated δ -diketone with activation of the nucleophile, which is poised to then attack at C6 (150). The second half reaction was originally proposed to occur via a *gem*-diol in which the catalytic serine acts as a general base to deprotonate water (151). This was subsequently disproven with the observation of a catalytically relevant acyl-enzyme intermediate (129). The acyl-enzyme intermediate was first observed in the crystal structure of BphD H265Q•HOPDA binary complex. Chemical quench and mass spectrometry studies further substantiated the formation of the benzoylated adduct in wild-type (WT) BphD which is formed and decayed in the time scale commensurate with the catalytic turnover. Further, only a single equivalent of ^{18}O was incorporated into the benzoate product during hydrolysis in H_2^{18}O . Similar observations were reported in DxnB2 . Together, the substrate-assisted nucleophile activation is consistent with a solvent kinetic isotope effect (sKIE), a $\beta_{\text{nuc}} \sim 1$, and the fact that the histidine of the catalytic triad does not appear to play a role in acyl-enzyme formation (131,150). Nevertheless, this proposed

mechanism cannot be directly translated to LigY as it lacks the catalytic triad despite performing the same net reaction.

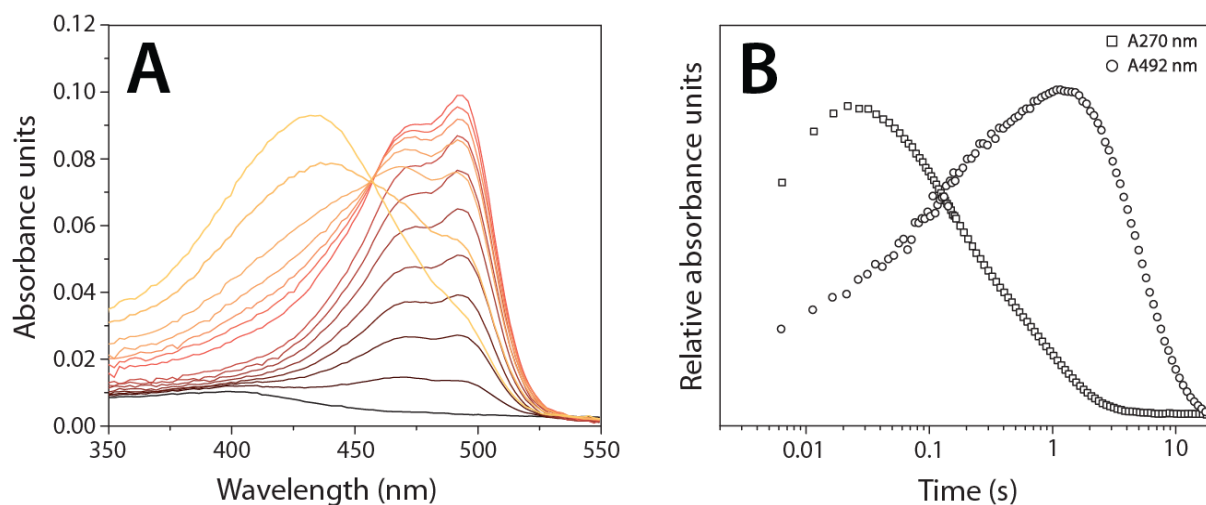


Figure 1.10. Representative stopped-flow experiment illustrating the formation of ES^{red} in the BphD-catalyzed single turnover of HOPDA and commensurate decay of ES^{red} and HPD formation.

Representative stopped-flow experiment illustrating a single turnover of 4 μM HOPDA by 8.1 μM $\text{BphD}_{\text{LB400}}$ at 3.2 °C. (A) Changes to the visible spectrum revealing ES^{red} . Spectra are color-coded according to time of acquisition, beginning with yellow (upon mixing), transitioning to red, and then to black. (B) Data showing that ES^{red} decay (492 nm) is commensurate with HPD production (270 nm). An additional post-catalytic process is visible at 270 nm, HPD ketonization. Adapted from Ruzzini (152).

1.4.2.2 Substrate ketonization

The mechanism of substrate activation in MCP hydrolases remains poorly understood. The formation of the electron sink, in the form of α,β -unsaturated δ -diketone, depends on the protonation of the MCP at C5 (Figure 1.7). Evidence supporting this process was first shown in MhpC, where the enzyme catalyzed the stereo-specific incorporation of deuterium into the H-5_E position of HPD (153). Similar incorporation was later observed in the BphD-catalyzed hydrolysis of HOPDA (131). Further, the ability of BphD to catalyze the transformation of HPD into (*E*)-2-oxo-3-pentenoate is also consistent with tautomerization (149). Several active site residues are implicated in this process: a conserved arginine and the histidine of the catalytic triad. This arginine is conserved

among the MCP hydrolases (MphC Arg-188, BphD Arg-190, and DxnB2 Arg-180), ion pairs with the C1 carboxylated of the MCP's dienoate moiety, and contributes towards substrate destabilization. On the other hand, the histidine has been proposed to facilitate the proton transfer between the C2 hydroxyl into C5 (131). This role assignment was due to the observed proximity of His-265 to the C2-oxo group of both substrate and product, as seen in the crystal structure of BphD S112A·HOPDA and BphD S112C·HPD, respectively (Figure 1.9). Furthermore, BphD H256A and BphD S112A/H256A were unable to accumulate an intermediate with a red-shifted spectrum (see below) which is thought to represent the enzyme destabilized form of the MCP. In BphD, Ser-112 is the catalytic nucleophile and its substitution rendered the enzyme inactive. Further, an extended Brønsted analysis in DxnB2 revealed a linear correlation between pK_{a2} of substituted HOPDAs and their rate of substrate ketonization (150). This suggests the reactivity of the substrates towards protonation at C5 directly reflects their enol:enolate equilibrium in solution.

1.4.2.3 Characterization of ES^{red}

An ES intermediate with a bathochromatically-shifted absorption spectrum, aptly termed ES^{red} , was first observed in the single turnover kinetic analysis of BphD-catalyzed hydrolysis of HOPDA (λ_{max} 473 and 492 nm, for enolate and ES^{red} , respectively) (Figure 1.10A) (131). A similar red-shifted intermediate with an extended half-life accumulated in MCP hydrolase whose catalytic serine is substituted with alanine, suggesting the contribution of the enzyme active site in substrate destabilization (134,150). In these enzymes, ES^{red} decay mirrored the formation of HPD (λ_{max} 270 nm) (Figure 1.10B) and was ascribed to the substrate ketonization step. Consistent with this observation, ES^{red} decay is subject to sKIE and is insensitive towards microviscogens (150). The exact nature of ES^{red} remains elusive. While pK_{a2} for enol:enolate equilibrium for HOPDA near physiological pH (7.3), its exact protonation state as bound in the enzyme active site remains unknown. For instance, the absorption spectrum of ES^{red} (λ_{max} 492 nm) is more consistent with an enolate form (λ_{max} 473 nm) rather than an enol form (λ_{max} 434 nm) of the substrate. This argues against a simple enol-to-keto tautomerization. Based on structural and spectroscopic data, ES^{red} has variously been proposed to be a strained enolate and a C5 carbanion (131,150). The strained enolate proposal stemmed from the comparison of different substrate binding mode and their corresponding spectroscopic signature in BphD binary complexes. The single crystal absorption spectrum was used to correlate the crystallographic data and aqueous absorption spectra. In the crystal structure of BphD

S112A•HOPDA complex, a large deviation of the torsion angle along the dieneoate moiety from planarity was observed and thought to represent a productive binding mode (Figure 1.9A) (131). By contrast, an unproductive planar binding mode was observed in BphD S112A/H265A•HOPDA complex (Figure 1.9B). This result is consistent with the *trans-transoid* configuration of the MCP in solution. The twisting of the MCP in a binary complex was also observed in HsaD and DxnB2. The C5 carbanion proposal was derived from the observation where the catalytic histidine plays no apparent role in the acyl-enzyme formation (150). The role of activating the catalytic serine was then relegated to the C5 carbanion, formed as the consequence of the tautomerization process.

1.4.3 Amidohydrolase superfamily

The amidohydrolase superfamily was first identified by Holm and Sander who recognized the sequence and structural similarities between urease, phosphotriesterase, and adenosine deaminase (154). The vast majority of the characterized enzymes catalyze the hydrolysis of ester and amide bonds associated with the amino acids, nucleic acids and sugars. Among these, the phosphoesterases have been engineered to bioremediate organophosphate nerve agents (e.g. sarin and VX gas) (155,156). Several superfamily members are involved in the microbial catabolism of lignin-derived aromatics, catalyzing hydrolysis, decarboxylation, and hydration reactions (29). Other reported activities include aldose/ketose isomerization, exemplified by uronate isomerase, which catalyzes the transformation between D-glucuronate and D-fructuronate (157). Since the discovery of the amidohydrolase superfamily, our knowledge of its catalytic diversity has expanded significantly. It is of considerable interest to understand how a single structural fold has evolved to support such a diverse set of chemical reactions.

The structural fold of the superfamily is a distorted $(\beta/\alpha)_8$ -TIM barrel. The active site is housed in the center of the β -barrel, and typically contains one or two divalent metal ions (158), such as Zn^{2+} , Fe^{2+} , Ni^{2+} , and Mn^{2+} . However, superfamily members containing 0 to 3 metal ions are known. The metal cofactors are utilized by the amidohydrolases as Lewis acids, typically to form a hydroxyl nucleophile or to activate the substrate. The metal ions are ligated by conserved residues which are located at the C-termini of the β -strands. The number of metal ions and the identity of the ligating residues have been used to delineate the superfamily into seven subtypes. More recently, the superfamily has been classified according to amino sequence similarity using databases such as protein families (Pfam) and clusters of orthologous groups (COGs) (159,160).

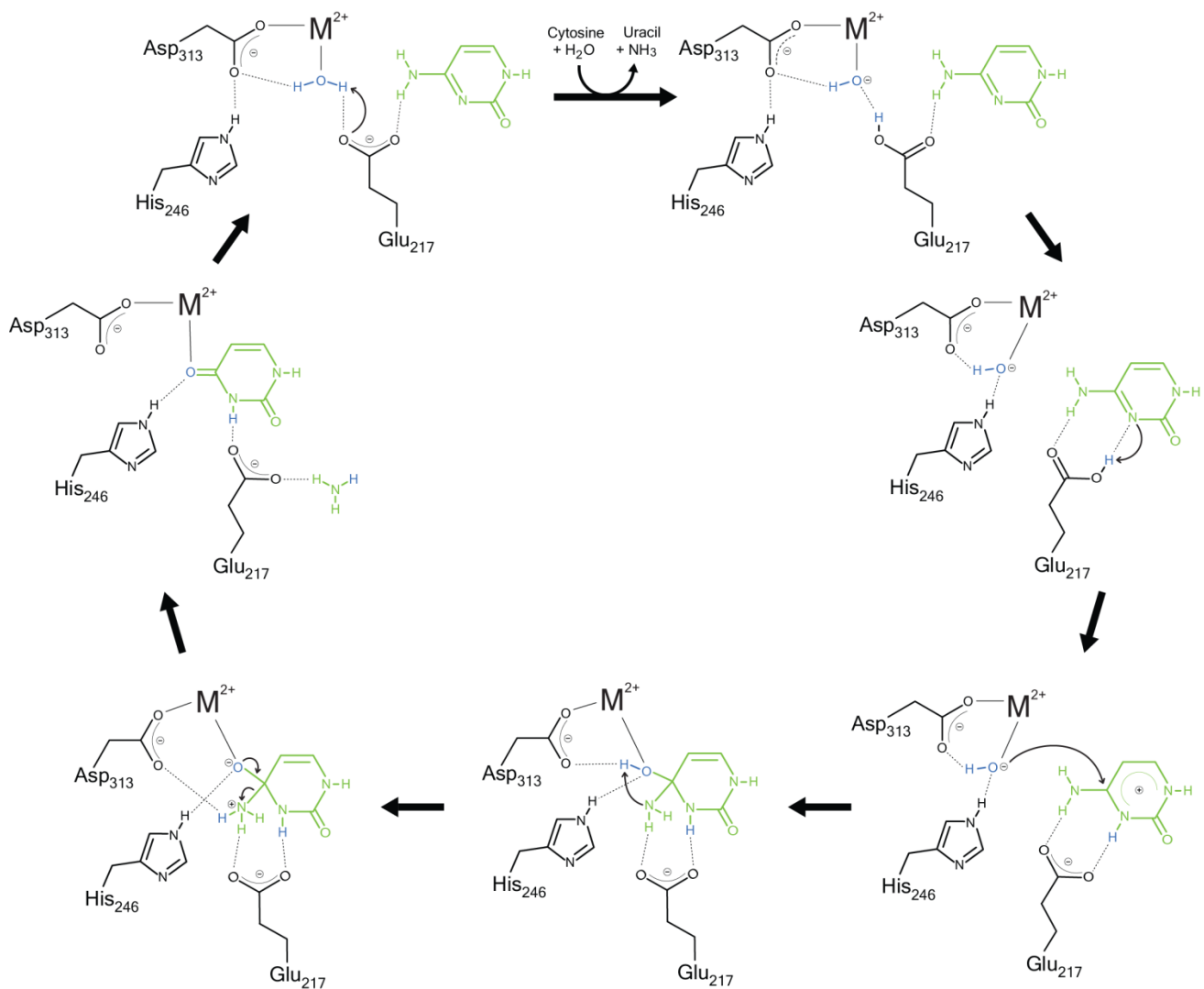


Figure 1.11. Proposed catalytic mechanism of the subtype III amidohydrolase.

A complete catalytic cycle of CDA-catalyzed deamination of cytosine (161). The organic substrate and hydrolytic water are colored as green and blue, respectively.

The prototypical mononuclear subtype III amidohydrolase is exemplified by hydrolytic deaminases such as adenosine and cytosine deaminase (CDA; EC 3.5.4.1), and belong to COG0402 (162-164). The adenosine deaminase is a Zn-dependent enzyme, whereas the CDA may use either Zn²⁺ or Fe²⁺ ions. These enzymes harbor a mononuclear α -site metal coordinated by a pair of histidines from the HXH motif of the β -strand 1, a histidine from the β -strand 5, and an aspartate from the β -strand 8. The bridging ligand from the β -strand 4 is missing. The conserved histidine in β -strand 6 does not directly ligate the metal but instead coordinates a metal-bound solvent molecule.

This β -strand 6 histidine had been proposed as a general base catalyst for the proton abstraction from the hydrolytic water, although studies on CDA suggested otherwise (162,163). The mechanistic proposal in CDA involves three active site residues required for catalysis: His-246 of the conserved β -strand 6, Asp-313 of the conserved β -strand 8, and Glu-217 (Figure 1.11) (162). The last residue is not conserved among the amidohydrolase superfamily, although the triad is conserved among closely related deaminase. In the proposed mechanism, Glu-217 initiates the reaction by acting as a base catalyst which activates the metal-bound water. This process is facilitated by His-246 which functions as a proton shuttle in between the water and the Glu-217. The nucleophilic attack of the hydroxide is accompanied by the protonation of the atom adjacent to the electrophilic center by Glu-217. This forms the tetrahedral intermediate. Further, the Asp-313 resolves the tetrahedral intermediate and protonates the amine leaving group. This proposal was corroborated by a subsequent quantum chemical study (165). Interestingly, several amidohydrolases are involved in the catabolism of lignin-derived aromatic compounds by SYK-6. For example, LigI catalyzes the reversible hydrolysis of 2-pyrone-4,6-dicarboxylate into 4-oxalomesaconate and 4-carboxy-2-hydroxymuconate in the *meta*-cleavage protocatechuate pathway (Figure 1.2A) (166). LigW and LigJ are COG2159 enzymes described below.

1.4.3.1 COG2159

Amidohydrolases belonging to COG2159 catalyze the more thermodynamically challenging C-C fission. Members of COG2159 contain a single α -site metal ion and predominantly catalyze a non-oxidative decarboxylation in which the carboxyl group is replaced with hydrogen (158,167,168). This contrasts to the more typical oxidative decarboxylation in which the carboxyl group is replaced with a hydroxyl group. The first described COG2159 enzyme was α -amino- β -carboxymuconate- ϵ -semialdehyde decarboxylase (ACMSD; EC 4.1.1.45) (169). In mammals, ACMSD is associated with the kynurenine pathway of tryptophan catabolism, where it protects neuronal cells from the accumulation of quinolinate, an excitotoxin (170). In bacteria, ACMSD is involved in the catabolism of 2-nitrobenzoate. Other COG2159 decarboxylases include: LigW, which catalyzes the decarboxylation of 5CVA in the catabolism of DDVA by SYK-6 (52); IDCcase, which catalyzes the decarboxylation of 5-carboxy uracil (isoorotate) in the fungal thymidine salvage pathway (171); γ -resorcylate decarboxylase (γ -RSD), which catalyzes the reversible decarboxylation of 2,6-dihydroxybenzoate to resorcinol in *Rhizobium* sp. MTP-10005 and *Polaromonas* sp. JS6666 (172,173); and PatG, which catalyzes the

decarboxylation of 6-methylsalicylate in the biosynthesis of the mycotoxin patullin (174). PatG catalyzes the decarboxylation of 6-methylsalicylate into *m*-cresol in the biosynthesis of mycotoxin patullin (174). Moreover, COG2159 enzymes also catalyze hydration and hydrolysis reactions. Thus, LigJ catalyzes the hydration of KCH to 4-carboxy-4-hydroxy-2-oxoadipate in the *meta*-cleavage protocatechuate pathway of SYK-6 (Figure 1.2A) (175). Similarly, CouO catalyzes C-C bond hydrolysis in 4-hydroxyphenyl- β -ketopropionate-coenzyme A hydrolase, in the bacterial catabolism of *p*-coumarate, (176). Of the characterized enzymes, ACMSD, IDCCase, γ -RSD_{MTP-10005}, and LigJ are Zn²⁺-dependent enzymes while LigW and γ -RSD_{JS6666}, are Mn²⁺-dependent.

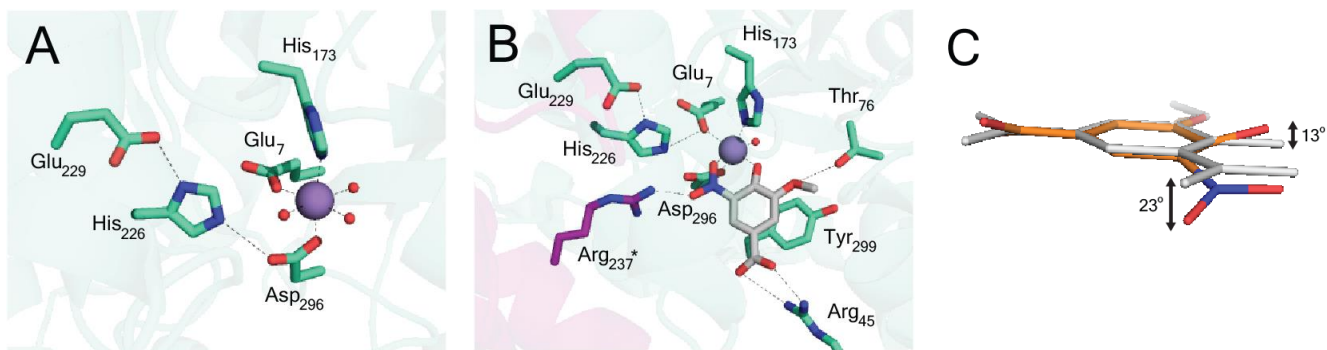


Figure 1.12. Active site architecture of 5CVA decarboxylase (LigW) from SYK-6.

Stick representations of LigW active site architecture in the resting-state (PDB ID: 4ICM) (A) and in complex with 5-nitrovanillate (PDB ID: 4NG3) (B) (177). Active site residues are shown in teal and residues from neighboring subunits are shown in purple. 5-nitrovanillate is shown in white. The Mn²⁺ ions and water are represented as purple and red spheres. (C) Superposition of LigW-bound (colored) and 'free' small molecule (white) 5-nitrovanillate.

Among the COG2159 enzymes, LigW has been the most extensively studied and provides a mechanistic paradigm (178). A crystal structure of LigW from SYK-6 reveals that the active site Mn²⁺ is coordinated by Glu-7, His-173, Asp-296, and three solvent molecules (Figure 1.12A). The crystal structure of LigW with a substrate analog, 5-nitrovanillate, revealed a remarkable enzyme-induced distortion of the nitro group relative to the phenyl ring by approximately 23° (Figure 1.12C) (177). This process is metal-independent, as similar out-of-plane bending was observed in variants lacking a metal cofactor. The crystal structure of the LigW-inhibitor complex also revealed that 5-nitrovanillate is bound to the metal in a bidentate manner via the C4 hydroxyl and the C5 nitro (Figure 1.12B). This binding mode precludes a metal-bound solvent, in contrast to the canonical hydro-

lytic amidohydrolases. Moreover, the other active site water molecules are ill-positioned for the nucleophilic attack suggesting that decarboxylation does not involve a hydrated intermediate.

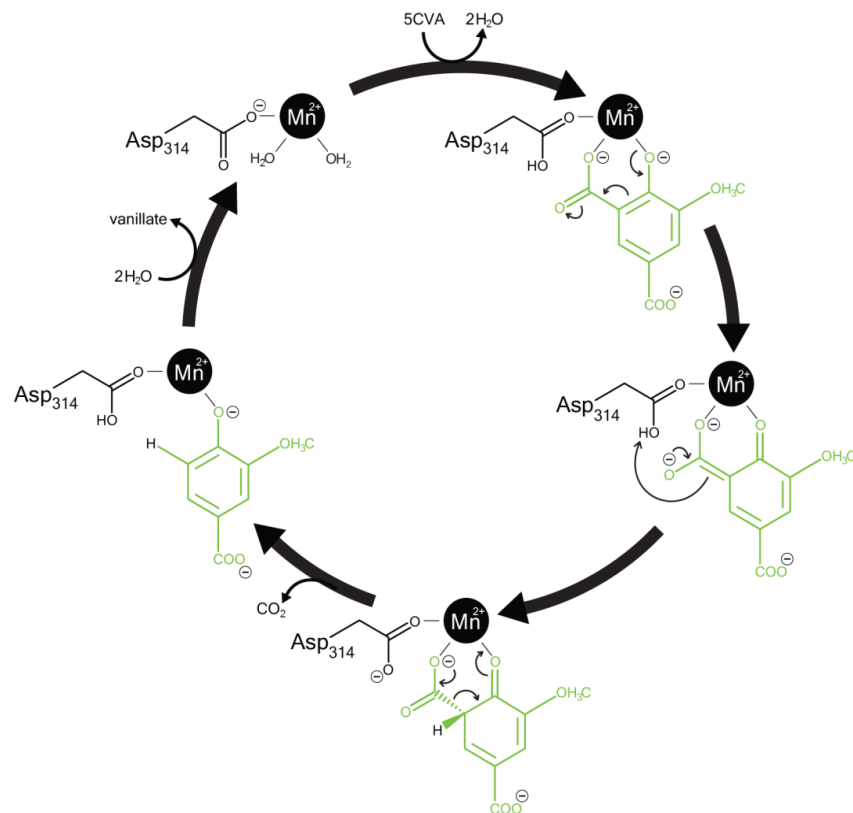


Figure 1.13. The proposed catalytic mechanism of LigW, a COG2159 decarboxylase.
The substrate, 5CVA, is in green (177).

In the proposed LigW mechanism, the substrate binds in a bidentate manner, similar to the 5-nitrovanillate inhibitor, with displacement of the metal coordinating Asp-296 (Figure 1.13). It is proposed that Asp-296 is deprotonates the C4 hydroxyl. Asp-296 then protonates C5, and followed by the decarboxylation. It is unclear whether the proton at C5 originates from the bulk solvent or from the substrate's C4 hydroxyl. Indeed, when the reaction was carried out in D₂O, the resulting vanillate contained a deuterium at C5. A substrate analog lacking a C4 hydroxyl was not cleaved by LigW, nor were related compounds such as 3-methoxysalicylate, 4-hydroxyisophthalate, and isophthalate (52). LigW also catalyzes proton exchange at C5 in vanillate but not in 3-methoxybenzoate, further supporting the role of the C4 hydroxyl in stabilizing a phenolate anion at C5. A product isotope effect corroborates the proposal that C5 is protonated prior to decarboxyla-

tion (177). Further, quantum chemical study and membrane inlet spectroscopy established that the LigW-catalyzed reaction releases CO_2 as an initial product, not HCO_3^- (179). Overall, this catalytic mechanism can be applied to other decarboxylases and provides insights into the reactivity of other COG2159 enzymes.

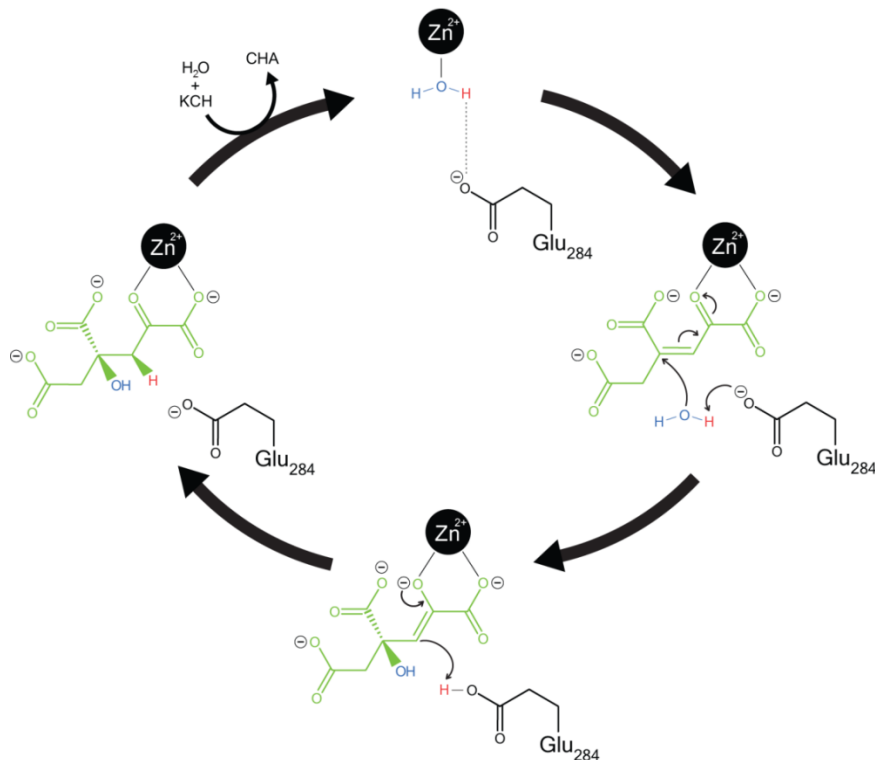


Figure 1.14. The proposed catalytic mechanism of LigJ, a COG2159 hydratase.
The substrate, KCH, is in green (180).

A recent characterization of LigJ further supports the role of the metal ion of COG2159 enzymes in polarizing the substrate (180). A crystal structure of LigJ from SYK-6 reveals a Zn^{2+} ion coordinated by His-8, His-10, His-179 and a solvent species in a typical subtype III architecture. The metal-bound solvent species is coordinated by His-223 and Glu-284. Interestingly, Glu-284 does not coordinate the active site metal. Structural evaluation of the LigJ·CHA and LigJ E284Q·KCH complexes revealed that the organic ligands were bound to the metal in a bidentate fashion, via the C1 carboxylate and the C2-oxo. This binding mode precludes the metal-bound solvent species typical of the hydrolytic amidohydrolases. In the proposed mechanism of LigJ, the ligand binding is accompanied by the displacement of a single solvent species from the metal coordination shell (Figure 1.14).

This reaction is facilitated by Glu-284, acting first as a general base to deprotonate a water molecule for nucleophilic attack at the C5 centre, and then as a general acid to protonate C3. The charge from the nucleophilic attack is delocalized via the contribution of Zn²⁺ as a Lewis acid.

Biochemical characterization of ACMSD has provided additional insights into the COG2159 enzymes. For example, it has been established that these enzymes generally function as dimers (181). The dimeric requirement is due to a conserved active site Arg, Arg-239 in ACMSD and Arg-237 in LigW. In these enzymes, this residue protrudes from one protomer into the active site of the neighbouring protomer (178,181). This arginine ion pairs with the substrate's carboxylate and is essential to orientating and stabilizing the substrate (Figure 1.12); substitution of this residue typically abolishes enzymatic activity.

1.5 Aims and scope of the dissertation

This dissertation aims to elucidate molecular processes involved in the bacterial catabolism of lignin-derived aromatics. More specifically, this study characterizes three sphingomonad metalloenzymes that catalyze C-C bond fission, each of which is presented in Chapters 2-4, respectively. Chapter 5 delves deeper into the catalytic mechanism of one of these enzymes.

Chapter 2 describes the biochemical characterization of lignostilbene- α,β -dioxygenase (LsdA) from *Sphingomonas paucimobilis* TMY1009. This work extends the collective contributions by Kamoda *et al.* (116). In this study LsdA was heterologously produced and purified from *E. coli*. The substrate specificity of LsdA was evaluated against a panel of stilbenoids using an oxygraph assay. Inhibition kinetics were evaluated using an azo-stilbene. Further, x-ray crystallography and mutagenesis analyses were used to identify the roles of key residues in catalysis.

Chapter 3 describes the biochemical characterization of OH-DDVA dioxygenase (LigZ) from *S. paucimobilis* SYK-6. This work extends the initial study by Peng *et al.* (50). A highly active preparation of LigZ was obtained using a modified purification scheme which considered the lability of the active site Fe²⁺ in extradiol dioxygenases. This preparation was used to provide more accurate kinetic parameters and to better characterize the enzyme's substrate range. An oxygraph assay was further used to evaluate LigZ's mechanism-based inactivation. A combination of chemical derivatization, NMR, MS, and spectroscopic analyses revealed the identity and properties of the MCP resulting from the LigZ-catalyzed cleavage of OH-DDVA.

Chapters 4 and 5 describe the characterization of DCHM-HOPDA hydrolase (LigY) from *S. paucimobilis* SYK-6. LigY succeeds LigZ in the catabolism of DDVA, so this work builds on the work presented in Chapter 3 (51). In Chapter 4, phylogenetic and structural analyses revealed the identity of LigY as a Zn²⁺-dependent member of the amidohydrolase superfamily. Chemical derivatization and MS analyses identified CHPD as the second hydrolysis product, consistent with the role of LigY as a MCP hydrolase. A combination of steady-state kinetics, mutagenesis, x-ray crystallography, and modelling was employed to characterize the LigY-catalyzed reaction. A catalytic mechanism for MCP hydrolysis by a metal-dependent enzyme was proposed and discussed with respect to that catalyzed by the serine-dependent MCP hydrolases.

Chapter 5 describes the substrate activation strategy of LigY and expands the mechanistic studies initiated in Chapter 4. Transient phase kinetics was used to investigate substrate activation.

The importance of the substrate's C4 carboxylate was highlighted by evaluating LigY's substrate specificity using substrate analogs. Spectroscopic and structural analyses of LigY in complex with one of these analogs were used to evaluate the role of conserved residues and the metal ion in catalysis. The results were discussed with respect to related amidohydrolases that catalyze decarboxylation reactions and were used to further refine the proposed mechanism of MCP hydrolysis by LigY. Chapter 6 discusses the results from the previous chapters in a broader perspective, including the study's caveats and future directions. Overall, this dissertation provides insights into three different enzyme classes and provides a frame work for the development of microbial biocatalyst in the valorization of lignocellulosic biomass.

Chapter 2:

Characterization of LsdA, a lignostilbene- α,β -dioxygenase

2.1 Introduction

In the catabolism of lignin derived diarylpropane and phenylcoumaran by TMY1009, LsdA catalyzes the cleavage of stilbenoids into two molecules of aldehyde. This is exemplified by the cleavage of stilbenoid model compound, lignostilbene into two molecules of vanillin (Figure 2.1). Despite the long historical precedence on the study of LsdA, these observations were never replicated owing to the challenges in purifying soluble and highly active LsdA. A *trans*- structure and 4-hydroxylation has long been recognized as a substrate determinant in the stilbene cleavage (126). Nevertheless, the protein ligands responsible for substrate recognition or catalysis remain poorly characterized.

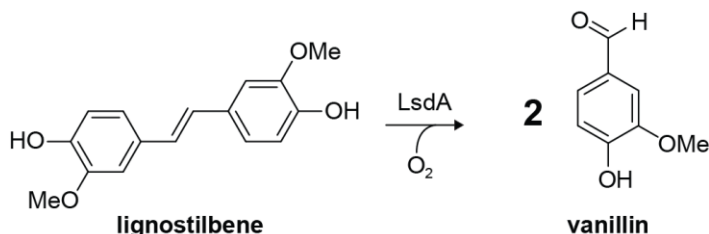


Figure 2.1. Reaction catalyzed by LsdA.

Herein, we report the kinetic and structural characterization of the original stilbene-cleaving oxygenase, LsdA from TMY1009. Steady-state kinetic studies were performed to evaluate the substrate specificity of the enzyme for a variety of stilbenes. X-ray crystal structures were determined including that of LsdA bound to a substrate analog. Conserved active site residues were substituted to evaluate their roles in substrate specificity and catalysis. These results are discussed with respect to carotenoid cleavage oxygenases and bacterial lignin catabolism.

2.2 Material and Methods

2.2.1 Chemical and reagents

All reagents were of analytical grade unless otherwise noted. Restriction enzymes and the Phusion PCR system used for cloning were from New England Biolabs. Water for buffers was purified using a Barnstead Nanopure DiamondTM system to a resistance of at least 18 mΩ.cm. Lig-nostilbene was a gift from Prof. Victor Snieckus and Dr. Timothy E. Hurst (Queens University, Ontario). All other stilbenes were commercially sourced (Figure 2.2).

2.2.2 DNA manipulation

DNA was purified, manipulated and propagated using standard procedures (182). The gene which encodes for the α -isoform of LSD_{TMY1009}, was synthesized by back-translating the protein's amino acid sequence translated from the *lsd-I* gene (locus tag: 1917171A) which encodes the α -subunit of the LSD_{TMY1009} using codon optimized for expression in *Escherichia coli* (GenScript USA Inc.) (Appendix A1). The gene was subcloned into pET41b (Novagen) to yield pET41bLsdA. Variants of LsdA were generated from pET41bLsdA using PCR-based mutagenesis using a pair of overlapping primers. The nucleotide sequences of key constructs were confirmed by sequencing. The oligonucleotides used in this study are listed in Appendix B2.

2.2.3 Protein production and purification

LsdA was produced heterologously using *E. coli* BL-21 λ(DE3) containing pET41LsdA and pGro7 (Takara Bio Inc.). Freshly transformed cells were grown at 37 °C in LB broth supplemented with 30 mg/liter of kanamycin, 30 mg/liter chloroamphenicol, and 1 mg/ml of L-arabinose to an Abs₆₀₀ of ~0.7. Expression of *lsdA* was induced with 1 mM isopropyl β -D-thiogalactopyranoside (IPTG), at which time the medium was further supplemented with 0.5 mM FeCl₃, and the cells were incubated at 16 °C for an additional 16 h. Cells were harvested by centrifugation and stored at -80 °C until further processing. Cells collected from 2 liters of culture were suspended in 20 ml of 20 mM 4-(2-hydroxyethyl)-1-piperazinepropanesulfonic acid (HEPPS), 2 mM dithiothreitol (DTT), 0.5 mM (NH₄)₂Fe(SO₄)₂, pH 8.0, and lysed at 4 °C using an EmulsiFlex-C5 homogenizer (Avestin). Cellular debris was removed by centrifugation. (NH₄)₂SO₄ was added to the cleared lysate to a final concentration of 1.2 M, and the supernatant was removed by centrifugation. The protein pellet was

resuspended in the cell resuspension buffer supplemented with 0.8 M $(\text{NH}_4)_2\text{SO}_4$ and the precipitate was removed by centrifugation and filtration at 0.45 μm . Subsequent purification steps were performed anaerobically by manipulating the sample inside a glovebox (Labmaster Model 100, Mbraun). Chromatography was performed using an ÄKTA Purifier interfaced to the glovebox with buffers and fraction collection inside the glovebox. Buffers used for purification were sparged with N_2 before being placed in the glovebox for equilibration overnight. The supernatant was loaded onto a Source 15 phenyl column and eluted with a linear gradient from 0.8 to 0 M $(\text{NH}_4)_2\text{SO}_4$ in 120 ml of 20 mM HEPES, 2 mM DTT, 0.5 mM $(\text{NH}_4)_2\text{Fe}(\text{SO}_4)_2$, pH 8.0 (ÄKTA Purifier, GE Healthcare). Fractions containing LigY, as determined through SDS-PAGE, were pooled and dialyzed into 20 mM HEPES, 2 mM DTT, pH 8.0. LigY was purified further using a MonoQ 10/100 GL column (GE Healthcare). The protein was eluted with a linear gradient from 0.2 to 1 M NaCl in 120 ml of 20 mM HEPES, 2 mM DTT, pH 8.0. Fractions containing LigY were pooled, dialyzed into 20 mM HEPES, 80 mM NaCl, 2 mM tris(2-carboxyethyl)phosphine hydrochloride (TCEP), pH 8.0, concentrated to \sim 10 mg/ml, flash-frozen as beads in liquid N_2 , and stored at -80 °C until further use. The variants were purified similarly. Apo-LsdA was purified using a similar protocol except that the purification was performed aerobically and neither the media nor the buffers were supplemented with iron.

2.2.4 Protein analytical methods

Protein purity was evaluated using SDS-polyacrylamide gel stained with Coomassie Blue according to established procedures (182). Protein concentration was determined using a micro BCA™ Protein Assay Kit (Pierce) using bovine serum albumin as a standard. Iron concentrations were determined colorimetrically using the Ferene S assay and ferric chloride solution as a standard (183). ICP-MS was performed using a NexION 300d (Perkin Elmer) calibrated using IV-Stock-4 synthetic standard (Inorganic Ventures). To liberate metals ions, the protein samples were treated with concentrated HNO_3 and H_2O_2 as previously described (184).

2.2.5 Steady-state kinetics

Kinetic assays were performed by monitoring the consumption of O_2 using a Clark-type polarographic O_2 electrode OXYG1 (Hansatech) connected to a circulating water bath. Assays were performed in 1 mL of air-saturated 40 mM N-[tris(hydroxymethyl)methyl]-3-aminopropanesulfonic

acid (TAPS) ($I = 0.1$ M, pH 8.5) at 25°C and initiated by adding the stilbene. Stock solutions of the stilbenes are made in dimethylformamide (DMF). The final concentration of DMF in the assay solutions was < 0.5 % (v/v). Reaction velocities were corrected for the background reading prior to substrate addition. The electrode was calibrated daily according to the manufacturer's instructions using air-saturated water and O₂-depleted water via addition of sodium hydrosulfite. Stock solutions were prepared fresh daily. Steady-state kinetic parameters were evaluated by fitting the Michaelis-Menten equation to the data using the least-squares fitting of LEONORA (185). The effect of pH on the rate of the LsdA-catalyzed reaction was evaluated using $I = 0.1$ M solutions of citrate (pH 6.0), HEPES (pH 7.0-9.0), and carbonate (pH 9.6 and 10.3). The apparent steady-state kinetic parameters for O₂ were evaluated using 125 μM lignostilbene and initial concentrations of O₂ from 16 to 600 μM. The initial O₂ concentrations were achieved by equilibrating the reaction mixture with humidified mixtures of O₂ and N₂ gasses. Final O₂ levels were normalized to the ambient O₂ level prior to the adjustment. The electrode was equilibrated with air-saturated buffer between runs. The inhibition of LsdA by phenylazophenol was evaluated by monitoring the initial velocity using varying concentration of lignostilbene and the inhibitor. The inhibition constants were determined by fitting an equation describing mixed inhibition to the data using LEONORA (185).

2.2.6 HPLC resolution of LsdA-catalyzed reaction

The sample for high performance liquid chromatography (HPLC) analysis was prepared by reacting ~100 μM lignostilbene dissolved in DMF and ~0.1 μM LsdA in air-saturated buffer. The reaction was quenched after 10 min with ~10% (v/v) glacial acetic acid. The enzyme was removed by centrifugation and passage through 0.22 μm filter. The sample was resolved using a Waters 2695 Separation HPLC module (Milford, MA) equipped with Waters 2996 photodiode array (PDA) detector and a Luna C18(2) 5-μm 150 x 3-mm column (Phenomenex) with linear gradient of 0.1% formic acid and methanol. Lignostilbene and vanillin were run as standards.

2.2.7 Protein structure determination

Crystals of apo-LsdA were grown aerobically by sitting drop at room temperature in a 1:1 mixture of ~10 mg/ml apo-LsdA in 20 mM HEPES, 80 mM NaCl, 2 mM TCEP, pH 8.0 with reservoir solution containing 0.2 M tri-potassium citrate and ~20% PEG3350 (v/v). Crystals were briefly soaked in reservoir buffer supplemented with ~30% glycerol (v/v) for cryoprotection and

flash frozen in liquid nitrogen. Diffraction data were collected at the Stanford Synchrotron Radiation Lightsource (SSRL) on beamline 7-1 and the data were processed and integrated using *AUTOXDS* (186). LsdA crystallized in the space group *P*3₂1 with two molecules in the asymmetric unit. The structure was solved by molecular replacement using the coordinates from the structure of apocarotenoid-15,15'-oxygenase from *Synechocystis* sp. strain PCC 6803/Kazusa (PDB ID: 2BIW) as a search model with the program PhaserMR from the Phenix package (187,188). The structure was manually edited using Coot and refinement was performed with phenix.refine (189,190). The refined structure has residues 2 to 483 modelled, out of 485 total residues, for chain A with a gap between 381 and 384 where poor electron density was not amendable to modelling. Residues 2 to 482 are modeled for chain B. The model also contains 547 waters, three magnesium ions, and four glycerol molecules.

Crystals of holo-LsdA were grown aerobically by sitting drop at room temperature in a 1:1 mixture of ~10 mg/ml holo-LsdA in 20 mM HEPES, 80 mM NaCl, 2 mM TCEP, pH 8.0 with reservoir solution containing 0.2 M sodium acetate and ~25% PEG3350 (v/v). Crystals were briefly soaked in reservoir buffer supplemented with ~30% glycerol (v/v) for cryoprotection and flash frozen in liquid nitrogen. Diffraction data were collected at the SSRL on beamline 7-1. Data were processed and integrated using Mosflm and CCP4 AIMLESS (191,192). Holo-LsdA crystallized in the space group *P*3₂1 with two molecules in the asymmetric unit. The structure was solved using molecular replacement with LsdA protomer coordinates from the solved apo-structure (described previously) as a search model in the program PhaserMR from the Phenix package (187,188). The refined structure has residues 2 to 481 modeled for chain A. Chain B has residues 2 to 481 modeled with two gaps spanning residues 306-315 and 381-386 that were not modeled due to poor electron density. The model also contains two iron molecules, one magnesium ion, three glycerol, and 351 water molecules.

A crystal structure of LsdA·phenylazophenol was obtained by co-crystallizing the enzyme and inhibitor. The crystals were prepared aerobically by sitting drop at room temperature using a 1:1 ratio of ~10 mg/mL LsdA in protein buffer and reservoir buffer containing 0.2 M sodium fluoride and ~17% PEG3350 (v/v) supplemented with ~1 mM of phenylazophenol in DMF. Crystals were flash frozen in liquid nitrogen. Diffraction data were collected at the Canadian Light Source on beamline 08ID-1 and data were processed and integrated using Mosflm and CCP4 AIMLESS

(191,192). The crystal was of space group $P3_221$ with two molecules in the asymmetric unit. The structure was also solved using molecular replacement with LsdA protomer coordinates from the solved apo-structure as a search model in PhaserMR from Phenix (187,188). The refined structure has residues 2 to 482 modeled for each protomer but there was poor electron density for residues 309-315 and 380-386 in both protomers. A single solvent molecule was modeled in each active site.

Data collection and refinement statistics for all three structures are summarized in Table 2.2. Structure figures were generated in PyMOL (The PyMOL Molecular Graphics System, Version 1.8 Schrödinger, LLC). Root-mean-square deviation (RMSD) calculations between different LsdA structures were performed using the least-squared superposition tool of Coot (189). RMSD calculations between different LsdA and LSD_{NOV1} structures were performed using DALI (193).

2.3 Results

2.3.1 Purification of LsdA

LsdA of TMY1009 was produced in *E. coli* using a pET vector containing the α -isoform of LSD_{TMY1009}. Most of the produced protein was insoluble, consistent with a previous account (114). However, the co-production of LsdA in a strain producing the GroEL and GroES chaperones significantly improved the level of soluble LsdA. LsdA was purified to >99% apparent homogeneity as judged by SDS-polyacrylamide gel electrophoresis (PAGE) analysis at yields of ~10-20 mg of purified protein per liter of cell culture. Inductively coupled plasma mass spectrometry analyses revealed that purified LsdA contained ~1 eq of iron per protomer and insignificant amounts of cadmium, cobalt, copper, zinc, manganese, nickel, and lead. Consistent with this result, a colorimetric assay based on Ferene-S yielded a value of 1.1 ± 0.2 equivalent of iron per LsdA protomer. Preparations of LsdA retained essentially 100% of its activity when exposed to ambient levels of O₂ for up to 16 h at room temperature.

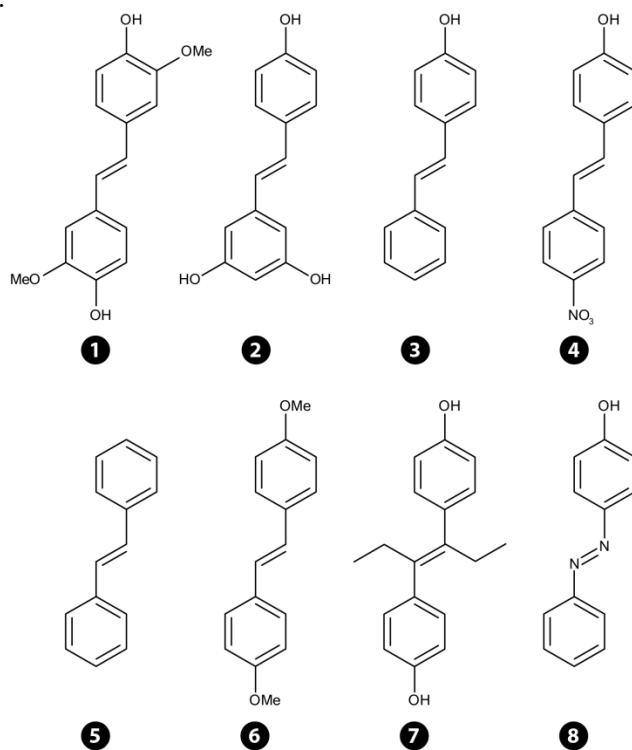


Figure 2.2. LsdA substrates and analogs.

Lignostilbene (1), resveratrol (2), 4-hydroxystilbene (3), 4-hydroxy-4'-nitrostilbene (4), stilbene (5), 4,4'-dimethoxystilbene (6), diethylstilbestrol (7), phenylazophenol (8).

2.3.2 Substrate specificity

In an oxygraph assay, LsdA was most active at pH 8.5 (Figure 2.3). Accordingly, the enzyme was subsequently characterized using air-saturated TAPS ($I = 0.1\text{ M}$), pH 8.5 at $25\text{ }^{\circ}\text{C}$. Similar activity was observed using 2-amino-2-(hydroxymethyl)propane-1,3-diol (Tris) as the buffer. LsdA cleaved 4-hydroxy *trans*-stilbenes such as lignostilbene, 4-hydroxystilbene, and resveratrol, but not 4-hydroxy-4'-nitrostilbene. The LsdA-catalyzed cleavage of lignostilbene to vanillin was validated using an HPLC-based assay (Figure 2.4). The initial rate of lignostilbene cleavage displayed Michaelis-Menten kinetics (Figure 2.5A). As summarized in Table 2.1, LsdA cleaved the substrates with the following specificity: lignostilbene $>$ 4-hydroxystilbene \approx resveratrol. LsdA also displayed Michaelis-Menten behavior with respect to O_2 concentration, with a K_{MO_2} value of $190 \pm 10\text{ }\mu\text{M}$ (Figure 2.5B).

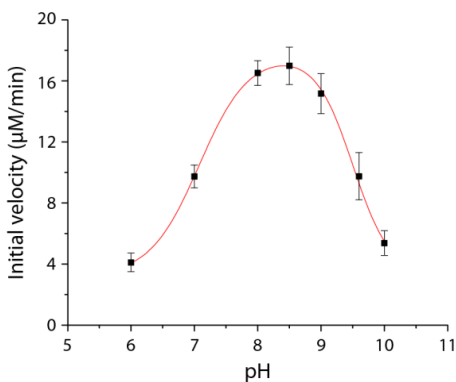


Figure 2.3. pH-dependent activity profile.

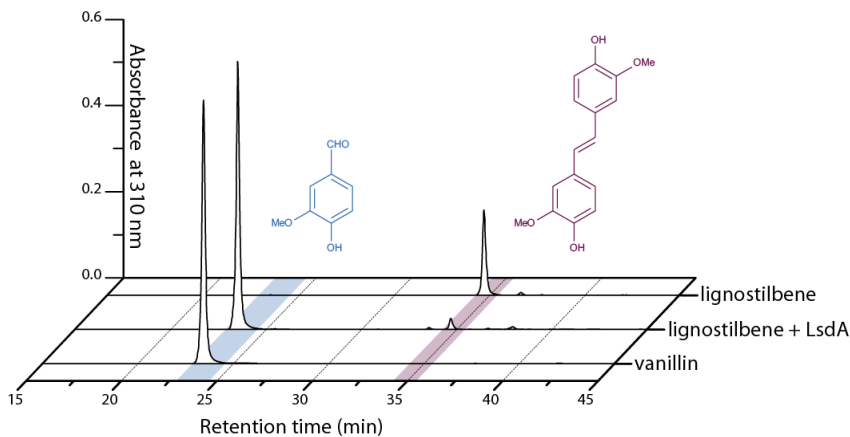


Figure 2.4. HPLC resolution of LsdA-catalyzed reaction.

Traces are of lignostilbene, lignostilbene incubated with LsdA, and vanillin. Peaks corresponding to lignostilbene and vanillin are highlighted with red and blue, respectively.

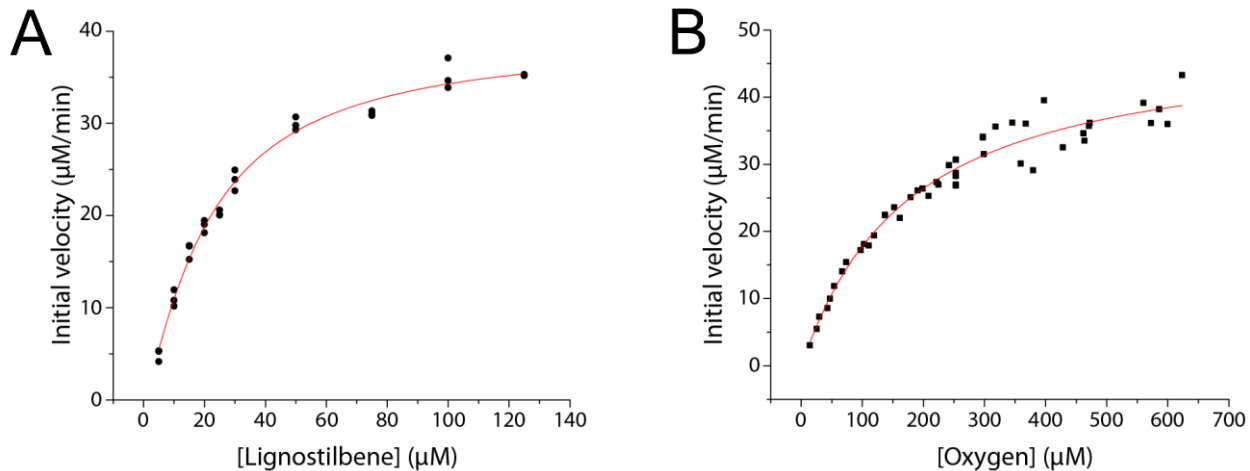


Figure 2.5. Steady-state kinetic analyses of the LsdA-catalyzed reaction.

(A) Dependence of initial velocity on lignostilbene concentration in air-saturated TAPS ($I = 0.1 \text{ M}$, pH 8.5), 25 °C. (B) Dependence of initial velocity on the O_2 concentration in the presence of 125 μM lignostilbene. Red lines represent fits of the Michaelis-Menten equation to the data.

In the oxygraph assay, neither stilbene nor 4,4'-dimethoxystilbene were detectably cleaved by LsdA, consistent with their lack of a 4-hydroxy substituent. Other compounds that were not cleaved include phenylazophenol and diethylstilbestrol. The identification of phenylazophenol as a non-hydrolysable substrate analog that bears a 4-hydroxy substituent prompted us to evaluate its ability to inhibit the LsdA-catalyzed reaction. In steady-state kinetic studies, phenylazophenol inhibited the LsdA-catalyzed cleavage of lignostilbene ($K_{ic} = 6 \pm 1 \mu\text{M}$ and $K_{iu} = 24 \pm 4 \mu\text{M}$; K_{ic} and K_{iu} refer to competitive and uncompetitive inhibition constant, respectively) (Figure 2.6). Preincubation of LsdA with up to 50 μM phenylazophenol for up to 30 minutes at room temperature did not significantly affect the enzymatic activity, consistent with reversible inhibition.

Table 2.1. Apparent steady-state kinetic parameters of LsdA for different substrates^a.

Substrate	k_{cat}^{app} s ⁻¹	K_M^{app} μM	k_{cat}^{app}/K_M^{app} s ⁻¹ . mM^{-1}
lignostilbene	30 ± 1	31 ± 3	1000 ± 50
resveratrol	0.63 ± 0.02	34 ± 4	19 ± 2
4-hydroxystilbene	0.21 ± 0.01	9 ± 1	24 ± 3

^aExperiments were performed using TAPS ($I = 0.1 \text{ M}$), pH 8.5, at 25 °C. Parameters were calculated using a minimum of 20 data points at various substrate concentrations and were obtained using air-saturated buffer and are thus apparent.

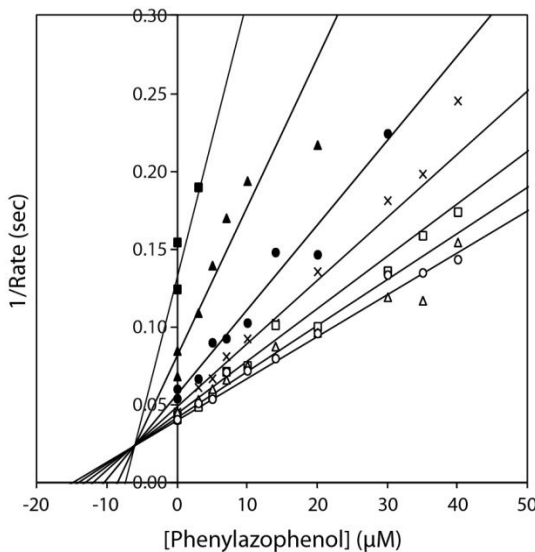


Figure 2.6. Dixon plot of the inhibition of LsdA-catalyzed lignostilbene cleavage by phenylazophenol.

Experiments were performed using TAPS ($I = 0.1$ M, pH 8.5), 25 °C and 10 μM (■), 20 μM (▲), 40 μM (●), 60 μM (×), 80 μM (□), 100 μM (Δ), and 120 μM (○) lignostilbene. The lines represent a best fit of an equation describing mixed inhibition to the data ($K_{ic} = 6 \pm 1 \mu\text{M}$; $K_{iu} = 24 \pm 4 \mu\text{M}$; $K_M = 32 \pm 3 \mu\text{M}$; $k_{cat} = 32 \pm 2 \text{ s}^{-1}$).

2.3.3 Structure of LsdA

LsdA crystallized in space group $P3_21$ with two LsdA protomers in the asymmetric unit. Structures were solved to 2.3 and 2.6 Å resolution for apo-LsdA and bound to Fe²⁺ (holo-LsdA), respectively (Table S2). The apo and holo-LsdA protomers are highly similar in structure, with an average RMSD over all C α atoms of ~0.3 Å. LsdA forms a dimer in solution (118) and this quaternary structure is likely represented crystallographically by the two protomers in the asymmetric unit (Fig. 4A). The buried surface area at the dimer interface is 1460 Å² and the protomers are related by an approximate 2-fold rotational symmetry. The structural scaffold of LsdA is that of a seven-bladed β-propeller fold, typical of the CCOs (Fig. 4B). The dimer interface is largely formed of polar interactions (Fig. 4C) and includes an anti-parallel β-sheet formed by the residues Glu-20 to Asp-22 of the first blade of the β-propeller in each protomer. Furthermore, the side-chain carboxylates of Asp-25 and Glu-27 form reciprocal salt bridges with Arg-15 and the amino-terminus (Ala-2) from the two protomers. Among stilbenoid-cleaving dioxygenases of known structure, LsdA is most similar

to the resveratrol-cleaving enzyme LSD_{NOV1} (Protein Data Bank (PDB) entry 5J53) (117), sharing an RMSD of 1.1 Å over 473 aligned C α atoms.

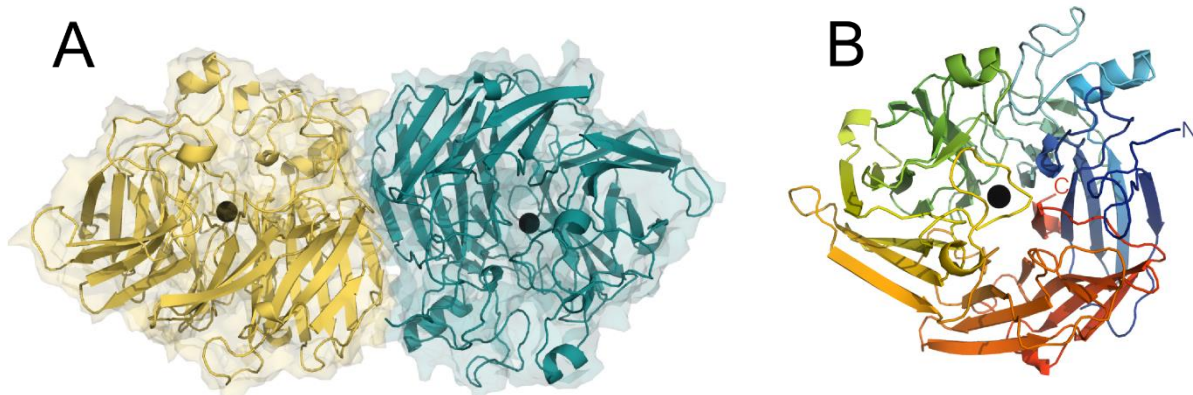


Figure 2.7. Crystal structure of LsdA dimer and protomer.

(A) Ribbon and surface representation of the dimeric assembly of LsdA. The different protomers of the asymmetric unit are yellow and teal, respectively. (B) Ribbon diagram of LsdA protomer in rainbow-color from blue (N terminus) to red (C terminus). Bound Fe²⁺ ions are shown as black spheres.

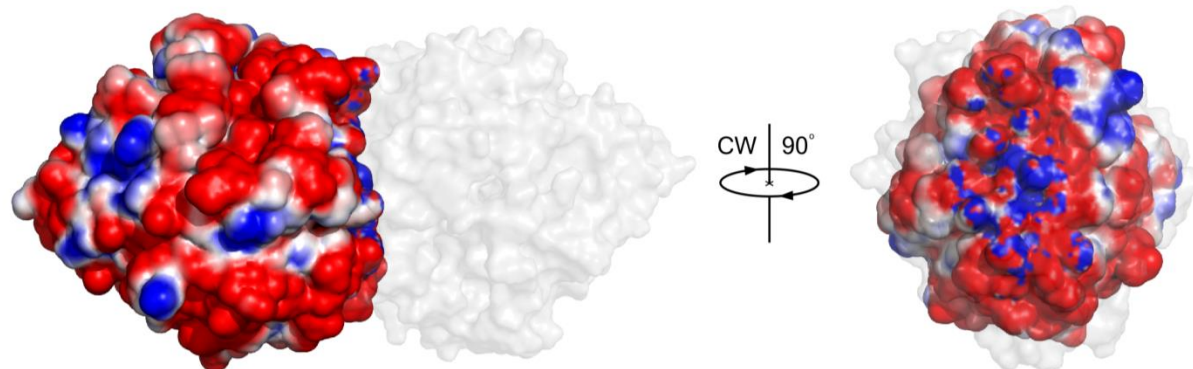


Figure 2.8. The surface electrostatic analyses of LsdA.

The analyses are shown as color-coded surface representations according to surface charge which ranges from negative (red) to positive (blue). The dimeric partner is shown in gray at a lower opacity.

Table 2.2. X-ray diffraction data collection and refinement statistics for LsdA structures ^a.

	Apo-LsdA	Holo-LsdA	LsdA·phenylazophenol
<i>Data Collection^a</i>			
Resolution Range (Å)	37.08 - 2.30 (2.38 – 2.30)	60.92 – 2.60 (2.69 – 2.60)	61.00 - 3.00 (3.11 - 3.00)
Space group			
	<i>P</i> 3 ₂ 1	<i>P</i> 3 ₂ 1	<i>P</i> 3 ₂ 1
Unit cell dimensions			
<i>a</i> , <i>b</i> , <i>c</i> (Å)	181.3, 181.3, 94.9	181.3, 181.3, 95.1	181.9, 181.9, 96.4
α, β, γ (°)	90, 90, 120	90, 90, 120	90, 90, 120
Unique reflections	79,776 (7876)	56,663 (5634)	34,286 (3443)
Completeness (%)	99.9 (99.4)	99.8 (99.6)	92.0 (93.6)
Redundancy	13.5 (13.2)	9.2 (9.9)	2.0 (2.0)
Average <i>I</i> / <i>σI</i>	20.3 (2.1)	15.4 (2.2)	9.9 (2.5)
R _{merge}	0.146 (1.353)	0.048 (0.337)	0.053 (0.259)
CC _{1/2}	0.998 (0.731)	0.996 (0.733)	0.990 (0.875)
Wilson <i>B</i> -factor (Å ²)	35.8	39.0	55.7
Anisotropy	0.356	0.115	0.637
<i>Refinement</i>			
R _{work} (R _{free})	0.180 (0.203)	0.187 (0.215)	0.198 (0.248)
Number of water molecules	547	351	0
RMSD bond length (Å)	0.003	0.003	0.010
Average <i>B</i> -values (Å ²)	40.9	43.0	53.9
Ramachandran plot (%)			
Most favored regions	97.6	96.3	91.8
Disallowed regions	0	0.2	0.8

^a Data collection values in parentheses represent the data for the highest resolution shell.

2.1.1 Metal-binding site

As observed in other CCOs, the LsdA active site harbors a single Fe^{2+} ion which resides at the center for the β -propeller. This metal ion is coordinated in a tetragonal pyramidal fashion by four conserved histidines (His-167, 218, 282, and 472) and a solvent molecule (Figure 2.9A). The average Fe^{2+} -His bond length in the resting state LsdA is $\sim 2.2 \text{ \AA}$, in agreement with values reported in other CCOs (114,117). Similar to other CCOs, the sixth metal coordination site (across from His-282) is unoccupied and is partly occluded by Thr-121 (194). Additionally, three of the metal-coordinating histidines are in hydrogen bonding interactions with three conserved acidic residues, Glu-135, 350, and 414.

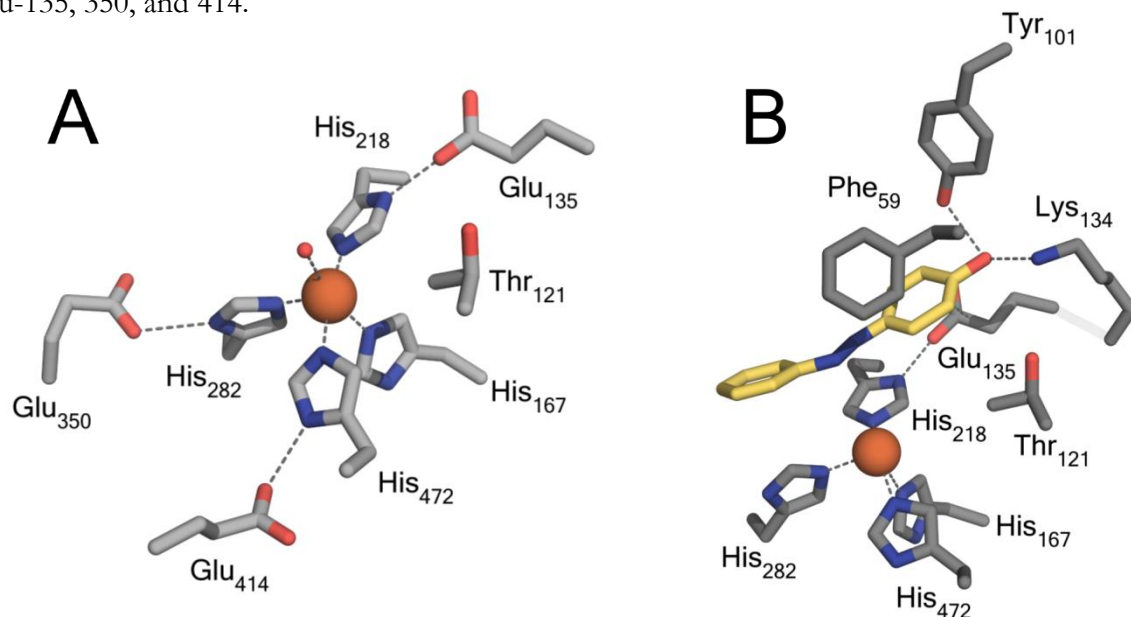


Figure 2.9. The active site of LsdA.

Stick representation of LsdA in the resting state (A) and in complex with phenylazophenol (B). The Fe^{2+} ion and solvent species are represented as orange and red spheres, respectively. Phenylazophenol is shown in yellow. Polar and hydrogen bonding interactions ($\leq 3.0 \text{ \AA}$) are indicated using dashed lines.

2.1.2 Structure of the LsdA·phenylazophenol complex

To further explore substrate binding in LsdA, the enzyme was co-crystallized with phenylazophenol. Co-crystals of LsdA·phenylazophenol were yellow, similar to that of the inhibitor. Similar to the inhibitor-free structures, two protomers constitute the asymmetric unit and the complex was refined to 3.0 \AA (Table S2). Inspection of an omit difference density map revealed positive density consistent with the presence of the inhibitor molecules adjacent to the metal at each active site. Phe-

nylazophenol was modelled at full occupancy; however, the resolution of the structure precluded defining the binding orientation on the basis of density fitting alone. Instead, the binding orientation was derived from the polarity of surrounding amino acid residues and by comparison to bound ligands homologous structures from the literature (114,117). In LsdA, the 4-hydroxy moiety of the phenylazophenol as modelled forms hydrogen bonds with each of Tyr-101 and Lys-134 (Fig. 5B). In addition, Phe-59 forms a π - π stacking interaction to the aromatic ring of the phenol group. Glu-350 is located within the active site pocket distal to Tyr-101 but does not contact the inhibitor which lacks substituents on the second ring. These residues are conserved throughout stilbene-cleaving dioxygenases and have been previously identified in binary complexes of LSD_{NOV1} and CAO1, respectively, with resveratrol (114,117). Ser-283 and Glu-353 of NOV1 form a hydrogen bonds to the ring hydroxyl resveratrol; however, only the glutamate is conserved (Glu-350 in LsdA). Ser-283 is replaced by glycine in both LsdA and CAO1. Phenylazophenol bound to LsdA covered by a layer of phenylalanine residues (Phe-305, Phe-307, Phe-308) from the cap in addition to the interaction with Phe-59 and is not solvent accessible.

Interestingly, the active site iron in the LsdA·phenylazophenol structure has a lower metal occupancy, as indicated by a weaker overall density. The polypeptide fold of phenylazophenol-bound LsdA is virtually indistinguishable from the inhibitor-free form as comparison between the two yielded an RMSD over all C α atoms of \sim 0.3 Å. Binding of the inhibitor is accompanied by conformational changes in the phenyl rings of Phe-305 and Phe-308. The phenylazophenol is not in direct contact with the Fe²⁺ ion. Also, no density corresponding to a metal-bound solvent or O₂ species was observed in the LsdA·phenylazophenol complex in contrast to in either CAO1 or LSD_{NOV1} structures bound to resveratrol, presumably owing to the low resolution.

2.1.3 Active-site variants

To evaluate the roles of key residues in substrate recognition and catalysis, we substituted each of three residues of LsdA identified to interact with the 4-hydroxy moiety of the phenylazophenol: Phe-59, Tyr-101 and Lys-134. These residues were substituted with histidine, phenylalanine, and methionine, respectively. The variants were purified in similar yields as the WT LsdA. Further, they all contained a full complement of iron. As summarized in Table 2.3, all of the variants had significantly lesser activity compared to the WT. Indeed, the K134M variant did not detectably

cleave resveratrol. The Y101F variant had $k_{\text{cat}}^{\text{app}}$ and $k_{\text{cat}}^{\text{app}}/K_M^{\text{app}}$ (the superscript *app* refers to apparent parameters) values that were 10% and 20% those of the WT while the corresponding values for the F59H variant were ~7% and 3% those of WT LsdA.

Table 2.3. Apparent steady-state kinetic parameters of LsdA and select variants^a.

Enzyme	$k_{\text{cat}}^{\text{app}}{}_b$	K_M^{app}	$k_{\text{cat}}^{\text{app}}/K_M^{\text{app}}$
	s ⁻¹	μM	s ⁻¹ .mM ⁻¹
WT	30 ± 1	31 ± 3	1000 ± 50
F59H	2.0 ± 0.1	72 ± 5	28 ± 2
Y101F	3.1 ± 0.1	15 ± 1	210 ± 20
K134M	n.d. ^c	n.d.	n.d.

^a Experiments were performed using air-saturated TAPS ($I = 0.1$ M), pH 8.5, at 25 °C. Parameters were calculated using a minimum of 20 data points at various lignostilbene concentrations.

^b Reported parameters are apparent.

^c Not detected.

2.2 Discussion

This study expands our understanding of LsdA and related stilbene-cleaving dioxygenase. Crystallographic analyses revealed a remarkable conservation of these enzymes to the CCOs. Kinetic and mutagenesis analyses elaborated on LsdA's substrate specificity and probed the role of three conserved active site residues. Among these residues, only Lys-134 was essential for catalysis; variants substituted in either Phe-59 or Tyr-101 retained significant activity.

The substrate specificity studies of LsdA are consistent with previous reports that the enzyme only cleaves 4-hydroxystilbenes. More particularly, it had previously been determined that LsdA does not cleave 2-hydroxy, 3-hydroxy or 4-methoxy stilbenes (126). Indeed, different LSD homologs have varying substrate specificities as seen in different isoforms of LSD_{TMY1009} (118). Although most characterized LSDs appear to require the 4-hydroxy moiety for activity (113,117,195), LSD_{NOV1} does not, cleaving rhabonigenin and rhabonticin, which are 4-methoxy stilbenes (123). As described previously, this 4-hydroxy substituent plays an important role in the proposed reaction mechanism of LSDs. In both mechanisms, Lys-134 and Tyr-101 have been proposed to assist in the deprotonation of the 4-hydroxyl (114,117). Of the two residues, Lys-134 is more critical for catalysis. Although the high pK_a of lysine's ε-amino group (~10) makes it ill-suited to function as a base catalyst; however, its role as such has been demonstrated in enzymes such as leucine dehydrogenase (196).

The inhibition of LsdA by phenylazophenol is consistent with previous studies in which LsdA was unable to cleave stilbenoids with substitutions at either C_α or C_β of the vinyl group (127,128). Further, both N-benzylideneaniline and N-benzylaniline potently inhibited LsdA (128). Similarly, CAO1 did not cleave fluoro-resveratrol (114). Phenylazophenol behaved as a mixed-inhibitor which suggests the presence of multiple binding sites. While only a single binding site was observed in the LsdA·phenylazophenol complex crystal structure, electron density consistent with multiple ligands was observed in a Co²⁺-substituted CAO1·resveratrol complex (114).

Although LsdA cleaves lignostilbene quite efficiently, the enzyme's physiological substrate remains unknown. Inspection of the substrate binding site of LsdA revealed several pockets adjacent to the phenyl groups of the inhibitor, suggesting the enzyme's physiological substrate has multiple substitutions along the aromatic groups. Interestingly, the stilbenoid 3-(4-hydroxy-3-(4-hydroxy-3-methoxystyryl)-5-methoxyphenyl)-acrylate (DCA-S) has been identified as a metabolite in the catab-

olism of dehydroniconiferyl alcohol in SYK-6 (55). Nevertheless, LsdA's specific activity for DCA-S was two orders of magnitude lower than for lignostilbene (116).

LSDs and other CCOs appear to be relatively resistant to the oxidative inactivation of their Fe²⁺ cofactor. This is in contrast to another class of non-heme Fe²⁺ dioxygenases, the extradiol dioxygenases, which are inactivated during turnover and upon exposure to O₂. While LSDs may use a gating mechanism similar to the extradiol dioxygenases, this protective measure is unlikely to involve structural changes to modulate the enzyme's affinity towards O₂. Substrate binding in CCO did not affect the protein structure, nor significantly change the electronic state of the metal (114). Indeed, the active site metal appears to have minimal contribution towards substrate binding and overall protein structure. However, ligand binding may have a steric or electronic effect in the formation of the ternary complex. Kinetic studies to evaluate whether the reaction proceeds via a compulsory- or random-order ternary-complex mechanism are currently underway.

Interestingly, the residues at the LsdA dimer interface are conserved in LsdB. These include Arg-15 and Glu-27 which form reciprocal salt bridges between from the two protomers of the LsdA dimer. The high degree of conservation between LsdA and LsdB rationalizes how LsdA and LsdB form homo- and heterodimers *in vivo* (118). Further, these residues are conserved in CAO1, consistent with its dimeric structure. By contrast, these residues are not conserved in LSD_{NOV1}, consistent with this protein functioning as a monomer.

Chapter 3:

Characterization of LigZ, OH-DDVA dioxygenase

3.1 Introduction

In the catabolism of lignin-derived biphenyl by SYK-6, LigZ catalyzes the cleavage of OH-DDVA into DCHM-HOPDA (Fig. 3.1). As described in the Introduction (1.2.3.1), the DDVA pathway was identified largely based on the common catabolic logic employed in the bacterial aerobic catabolism of aromatic compounds; despite the minimal sequence homology of these enzymes to known pathways in addition to the lack of identification of metabolites involved (Figure 3.1). Studies of LigZ and LigY are complicated by the instability of DCHM-HOPDA: when produced *in situ* from OH-DDVA using LigZ, 5CVA was only produced if LigY was also present in the reaction mixture (51). Moreover, DCHM-HOPDA decomposed upon derivatization and analysis by GC-MS (50).

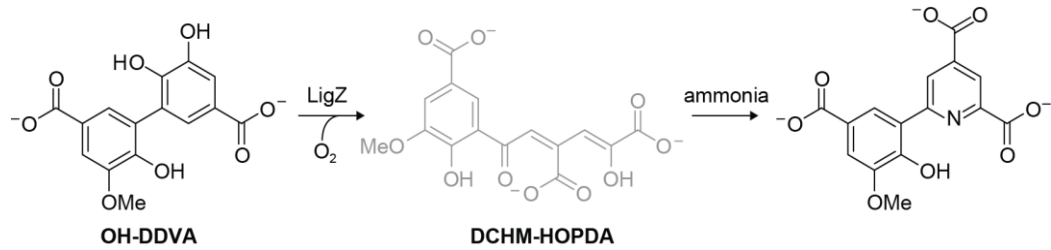


Figure 3.1. Proposed reaction catalyzed by LigZ of SYK-6.

MCPs form stable pyridine derivatives in the presence of ammonia. DCHM-HOPDA (gray) has not been experimentally validated.

Herein, we report the biochemical characterization of LigZ to extend initial work by Peng *et al.* (50). The enzyme was purified and its reaction product was characterized using mass spectrometry and NMR. The reaction products and its non-enzymatic transformation were characterized. An oxygraph assay was used to evaluate LigZ's steady-state kinetic parameters, substrate specificities, as well as the enzyme's susceptibility to inactivation by various substrates. The results are discussed with respect to the type II extradiol dioxygenases and bacterial lignin catabolism.

3.2 Material and Methods

3.2.1 Chemical and reagents

All reagents were of at least analytical grade unless otherwise noted. OH-DDVA was synthesized as described previously (50). Restriction enzymes and the Phusion PCR system were purchased from New England Biolabs. Water for buffers was purified using a Barnstead Nanopure Diamond™ system to a resistance of at least 18 mΩ.cm. Protocatechuate-4,5-dioxygenase (PCD) was a kind gift from Prof. John Lipscomb. LigY was produced as described elsewhere (2).

3.2.2 Cloning of *ligZ*

DNA was purified, manipulated, and propagated using standard procedures (182). The *ligZ* gene was amplified from genomic DNA prepared from SYK-6 (NBRC 103272) using the following primers (restriction sites underlined): 5'-CCTCATATGGCCGAAATCGTGCTG-3' and 5'-GGTAAGCTTGCCTGAAAATACAGGTTTCITGCCAGGCGACGAAGC-3'. The resulting amplicon was cloned into pET41b (Novagen, Madison, WI, USA) and its nucleotide sequence was confirmed to match the locus tag SLG_07720. The resulting construct, pET41LigZ_His, produces LigZ with a C-terminal His-tag that can be removed with the tobacco etch virus (TEV) protease.

3.2.3 Production and purification of LigZ

LigZ was heterologously produced using *E. coli* BL21 λ(DE3) containing pET41LigZ_His. Freshly transformed cells were used to inoculate 4 L LB supplemented with 30 µg/mL kanamycin at 37 °C and grown to an optical density of ~0.7. Gene expression was induced with 1 mM IPTG, and the cells were further incubated overnight at 20 °C. Cells were harvested by centrifugation and stored at -80 °C until further use. Cells were suspended in 40 mL ice-cold 20 mM HEPES, pH 7.5 and lysed at 4 °C using an EmulsiFlex-C5 homogenizer (Avestin, Ottawa, ON, Canada). Cellular debris was removed by centrifugation. LigZ was purified using Ni Sepharose 6 Fast Flow resin (GE Healthcare, Mississauga, ON, Canada) according to the manufacturer's instructions. The His-tag was removed by digestion with TEV protease at room temperature in 20 mM 4-(2-hydroxyethyl)-1-piperazineethanesulfonic acid (HEPES), pH 7.5 supplemented with 1 mM DTT and 10 mM ethylenediaminetetraacetic acid (EDTA). Uncleaved LigZ and TEV were removed by passing the dialyzed digestion mix through the Ni Sepharose 6 Fast Flow resin. LigZ was further purified using a

MonoQ 10/100 GL and an ÄKTA Purifier (GE Healthcare). The protein was eluted with a linear gradient from 0 to 0.5 M NaCl in 20 mM HEPES, pH 7.5. Fractions containing LigZ were pooled and dialyzed into 20 mM HEPES, pH 7.5, concentrated to ~30 mg/mL, and brought inside a Labmaster Model 100 glovebox (Mbraun, Peabody, MA, USA) to equilibrate overnight. The deoxygenated LigZ was incubated with a 10x molar excess of $(\text{NH}_4)_2\text{Fe}(\text{SO}_4)_2 \cdot 6\text{H}_2\text{O}$, applied to Sephadex G-25 resin (GE Healthcare) to remove excess metal, flash frozen as beads in liquid N₂, and stored at -80 °C.

3.2.4 Protein analysis method

Protein purity was evaluated using SDS-polyacrylamide gel stained with Coomassie Blue according to established procedures (182). Protein concentrations were determined using micro BCA™ Protein Assay Kit (Thermo Fisher Scientific, Bothell, WA, USA) using bovine serum albumin as a standard. Iron concentrations were determined colorimetrically using the Ferene-S assay and ferric chloride solution as a standard (183). The metal species contained in the LigZ preparation were determined using a NexION 300d ICP-MS instrument (Perkin Elmer) calibrated using IV-Stock-4 synthetic standard (Inorganic Ventures). The protein samples were treated with concentrated HNO₃ and H₂O₂ as previously described (184).

3.2.5 Steady-state kinetics

Kinetic assays were performed by monitoring the consumption of O₂ using a Clark-type polarographic O₂ electrode OXYG1 (Hansatech, Pentney, UK) connected to a circulating water bath. Assays were performed in 1 mL of air-saturated 40 mM HEPES ($I = 0.1$ M, pH 7.5) at 25 °C, 0.2% dimethyl sulfoxide (DMSO) and initiated by the addition of 5 nM of LigZ. Reaction velocities were corrected for the background reading prior to LigZ addition. The electrode was calibrated daily by a two-point calibration using air-saturated water and O₂-depleted water via addition of sodium hydrosulfite, according to the manufacturer's instructions. Stock solutions were prepared fresh daily. LigZ stock solution was prepared anaerobically, stored in a sealed vial on ice, and aliquoted using a gas-tight syringe for use. Steady-state kinetic parameters were evaluated by fitting the Michaelis–Menten equation to the data using the least-squares fitting of LEONORA.

To determine the reaction rate over a pH range of 6–9, a composite buffer containing 50 mM acetate, 50 mM 2-(N-morpholino)ethanesulfonic acid (MES), and 100 mM Tris was used. The

assay contained 100 μM OH-DDVA and was initiated with the addition of 50 nM LigZ. To determine the apparent steady-state kinetic parameters for the organic substrate, the concentration of OH-DDVA was varied from 3.1 to 400 μM . To determine the apparent steady-state kinetic parameters for O_2 , 400 μM OH-DDVA was used and the initial concentration of O_2 was varied by equilibrating the reaction mixture with humidified mixtures of O_2 or N_2 gasses. Final O_2 levels were normalized to the resting ambient O_2 level prior to the adjustment. The electrode was equilibrated with air-saturated buffer between runs.

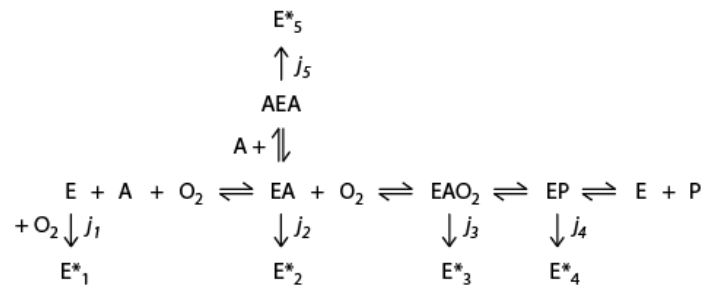


Figure 3.2. Potential modes of inactivation in extradiol dioxygenases during steady-state turnover.

E^* represents inactivated enzyme. Taken from (86).

3.2.6 Inactivation kinetics

The susceptibility of LigZ to inactivation was evaluated according to the different modes summarized in (Figure 3.2). The stability of LigZ in air-saturated buffer was evaluated by incubating the enzyme in the oxygraph cuvette under ambient conditions and measuring the residual activity, A_t , at different incubation times, t . Activity was determined by adding 400 μM OH-DDVA. The apparent first-order rate constant of inactivation, j_1^{app} , was evaluated by fitting the following equation to the data where A_{max} is the activity observed without pre-incubation:

$$A_t = A_{max} \cdot e^{j_1^{app} t} \quad (\text{Equation 1})$$

The apparent rate constant of inactivation during catalytic turnover in air-saturated buffer, j_3^{app} , was calculated from the partition ratio and k_{cat}^{app} :

$$\text{Partition ratio} = k_{cat}^{app} / j_3^{app} \quad (\text{Equation 2})$$

The partition ratio was obtained from the slope of a line fitted to a plot of total O_2 consumed versus the amount of LigZ added to the reaction. Cleavage product characterization

DCHM-HOPDA was prepared by reacting 200 μ M OH-DDVA with excess LigZ (\sim 1 μ M) in air-saturated buffer. Reactions were monitored to completion using the oxygraph. LigZ was removed by ultra-filtration using a membrane with a 30 kDa cut-off. For NMR, DCHM-HOPDA was prepared using 5 mM potassium phosphate, pH 7.5, and the pooled filtrate was derivatized with 2 mM ammonium hydroxide and freeze dried. The dried sample was suspended in D₂O (Sigma-Aldrich, St. Louis, MO, USA) to a final concentration of \sim 4 mM. NMR spectra were collected using cryoprobe-equipped Bruker Avance III 600 MHz spectrometer and processed using ACD/NMR Processor Academic Edition version 12.01 (ACD/Labs). For high accuracy mass determination, DCHM-HOPDA prepared using 20 mM ammonium acetate, pH 8.0 was run on a LC-MS system equipped with 80 x 0.25 mm Luna 3 μ m PFP2 analytical column (Phenomenex, Torrance, CA, USA). The pyridine derivative of DCHM-HOPDA was eluted using a mobile phase of 100 mM ammonium acetate, pH 4.5: methanol. Mass spectra were acquired using an Agilent 6460 Triple Quadrupole mass spectrometer equipped with an electrospray ion source operated in positive ion mode. Data were processed using MassHunter Qualitative Analysis ver. B.06.00 (Agilent Technologies, Santa Clara, CA, USA).

To identify the LigZ cleavage product of PCA, the cleavage reaction was performed in 20 mM ammonium bicarbonate, pH 8.0 to form the pyridine derivative. Upon completion, the reaction was quenched with formic acid to a final concentration of \sim 1%. The pyridine derivative was resolved on a Waters 2695 Separation HPLC module (Milford, MA, USA) equipped with a Waters 2996 PDA detector and an Aqua 5 μ m C18 250 x 4.6 mm column (Phenomenex). The derivative was eluted using 0.1% formic acid and monitored at 270 nm. For stability and apparent pK_a determination, DCHM-HOPDA was prepared using 100 mM phosphate, pH 7.5 as described above. Aliquots of enzyme-free filtrate were titrated with sodium hydroxide from pH 7.6 to 13.2, as measured with a pH electrode, while keeping the concentration of DCHM-HOPDA constant at \sim 20 μ M. Absorbance spectra were recorded using a Cary 60 UV-vis spectrophotometer (Agilent). The non-enzymatic transformation of DCHM-HOPDA was monitored spectrophotometrically at 480 nm. The half-life was evaluated by fitting a first-order exponential curve to the data. The pK_a values and relative chemical distributions were estimated using MarvinSketch 6.0.0 (ChemAxon, Cambridge, MA, USA).

3.3 Results & Discussion

3.3.1 Purification of LigZ

Heterologously produced LigZ was purified using immobilized metal ion affinity chromatography and anion exchange chromatography to >98% apparent homogeneity as judged from SDS/PAGE at yields of 5–10 mg of protein per liter of cell culture. However, this procedure yielded apo-enzyme with no detectable iron or OH-DDVA-cleavage activity, likely due to the aerobic treatment and EDTA in the TEV protease buffer. Incubation of the LigZ with excess Fe²⁺ yielded preparations containing ~1.2:1 M ratio of iron and possessing a specific activity of 210 μmol·min⁻¹mg⁻¹. This specific activity is approximately four orders of magnitude higher than what was previously reported (50).

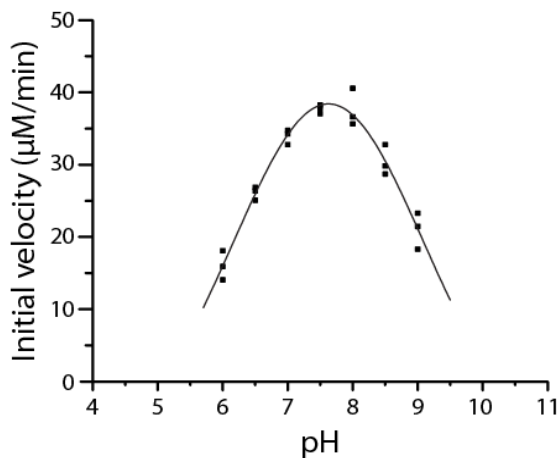


Figure 3.3. pH-dependence of LigZ activity.

The pH-dependence was measured in an oxygraph assay, using a buffer containing 50 mM acetate, 50 mM MES, and 100 mM Tris.

3.3.2 Substrate specificity

In an oxygraph assay using a composite buffer, LigZ was most active at pH 7.5 (Figure 3.3). Accordingly, the enzyme was subsequently characterized using 40 mM HEPES ($I = 0.1\text{ M}$), pH 7.5 at 25 °C. Under these conditions, the initial rate of O₂ consumption displayed Michaelis–Menten kinetics at up to 400 μM OH-DDVA (Figure 3.4A), with apparent k_{cat} and K_{M} values for OH-DDVA of $129 \pm 2\text{ s}^{-1}$ and $6.0 \pm 0.6\text{ }\mu\text{M}$, respectively (Table 3.1). The apparent $k_{\text{cat}}/K_{\text{M}}$ value of LigZ for OH-DDVA, $2.20 \pm 0.02 \times 10^7\text{ s}^{-1}\text{M}^{-1}$, is comparable to what has been reported for BphC and protocatechuate 2,3-dioxygenase for their respective physiological substrates. LigZ also displayed

Michaelis–Menten behavior with respect to O₂ concentration with a K_{M,O_2} value of $67 \pm 3 \mu\text{M}$ (Figure 3.4B).

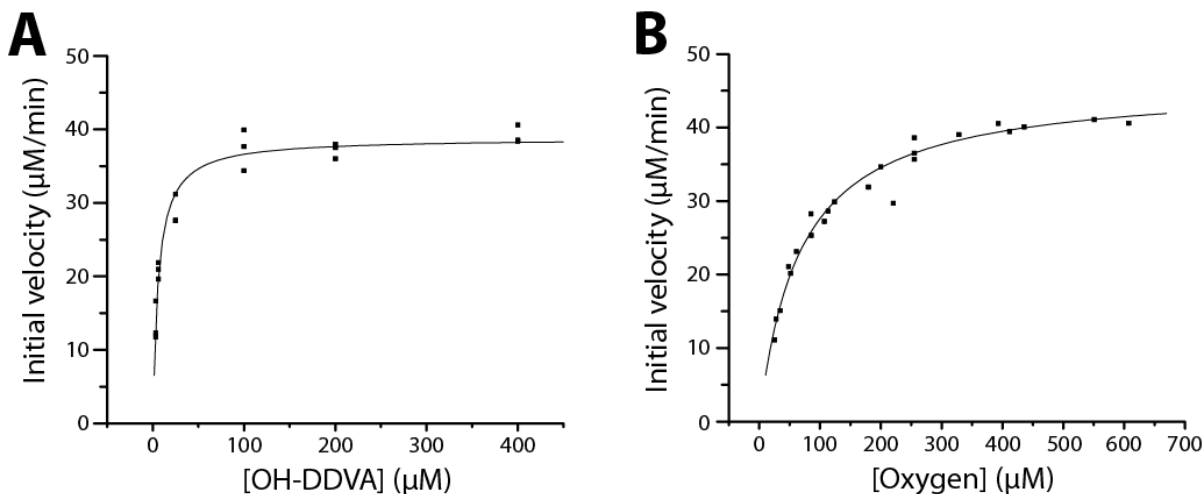


Figure 3.4. Steady-state kinetic analyses of the LigZ-catalyzed reaction.

(A) Dependence of initial velocity on OH-DDVA concentration in air-saturated buffer. (B) Dependence of initial velocity on the oxygen concentration in the presence of saturating amount of OH-DDVA. Black lines represent fits of the Michaelis–Menten equation to the data using LEO-NORA.

The high specific activity of LigZ preparations afforded a re-examination of the enzyme's substrate specificity. As previously reported, LigZ did not detectably cleave catechol, 2,3-dihydroxybiphenyl (DHB), gallate, or *ortho*-methylgallate (50). However, LigZ cleaved PCA with an apparent k_{cat}/K_M value of $7 \pm 1 \times 10^2 \text{ s}^{-1} \text{ M}^{-1}$ (Table 3.1). The addition of vanillate to the reaction mixture did not alter this value. Overall, the apparent preference of LigZ for OH-DDVA over PCA is $\sim 30,000$ -fold. By comparison, the preference of BphC for DHB over catechol is ~ 350 -fold (87).

3.3.3 Inactivation of LigZ

In the presence of higher concentrations of OH-DDVA, the activity of LigZ decreased to zero prior to substrate depletion. Moreover, O₂ consumption resumed upon addition of fresh enzyme. Because extradiol dioxygenases are O₂ labile, we investigated the stability of LigZ in air-saturated buffer at 25 °C (40 mM HEPES ($I = 0.1 \text{ M}$), pH 7.5). Under these conditions, the enzyme's activity decayed with an apparent pseudo first-order rate constant of inactivation, j_1^{app} , of $1.8 \pm 0.2 \times 10^{-2} \text{ s}^{-1}$ (Figure 3.5A), which corresponds to a half-life of $39 \pm 4 \text{ s}$. Importantly, the activity

of LigZ did not significantly decrease upon anaerobic incubation for up to 1 h, either with or without OH-DDVA, suggesting that j_2 and j_5 are negligible. Thus, LigZ seems to be quite O₂ labile. By comparison, the half-life of BphC, a Type I extradiol dioxygenase, is 16 ± 2 min (197) and that of LigAB, another Type II enzyme, is ~3 h (103). This inactivation of LigZ appears to be due to the oxidation of the active site iron because the activity could be at least partially restored upon anaerobic incubation with Fe²⁺.

Table 3.1. Apparent steady-state kinetic and inactivation parameters of LigZ.^a

Substrate	K_{MA}^{app} (μM)	k_{cat}^{app} (s ⁻¹)	$k_{cat}^{app}/k_{cat}^{app}$ (× 10 ⁴ M ⁻¹ s ⁻¹)	Partition ratio ^b	j_3^{app} (× 10 ⁻² s ⁻¹)	j_3^{app}/K_{MA}^{app} (M ⁻¹ s ⁻¹)
OH-DDVA	6.0 (0.6)	129 (2)	2200 (200)	18 000 (600)	0.72 (0.03)	1000 (100)
PCA	8000 (1000)	5.2 (0.3)	0.07 (0.01)	50 (5)	10 (1)	13 (2)

^aExperiments were performed using 40 mM HEPES ($I = 0.1$ M), pH 7.5 at 25 °C. The values in parentheses represent standard errors.

^b Partition ratio is defined as the maximum number of turn over prior to complete inactivation per unit enzyme. The total O₂ consumed was taken to represent the number of times LigZ turned over, and the amount of LigZ added to the reaction was determined from the reaction's initial velocity.

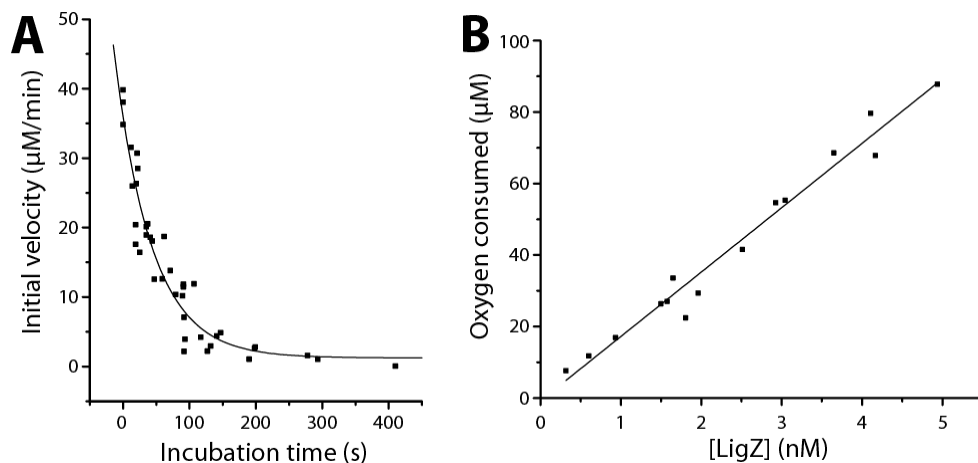


Figure 3.5. Inactivation of LigZ.

(A) The decay of LigZ activity upon incubation of the enzyme in air-saturated buffer. The red line represents a fit of Equation 1 to the data. (B) Total O₂ consumed in steady-state reactions as a function of LigZ concentration. The partition ratio was calculated from a linear fit (black line) of the data. That value for j_3^{app} was calculated from Equation 2.

To determine the apparent rate constant of inactivation during catalytic turnover, j_3^{app} , we measured the partition ratio. Values of $18\ 000 \pm 900$ and 50 ± 5 were measured for OH-DDVA (Figure 3.5B) and PCA, respectively, which correspond to j_3^{app} values of $7.2 \pm 0.3\ \text{ms}^{-1}$ and $100 \pm 10\ \text{ms}^{-1}$ (Table 3.1). These values are within a factor of two of those reported for the inactivation of BphC by DHB and catechol, respectively (87). Nevertheless, PCA is unlikely to inactivate LigZ *in vivo* given the relatively low specificity of the enzyme for this substrate. Thus, the estimated j_3^{app} / K_M^{app} value, $\sim 130\ \text{s}^{-1}\text{M}^{-1}$, is about three orders of magnitude lower than that of BphC for either 3-Cl catechol (87) or 2',6'-diCl DHB (198). Finally, although the partition ratio of LigZ for OH-DDVA is significantly lower than that of BphC ($85,000 \pm 1000$ for DHB) (87) and Xyle (1,400,000 for catechol) (96) for their physiological substrates, it is comparable to that of LigAB (18,000 for PCA) (103). The similar susceptibilities of LigZ and LigAB to inactivation during catalytic turnover do not have a ready structural explanation given that LigAB has a cap domain and LigZ does not.

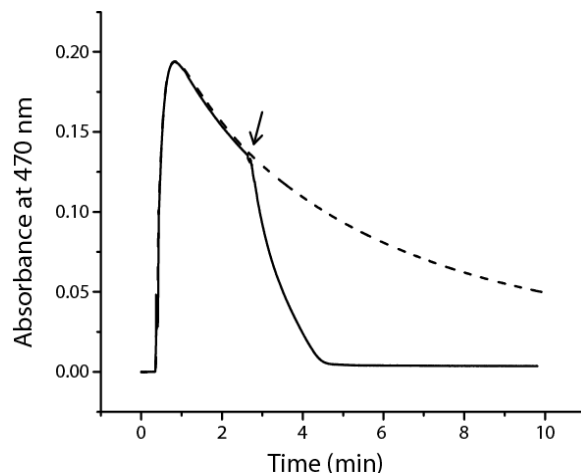


Figure 3.6. Decay of DCHM-HOPDA.

DCHM-HOPDA was generated by cleaving OH-DDVA with an excess of LigZ (potassium phosphate ($I = 0.1\ \text{M}$), pH 7.5). The dashed line depicts the non-enzymatic decay of the dienolate absorbance band ($t_{1/2} = 5.5 \pm 0.4\ \text{min}$). The solid line depicts the decay of the dienolate absorbance band upon the addition of 200 nM LigY (arrow).

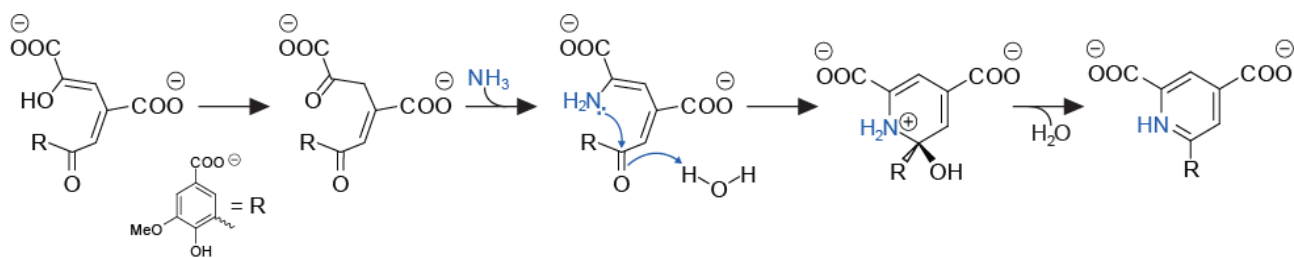


Figure 3.7. Derivatization of DCHM-HOPDA with ammonia.

3.3.4 Product identification

Cleavage of OH-DDVA by LigZ yielded a yellow colored compound ($\lambda_{\max} = 480$ nm), consistent with a dienolate anion. This species decayed rapidly in solution ($t_{1/2} = 5.5 \pm 0.4$ min, potassium phosphate ($I = 0.1$ M) pH 7.5 (Figure 3.6)), complicating characterization. To facilitate identification of the MCPs derived from OH-DDVA and PCA, they were derivatized with ammonia to form stable pyridine derivatives (Figure 3.7) (199). High-resolution liquid chromatography (LC)-MS of the OH-DDVA derived compound revealed a parent ion with an m/z value of 334.0564, which agrees well with the predicted mass of the singly protonated pyridine derivative of DCHM-HOPDA (334.0563) (Figure 3.8). The identification of the pyridine derivative of DCHM-HOPDA was further validated by 1D proton NMR and heteronuclear single quantum coherence (HSQC) analysis (^1H NMR (D_2O , 600 MHz): d 8.55 (d, 1 H, Ar-H), 8.28 (d, 1 H, Ar-H), 8.21 (d, 1 H, Ar-H), 7.62 (d, 1 H, Ar-H), 3.98 (s, 3 H, OCH₃)) (Figure 3.9A&B). Moreover, while lacking in resolution, signal counts from 1D carbon NMR were consistent with 15 carbon nuclei found in the pyridine derivative of DCHM-HOPDA (^{13}C NMR (D_2O , 600 MHz): 177.50, 175.17, 173.49, 158.99, 155.09, 152.37, 150.97, 150.65, 128.95, 123.95, 123.66, 123.13, 123.10, 120.12, 116.46, 58.58) (Figure 3.9C). Similarly, the LigZ-catalyzed cleavage of PCA, performed in an ammonium bicarbonate buffer to trap the MCP as a pyridine derivative, yielded a product that co-migrated with that formed by the PCD-catalyzed cleavage of PCA as well as 2,4-pyridinedicarboxylic acid ($t_{\text{R}} = 9.2$ min, $\lambda_{\max} = 274$ nm) (Figure 3.10). In contrast, 2,5-pyridinedicarboxylic acid eluted later ($t_{\text{R}} = 11.5$ min, $\lambda_{\max} = 270$ nm). This result indicates that LigZ catalyzes the 4,5-cleavage of PCA to 4-carboxy-2-hydroxymuconate-6-semialdehyde.

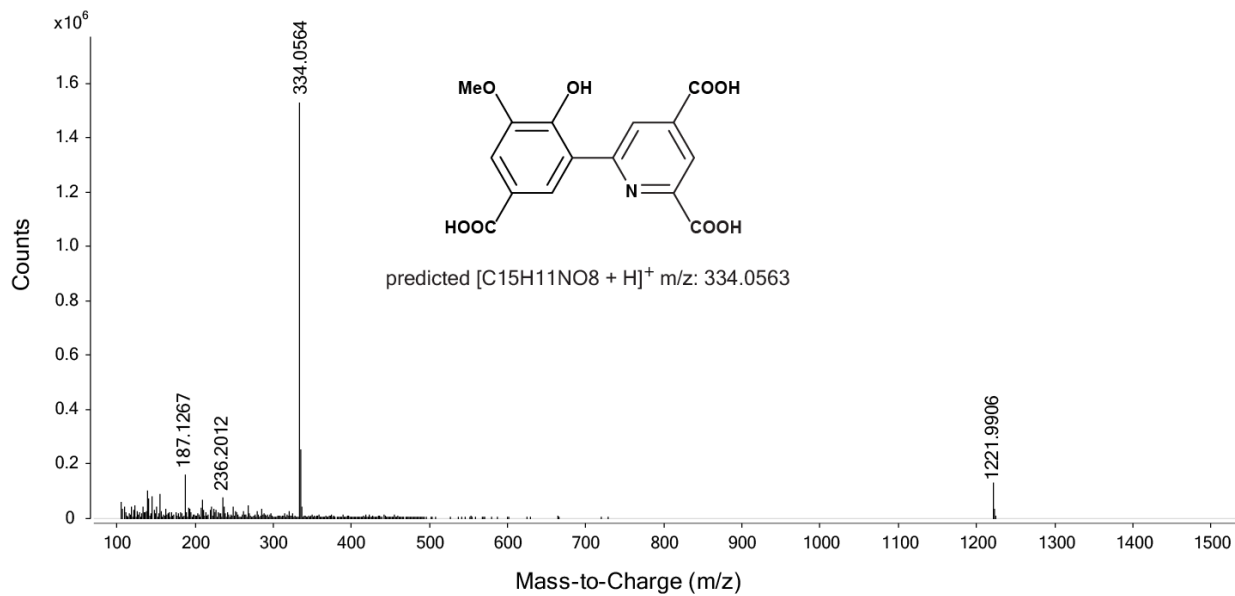
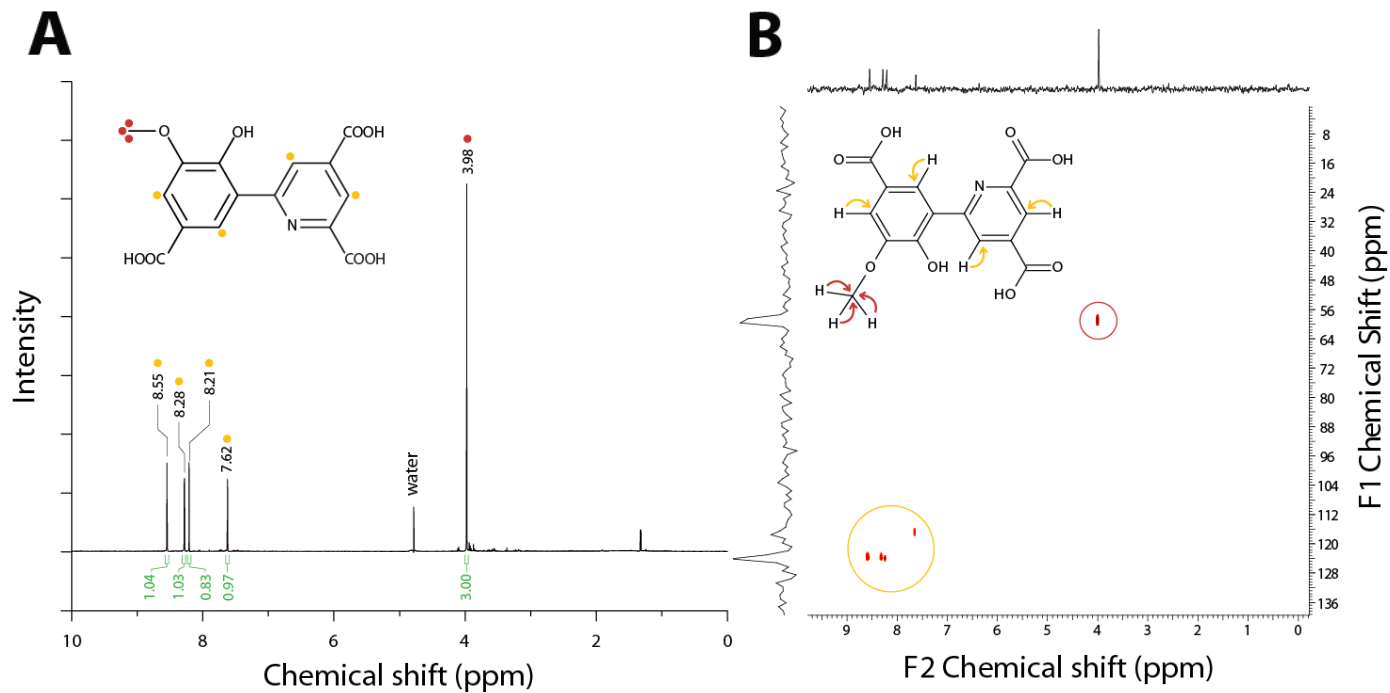


Figure 3.8. High-resolution MS spectrum of ammonia derivatized DCHM-HOPDA..



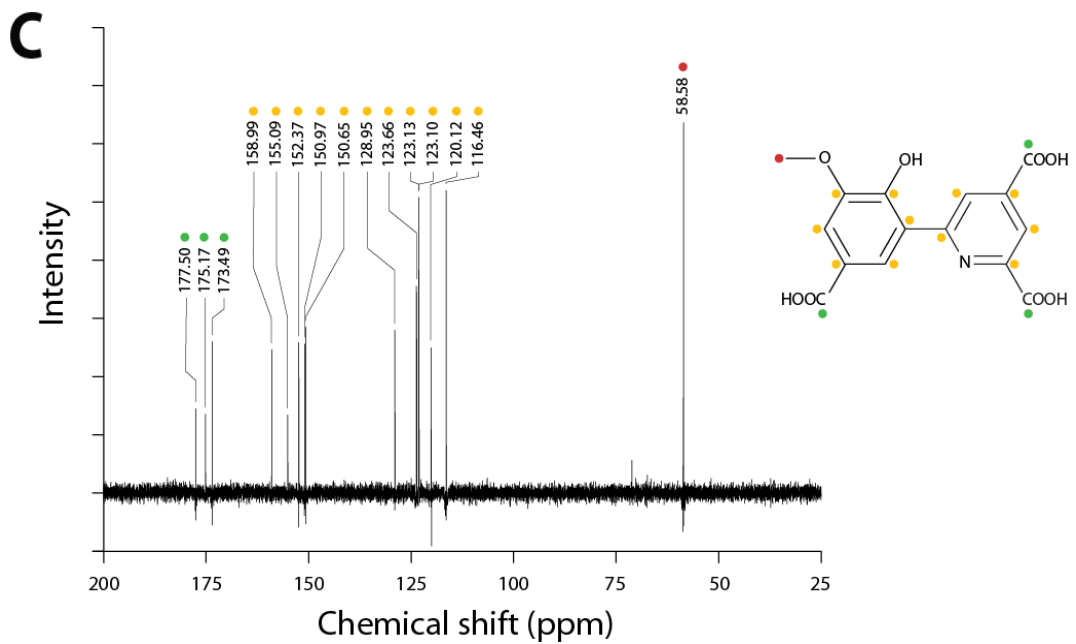


Figure 3.9. NMR analyses of ammonia-derivatized DCHM-HOPDA.

(A) ^1H NMR spectrum. Numbers in green denote integration values. The aromatic and methoxy protons are annotated as yellow and red, respectively. (B) HSQC NMR spectra. F1 and F2 axis represents ^{13}C and ^1H nuclei, respectively. The aromatic and methoxy protons are annotated as yellow and red, respectively. (C) ^{13}C NMR spectra. The carboxylates, aromatic and methoxy carbons are annotated as green, yellow and red, respectively.

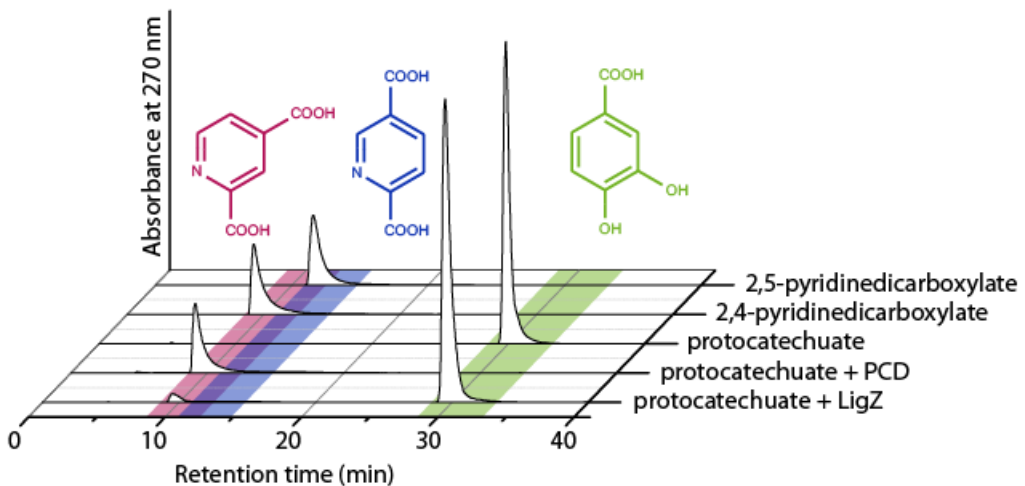


Figure 3.10. HPLC chromatograms of the pyridine derivatives of PCA cleavage products.

LigZ- and PCD-catalyzed cleavage reactions were performed in ammonium bicarbonate buffer. PCA (pink), 2,4-pyridinedicarboxylic (pink), 2,5-pyridinedicarboxylic (blue) acids were run as controls.

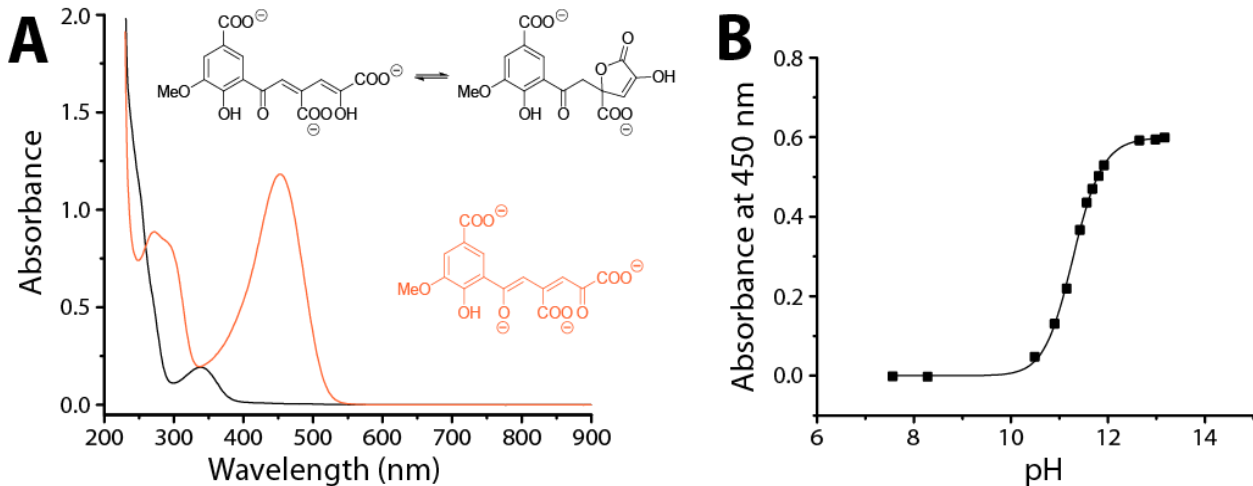


Figure 3.11. UV-visible absorption spectra of DCHM-HOPDA.

(A) Spectra were recorded at pH 7.5 (black) and 13.0 (orange). (B) The pH-dependent titration of the absorbance band at 450 nm.

3.3.5 Non-enzymatic transformation of DCHM-HOPDA

As noted above, yellow-colored DCHM-HOPDA decayed rapidly in solution. The decay rate increased with pH and ionic strength, and gave rise to a stable species characterized by a λ_{\max} of 340 nm (Figure 3.11A). This species is likely to be a γ -lactone similar to those formed by muconates and HOPDA (151,200). Consistent with this interpretation, the dienolate species was regenerated under alkaline condition ($\lambda_{\max} = 452$ nm, pH > 13), and decayed again when the pH was neutralized. Moreover, equilibration between the dienolate and the lactone took several minutes after perturbation of the pH. Despite the low sensitivity, LC-MS analysis of the products from LigZ-catalyzed OH-DDVA cleavage under acidic condition also revealed two species with m/z consistent with a singly protonated DCHM-HOPDA or its γ -lactone ($m/z 353.05$). Nevertheless, titration of DCHM-HOPDA with base yielded an apparent pKa value of 11.3 (Figure 3.11B). This value is commensurate with the predicted pKa for the C2 hydroxyl of DCHM-HOPDA. In HOPDA and its chlorinated congeners, the pKa of the C2 hydroxyl correlated with the stability of the dienolate in solution (201). That is, a lower pKa of the C2 hydroxyl favors the dienolate form. The decay of the MCP was accelerated in the presence of LigY (Figure 3.6), suggesting that the dienolate species is the substrate for LigY. The half-life of DCHM-HOPDA could be confirmed indirectly by quenching the non-enzymatic transformation of the dienolate with excess LigY after various non-enzymatic incubation times and quantifying the non-enzymatically transformed MCP by adding NaOH to generate the

dienolate (Figure 3.12). The half-life calculated in this manner was similar to that calculated by spectrophotometrically monitoring the decay of the dienolate (~ 5 min). This result also indicated that only the dienolate is a substrate for LigY. The non-enzymatic transformation of DCHM-HOPDA to the γ -lactone and inability of LigY to transform the latter explains the lack of hydrolysis product upon delayed addition of LigY (51). At the same time, characterization of DCHM-HOPDA and its stability facilitates further characterization of LigY.

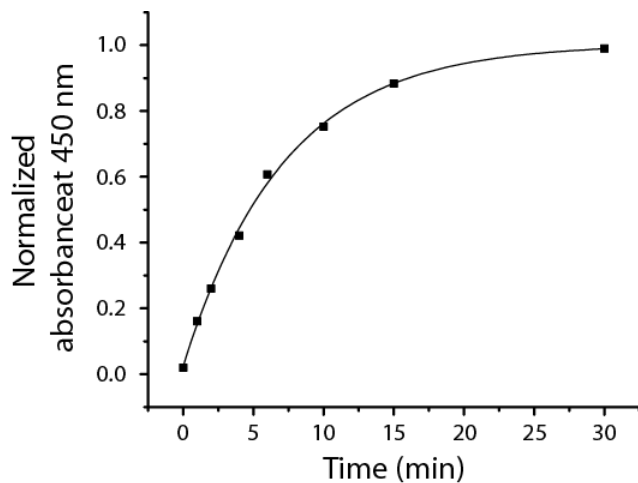


Figure 3.12. Discontinuous measurement of DCHM-HOPDA stability.

DCHM-HOPDA was allowed to decay non-enzymatically. At the plotted time points, the reaction was ‘quenched’ with excess amount of LigY. The amount of dienolate that had decayed non-enzymatically was determined by the remaining enolate signal upon addition of sodium hydroxide. A first order growth was fitted to the data ($t_{1/2} \sim 5$ min).

Chapter 4:

Characterization of LigY, DCHM-HOPDA hydrolase

4.1 Introduction

LigY is proposed to catalyze the hydrolysis of DCHM-HOPDA to 5CVA and CHPD in the catabolism of lignin-derived biphenyl by SYK-6 (Figure 4.1). Further, as described in the Introduction (1.2.3.1), this enzyme was proposed to be a MCP hydrolase. However, LigY does not share significant amino acid sequence identity with known MCP hydrolases (51). As described in Chapter 3, I identified DCHM-HOPDA as the product of the LigZ-catalyzed cleavage of OH-DDVA, and further established that the enolate form of the MCP is the substrate of LigY-catalyzed reaction (202). Nevertheless, the reaction catalyzed by LigY remains uncertain as CHPD has not been verified as the second hydrolysis product.

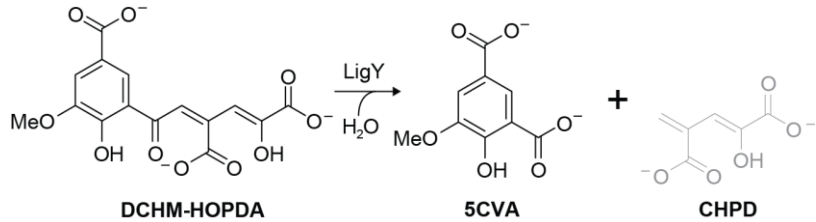


Figure 4.1. Proposed reaction catalyzed by LigY of SYK-6.
CHPD (gray) has not been experimentally validated

Herein, we report the characterization of LigY. The phylogeny of this enzyme was established based on sequence analyses. The reaction products were characterized using mass spectrometry. A fluorescence-based assay was developed for steady-state kinetic characterization, and a crystal structure was obtained to reveal the catalytic machinery of LigY. The roles of key residues were investigated using directed mutagenesis. A molecular mechanism of catalysis is proposed based on precedents with related enzymes as well as the presented data. These results are discussed with respect to MCP hydrolases and the amidohydrolase superfamily.

4.2 Material and Methods

4.2.1 Chemicals and reagents

All reagents were of analytical grade unless otherwise noted. OH-DDVA was synthesized as described previously (1). Restriction enzymes and the Phusion PCR system used for cloning were from New England Biolabs. Water for buffers was purified using a Barnstead Nanopure DiamondTM system to a resistance of at least 18 18 mΩ.cm.

4.2.2 Cloning and mutagenesis

DNA was purified, manipulated, and propagated using standard procedures (182). A gene encoding *ligY* (locus tag: SLG_07750) was synthesized by back-translating the protein's amino acid sequence using codons optimized for expression in *E. coli* (GenScript USA Inc.) (Appendix A2). The *ligY* gene was amplified from the synthetic gene, and the resulting amplicon was cloned into pET41b (Novagen). Two constructs were made: pET41LigY and pET41LigY_His. The latter encodes the enzyme with a C-terminal TEVpro-cleavable octahistidine tag (LigY-Ht). Variants of LigY were generated from pET41LigY using PCR-based mutagenesis and either a pair of overlapping primers or a single phosphorylated primer. The *ligW* gene (locus tag: SLG_07850) was amplified from genomic DNA prepared from SYK-6 (NBRC 103272). The resulting amplicon was cloned into pET41b to generate pETLigW, encoding LigW with no affinity tag. The nucleotide sequence of all constructs was confirmed by sequencing. The oligonucleotides used in this study are listed in Appendix B2.

4.2.3 Protein production and purification

For kinetic characterization, LigY was produced heterologously using *E. coli* BL-21 λ(DE3) containing pET41LigY. Freshly transformed cells were grown at 37 °C in LB broth supplemented with 30 mg/liter kanamycin to an A_{600} of ~0.7. Expression of *ligY* was induced with 1 mM IPTG, at which time the medium was further supplemented with 1 mM ZnSO₄ and the cells were incubated at 30 °C for an additional 16 h. Cells were harvested by centrifugation and stored at -80 °C until further processing. Cells collected from 2 liters of culture were suspended in 20 ml of 20 mM HEPPS, pH 8.0, and lysed at 4 °C using an EmuliFlex-C5 homogenizer (Avestin). Cellular debris was removed by centrifugation. Ammonium sulfate was added to the cleared lysate to a final concentration

of 1.6 M, and the precipitated protein was removed by centrifugation. The supernatant was loaded onto a Source 15 phenyl column and eluted with a linear gradient from 1.6 to 0 M ammonium sulfate in 120 ml of 20 mM HEPES, pH 8.0 (ÄKTA Purifier, GE Healthcare). Fractions containing LigY, as determined through SDS-PAGE, were pooled and dialyzed into 20 mM HEPES, pH 8.0. LigY was purified further using a MonoQ 10/100 GL column (GE Healthcare). The protein was eluted with a linear gradient from 0.2 to 0.6 M NaCl in 120 ml of 20 mM HEPES, pH 8.0. Fractions containing LigY were pooled, dialyzed into 20 mM HEPES, pH 8.0, concentrated to ~30 mg/ml, flash-frozen as beads in liquid N₂, and stored at -80 °C until needed.

LigY-Ht was produced for crystallization using *E. coli* BL-21 λ(DE3) containing pET41LigY_His. Cells were grown, and cell extracts were produced as described above. LigY-Ht was purified from the cell extract using immobilized metal affinity chromatography (nickel-nitrilotriacetic acid, Qiagen) according to the manufacturer's instructions. The His tag was proteolytically removed by overnight incubation with TEV protease, leaving a 6-residue tail at the C terminus (ENLYFQ), and was further purified using anion exchange chromatography as described above for LigY. Selenomethionyl LigY-Ht was similarly prepared with labeling performed as described previously (203). LigY variants were prepared the same way as non-tagged LigY. The mass of purified LigY and its variants was validated using Quadropole Time of Flight MS. LigW was produced heterologously using *E. coli* BL-21 λ(DE3) containing pET41LigW and was purified essentially as for non-tagged LigY. LigZ was purified as described previously (1).

4.2.4 Protein analytical methods

Protein purity was evaluated using SDS-polyacrylamide gel stained with Coomassie Blue (182). Protein concentrations were determined using the Micro BCA™ protein assay kit (Pierce) using bovine serum albumin as a standard. The metal content of LigY preparations was determined both (*a*) colorimetrically using 4-(2-pyridylazo)-resorcinol (PAR) and ZnCl₂ as a standard (204) and (*b*) using a NexION 300d ICP-MS (PerkinElmer Life Sciences) calibrated using IVStock-4 synthetic standard (Inorganic Ventures). Protein samples for ICP-MS analysis were treated with concentrated HNO₃ and H₂O₂ as described previously (184).

4.2.5 SEC-MALS

In preparation for Size exclusion chromatography-multi-angle light scattering (SEC-MALS) analysis, 0.5 mg/ml of LigY in 20 mM HEPES, pH 8.0, 100 mM NaCl was loaded onto a Superdex 200 10/300 column (GE Healthcare) attached to a 1260 Infinity LC (Agilent Technologies) and operated at 0.2 ml/min at room temperature. Data were collected using a miniDAWN TREOS multi-angle static light scatterer and an Optilab T-rEX refractive index detector (Wyatt Technologies). Data were analyzed using the ASTRA6 software (Wyatt Technologies).

4.2.6 CD spectroscopy

Spectra were recorded using a Jasco J-810 circular dichroism (CD) spectrometer equipped with a Peltier temperature controller and a 1-mm path length quartz cuvette. Spectra were collected at 25 °C between 300 and 195 nm at a scan rate of 100 nm/min and a response time of 2 s. Samples contained 5 µM protein in potassium phosphate ($I = 0.1$ M, pH 7.5).

4.2.7 Steady-state kinetic analysis

Kinetic assays were performed by monitoring the fluorescence of 5CVA using a Cary Eclipse spectrofluorometer (Agilent) with excitation and emission wavelengths of 310 and 420 nm, respectively, and slit widths of 2.5 and 10 nm, respectively. The standard assay was performed in 0.5 ml of potassium phosphate ($I = 0.1$ M, pH 7.5) at 25 °C containing 30 µM OH-DDVA (1% DMSO final concentration) and 10 nM LigY. Assays were initiated by adding LigZ to ~0.5 µM to generate the MCP *in situ*. Rates of 5CVA production were calculated from fluorescence using a standard curve of 0 – 20 µM 5CVA established each day the kinetics experiments were performed. Rates were corrected by subtracting fluorescence changes observed in the absence of LigY. Steady-state kinetic parameters were evaluated by fitting the Michaelis-Menten equation to the data using least-squares fitting and the program LEONORA (185). Kinetic parameters and specific activities were calculated as a function of the zinc content of the enzyme preparation when this content was less than 100%.

The effect of pH on the rate of the LigY-catalyzed reaction was evaluated using 100 mM solutions of MES (pH 6.0), piperazine-N,N'-bis(2-ethanesulfonic acid) (PIPES) (pH 6.5), 3-(N-morpholino)propanesulfonic acid (MOPS) (pH 7.0), HEPES (pH 7.5), HEPES (pH 8.0), TAPS (pH 8.5), and N-cyclohexyl-2-aminoethanesulfonic acid (CHES) (pH 9.0). The effect of ionic strength on the reaction rate was evaluated at pH 7.5 using buffers with varying amounts of potassium phos-

phate to modulate the buffer's ionic strength. The effect of Cl⁻ on the reaction rate was evaluated at pH 7.5 using solutions of 38 mM potassium phosphate, 0.9 M potassium chloride, pH 7.5, and 370 mM potassium phosphate, pH 7.5, in different proportions.

4.2.8 Metal chelation and reconstitution

Apo-LigY was prepared by dialyzing LigY against 20 mM MES, pH 6.0, containing 10 mM *o*-phenanthroline, 5 mM EDTA, and 1 mM DTT for 2 days at 4 °C. The apoprotein was dialyzed against chelex-treated 20 mM HEPES, pH 8.0, to remove the chelators and concentrated using ultra-filtration. LigY was reconstituted with different metals by incubating ~200 μM apoprotein overnight at 4 °C with 500 μM ZnCl₂, CoCl₂, CuCl₂, CaCl₂, CdCl₂, MnCl₂, or FeCl₃. Reconstitution with 500 μM Fe(NH₄)₂(SO₄) was carried out anaerobically. Excess metal was removed using G25-Fine resin (Superdex).

4.2.9 CHPD characterization

The dienoate hydrolysis product was prepared by reacting 200 μM OH-DDVA with a mixture of ~1 μM LigZ and ~1 μM LigY in air-saturated buffer. The reaction was quenched after 5 min with formic acid (final concentration ~1% (v/v)), and the enzymes were removed by centrifugation. CHPD was resolved using a Waters 2695 Separation HPLC module (Milford, MA) equipped with a Waters 2996 PDA detector and an Aqua 5-μm C18 250 x 4.6-mm column (Phenomenex). CHPD was eluted using an isocratic flow of 0.1% formic acid, and the eluate was monitored at 220 nm. CHPD was derivatized using dinitrophenylhydrazine (DNPH) under acidic conditions as described previously (30). The CHPD-DNPH was purified by HPLC using a Kinetex 5 μm EVO C18 100 Å 150 3.0-mm column (Phenomenex). CHPD-DNPH was eluted using a linear gradient of 0 – 100% methanol in 0.1% formic acid, and the eluate was monitored at 470 nm. Mass spectra were measured using a Applied Biosystems Qstar mass spectrometer in negative ion mode using methanol or acetonitrile as solvents.

4.2.10 Protein structure determination

LigY was crystallized aerobically at room temperature using the sitting drop vapor diffusion method. Drops consisted of 2 μl of ~350 μM LigY and 2 μl of precipitant solution (0.1 M Tris-Cl, pH 7.5, 0.2 M lithium sulfate, ~24% PEG 4000) equilibrating over 1.0 ml of precipitant solution.

Before data collection, the crystals were soaked briefly in the mother liquor supplemented with ~30% glycerol and flash-frozen in liquid nitrogen. Diffraction data of WT LigY were collected at the CLS on beamline 08B1-1. Single-wavelength anomalous diffraction data of selenomethionyl LigY were collected at the SSRL on Beamline 7-1. Data were processed using iMOSFLM and Aimless from the CCP4 program suite (189,191,192). Phase determination and initial model building of selenomethionyl-LigY were done using AutoSol and Autobuild programs in Phenix (188). The structure of WT LigY was solved by molecular replacement using the preliminary coordinates for selenomethionyl-LigY as the search model using Phaser-MR (187). Manual building was performed using Coot (189), and refinement was performed using phenix.refine (190). Data collection and refinement statistics are shown in Table 4.1. The subsequent calculations and analyses of the crystallographic model, including the calculation of the secondary structure with DSSP (205,206), were performed using the WHAT IF server (207). Protein surface and oligomeric assembly were calculated with PISA (208). Protein surface charge analysis was done using PDB2PQR (209,210) and APBS (211). Amino acid conservation was performed using Consurf (212,213) using the T-COFFEE (Expresso) (214) alignment algorithm and sequences from the RefSeq NR protein database (215) sharing 35–95% sequence identity. Graphical representation of the crystallographic model was generated using the PyMOL Molecular Graphic System version 1.3 (Schrödinger LLC, New York).

4.3 Results

4.3.1 LigY is an amidohydrolase

LigY was previously reported to have low amino acid sequence identity with previously characterized MCP hydrolases (51). A BLASTp search against the non-redundant protein sequences of the NCBI database identified LigY as a member of the amidohydrolase superfamily. Sequence alignments using LigY as a search query against COG (159) and Pfam (216) databases placed LigY in COG2159 and Pfam04909, respectively. Among characterized COG2159 enzymes, LigY has the greatest amino acid sequence identity with LigJ (38%, T-Coffee) (217) and ~20% identity with a number of decarboxylases: ACMSD (169), 2,6-dihydroxybenzoate decarboxylase (172), uracil-5-carboxylate decarboxylase (iso-orotate decarboxylase (IDCase)) (171), and LigW (177). Alignment of LigY with these homologs indicated that LigY has the motif that binds Zn²⁺ in these enzymes (170).

4.3.2 Purified LigY contains zinc

Heterologously produced LigY was purified to >99% apparent homogeneity as judged by SDS-PAGE analysis at yields of 5–10 mg of protein/liter of cell culture. Mass spectrometric analysis of the purified protein (37,278.2 Da) agreed with the predicted molecular mass of LigY (37,278 Da), indicating the presence of the N-terminal methionine. ICP-MS analysis revealed that the purified LigY contained 0.93 ± 0.07 eq. of zinc per protomer and insignificant amounts of cadmium, cobalt, copper, iron, manganese, and nickel. Consistent with this result, a colorimetric assay based on 4-(2-pyridylazo)-resorcinol yielded a value of 1.02 ± 0.09 eq. of zinc per protomer. SEC-MALS analysis indicated that LigY exists in solution as a mono-dispersed species with a mass of 208 ± 2 kDa, consistent with a hexamer (Figure 4.2A). Analysis of the protein absorbance at 280 nm ($\epsilon = 36,900 \text{ mM}^{-1} \text{ cm}^{-1}$) was in good agreement with protein concentrations determined using a BCA assay. Preparations of LigY had no significant absorbance bands in the visible region. The far-UV CD spectra minima at 222 and 212 nm indicate a high content of α -helical secondary structure (Figure 4.2B). When the growth medium was not supplemented with Zn²⁺, purified LigY contained ~0.5 eq. of zinc. Enzyme preparations containing different amounts of zinc showed no differences in their oligomeric states or overall secondary structures.

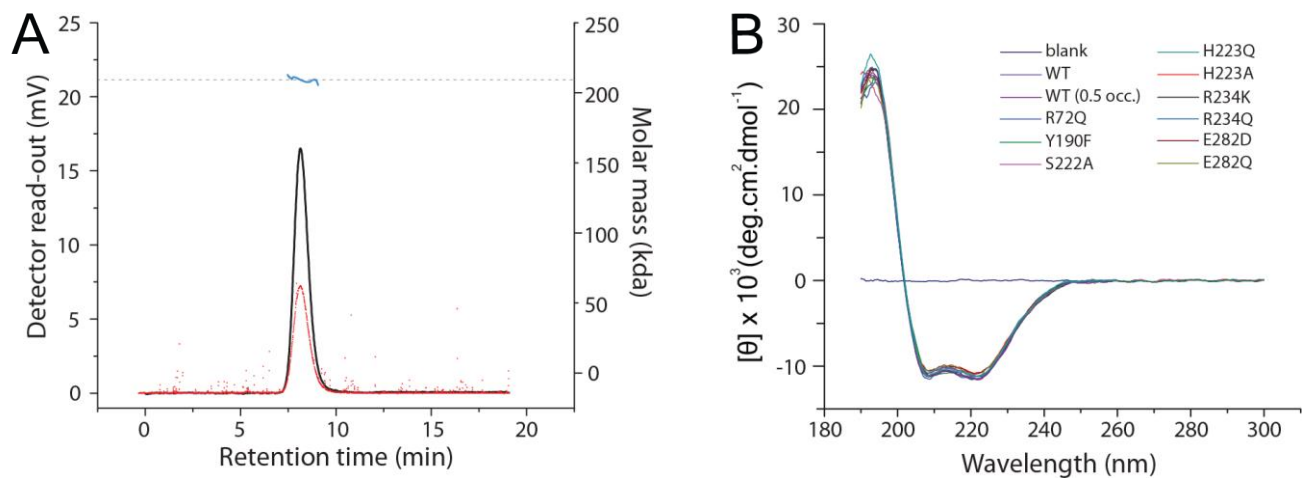


Figure 4.2. Biophysical properties of LigY.

(A) SEC-MALS analysis of LigY. The black and red traces represent absorbance at 280 nm and light-scattering, respectively. The calculated molar mass is shown in blue. (B) CD spectra of WT and LigY variants. A preparation containing ~50% Zn (0.5 Zn) was also run.

4.3.3 LigY hydrolyzes DCHM-HOPDA to 5CVA and CHPD

To identify the LigY reaction products, OH-DDVA was incubated with a mixture of LigZ and LigY (potassium phosphate ($I = 0.1$ M), pH 7.5). This approach minimized the non-enzymatic transformation of DCHM-HOPDA, the LigZ-produced MCP (1). HPLC analysis of the reaction products revealed the presence of 5CVA, consistent with an earlier report (51), together with another major peak (retention time (t_R) = 8 min), the amount of which was proportional to 5CVA (Figure 4.3A). Mass spectrometric analysis of this compound revealed a parent ion with an m/z value of 157.01, consistent with the predicted mass of singly deprotonated CHPD (157.01) (Figure 4.3B). Furthermore, this compound could be derivatized with DNPH, consistent with the presence of an α -keto acid (218). On reverse phase HPLC, the derivatized compound eluted with an absorbance ($\lambda_{max} = 470$ nm) and polarity consistent with DNPH-CHPD (*i.e.* its $t_R = 31$ min was between those of derivatives of α -ketoglutaric acid ($t_R = 28$ min) and 2-hydroxypenta-2,4-dienoic acid ($t_R = 41$ min)) (Figure 4.4A). The identities of the DNPH-derivatized α -keto acids were confirmed with mass spectrometry (Figure 4.4B). Overall, DNPH derivatization confirmed that CHPD is the second product of the LigY-catalyzed reaction. Together with the previous identification of 5CVA (51), these data establish that LigY catalyzes the hydrolysis of DCHM-HOPDA.

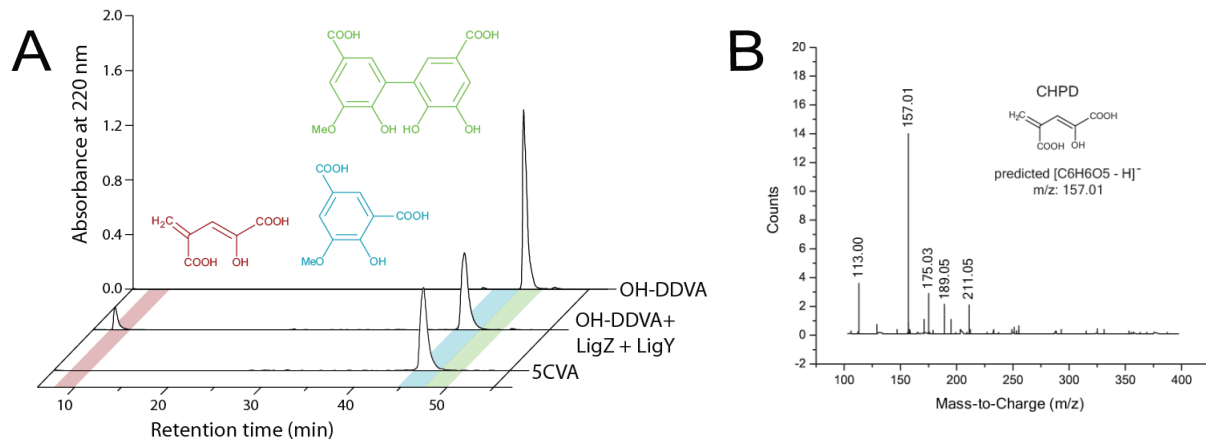


Figure 4.3. HPLC resolution of LigY-catalyzed DCHM-HOPDA hydrolysis products and MS analysis of CHPD.

(A) Traces are of OH-DDVA, OH-DDVA incubated with LigZ and LigY, and 5CVA. Peaks corresponding to OH-DDVA, 5CVA, and CHPD are highlighted with green, blue, and red, respectively. (B) Mass spectrum of CHPD.

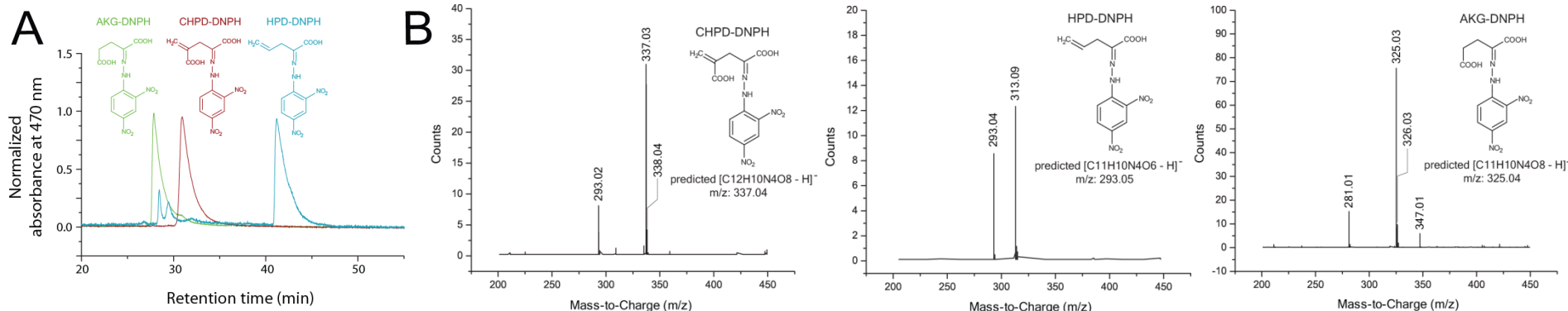


Figure 4.4. HPLC and MS analyses of DNPH-derivatized α -ketoacids.

(A) The three derivatized α -ketoacids are α KG (green), CHPD (red) and HPD (blue). (B) Mass spectra of the derivatized α -ketoacids.

4.3.4 Steady-state kinetic analyses of LigY

To evaluate the steady-state kinetic parameters of LigY, we developed an assay based on the fluorescence of 5CVA. The dependence of the fluorescence signal on 5CVA was investigated using LigW, which decarboxylates 5CVA (177) to the significantly less fluorogenic vanillate. In the presence of excess LigW, no fluorescence was detected from the activity assay. Importantly, at pH 7.5, neither OH-DDVA, DCHM-HOPDA, nor CHPD fluoresced significantly. However, DCHM-HOPDA fluoresced significantly at pH values above 7.5, particularly in the presence of Good's buffers.

By contrast, the fluorescent quantum yield of 5CVA did not change significantly from pH 6 to 9. Correcting for the background fluorescence of DCHM-HOPDA, LigY had maximal activity between pH 7.5 and 8.0 (Figure 4.5A). Considering the pH dependence of LigZ activity and to minimize the background fluorescent observed at elevated pH, subsequent kinetic assays were performed at pH 7.5 using potassium phosphate ($I = 0.1$ M). The steady-state hydrolysis of DCHM-HOPDA by LigY displayed Michaelis–Menten behavior (Figure 4.5B). At pH 7.5, LigY had a turnover number of 9.3 ± 0.6 s⁻¹ and a k_{cat}/K_m value of 2.5 ± 0.2 10⁷ M⁻¹ s⁻¹ calculated based on the metal ion content of the preparation. As reported previously (51), LigY did not detectably hydrolyze 2-hydroxy-6-oxo-6-phenylhexa-2,4-dienoate, the MCP from biphenyl degradation.

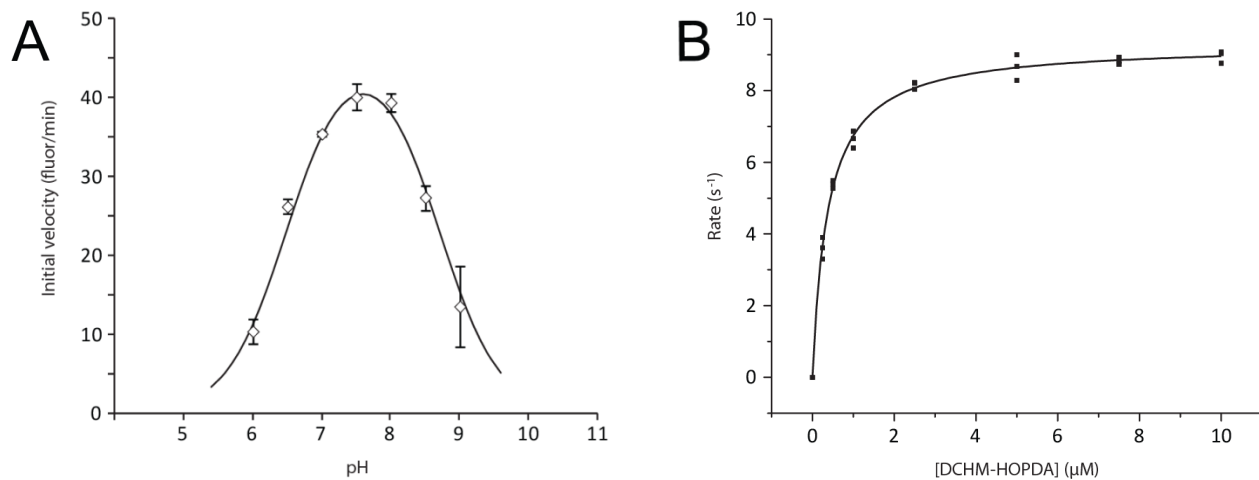


Figure 4.5. Steady-state kinetic hydrolysis of DCHM-HOPDA by LigY.

(A) pH-dependence of LigY activity. Error bar represents S.D. (B) Shown is the dependence of the initial velocity of 5CVA production on DCHM-HOPDA concentration (potassium phosphate ($I = 0.1$ M), pH 7.5). The solid line represents a best fit of the Michaelis–Menten equation to the data using the least squares dynamic weighting options of LEONORA ($K_m = 0.38 \pm 0.02$ μM and $k_{\text{cat}} = 9.3 \pm 0.6$ s⁻¹).

4.3.5 Metal dependence of LigY activity

To evaluate the importance of the metal cofactor, it was removed from LigY by chelation. Apo-LigY was generated by dialyzing the enzyme for 48 h against *o*-phenanthroline and EDTA at pH 6.0. At pH 7–8, the metal ion was not detectably removed, and below pH 5.5, LigY was irreversibly denatured. Apo-LigY had 5% of the specific activity of WT LigY. Incubation of apo-LigY with ZnCl₂ partially restored the enzymatic activity. However, we were unable to restore apo-LigY to the same specific activity as the purified enzyme. Nevertheless, the specific activity of purified LigY with ~0.5 zinc occupancy was ~50% that of purified LigY with full zinc occupancy.

Table 4.1. LigY data collection and refinement statistics.

	Selenomethionyl LigY <i>Peak</i>	LigY
Data Collection		
Wavelength (Å)	0.97591	0.97950
Resolution Range (Å)	37.81 – 2.22 (2.34 – 2.22) ^a	59.42 – 1.90 (1.94 – 1.90)
Space group	<i>C</i> 2 <i>2</i> ₂ ₁ <i>a</i> = 60.24	<i>C</i> 2 <i>2</i> ₂ ₁ <i>a</i> = 60.02
Unit cell dimension (Å)	<i>b</i> = 195.91 <i>c</i> = 178.42	<i>b</i> = 195.36 <i>c</i> = 178.25
Unique reflections	52630	82888
Completeness (%)	99.4 (96.3)	100.0 (100.0)
Redundancy	10.9 (10.6)	6.2 (6.1)
Mean I/ σ I	17.8 (2.4)	13.2 (3.2)
CC1/2	0.999 (0.779)	0.998 (0.825)
Wilson B-factor (Å ²)	38.3	22.9
Refinement		
R _{work} (R _{free} ^b)	--	16.2 (18.9)
No. of water molecules	--	535
r.m.s.d. bond length (Å)	--	0.008
Average B-values (Å ²)		
Overall	--	34.4
Protein	--	34.5
Ligands - Zn	--	23.2
Ligands - Cl	--	30.0
Water	--	34.3
Ramachandran plot (%)		
in most-favorable	--	97.2
in disallowed	--	0.9
PDB Accession Code	--	5VN5

^aValues in parentheses are for highest-resolution shell.

^bR_{free} is the R_{work} value for 5% of the reflections excluded from the refinement.

4.3.6 Structure of LigY

The crystal structure of LigY was solved to a resolution of 1.9 Å (Table 4.1). The asymmetric unit has three complete protomers (A, B, and C). The model for each contains all 332 residues of the encoded gene product with additional residues at the C-terminal end from TEV protease recognition sequences. The protomers share highly similar structures, with an average RMSD over all C α of ~0.33 Å as determined using the least squared superposition tool from COOT. Protomers A and B are related by non-crystallographic 2-fold symmetry and have an interface of 2200 Å². Protomer A is also bound to Protomer C with a smaller interface of 900 Å² (Figure 4.6A). Protomers sharing the larger interface (*i.e.* BA, CC', and A'B') are considered to be functional dimers because Arg-234, which is part of this interface, contributes to the active site of its respective dimeric partner as described below. Accordingly, the interface between protomers of a functional dimer is defined as the intradimer interface. The hexamer observed in solution can be reconstructed through crystallographic 2-fold rotational symmetry of the asymmetric unit and characterized as a trimer of dimers based on the non-crystallographic 3-fold symmetry of the hexamer. The functional dimers are related through 2-fold rotational symmetry (*e.g.* the RMSD value of AB and CC' is 0.37 Å over all C α atoms, close to that of the individual protomers). Phylogenetic analysis of closely related sequences mapped to the structure of LigY revealed highly conserved regions at the intradimer interface (Figure 4.7A). In contrast, the residues at other interfaces are poorly conserved. Surface electrostatic analysis further indicated that the intradimer interactions consist of several patches of polar interactions (Figure 4.7B), whereas other interfaces are dominated by hydrophobic interactions. A channel leading to the active site is formed at the interface between three protomers. Residues derived from the functional dimer construct the majority of the channel, and a third protomer contributes to the mouth of the channel (Figure 4.6A, white dotted circle). Due to 3-fold symmetry of LigY, three active-site channels are orientated toward each of the two faces of the hexameric ring. The LigY protomer has a skewed (β/α)₈ barrel fold with the α-helices encapsulating the parallel β-sheets of the inner core (Figure 4.6B). This fold, reminiscent of the TIM-barrel, is typical of the amidohydrolase superfamily (158). Of the characterized amidohydrolases, LigY is most structurally similar to LigJ from *Rhodopseudomonas palustris* (PDB ID: 2GWG), consistent with the amino acid sequence identity. Using Dali-Lite to perform a pairwise analysis, an RMSD of 1.6 Å was calculated over 309 C α atoms (χ -score 40.9). LigY retains the core (β/α)₈ secondary structure elements of LigJ but has five additional α-

helical elements (Figure 4.8). The key secondary structure elements, eight pairs of alternating β -strand and α -helix, were numbered as in ACMSD (PDB ID: 2HBV) to simplify comparison. The first, helix $\alpha 1'$ is a 13-residue insertion between strand $\beta 1$ and helix $\alpha 1$. The next three insertions are of ~ 3 residues each and occur as small helices $\alpha 2'$, $\alpha 5'$, and $\alpha 6'$. Finally, the last insertion, the C-terminal $\alpha 9A$ and $\alpha 9B$, also occurs in ACMSD (21).

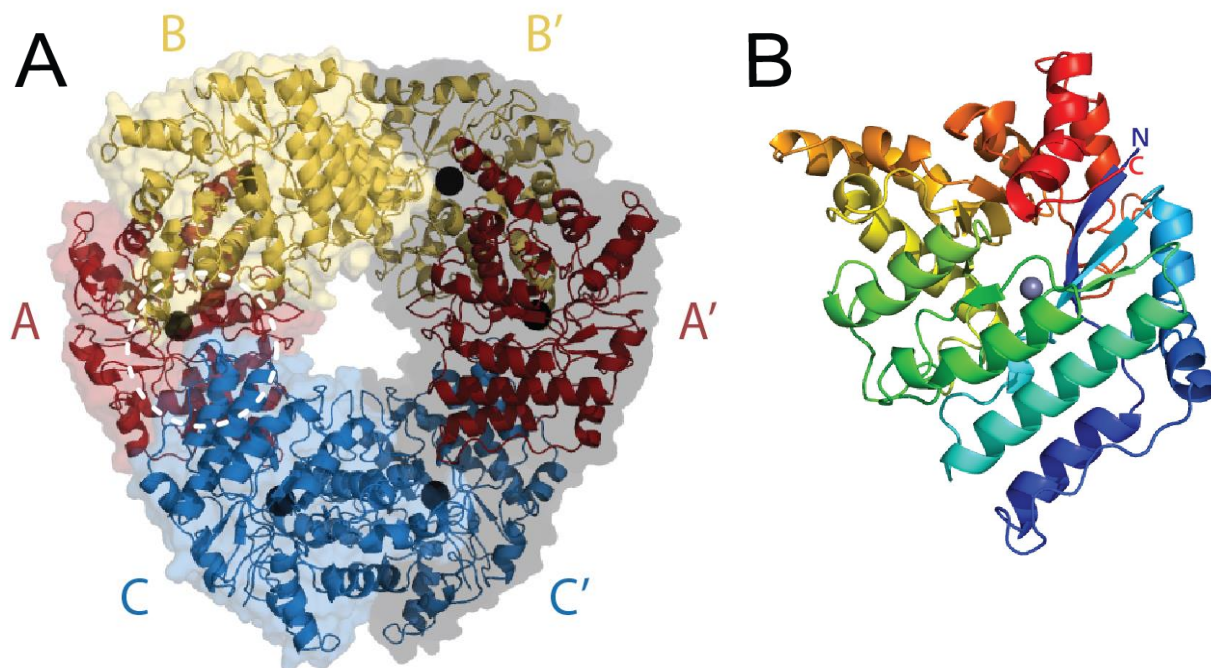


Figure 4.6. Structures of the LigY hexamer and protomer.

(A) The hexameric assembly of LigY. The different LigY protomers of the asymmetric unit are red, yellow, and blue, respectively. The protomers are depicted with their surfaces and underlying secondary structure. The LigY hexamer comprises two trimers of adjacent asymmetric units related by a rotational 2-fold symmetry. The symmetry-related trimer is depicted with a gray surface representation. The white dotted circle marks the entrance to the active-site channel. (B) Ribbon diagram of LigY rainbow-colored from blue (N terminus) to red (C terminus). Bound Zn^{2+} ions are shown as gray spheres.

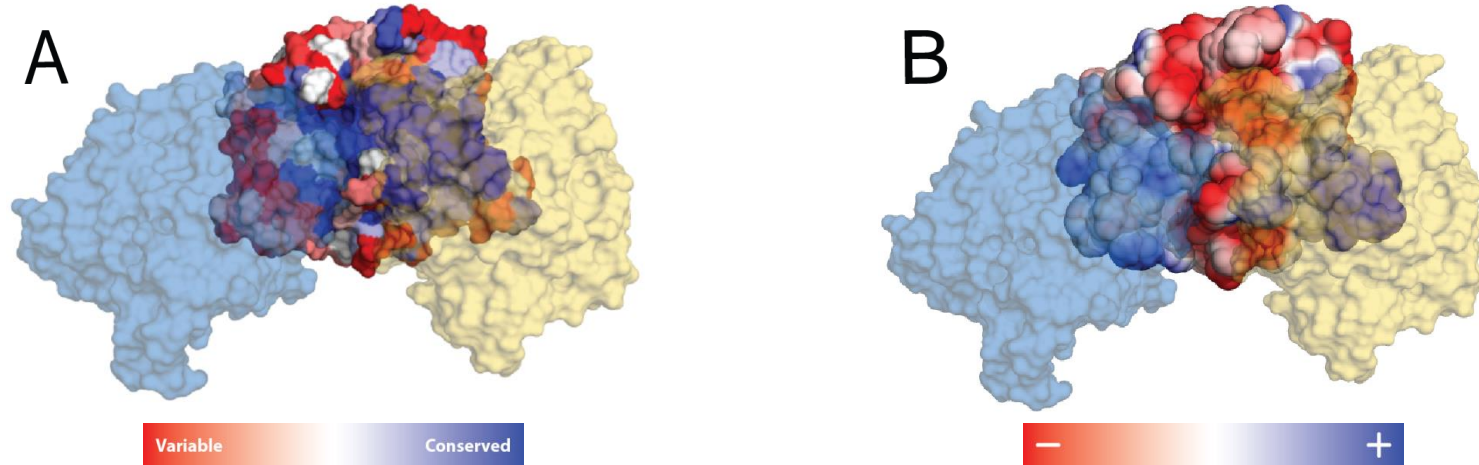


Figure 4.7. The amino acid conservation and surface electrostatic analyses of the inter-protomer interactions.

The analyses are shown as color-coded surface representations according to the degree of (A) conservation or (B) surface electrostatic charge. The degree of conservation ranges from least conserved (red) to highly conserved (blue). Surface charge ranges from negative (red) to positive (blue). Protomers of the same and neighboring dimer are colored in yellow and blue, respectively. The dotted circle marks the active site channel, as in Figure 4.6A.

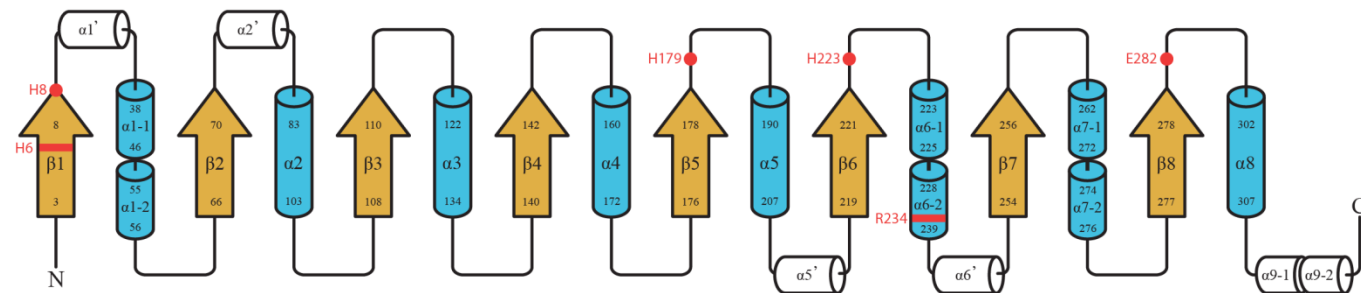


Figure 4.8. Topology diagram of LigY.

The β -strands (yellow) and α -helices (blue) of the $(\beta/\alpha)_8$ core are numbered according to ACMSD (PDB ID: 2HBV). The first and last residues of each core secondary element are indicated on the element. The α -helical insertions are represented as white cylinders. Residues of potential catalytic importance are indicated in red.

4.3.7 LigY metal-binding site

LigY's active site is at the center of the β -sheet core as observed in other subtype III amidohydrolases (158), such as ACMSD (169). The anomalous map corroborates that LigY is mononuclear with a single anomalous peak observed in the active site of each protomer (Figure 4.9). The metal fluorescence scan and an anomalous map density peak calculation were also consistent with Zn^{2+} being the active-site ion (data not shown). This metal ion is coordinated by His-6, His-8, and His-179 and is partially coordinated by Glu-282. These four residues correspond to the metal-binding ligands in other members of the amidohydrolase superfamily, although the acidic ligand is often aspartate. The electron density indicates conformational heterogeneity in the active sites of the three LigY protomers. These are highlighted by Glu-282, which is observed in two conformations. In one conformation, the side chain is oriented toward the Zn^{2+} and coordinates the metal (Figure 4.10A). In the second conformation, the carboxylate is oriented away from the metal ion (Figure 4.10A). In Protomer C, Glu-282 is in a single conformation, oriented away from the metal ion (Figure 4.10A). In Protomers A and B, Glu-282 appears to adopt both conformations, with ~60 and 30% occupancies, respectively, for the metal-coordinating conformation as estimated from the refinement by Phenix.refine (Fig. 6A). A second difference, which correlated with the conformation of Glu-282, concerned a large spherical electron density located adjacent to the Zn^{2+} in Protomer C (Figure 4.10A and Figure 4.9). This density was too large for a water molecule and was modeled as a Cl^- ion, which is present in the mother liquor. No peak was observed in an anomalous map, indicating that it is not a transition metal ion. The interatomic $Zn^{2+} - Cl^-$ distance is 1.9 Å, as compared with a value of 2.2 Å reported for an inorganic zinc complex (219). Electron density corresponding to Cl^- at a lower occupancy is present in Protomers A and B. However, the anion was not included in the models of these chains due to steric clash. Overall, two active-site metal coordination geometries were modeled in LigY. In the pentacoordinate geometry (Figure 4.10B), which predominates in Protomer A, the Zn^{2+} is coordinated by the three histidines, Glu-282, and a solvent species. In the tetracoordinate geometry, modeled in Protomer C (Figure 4.10C), the Zn^{2+} is coordinated by the three histidines and a Cl^- ion. The state observed in Protomer B appears to be a mixture of the two geometries (Figure 4.10A). The LigY active site contains several other notable residues in addition to the metal ligands (Figure 4.10). First, His-223 is conserved in subtype III amidohydrolases and, as in these enzymes, acts as a second shell metal ligand via a water molecule. His-223 is not within hydrogen-bonding distance of the metal-bound solvent species in any of the LigY protomers but may

form a hydrogen bond with Glu-282 when the latter is coordinated to the Zn^{2+} . As noted above, the active site also contains Arg-234 from its dimeric partner, an arrangement that is conserved in COG2159 enzymes of known structure. In ACSMD, this arginine has been proposed to bind the C1 carboxylate of α -amino- β -carboxymuconate- ϵ -semialdehyde (220). In LigW, this arginine interacts with the nitro group of the substrate analog 5-nitrovanillate (177). The LigY active site also contains Ser-222. This residue is not conserved in amidohydrolases but lies in close proximity with His-223 and Glu-198 (Figure 4.10B,C). Finally, LigY does not contain the glutamate that is conserved in COG0402 subtype III amidohydrolases. This residue is exemplified by Glu-217 in CDA (162) and is proposed to act as an acid-base catalyst deprotonating the metal-bound hydrolytic water in COG0402 enzymes.

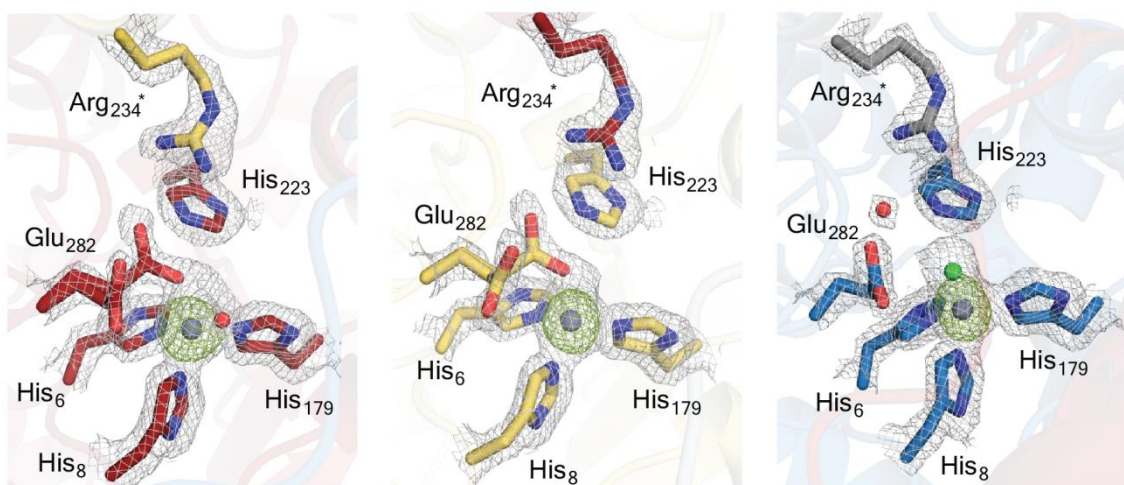


Figure 4.9. The anomalous density map of LigY active site.

The Zn^{2+} coordination sphere of Protomer A (red), Protomer B (yellow), and Protomer C (blue). The grey mesh represents a $2F_o - F_c$ map of features within a 2 Å of select residues contoured at 1.4 σ . The anomalous density map (green-mesh) is contoured at 6 σ . The Zn^{2+} , Cl^- and solvent species are represented as gray, green and red spheres, respectively.

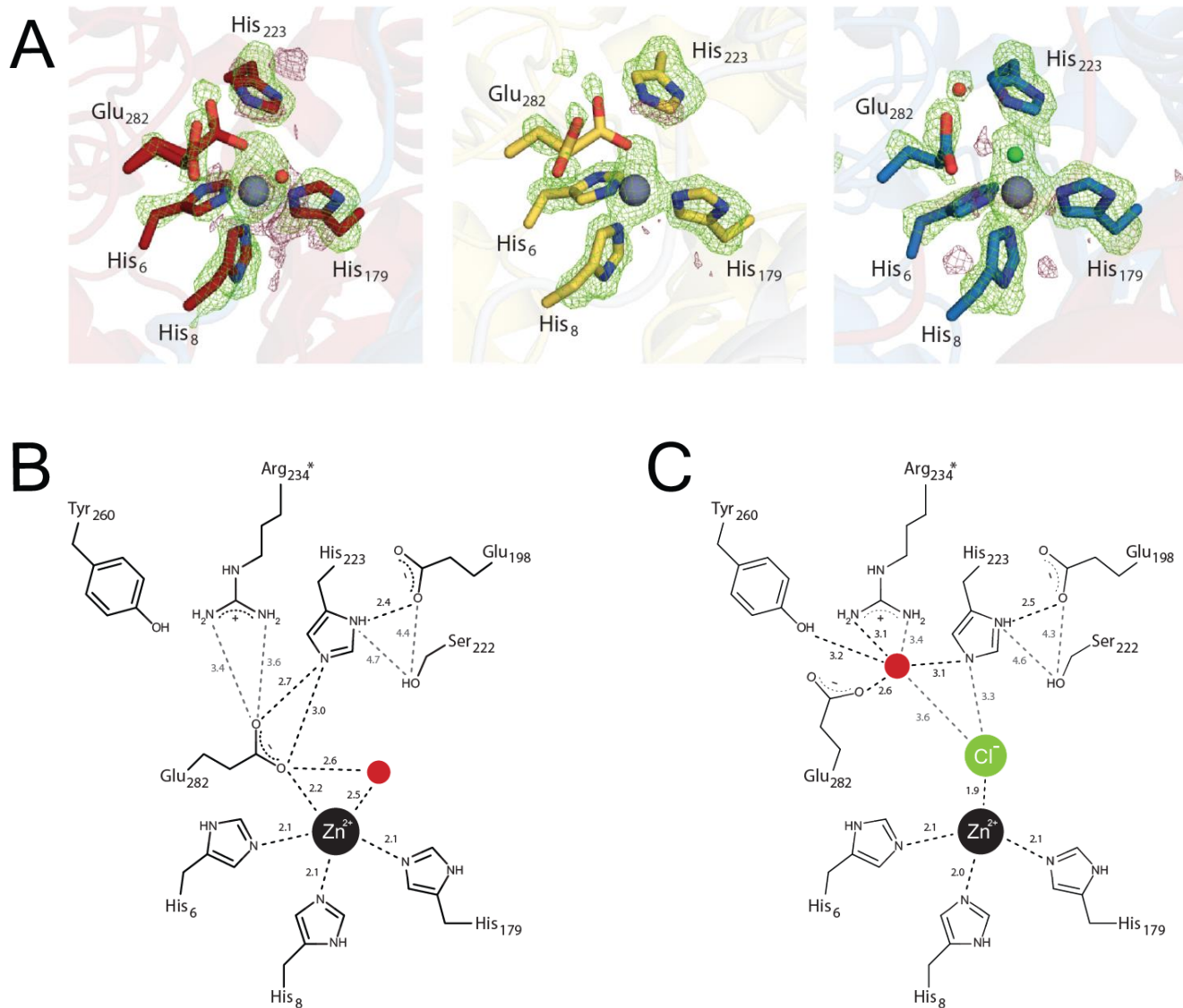


Figure 4.10. The Zn^{2+} -binding site of LigY.

(A) The Zn^{2+} coordination sphere of Protomer A (red), Protomer B (yellow), and Protomer C (blue). The green and red mesh represents a positive and negative $F_o - F_c$ map of features within 3 Å of select residues contoured at 3.5σ . The Zn^{2+} , Cl^- , and solvent species are represented as gray, green, and red spheres, respectively. Stick representations of the Zn^{2+} coordination spheres in “Glu-on” (B) and “Glu-off” (C) configurations. Zn^{2+} -ligand and hydrogen bonds are depicted as black dotted lines with distances indicated in Å. Distances exceeding hydrogen bond lengths (3.2 Å) are denoted as gray dotted lines.

4.3.8 Inhibition of LigY activity by chloride

The observation of a Zn^{2+} -bound Cl^- in one of the protomers suggests two hypotheses: (a) Glu-282 is readily displaceable, and (b) Cl^- inhibits LigY's activity. To test the latter hypothesis, we measured the activity of LigY at increasing ionic strength, where ionic strength was increased using either KCl or potassium phosphate. In these experiments, the specific activity of LigY decayed exponentially with increasing concentration of Cl^- but not phosphate (Figure 4.11), indicating that this effect is specific. Importantly, high concentrations of KCl had negligible effect on the activity of LigZ used in the assay. Finally, similar inhibition was observed whether NaCl or KCl was used (data not shown), indicating that the chloride anion is the inhibitory species.

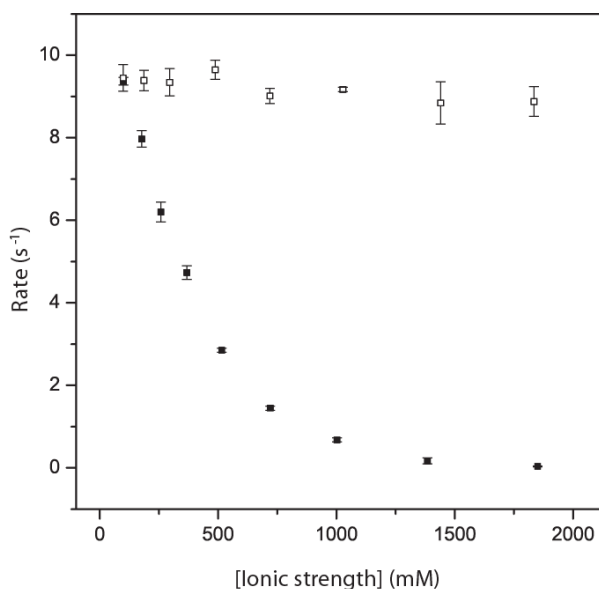


Figure 4.11. The effect of chloride on LigY activity.

Activity was measured under standard assay conditions following 5CVA fluorescence (pH 7.5, 25 °C). Ionic strength was increased using either KCl (filled squares) or potassium phosphate (open squares). Error bars, S.D.

4.3.9 Methanolysis

Serine-dependent MCP hydrolases, such as BphD, are capable of performing alcoholysis of HOPDA and *p*-nitrophenyl benzoate (221). For example, BphD-catalyzed methanolysis of HOPDA results in a product partitioning between benzoic acid and methyl benzoate. Subsequently, LigY is evaluated for its capacity to utilize alcohol as an alternative nucleophile. The carboxylic acid product ,5CVA , was the only product observed in LigY-catalyzed hydrolysis of DCHM-HOPDA supplemented with up to 6% (v/v, ~1.5 M) methanol (Figure 4.12).

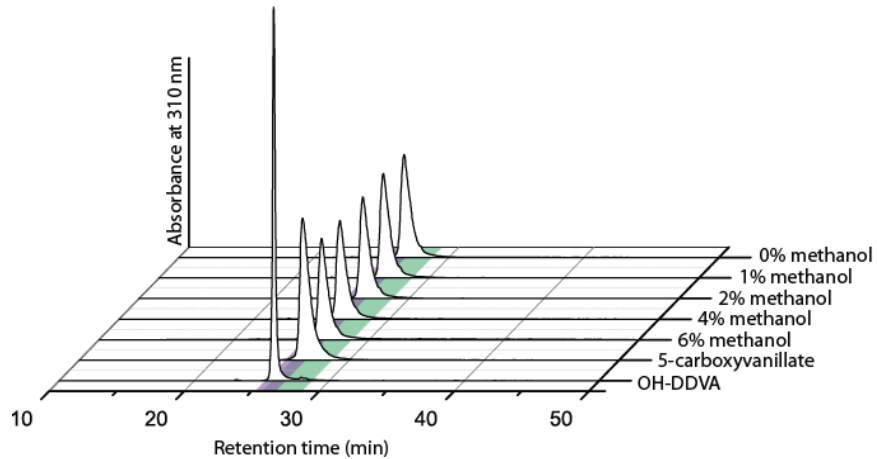


Figure 4.12. LigY-catalyzed hydrolysis of DCHM-HOPDA in presence of methanol.

Traces are of OH-DDVA incubated with LigZ and LigY with increasing amount (0-6% v/v) of methanol. Peaks corresponding to OH-DDVA and 5CVA are highlighted with purple and green, respectively.

4.3.10 Active-site variants

We evaluated the catalytic roles of six LigY residues by substituting each of them. Briefly, the H223Q, H223A, R234K, R234Q, E282Q, and E282D variants were designed to evaluate the roles of three conserved residues with respect to other members of the amidohydrolase superfamily. The S222A variant was generated to evaluate the possible role of Ser-222 in a nucleophilic mechanism. Finally, R72Q and Y190F were constructed to evaluate the substrate docking studies. None of the substitutions significantly perturbed the secondary structure or oligomeric state of LigY as determined using CD spectroscopy (Figure 4.2B) and SEC-MALS (data not shown), respectively. As summarized in Table 4.2, all of the variants contained at least 0.7 eq of Zn²⁺ as determined by the PAR-based assay; significant levels of other metal ions were not detected using ICP-MS. For those preparations containing less than a full equivalent of Zn²⁺, the activities and kinetic parameters were adjusted according to the metal ion content. Among the conserved residues tested, Glu-282 was most sensitive to substitution; neither E282Q nor E282D had detectable activity (Table 4.2). By contrast, the H223Q and R234K variants had significant activity, whereas the H223A and R234Q variants had 2% that of WT LigY. Interestingly, both the R72Q and Y190F variants also had very little activity. Finally, the activity of S222A was similar to that of WT. Variants with significant activity (<2% that of WT LigY) were further subjected to steady-state kinetic analyses (Table 4.3). The steady-state kinetic parameters of S222A were perturbed 3-fold *versus* WT LigY, indicating that Ser-

222 does not play a significant catalytic role. The substrate specificity (k_{cat}/K_M value) of H223Q was ~6-fold lower than that of WT LigY, although both the k_{cat} and K_M values were affected to a lesser extent. By contrast, the substrate specificity of R234K was 1% that of WT LigY with significant perturbation of both the k_{cat} and K_M values.

Table 4.2. Relative activity of LigY variants.^a

Enzyme	Zinc content ^b	Relative activity (%)
WT	1.0 ± 0.1	100 ± 10
R72Q	1.0 ± 0.1	ND ^c
Y190F	0.7 ± 0.1	0.8 ± 0.1
S222A	0.9 ± 0.1	80 ± 10
H223Q	0.8 ± 0.1	46 ± 2
H223A	1.3 ± 0.2	1.7 ± 0.2
E282Q	1.0 ± 0.1	ND
E282D	0.8 ± 0.1	ND
R234K	1.2 ± 0.3	16 ± 4
R234Q	1.1 ± 0.1	0.18 ± 0.02

^a Experiments were performed using 50 μM DCHM-HOPDA in potassium phosphate ($I = 0.1$ M), pH 7.5, at 25 °C. Reported values are mean ± S.D. based on a minimum of three replicates.

^b Zinc content represents the ratio of Zn²⁺ *versus* protein concentrations. Relative activity was normalized to zinc content when this content was 1 eq (e.g. the relative activity of the H223Q variant was corrected for the lower Zn²⁺ content of this variant *versus* WT).

^c ND, not detected.

Table 4.3. Steady-state kinetic parameters of LigY and select variants.^a

Enzyme	k_{cat} (s ⁻¹)	K_M (μM)	k_{cat}/K_M (× 10 ⁶ s ⁻¹ · M ⁻¹)
WT	9.3 ± 0.6	0.38 ± 0.02	25 ± 2
S222A	7.9 ± 0.9	1.01 ± 0.06	7.8 ± 0.9
H223Q	5.3 ± 0.7	1.30 ± 0.07	4.1 ± 0.6
R234K	1.4 ± 0.4	11 ± 1	0.12 ± 0.03

^a Experiments were performed using potassium phosphate ($I = 0.1$ M), pH 7.5, at 25 °C. Parameters were calculated using a minimum of three replicates at each of seven substrate concentrations. Values are mean ± S.E.

4.3.11 Modeling substrate-binding

To date, attempts to obtain a structure of a LigY·DCHM-HOPDA complex have not succeeded. In the absence of such data, we modeled DCHM-HOPDA into the Zn²⁺-containing pocket to evaluate how LigY might bind its substrate. For this experiment, we based the structure of DCHM-HOPDA on that of 2-hydroxy-6-oxo-6-phenyl-hexa-2,4-dienoate as found in complex with the S112A variant of BphD (149). DCHM-HOPDA was modeled in its enol form, (2Z,4Z)-2-hydroxy-6-oxo-4-carboxylato-6-(5-carboxylato-2-hydroxy-3-methoxyphenyl)-hexa-2,4-dienoate, to account for the substrate's tautomeric state at neutral pH. We further reasoned that the substrate likely coordinates the metal ion through one of its carboxylates based on: (a) the precedence for this binding mode in the COG2159 enzymes LigW and IDCcase (171,177); and (b) the ability of Cl⁻ to coordinate the Zn²⁺ in LigY. Accordingly, we modeled DCHM-HOPDA into the active site of Pro-tomer C, positioning a carboxylate oxygen in place of the Cl⁻. We considered three orientations of the substrate: tail-in, side-on and head-in in which DCHM-HOPDA was coordinated to Zn²⁺ by the C1-, C4- and C11-carboxylates, respectively. Of these three, the tail-in orientation was the only one that presented no steric clashes (Figure 4.13A). In this configuration, DCHM-HOPDA is stabilized by a number of interactions with polar residues that would help neutralize the charged groups of the substrate. More specifically, the C1-carboxylate is stabilized by Arg-234 and His-223; the C4-carboxylate is positioned to interact with Arg-72; and finally, the solvent-exposed C11-carboxylate can interact with His-29. By contrast, coordination of the C11-carboxylate to the Zn²⁺ (head-in) results in clashes between the C9-methoxyl group of the substrate and Arg-72/Phe-74 (Figure 4.13B). Additionally, the C4-carboxylate is not positioned to interact with Arg-72 or any other charged residue, while the surface exposed C1-carboxylate cannot interact with His-29 or other residue without clashing with the C4-carboxylate. Lastly, the side-on orientation cannot be modeled due to numerous steric clashes with the residues lining the elongated substrate-binding pocket.

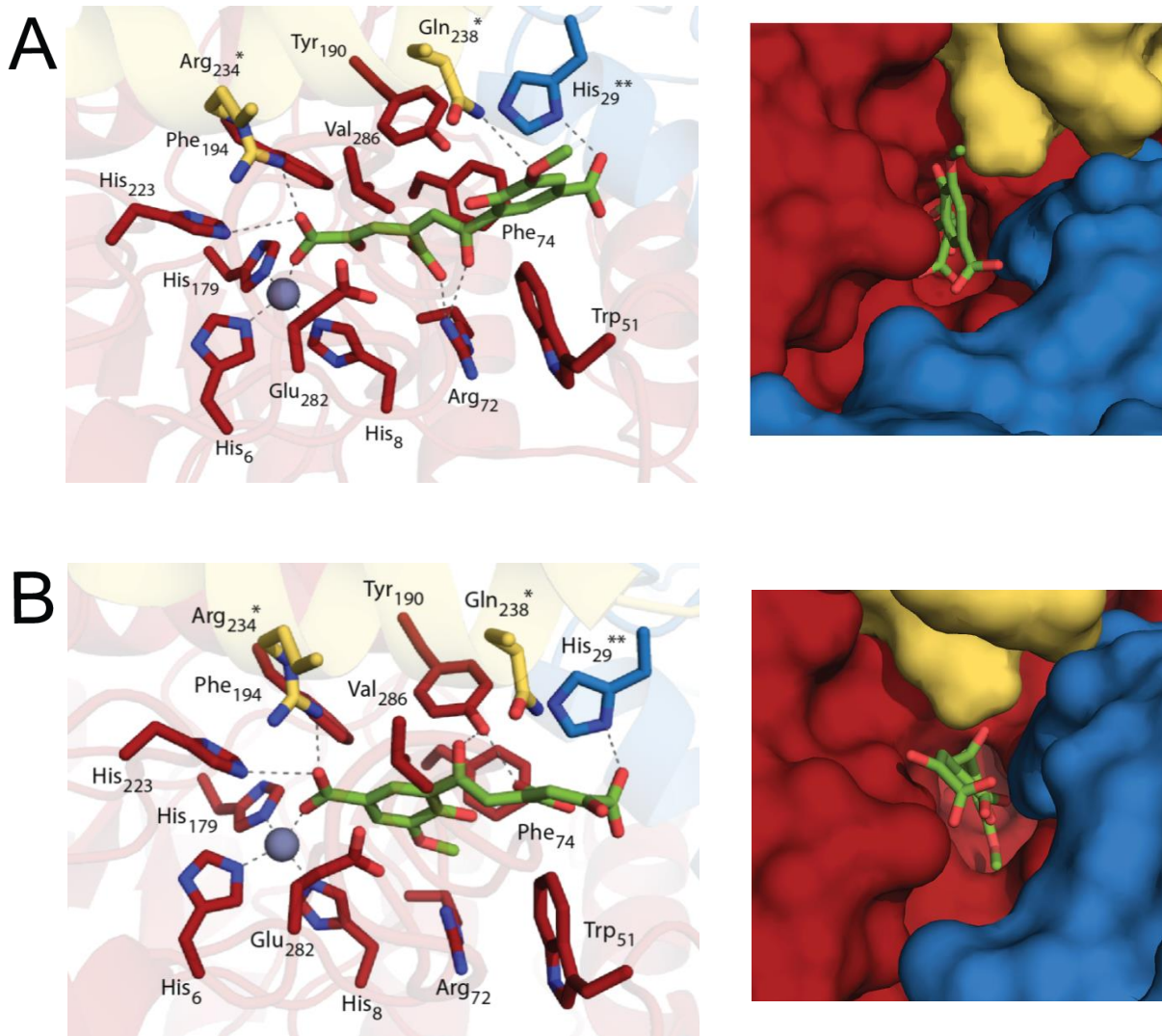


Figure 4.13. Models of the LigY·DCHM-HOPDA complex.

The model was constructed using Protomer C with the Cl^- removed and DCHM-HOPDA (green) with its dienoate moiety (A – ‘tail-in’) or phenyl moiety (B – ‘head-in’) orientated toward the metal center. Left, putative substrate-binding residues are shown in red, and residues from neighboring subunits are shown in yellow and blue. Potential hydrogen bonds are denoted with a dashed line. Right, surface representation of the active-site channel from figure 4.6 with substrate modeled in.

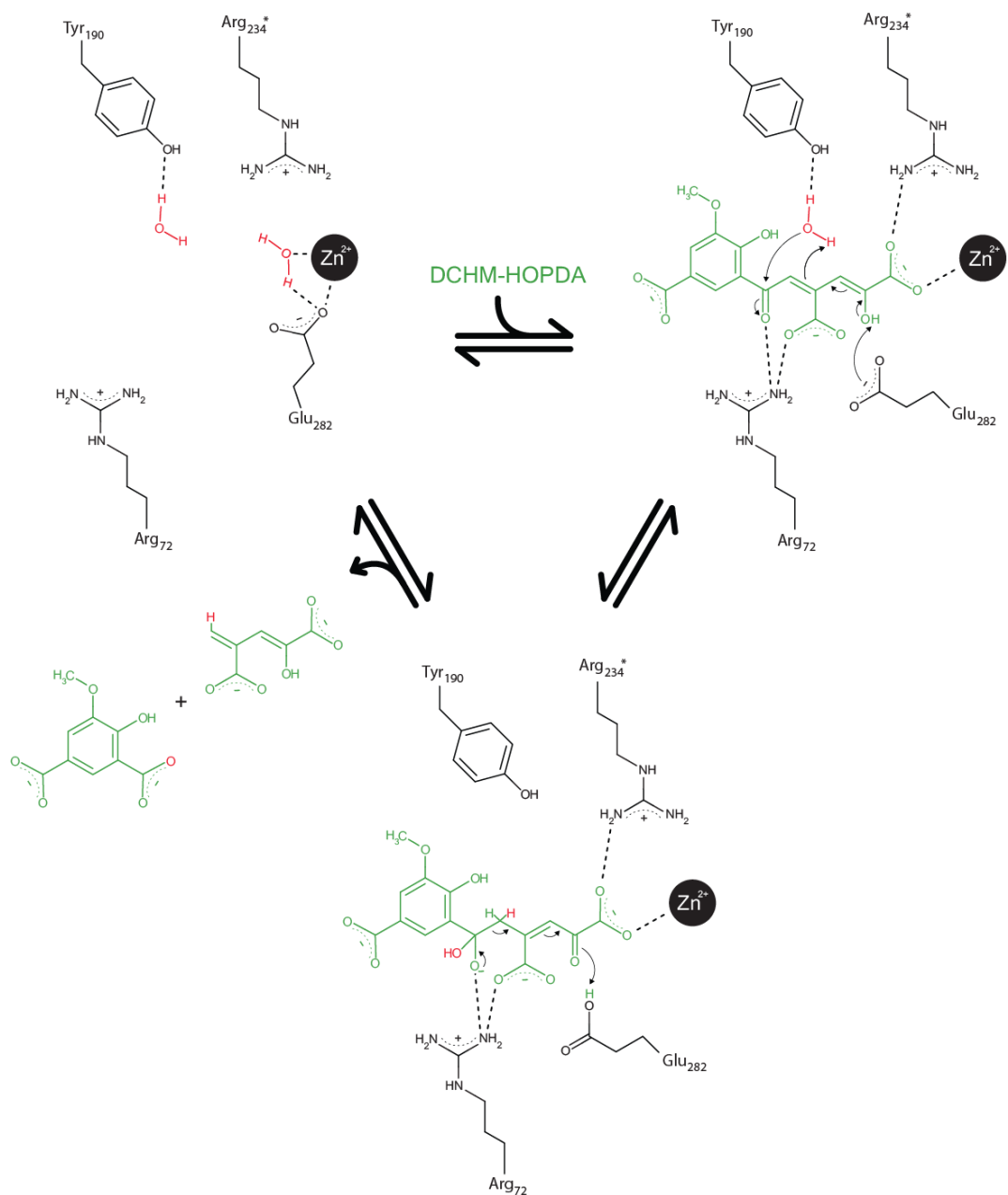


Figure 4.14. Proposed mechanism of LigY.

The suggested roles of particular residues are discussed under 'Discussion'

4.4 Discussion

The identification of LigY as an MCP hydrolase expands the known range of reactions catalyzed by amidohydrolases. More specifically, the definitive identifications of LigY's substrate as DCHM-HOPDA (1) and CHPD as the second reaction product establish that LigY catalyzes the hydrolysis of a vinylogous 1,5-diketone typical of MCP hydrolases. These results are consistent with a previous report that LigY catalyzes a hydrolytic reaction (51). This is the first report of an MCP hydrolase that is not a serine-dependent α/β -hydrolase. Nevertheless, LigY belongs to COG2159, which includes superfamily members that catalyze other C–C cleavage reactions, such as ACSMD (169), LigW (177), and CouO (176). Our data indicate that LigY's cognate metal ion is Zn^{2+} , typical of subtype III amidohydrolases. First, zinc was the predominant metal found in LigY when the growth medium used for protein production was not supplemented with metals. Second, LigY's specific activity was proportional to its zinc content. Unfortunately, LigY does not appear to take up or release its metal ion as readily as other amidohydrolases. For example, neither preincubation with Zn^{2+} nor its presence in the assay buffer improved the activity of LigY preparations with partial zinc occupancy. In other amidohydrolases, titration of the apoprotein with the metal ion resulted in rapid binding and a linear relationship between enzymatic activity and the amount of metal added (162,169,222). In this respect, LigY appears to be similar to adenosine deaminase (ADA) in that both are resistant to metal chelation at neutral pH (222). However, the inclusion of a reducing agent enabled rapid and complete reconstitution of ADA (222) but not LigY. Optimization for metal substitution in LigY is currently under way to facilitate further study of the enzyme.

Based on the mechanism of serine-dependent MCP hydrolases, the precedents in related amidohydrolases, and the presented data, we propose a mechanism for LigY that proceeds via an enol-keto tautomerization followed by a *gem*-diol intermediate and C–C bond fission (Figure 4.14). Tautomerization occurs in serine-dependent MCP hydrolases (130), acting as an electron sink to facilitate the subsequent C–C fragmentation reaction. The docking studies suggest that the Zn^{2+} and Arg-234 coordinate the C1-carboxylate, which would enable them to play a role in tautomerization by inducing strain on the dioenoate, as has been proposed for Arg-190 in BphD (131). The respective activities of the R234K and R234Q variants suggest that Arg-234 has such a catalytic role, as opposed to simply binding the substrate as would occur if DCHM-HOPDA bound in the head-in mode. Formation of a *gem*-diol intermediate is consistent with the absence of an active-site nucleophile. The modeled LigY.DCHM-HOPDA complex predicts that Arg-72 plays a major role by (*a*) interacting with the 4-carboxylate of the substrate and (*b*) contributing to an oxyanion hole to stabi-

lize the tetrahedral intermediate. The lack of activity of the R72Q variant is consistent with such a major role, as is the inability of LigY to hydrolyze HOPDA, which lacks the 4-carboxylate. Finally, neither the proposed mechanism nor the docking models explain the lack of activity of the Y190F variant. The proposed *gem*-diol intermediate differs from the acylenzyme intermediate of serine-dependent MCP hydrolases (129). However, the substrate-assisted activation of the nucleophile is analogous (150). Thus, a notable feature of the proposed mechanism is the requisite protonation at C5 of DCHM-HOPDA to complete ketonization and the concomitant activation of water for nucleophilic attack of the C6-carbonyl. In serine-dependent MCP hydrolases, ketonization involves an intermediate, ES^{red} , which possesses a remarkable bathochromically shifted absorption spectrum (131). ES^{red} has been proposed to be a dianionic intermediate that acts as a general base to activate the serine nucleophile (150). Further work is required to substantiate aspects of this mechanism, including the involvement of an ES^{red} species in tautomerization and water activation. The proposed mechanism postulates roles for Glu-282 in each half-reaction that are consistent with the *in crystallo* and mutagenesis data. In other words, the structural data suggest that Glu-282 is easily displaced, whereas the mutagenesis data indicate that the residue is essential for catalysis but not metal ion binding. Mechanistically, the displacement of Glu-282 by DCHM-HOPDA leaves it well-positioned to assist substrate tautomerization in the first half-reaction by deprotonating the C2-hydroxyl of DCHM-HOPDA. This role as a base catalyst is similar to what has been proposed for the equivalent residue in LigW, where an aspartate deprotonates the C4-hydroxyl of 5CVA, allowing 5CVA to bind the metallocenter (177). Importantly, the $\text{p}K_a$ of the C2-hydroxyl of DCHM-HOPDA is ~ 11.3 (1) and thus requires a base catalyst for tautomerization to occur. By contrast, BphD contains no such base, but none is required; 2-hydroxy-6-oxo-6-phenylhexa-2,4-dienoate probably binds as an enolate because the $\text{p}K_a$ of its C2-hydroxyl is 7.3 (201). In the second half-reaction, Glu-282 donates a proton to the dienoate leaving group. Overall, the role of Glu-282 as a proton shuttle is similar to what has been proposed in other amidohydrolases (158). Finally, like Glu-282 in LigY, the aspartyl ligand in LigW also adopts two conformations (177). However, the difference between the two conformations of the carboxylate is not as dramatic as in LigY. The glutamate in LigY, which also occurs in LigJ, may afford the greater conformation flexibility required for its catalytic role. The proposed mechanism diverges from that of other hydrolytic amidohydrolases, which exclusively favor a nucleophilic attack by a hydroxide to an electrophilic carbonyl or phosphoryl center (158). However, our docking studies suggest that in the absence of a major conformational change in the enzyme, the C6-carbonyl cannot approach the metal ion, precluding the conventional role of the metallocenter in

amidohydrolases (158). Most proposed amidohydrolase mechanisms favor the formation of metal-hydroxo species as a means of generating the hydrolytic nucleophile (158) because the binding of water to Zn^{2+} effectively lowers its pK_a to near 7 (223). LigY probably uses a different mechanism to activate the solvent species for hydrolysis because LigY lacks a metal-bound solvent species that is within hydrogen bonding distance to His-223, substrate binding probably displaces the metal-bound solvent species, and LigY lacks an acidic residue equivalent to Glu- 217 in CDA. The relative activities of the H223Q and H223A variants suggest that His-223 may help stabilize a catalytic intermediate via hydrogen bonding. Nevertheless, substitution of this conserved His is less deleterious than in other amidohydrolases, such as CDA, LigW, ACMSD, and IDCCase (162,170,171,177).

In conclusion, the proposed mechanism for LigY suggests specific roles for catalytic residues in the proposed two half reactions of MCP hydrolysis that are consistent with the available data as well as the modeled LigY.DCHM-HOPDA complex (Figure 4.13). Further studies are aimed at substantiating this mechanism and the proposed roles of individual residues.

Chapter 5:

Substrate activation strategy in a metal-dependent MCP hydrolase

5.1 Introduction

Work described in Chapters 3 and 4 established that LigY is a Zn²⁺-dependent MCP hydrolase that catalyzes the hydrolysis of DCHM-HOPDA to 5CVA and CHPD. This was done by identifying the enzyme's MCP substrate and both hydrolysis products. Further, x-ray crystallography established LigY as a member of the amidohydrolase superfamily, in contrast to all previously characterized MCP hydrolases, which belong to the α/β hydrolase superfamily. It remains unclear how LigY performs MCP hydrolysis given the absence of the catalytic triad critical to serine-dependent MCP hydrolysis. Modeling the substrate into the LigY active site further suggested the lack of the metal-bound solvent species typical of the hydrolytic amidohydrolases. Overall, it is of considerable interest to understand how a scaffold which predominantly catalyzes the hydrolysis of ester and phosphate bonds evolved to perform C-C bond hydrolysis.

In this study, we investigated the catalytic mechanism of LigY. The hydrolysis of DCHM-HOPDA by LigY was monitored using stopped-flow spectrophotometry to elucidate catalytic intermediates and their rates of formation. sKIEs were measured to better define the nature of the observed intermediates. The reactivity of LigY with substrate analogs was investigated to probe the importance of the substrate's 4-carboxylate in catalysis. Finally, the mode of substrate binding was investigated *in crystallo* using a LigY 4-methyl HOPDA binary complex. A catalytic mechanism for metal-dependent MCP hydrolases is proposed. The results are discussed with respect to C-C hydrolyzing enzymes and the catalytic machinery of metallohydrolases.

5.2 Material and Methods

5.2.1 Chemicals, reagents and enzymes.

All reagents were of analytical grade unless otherwise noted. OH-DDVA, 5-methyldihydroxybiphenyl (DHB), and 5-carboxy-DHB were synthesized as described previously (4). Water for buffers was purified in a Barnstead Nanopure Diamond system to a resistance of at least 18 MΩ. LigY, LigZ, and BphC were purified as described elsewhere (1,2,87). PCD was a gift from Professor John D. Lipscomb.

5.2.2 Production and characterization of 4-carboxy HOPDA and its cleavage products.

4-Carboxy-HOPDA was prepared in 100 mM phosphate buffer, pH 7.5, by reacting 5-carboxy-DHB with PCD. The pyridinal derivative of 4-carboxy-HOPDA was prepared by treatment of enzymatically prepared 4-carboxy-HOPDA with ammonium carbonate (0.1 M), acidification with 1% (v/v) glacial acetic acid, and passage through a 0.22 μm syringe-driven filter (1). The samples were resolved on an Agilent 1100 series HPLC unit equipped with an ACE Excel 2 C18-PFP (50 × 2.1 mm) column with a gradient of formic acid and acetonitrile (4). Mass spectra were measured on an Applied Biosystem Qstar mass spectrometer. The pyridinal derivative of 4-carboxy-HOPDA for NMR analysis was prepared in minimal potassium phosphate buffer and treated with ammonium hydroxide. The sample was passed through a 3 kDa membrane, lyophilized, and reconstituted in D₂O. NMR spectra were collected on a cryoprobe-equipped Bruker Avance III 600 MHz spectrometer and processed with ACD/NMR processor, academic edition, v12.01 (ACD/Laboratories).

For pK_a determination, aliquots of enzyme-free filtrate were titrated with sodium hydroxide or hydrochloric acid from pH ~6.5 to ~12, as measured with a pH electrode, while the concentration of 4-carboxy-HOPDA was kept constant at ~20 μM. Absorbance spectra were recorded on a Cary 60 UV-vis spectrophotometer (Agilent). The nonenzymatic transformation of 4-carboxy-HOPDA as a function of pH was monitored spectrophotometrically at 453 nm. The Hill equation was fitted to the data by use of Origin 8.1 software (Northampton, MA).

To characterize the products of LigY-catalyzed hydrolysis of 4-carboxy-HOPDA, they were first resolved by a Waters 2695 Separation HPLC module equipped with a Waters 2996 PDA detector and an Aqua 5-μm C18 250 × 4.6 mm column (Phenomenex). CHPD was eluted with an iso-

cratic flow of 0.1% formic acid. Benzoic acid was then eluted with a linear gradient to 100% methanol. The eluate was monitored at 220 nm. The retention times of the reaction products were compared to those of CHPD generated from LigY-catalyzed hydrolysis of DCHM-HOPDA and to an authentic standard of benzoic acid. The hydrolysis products were prepared by reacting 200 μ M of 5-carboxy-DHB with a mixture of PCD and LigY in air-saturated buffer. The reaction was quenched after \sim 10 min with glacial acetic acid (final concentration 1%), the enzymes were removed by centrifugation, and the solution was passed through a 0.22 μ m syringe-driven filter. Control samples were prepared under similar conditions.

5.2.3 Steady-State kinetic analyses.

Steady-state kinetic parameters for LigY-catalyzed hydrolysis of DCHM-HOPDA were determined in the presence of potassium phosphate buffer ($I = 0.5$ mM, pH 7.5) at 25 °C by monitoring the fluorescence of 5-carboxyvanillate as described previously (2). Parameters for LigY-catalyzed hydrolysis of 4-carboxy-HOPDA were determined discontinuously by monitoring the residual dienolate signal of 4-carboxy-HOPDA after quenching of the reaction after 60 s with KOH. Reactions were performed in volumes of 100 μ L containing potassium phosphate buffer ($I = 0.1$ mM, pH 7.5) at room temperature using a 96-well plate. The absorbance of the quenched reaction was measured at 562 nm on a VMax Kinetic microplate reader (Molecular Devices, San Jose, CA). Reaction mixtures contained 0–250 μ M 5-carboxy-DHB and 100 nM LigY and were initiated by adding 2 μ L of \sim 1 mM PCD. Absorbance readings were corrected by use of control reactions containing no LigY. Steady-state kinetic parameters were evaluated by fitting the Michaelis–Menten equation to the data, using the least-squares, dynamic weighting options of LEONORA (185). The inhibition of LigY by 4-methyl-HOPDA was monitored by the fluorescence assay with 0–300 μ M 4-methyl-HOPDA and 0–20 μ M DCHM-HOPDA [in potassium phosphate buffer ($I = 0.5$ mM, pH 7.5) at 25 °C]. Inhibition constants were evaluated by fitting equations describing reversible inhibition to the data, using the least-squares, dynamic weighting options of LEONORA (185).

5.2.4 K_d determination for 4-methyl HOPDA.

4-Methyl-HOPDA was prepared in 100 mM phosphate buffer, pH 7.5, by reacting 5-methyl-DHB with BphC. The enzyme was removed by filtration through a 30 kDa membrane. The 4-methyl-HOPDA was concentrated by evaporation and titrated into a solution of 100 mM phosphate buffer, pH 7.5, containing \sim 5.4 μ M LigY. The absorbance of the LigY·4-methyl-HOPDA complex

was recorded on a Cary 60 UV-vis spectrophotometer (Agilent). K_d values were evaluated by fitting the Hill equation to absorbance at 490 nm plotted as a function of 4-methyl-HOPDA concentration, by use of Origin 8.1 software (Northampton, MA).

5.2.5 Transient-state kinetic analyses.

Transient-state kinetic measurements were performed on an SX.18MV stopped-flow reaction analyzer (Applied Photophysics Ltd.). The temperature of the optical cell and drive syringe chamber were maintained at 25 °C with a Peltier device and a circulating water bath. Solutions of DCHM-HOPDA were prepared immediately prior to use by reacting OH-DDVA with excess LigZ and were diluted to 10 μM in 0.1 M KOH to favor the dienolate. Solutions of 40 μM LigY were also freshly prepared in potassium phosphate buffer (pH ≈ 7, I = 0.9 M). In standard reactions, mixing equal volumes of the DCHM-HOPDA and LigY solutions yielded potassium phosphate solution (I = 0.5 M), pH 7.5, containing enzyme and substrate in a 4:1 ratio. Multiple-wavelength data were collected by use of a PDA detector and Xe light source. Single-wavelength data were collected by use of a monochromator (4.96 nm/mm bandpass) open to 0.5 mm. Reported values were derived from at least three replicates, where each replicate represents an average of at least five successive reaction traces. Errors are reported as the standard deviation between replicates. The values were determined by use of Applied Photophysics Pro-Data software. Deuterated solutions of KOD or potassium phosphate were prepared by successive cycles of lyophilization and suspension in D₂O. Stock solutions of substrate and enzyme were added (total 5% v/v) to deuterated KOD and potassium phosphate, respectively.

5.2.6 Protein structure determination.

Crystals of LigY were prepared as previously described except that LigY was produced as an untagged protein (2). 4-Methyl-HOPDA, prepared by enzymatic transformation of 5-methyl-DHB with BphC in 20 mM HEPES, pH 8.0, was concentrated through evaporation and reconstituted with at least 75% (v/v) of the mother liquor. The crystals were transferred to mother liquor prior to soaking in mother liquor supplemented with ~10 mM 4-methyl-HOPDA for ~1 h. The crystals were cryoprotected in mother liquor solution supplemented with ~30% glycerol and flash-frozen in liquid nitrogen. Diffraction data were collected at the Stanford Synchrotron Radiation Laboratory on beamline 9-2 and processed with the XDS program suite using SCALA for data merging (186). Initial phases were determined by use of the ligand-free LigY structure (PDB entry 5VN5) as the search

model and the program Phaser-MR (187). The resulting model was refined by a successive combination of manual building using COOT and automated refinement with phenix.refine (189,190). Graphical representation of the crystallographic model was generated by the PyMOL molecular graphic system v1.3 (Schroödinger LLC).

5.2.7 Single crystal spectrophotometry.

UV-visible spectra were collected by use of beamline 9-2, which is equipped with an in situ single-crystal microspectrophotometer, essentially as described (224). Crystals were mounted at 100 K prior to data collection, and spectra were recorded with default settings. Briefly, dark and reference scans were collected prior to recording of spectra, followed by alignment of the crystal within the 50 μm microspec light spot. Phi-Rotation mode was used to determine the optimal orientation of the crystal, which was then applied to the collection strategy.

5.3 Results

5.3.1 Single turnover stopped-flow kinetic analysis.

To better understand the mechanism of LigY, we performed stopped-flow kinetic experiments. A complicating factor in these experiments is the rapid, nonenzymatic conversion of DCHM-HOPDA at physiological pH to a species, presumed to be a lactone (Figure 5.1), that is not a substrate for LigY (1). To overcome this problem, DCHM-HOPDA was maintained as the dienolate in one syringe by use of 0.1 N KOH, pH \approx 13. This was mixed with LigY in potassium phosphate buffer ($I = 0.9$ M), pH \approx 7. The mixture of the two reactants in equal volumes yielded potassium phosphate buffer ($I = 0.5$ M), pH 7.5. In this reaction buffer, LigY catalyzed the steady-state hydrolysis of DCHM-HOPDA with k_{cat} and K_M values of $9.7 \pm 0.3 \text{ s}^{-1}$ and $3.3 \pm 0.3 \mu\text{M}$, respectively, at 25°C . This turnover number is very similar to that determined at lower ionic strength at the same pH, while the Michaelis constant is approximately an order of magnitude higher (2).

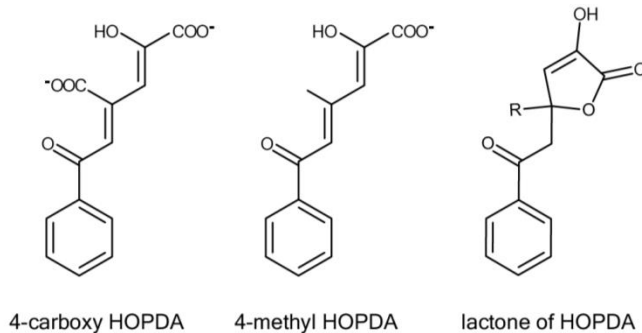


Figure 5.1. Substrate analog used in this study and the putative lactone of HOPDA.

Stopped-flow reactions were performed with an excess of enzyme (20 μM) over substrate (5 μM). Monitoring the reaction with a PDA detector revealed that DCHM-HOPDA was essentially in the dienolate form upon mixing, with characteristic absorbance bands at 366 and 474 nm (Figure 5.2A, yellow trace). This was converted to a second species characterized by a red-shifted spectrum ($\lambda_{\text{max}} = 508 \text{ nm}$; Figure 5.2A, red trace). We termed the species ES^{red} since its spectrum is similar to that reported in serine-dependent MCP hydrolases (131). Monitoring the reaction at 508 nm revealed that ES^{red} formed rapidly with a reciprocal relaxation time, $1/\tau_1$, of $137 \pm 7 \text{ s}^{-1}$, and decayed in a biphasic manner (Table 5.1). The first decay phase, accounting for >99% of the signal amplitude, occurred with $1/\tau_2 = 23 \pm 1 \text{ s}^{-1}$. The second decay phase accounted for $\sim 1\%$ of the signal amplitude and occurred with $1/\tau_3 = 0.7 \pm 0.2 \text{ s}^{-1}$. Given its small amplitude and as it was slower

than the rate-limiting step (k_{cat}), this second decay phase may represent a posthydrolytic process as reported for BphD and DxnB2 (129,131). Decreasing the amount of enzyme in the reaction by 50% did not affect the rate of decay of ES^{red} , indicating that this is a zero-order process. However, the rate of formation of ES^{red} became biphasic ($1/\tau_1 = 138 \pm 3 \text{ s}^{-1}$ and $1/\tau_2 = 44 \pm 2 \text{ s}^{-1}$). In control reactions with no LigY, ES^{red} was not detected and the dienolate bands decayed with $1/\tau$ of $7.4 \pm 0.2 \text{ s}^{-1}$, which is faster than previously reported due to the higher ionic strength (1).

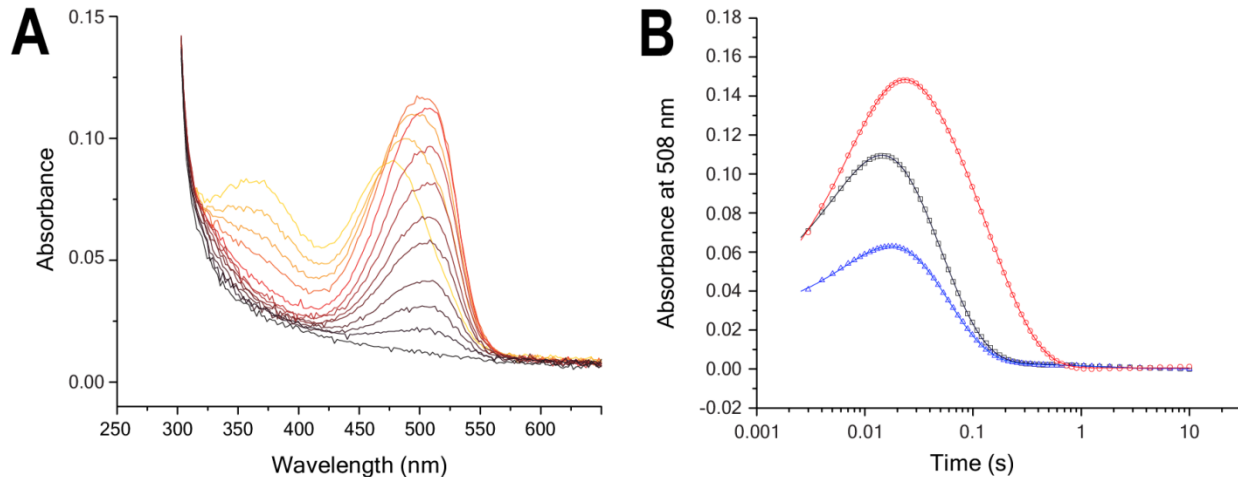


Figure 5.2. The single turnover of DCHM-HOPDA by LigY.

(A) Selected spectra recorded using a PDA detector. Spectra are color-coded according to time of acquisition, beginning with yellow (upon mixing), transitioning to red (0.02 s), then to black (10 s). (B) Reaction monitored at 508 nm, the λ_{max} of ES^{red} , in each of H_2O (black), 95% D_2O (v/v, red), and 30% sucrose (w/v, blue). For clarity not all data points are shown. Reactions contained 5 μM DCHM-HOPDA and 20 μM LigY (potassium phosphate ($I = 0.5 \text{ mM}$, pH 7.5) at 25 °C).

To further explore the reactivity of ES^{red} , we investigated the occurrence of an sKIE by performing the single-turnover experiment in deuterated buffer. Assay buffer reconstituted with D_2O had a measured pH of 7.1 ± 0.1 , which corresponds to pD 7.5 ± 0.1 . In the deuterated buffer, ES^{red} formed at essentially the same rate as in protiated buffer (Figure 5.2B and Table 5.1). The intermediate also decayed in a biphasic manner. However, the first decay phase accounted for almost 100% of the signal amplitude and occurred at a rate that was $\sim 30\%$ of that in protiated buffer. Similar results were obtained at pH 8.1 (results not shown). To evaluate whether the observed changes were due to a change in viscosity, the experiment was repeated in 30% (w/v) sucrose (protiated buffer). In the presence of the microviscogen, the rate of ES^{red} formation was slowed down by $\sim 45\%$. By contrast, the decay of ES^{red} was minimally perturbed. Overall, these results indicate that ES^{red} formation and decay are second- and first-order processes, respectively. Furthermore, the effect of D_2O on ES^{red}

decay is consistent with an sKIE, suggesting that this decay involves a proton-transfer step. The inability to directly monitor DCHM-HOPDA by NMR prevented determination of the rate of H/D exchange with solvent. Nevertheless, incubation of HOPDA for ~1 h in deuterated buffer resulted in the exchange of 2 equiv of deuterium into the dienol portion of the MCP (150). In HOPDA and its hydrolysis product, HPD, ¹H NMR established that this exchange occurs at positions C3-H and C5-H (131).

Table 5.1. Reciprocal relaxation times and amplitudes for single-turnover reactions^a.

solvent	ES ^{red} formation		ES ^{red} decay		
	1/τ ₁ (s ⁻¹)	1/τ ₂ (s ⁻¹)	[% Amp] ^b	1/τ ₃ (s ⁻¹)	[% Amp]
H ₂ O	137 ± 7	23 ± 1	99 ± 3	0.7 ± 0.2	1.2 ± 0.5
30% sucrose ^c	95 ± 2	20.4 ± 0.4	97 ± 2	0.5 ± 0.1	2.7 ± 0.3
D ₂ O ^d	127 ± 1	6.8 ± 0.1	100 ± 1	-0.27 ± 0.04	0.06 ± 0.03

^aReactions contained 20 μM LigY and 5 μM DCHM-HOPDA (potassium phosphate (*I* = 0.5 mM), pH 7.5 at 25 °C) and were monitored at 508 nm. Errors are reported as the standard deviation of at least three measurements.

^bThe amplitudes are reported as a percentage of the total amplitude of phases 2 and 3 combined.

^cThe protiated buffer contained 30% (w/v) sucrose. ^d95% D₂O (v/v).

5.3.2 Reactivity of LigY with substrate analogs.

We have previously reported that LigY does not detectably transform HOPDA (2). We hypothesized that the 4-carboxylate of DCHM-HOPDA contributes to the enzyme's ability to hydrolyze this substrate. Accordingly, we investigated LigY's ability to transform 4-carboxy-HOPDA and 4-methyl-HOPDA. 4-Methyl-HOPDA was produced from 5-methyl-DHB as described previously (4). 4-Carboxy-HOPDA was prepared by reacting 5-carboxy-DHB with PCD. This is analogous to the preparation of DCHM-HOPDA and 4-methyl-HOPDA, which were generated by the extradiol cleavage of (a) OH-DDVA by LigZ and (b) 5-methyl-DHB by BphC (1,4). For both DCHM-HOPDA and 4-methyl-HOPDA, 1,2-cleavage yielded a yellow dienolate anion, which converted to a colorless species at pH 7.5, presumed to be a lactone (Figure 5.1). Similarly, PCD converted 5-carboxy-DHB to a yellow product ($\lambda_{\text{max}} = 453$ nm) that rapidly converted to a colorless species in a biphasic manner ($t_{1/2} \approx 4$ and 0.3 min with signal amplitudes of 25% and 75%, respectively), consistent with 1,2-cleavage to 4-carboxy-HOPDA and its conversion to the lactone. Furthermore, as reported for DCHM-HOPDA and 4-methyl-HOPDA, the dienolate form of 4-carboxy-HOPDA could be regenerated under alkaline pH (Figure 5.3) (1,4). To further characterize 4-carboxy-

HOPDA, its more stable pyridinal derivative was prepared by treating 4-carboxy-HOPDA with ammonium, as described for DCHM-HOPDA (1). High-resolution LC-MS of the compound revealed a parent ion with an m/z value of 244.06, which agrees well with the predicted mass of the singly protonated pyridinal derivative of 4-carboxy-HOPDA (Figure 5.4). The latter's identity was further validated by ^1H NMR and heteronuclear single quantum coherence (HSQC) analyses (Figure 5.5).

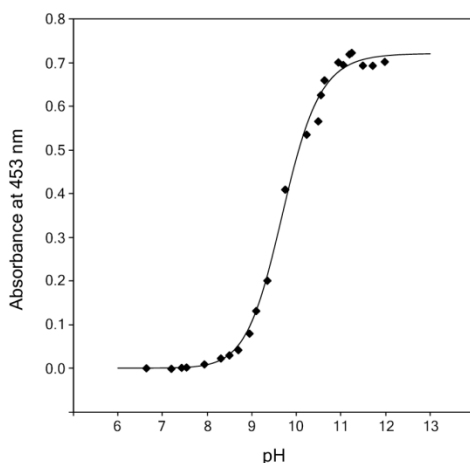


Figure 5.3. Apparent pK_a of 4-carboxy HOPDA.

Titration of 4-carboxy HOPDA's dienolate signal, absorbance at 453 nm, as a function of pH.

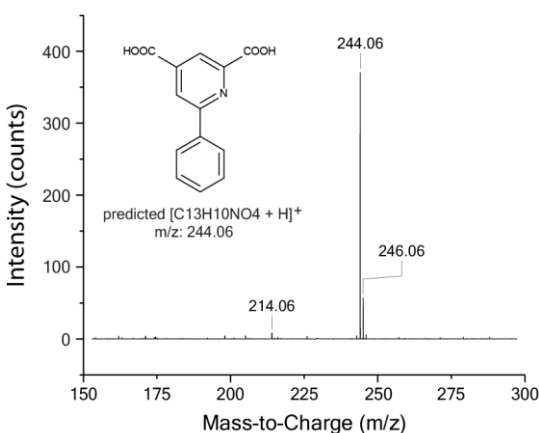


Figure 5.4. MS analysis of ammonium-derivatized 4-carboxy HOPDA.

Inset shows structure and calculated m/z value.

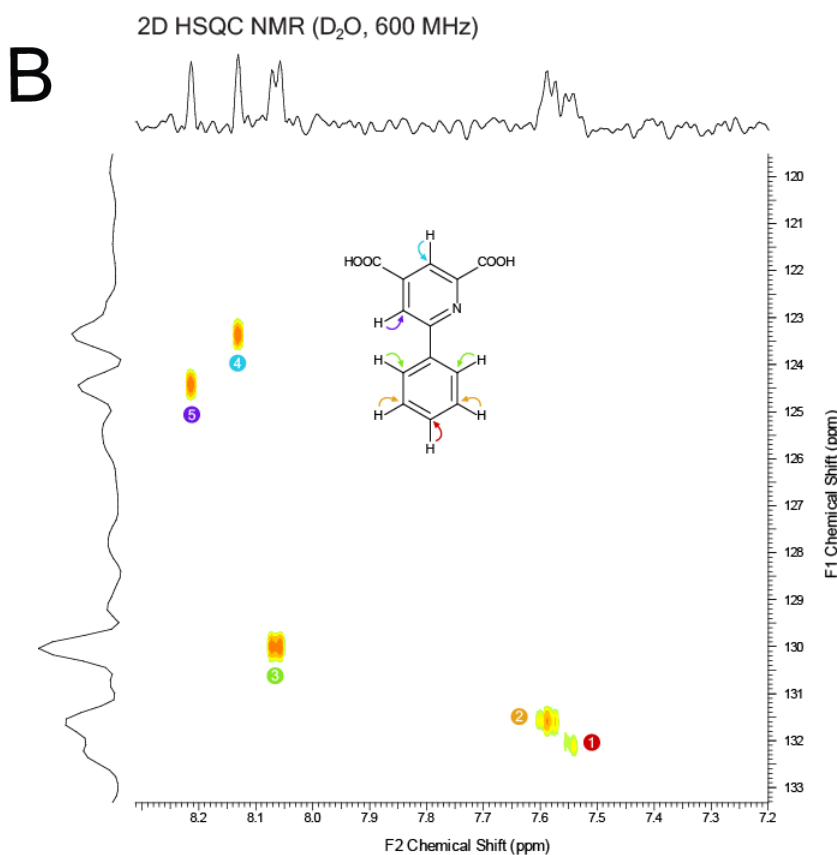
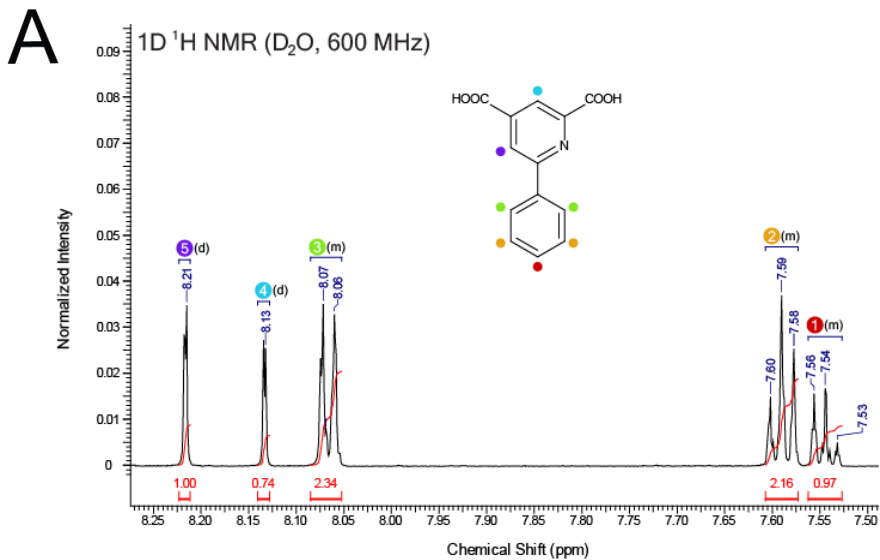


Figure 5.5. NMR analyses of ammonium-derivatized 4-carboxy HOPDA.

^1H NMR (A) and HSQC (B) (600 MHz; D_2O). Peaks and assignments are color-coded and similarly numbered in the two spectra: δ 8.21 (d, 1 H, $J = 1.8$, Py-H), 8.13 (d, 1 H, $J = 1.2$, Py-H), 8.07 (m, 2 H, Ar-H), 7.59 (m, 2 H, Ar-H), and 7.54 (m, 1 H, Ar-H).

These 4-substituted HOPDAs have pK_a values (~ 10) much closer to DCHM-HOPDA (11.3) than to HOPDA (7.3) (Figure 5.3). (4,201). Analysis of the reaction mixtures by HPLC revealed that LigY catalyzed the hydrolysis of 4-carboxy-HOPDA to benzoate and CHPD (Figure 5.6). By contrast, LigY did not detectably transform 4-methyl-HOPDA. Steady-state kinetic studies established that LigY catalyzed the hydrolysis of 4-carboxy-HOPDA with k_{cat} and K_M values of $1.4 \pm 0.1 \text{ s}^{-1}$ and $13 \pm 2 \mu\text{M}$, respectively [in potassium phosphate buffer ($I = 0.1 \text{ M}$), pH 7.5, 25 °C] (Figure 5.7). Finally, 4-methyl-HOPDA competitively inhibited LigY- catalyzed hydrolysis of DCHM-HOPDA with a K_{ic} value of $21 \pm 1 \mu\text{M}$ (Figure 5.8).

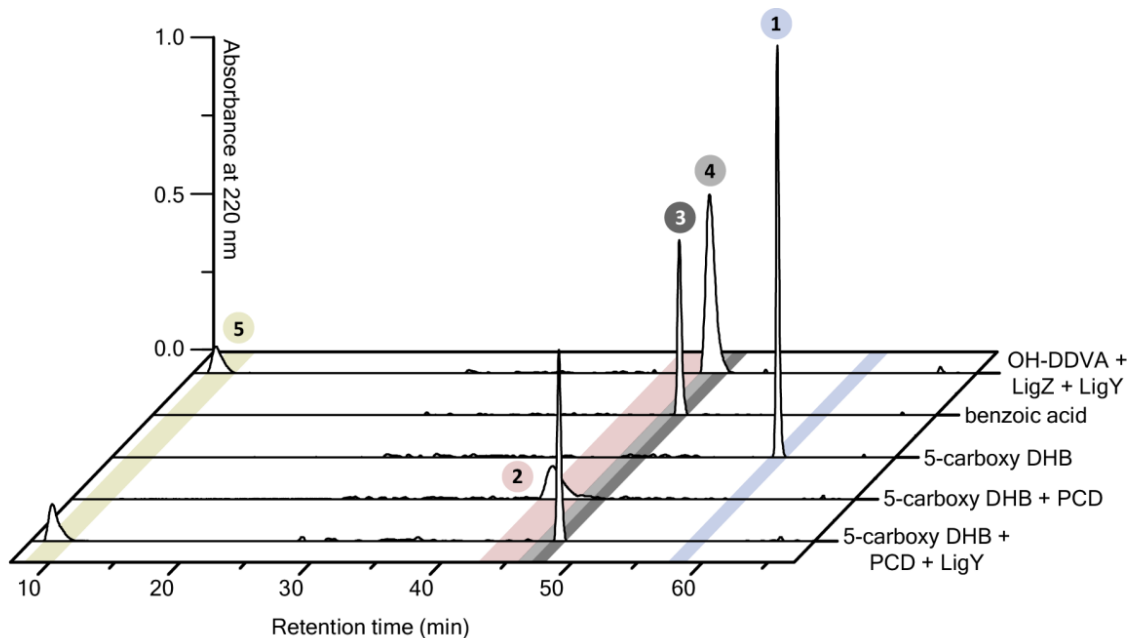


Figure 5.6. HPLC resolution of 4-carboxy HOPDA hydrolysis products.

Traces are OH-DDVA incubated with LigZ and LigY, benzoic acid, 5-carboxy DHB, 5-carboxy DHB incubated with PCD, and 5-carboxy DHB incubated with PCD and LigY. Peaks corresponding to specific compounds are labeled as such, 5-carboxy DHB as 1 – blue, 4-carboxy HOPDA as 2 – red, benzoic acid as 3 – dark grey, 5-carboxyvanillic acid as 4 - light grey, and CHPD as 5 – yellow.

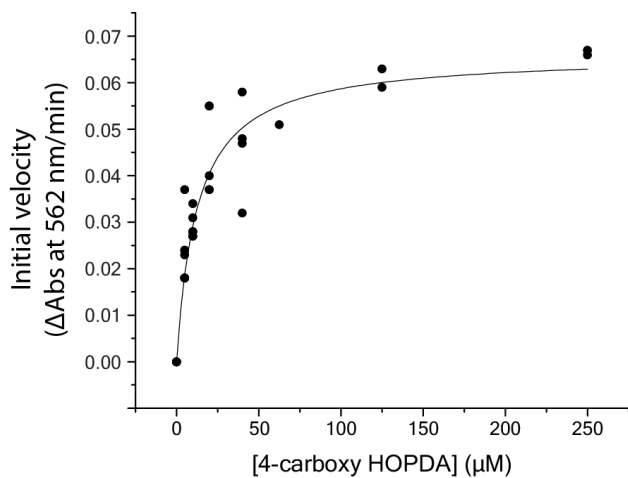


Figure 5.7. The steady-state hydrolysis of 4-carboxy HOPDA by LigY.

Experiments were performed using potassium phosphate ($I = 0.1$ M, pH 7.5), 25 °C. The line represent a best fit of the Michaelis-Menten equation to the data ($K_M = 13 \pm 2$ μM; $k_{cat} = 1.4 \pm 0.1$ s⁻¹).

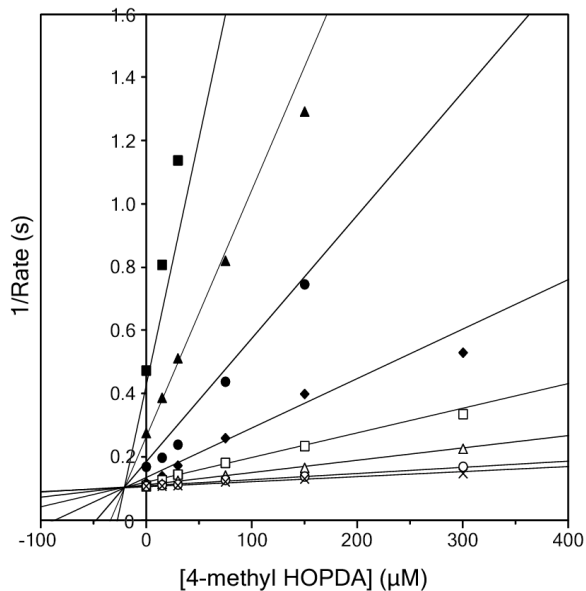


Figure 5.8. Dixon plot of the inhibition of LigY-catalyzed DCHM-HOPDA hydrolysis by 4-methyl HOPDA.

Experiments were performed using potassium phosphate ($I = 0.1$ M, pH 7.5), 25 °C and 0.2 μM (■), 0.4 μM (▲), 0.8 μM (●), 2 μM (◆), 4 μM (□), 8 μM (△), 16 μM (○), or 20 μM (×) OH-DDVA. The lines represent a best fit of an equation describing competitive inhibition to the data ($K_{ic} = 21 \pm 1$ μM; $K_M = 0.6 \pm 0.1$ μM; $k_{cat} = 9.7 \pm 0.1$ s⁻¹).

The ability of 4-methyl-HOPDA to competitively inhibit LigY led us to investigate the nature of the LigY·4-methyl-HOPDA complex. Titration of LigY with 4-methyl-HOPDA yielded a species with a spectrum characterized by λ_{max} of 490 nm [in potassium phosphate buffer ($I = 0.1 \text{ M}$), pH 7.5, 25 °C] (Figure 5.9A). This species had $t_{1/2} \approx 16.5 \text{ h}$, which is 4 orders of magnitude greater than that of the dienolate under these conditions. Moreover, the spectrum is bathochromically shifted with respect to that of the dienolate in solution ($\lambda_{\text{max}} = 445 \text{ nm}$, pH ≈ 13) and is reminiscent of ES^{red} observed in the turnover of DCHM-HOPDA as well as the species trapped by the S112A variant of BphD (149). This spectral signature was further exploited to obtain a binding isotherm, which yielded a K_d value of $25 \pm 1 \mu\text{M}$ and Hill coefficient of ~1 (Figure 5.9B). The ability of LigY to bind 4-methyl-HOPDA at physiological pH indicates this compound does not readily form a lactone, in contrast to what has been proposed for DCHM-HOPDA (4).

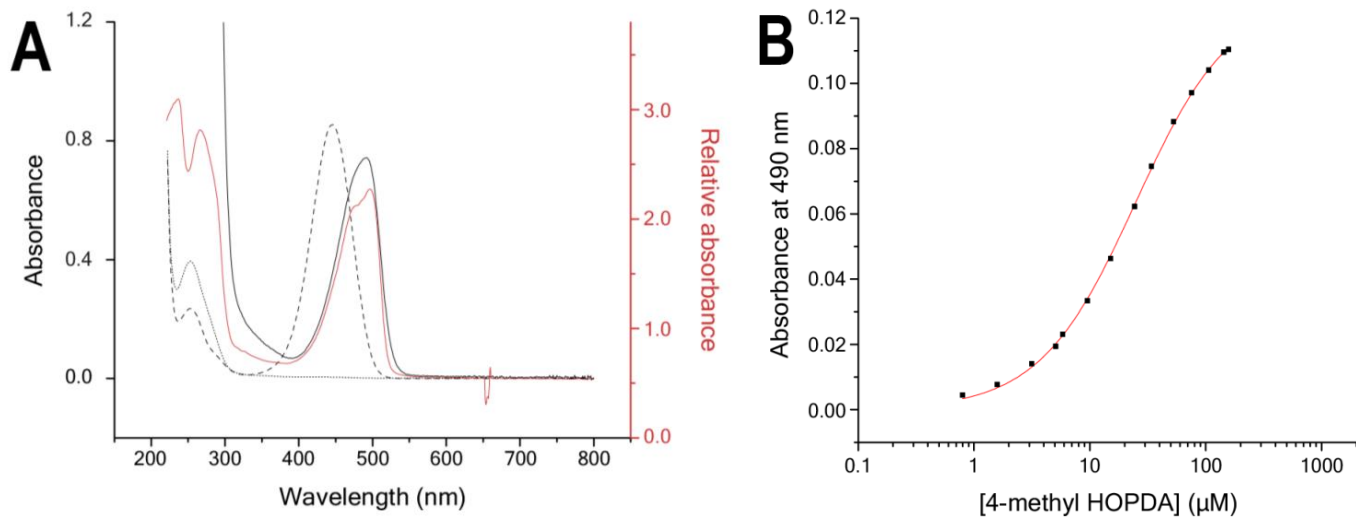


Figure 5.9. Binding of 4-methyl HOPDA to LigY.

(A) UV-vis spectra of 4-methyl HOPDA at pH 7.5 (dotted black), at pH > 13 (dashed black), in the presence of $\sim 5 \mu\text{M}$ LigY (solid black) (potassium phosphate ($I = 0.1 \text{ M}$)), and in single crystals of LigY·4-methyl HOPDA (solid red). (B) Binding isotherm. The solid line represents a best fit of the binding equation to the data ($K_d = 25 \pm 1 \mu\text{M}$).

5.3.3 Structure of LigY·4-methyl HOPDA complex

The formation of a stable LigY·4-methyl-HOPDA complex in solution prompted us to structurally characterize the complex. Colorless crystals of LigY, grown as previously described, were soaked with 4-methyl-HOPDA, yielding crystals with an orange-yellow tinge (2). The structure was refined to 2.4 Å resolution. Data collection and refinement statistics are shown in Table 5.2. Inter-

estingly, the space group was C222₁ as before (2). However, the unit cell increased 3-fold along the *a* axis due to noncrystallographic translational symmetry. As a result, the asymmetric unit of the soaked crystal was composed of nine protomers (i.e., 1.5 hexamer assemblies) instead of three (0.5 hexamer assembly) observed previously. The full length of each protomer was modeled except for the last amino acid in protomers F, G, and H. The overall structures of the protomers are very similar to each other and to the ligand-free LigY structure, with a RMSD of less than 0.3 Å over >330 α -carbons.

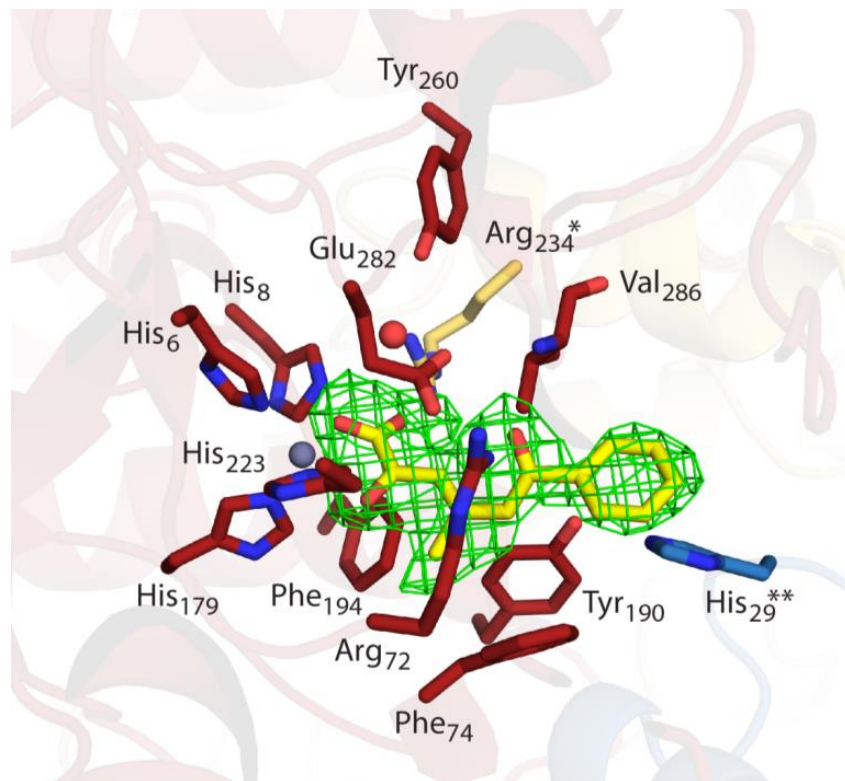


Figure 5.10. Structure of the LigY·4-methyl HOPDA complex.

An omit difference map of the substrate binding site produced prior to the modeling and refinement of 4-methyl HOPDA into the structure of LigY (contoured at 2.5 σ) is shown in green. Binding site residues are shown as sticks and are colored according to the chain of origin. The active site zinc ion and bound water are colored grey and red, respectively. The final refined model of the inhibitor 4-methyl HOPDA is shown in yellow. Asterisks (*) are used to denote residues that originate from neighboring chains.

Table 5.2. LigY·4-methyl HOPDA data collection and refinement statistics.

LigY·4-methyl HOPDA	
Data Collection	
Wavelength (Å)	0.97896
Resolution Range (Å)	38.73 – 2.40 (2.52 – 2.40) ^a
Space group	<i>C</i> 2 <i>2</i> ₂ ,
Unit cell dimension (Å)	<i>a</i> = 180.65 <i>b</i> = 195.10 <i>c</i> = 179.92
Unique reflections	238315
Completeness (%)	98.6 (91.1)
Redundancy	6.8 (5.9)
Mean I/σI	6.2 (2.1)
CC1/2	0.993 (0.685)
Wilson B-factor (Å ²)	48.5
Refinement	
R _{work} (R _{free})	18.3 (21.9)
No. of water molecules	631
r.m.s.d. bond length (Å)	0.003
Average B-values (Å ²)	
Overall	47.1
Protein	47.0
Ligand - Zn	36.5
Ligand – 4Me-HOPDA	58.9
Water	46.1
Ramachandran plot (%)	
in most-favorable	96.5
in allowed	2.6
in disallowed	0.9
PDB Accession Code	6E6I

^aValues in parentheses are for highest-resolution shell.

Strong positive density was observed in a difference map produced prior to inclusion of ligands into the model and was consistent with the presence of 4-methyl-HOPDA coordinated to the active-site metal in each protomer. The ligand was modeled as 4-methyl-HOPDA at full occupancy except for protomer D, for which refinement with occupancy of 70% best accounted for the density distribution (Figure 5.10). Due to the clearest continuous density depicting features consistent with 4-methyl-HOPDA, protomer A is used to describe the mode of ligand coordination. However, the density in all other protomers is consistent with this interpretation. In this binary complex, 4-methyl-HOPDA approaches the active-site Zn²⁺ via the 1-carboxylate and 2-oxo groups of the dienoate moiety. Attempts to refine the ligand with the phenyl group oriented toward the active-site metal resulted in poor density fitting and bond geometries (not shown). The Zn–O distances of the 1-carboxylate and 2-oxo groups are 1.9 and 2.5 Å, respectively. These are similar to the Zn–O bond

lengths reported for pyruvate (1.90 and 2.40 Å, respectively), an α -keto acid, bound in a bidentate manner to Zn²⁺ coordinated by an N-tripodal ligand in a biomimetic complex (225). Accordingly, we interpret 4-methyl-HOPDA to be bound to the Zn²⁺ in a similar bidentate manner. Overall, this is similar to the predicted tail-in binding mode modeled in the LigY·DCHM-HOPDA complex, in which the phenyl group is oriented toward the solvent at the opening of the active-site pocket (2). Although the Zn–O distance of the 2-oxo is 3.8 Å in the previously modeled complex, indicative of monodentate binding, the active site can accommodate bidentate-bound DCHM-HOPDA without significant structural change (Figure 5.11). Also, while the resolution of the diffraction data was sufficient to distinguish the ligand's binding mode, it was not sufficient to define the ligand's tautomeric state from the bond angles of the dienoate moiety. Ultimately, the bound ligand was modeled as the 2-keto-6-oxido form, similar to the ligand-binding mode observed in the S112A BphD·HOPDA crystal structure (149). However, this does not preclude the coexistence of 2-hydroxy-6-keto or 2,6-diketo tautomers (in some proportion), as both can be modeled into the electron density with similar degrees of confidence.

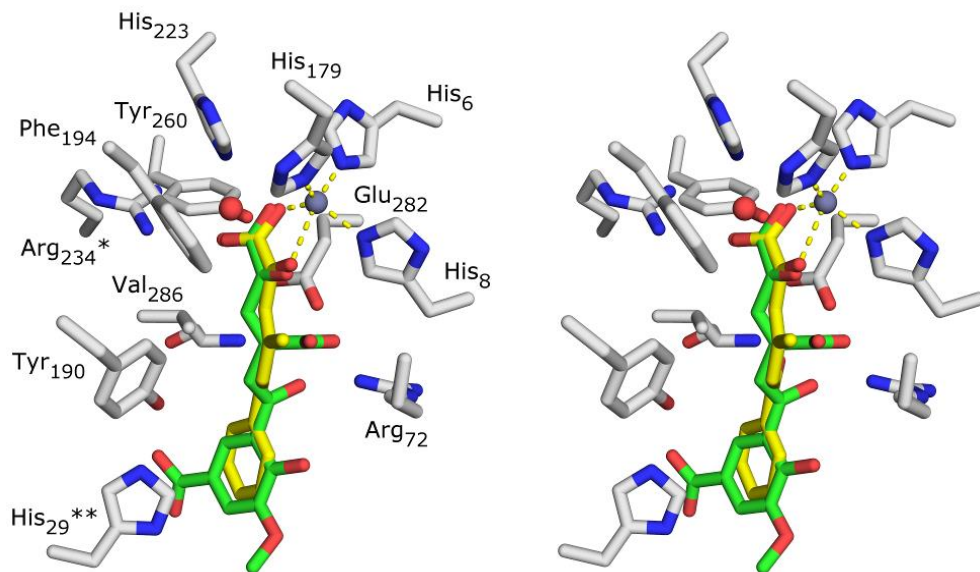


Figure 5.11. The configuration of 4-methyl HOPDA and DCHM HOPDA in the LigY active site.

Stereoview of an overlay between the structure of 4-methyl HOPDA (yellow) bound to LigY (white) and the predicted binding mode of DCHM-HOPDA (green) based on the LigY·4-methyl HOPDA structure. The Zn²⁺ ion and an active site solvent species are represented by grey and red spheres, respectively. The solvent species is also shown in Figure 5.12. Dotted lines indicate metal-ligand interactions (4-methyl HOPDA). Asterisks denote residues that originate from neighboring protomers.

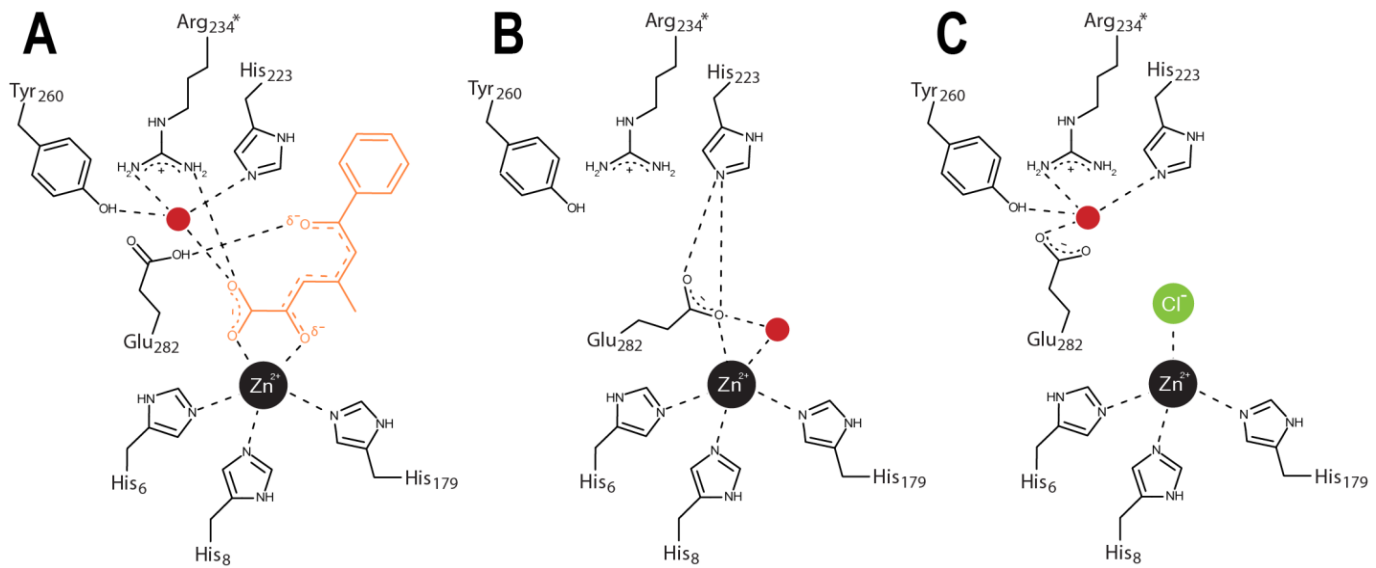


Figure 5.12. The Zn^{2+} coordination sphere of LigY in the presence of different ligands.

The 2D ligand-protein interaction diagrams of: (A) LigY·4-methyl HOPDA; (B) chain A of resting state LigY; and (C) chain C of resting state LigY. (B) and (C) are based on the previously published crystal structure (PDB ID: 5VN5). Water molecules are colored red and H-bonds are depicted as dashed lines. An asterisk (*) is used to denote residues that originate from neighboring chains.

Inspection of the active site of the LigY·4-methyl-HOPDA complex reveals a number of notable features. First, the Zn^{2+} is pentacoordinate: in addition to the 1-carboxylate and 2-oxo groups of the ligand, the metal ion is coordinated by His-6, His-8, and His-179 (Figure 5.12). The bidentate-bound 4-methyl-HOPDA replaces two Zn^{2+} ligands of the resting-state enzyme: Glu-282 and a water. The displaced Glu-282 is orientated away from the Zn^{2+} , similar to that observed in the LigY·Cl complex, and is within H-bonding distance to the 6-oxo group of 4-methyl-HOPDA (Glu- O^{δ} to 6-oxo distance of 2.8 Å) (2). The relative positioning of Glu-282 and the 6-oxo group suggests that the former is protonated. The 6-oxo group also forms an H-bond with the amide of Val-286. Second, the active site contains a water (B -factors ranging from 28 to 53 Å² in different protomers). This water molecule is coordinated by His-223, Tyr-260, an oxygen atom of the C1 carboxylate of 4-methyl-HOPDA, and Arg-234 from the neighboring protomer. This water was modeled in five of the nine protomers and was observable as residual positive density in the other four. A similarly coordinated water has been reported in LigY·Cl⁻ complex as well as in LigW·5-nitrovanillate complexes and isoorotate decarboxylase (IDCase) complexes: WT with the substrate analogue 5-nitouracil (PDB entry 4HK6) and the D323N variant with 5-carboxyuracil (PDB entry 4LAM) (2,171,177).

Finally, in the LigY·4-methyl-HOPDA complex, the 4-methyl group of the ligand is in van der Waals contact with Pro-73 and the aromatic ring of Phe-74.

5.3.4 Optical spectroscopy with single crystals

To correlate the structure of the LigY·4-methyl-HOPDA complex with the complex formed in solution, UV-visible absorption spectra were collected in conjunction with X-ray diffraction data. As seen in Figure 5.9, the spectrum of the complex in crystallo closely matched that of LigY·4-methyl-HOPDA in solution, with $\lambda_{\text{max}} = 490$ nm. The more defined features of the crystalline complex spectra likely reflect the fact that the data were collected at 100 K. Overall, the similarity of the spectra of the complexes in crystallo and in solution indicates that the structural model captures important elements of the complex

5.4 Discussion

This study provides insights into how LigY, a Zn^{2+} -dependent member of the amidohydro-lase superfamily, catalyzes C–C bond hydrolysis. The proposed mechanism (Figure 5.13) shares features with those of the serine-dependent MCP hydrolases and COG2159 decarboxylases. With respect to the former, the data indicate that LigY catalyzes the same enol–keto tautomerization and that this tautomerization involves the same type of ES^{red} intermediate (131). The similarity of these intermediates is illustrated by their respective spectra, which are bathochromically shifted to similar extents relative to those of the relevant dienolates. Thus, the spectrum of ES^{red} in LigY is shifted 56 nm with respect to that of the DCHM-HOPDA dienolate. In BphD, the spectrum of ES^{red} is shifted 58 nm with respect to that of the HOPDA dienolate (131). Importantly, ES^{red} formed and decayed in LigY at rates commensurate with k_{cat} . Moreover, the observation of an ES^{red} -like species with a nonhydrolyzable substrate analogue, 4-methyl-HOPDA, indicates that this species forms prior to C–C bond fission. Indeed, the trapping of ES^{red} in LigY by use of a substrate analogue is similar to its trapping via substitution of the active-site serine in BphD (149).

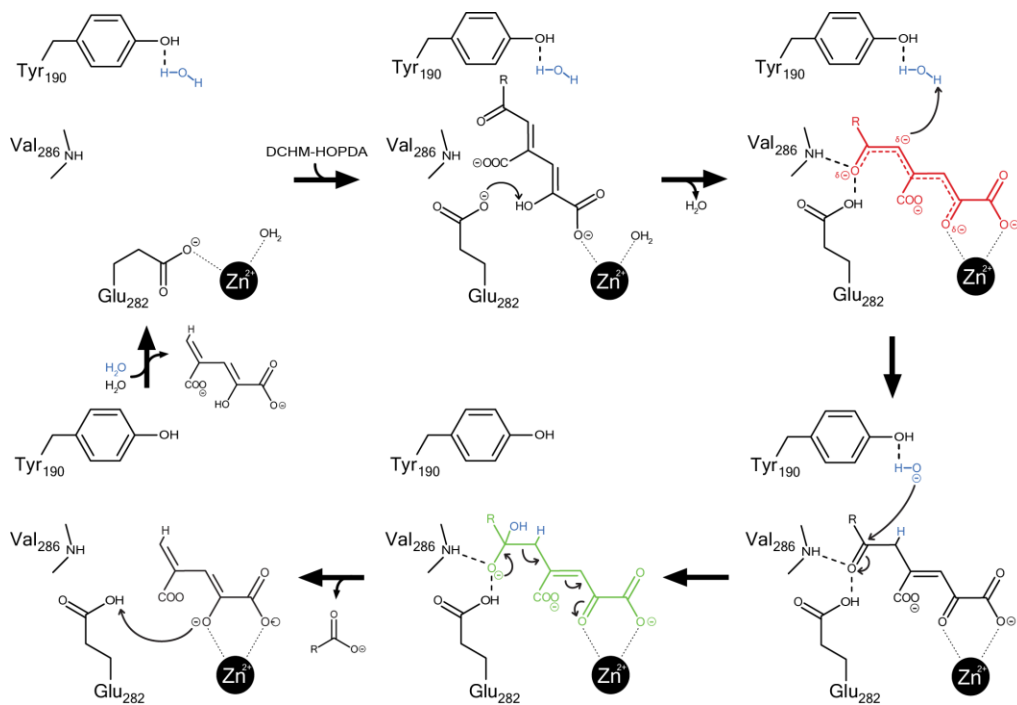


Figure 5.13. An updated mechanism for LigY.

A complete catalytic cycle is shown, beginning with binding of the DCHM-HOPDA dienol. The intermediate ES^{red} , in red, is hypothesized to possess a carbanion-like property. The nucleophilic H_2O is colored blue, and the proposed *gem*-diol intermediate, green.

LigY shares notable mechanistic features with LigW, whose mechanism is a paradigm for COG2159 decarboxylases, and LigJ, a hydratase (177,180). Shared features include the mode of substrate binding and the role of the conserved acidic metal ion ligand. In all three mechanisms, the substrate binds the metal ion in a bidentate fashion via a carboxylate and either a hydroxyl or oxo group on an adjacent carbon atom. Similar binding has been reported for γ -resorcylate decarboxylase (γ -RSD) from *Polaromonas* sp. and for IDCCase, although monodentate binding was observed in γ -RSD from *Rhizobium* sp. MTP-10005 (171-173). In all of these enzymes, the role of the metal ion is to anchor and polarize the substrate. This is in contrast to the typical role of the metal ion in other amidohydrolases, which lowers the pK_a of the hydrolytic water molecule, activating it for nucleophilic attack of the substrate's carbonyl or phosphoryl group (158). A second similarity concerns the role of the conserved acidic metal ion ligand located in the enzymes' β -8 strand: Glu-282 in LigY and Asp-314 in LigW. This residue deprotonates the substrate's hydroxyl moiety, assisting the latter's binding to the metal ion. In LigW, the proton is transferred to C5 of 5-carboxyvanillate prior to its decarboxylation (177). As noted above, the protonated Glu-282 in LigY is positioned to form the oxyanion hole together with the amide of Val-286 and, in the final steps of the reaction, could protonate the C2 oxido of CHPD as it is released from the enzyme (Figure 5.13) (158). In LigJ, Glu-284 does not appear to ligate the metal ion but is proposed to act as a base to activate water for attack at the substrate's C3 (180). Finally, LigY and LigJ also share a hydrogen-bonding network involving His-223, Arg-234, Tyr-260, a water molecule, and the ligand's C1 carboxylate (LigY numbering). With the exception of the tyrosine, these residues and interactions are also conserved in LigW. However, the role of this network remains unclear. In LigY, the water molecule within this network is located too far from C6 of 4-methyl-HOPDA ($\sim 7 \text{ \AA}$) to be the nucleophilic species (Figure 5.11). In LigW, it has been suggested that this network plays a role in correctly positioning the substrate (177).

The structural and kinetic data further indicate that substrate binding in LigY is a multistep process. As noted above, the structure of the LigY·4-methyl-HOPDA complex indicates that 4-methyl-HOPDA coordinates the active-site Zn^{2+} in a bidentate manner. The similarity of the spectrum of the bound ligand to that of ES^{red} generated in the turnover of DCHM-HOPDA strongly indicates that the binding mode of the two species is very similar. Importantly, this binding requires the displacement of Glu-282 and H_2O , two metal ligands in the resting-state enzyme (2). A multi-step binding process is consistent with the biphasic formation of ES^{red} at lower concentrations of LigY. A multistep ligand exchange may also explain why, even at higher concentrations of LigY, the

rate of ES^{red} formation ($1/\tau_1 = 137 \pm 7 \text{ s}^{-1}$) is still much slower than that in BphD and DxnB2, where it exceeds the dead time of the instrument ($1/\tau_1 > 500 \text{ s}^{-1}$) (131,150). Nevertheless, our data do not formally rule out the formation of a bidentate complex in a single step.

In the mechanism, Tyr-190 is proposed to position the catalytic H₂O (Figure 5.13). No such water is present in the LigY· 4-methyl-HOPDA structure. However, a water is hydrogen-bonded to Tyr-190 in the resting-state enzyme (2). Superpositioning of the two active sites (Figure 5.14) indicates that while the water hydrogen-bonded to Tyr-190 in the resting-state enzyme is closest to C5 (1.1 Å) and C6 (1.9 Å) of the overlaid 4-methyl-HOPDA, this water cannot be accommodated in the complex without some minor rearrangements. Such rearrangements might occur in the LigY·substrate complex as a result of functional groups on the phenyl ring of DCHM-HOPDA and/or this substrate's C4 carboxylate. The absence of a catalytically important water molecule could explain why LigY does not turn over 4-methyl-HOPDA despite transforming it to an ES^{red}-like species. Consistent with Tyr-190 playing a catalytically important role, substitution of this residue with phenylalanine reduces the activity of LigY by over 2 orders of magnitude (2). Nevertheless, we cannot definitively rule out that Tyr-190 acts as the nucleophile, as has been demonstrated in sialidases (226).

As noted above, it is likely that LigY binds DCHM-HOPDA in a slightly different configuration than 4-methyl-HOPDA. In this respect, it is possible that the 4-carboxylate group of DCHM-HOPDA forms an ion pair with Arg-72, helping to orientate the dienoate moiety in the active site and thereby accommodate the catalytic H₂O. Arg-72 is not positioned to form an ion pair with the 4-carboxylate group in the modeled complex (Figure 5.11). However, this residue adopts different conformations in the ligand-free and ligand-bound enzymes (Figure 5.14) (2). Moreover, analogous arginyl residues form ion pairs with substrate carboxylates in other COG2159 enzymes: in LigW, Arg-45 is proposed to pair with the C1 carboxylate group of the substrate (177); in ACMSD, Arg-51 is proposed to pair with the β -carboxy moiety of α -amino- β -carboxymuconate- ε -semialdehyde (181); and in LigJ, Arg-71 and Arg-290 coordinate the substrate's C6 carboxylate group (180). These arginyl residues are not conserved in COG2159 enzymes, presumably due to the different substrates of each enzyme. However, their substitution in each enzyme reduces activity by over 2 orders of magnitude (2,177,181). In considering the role of Arg-72, it is possible that orientation of the dienoate moiety in the active site for C–C bond cleavage results in monodentate binding of the substrate to the metal ion.

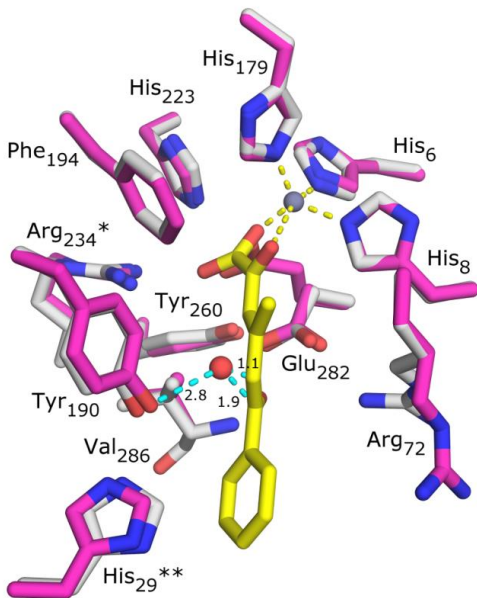


Figure 5.14. An active site overlay of the LigY·4-methyl HOPDA and ligand-free LigY structures.

In the LigY·4-methyl HOPDA complex, LigY and ligand carbon atoms are light grey and yellow, respectively. Carbon atoms of the ligand-free LigY (PDB ID: 5VN5) are pink. The Zn^{2+} ion is represented by a grey sphere. The solvent species in red is present only in the ligand-free structure. Yellow dotted lines indicate metal-ligand interactions (4-methyl HOPDA) and cyan dotted lines indicate distances between the solvent species, Tyr-190 (pink), and the overlaid C5 and C6 of 4-methyl HOPDA. Asterisks (*) denote residues that originate from neighboring protomers.

An intriguing feature of LigW that may be shared with LigY is the strain on the substrate induced by the enzyme's active site. High-resolution crystal structures of LigW·5-nitrovanillate complexes established that the substrate-binding pocket significantly distorts the nitro substituent out of the plane of the phenyl ring and that this does not require the metal (177). The resolution of the LigY·4-methyl-HOPDA data set is too low to establish the conformation of the dienoate. However, as noted above, interactions involving the C4 carboxylate may induce strain along the dienolate, which may distort the planarity of the dienolate moiety in BphD and thereby facilitate tautomerization (149). We are currently investigating the induction of strain by LigY and the nature of ES^{red} .

The observations of ES^{red} in LigY and of an sKIE in the decay of this intermediate establish a convergence of mechanisms in two independent families of C–C bond hydrolases that utilize different catalytic machinery. More specifically, Zn^{2+} - and Ser-dependent MCP hydrolases catalyze the same enol–keto tautomerization via ES^{red} and activate the nucleophile required for the hydrolytic

half-reaction in a substrate-assisted manner. Moreover, the structural data reveal similarities in the mechanisms of LigY and COG2159 decarboxylases, which in turn highlight how the catalytic machinery of the amidohydrolases has evolved to catalyze a variety of reactions, including C–C bond fission. An emerging theme in this family of amidohydrolases is that the primary role of the metallo-center is to bind and polarize the organic substrate.

Chapter 6:

Conclusion and future outlook

6.1 Overview

The work presented in this thesis provides important insights into a series of metalloenzymes that catalyze various C-C bond fission reactions in the bacterial catabolism of lignin-derived aromatic compounds. In the case of LigY, this insight extends into understanding how the hydrolytic machinery of the amidohydrolase superfamily has been adapted to catalyze an unusual C-C hydrolytic reaction. Nevertheless, important aspects of the enzymes' mechanisms and *in vivo* function remain to be elucidated, as summarized below.

6.2 Catalytic mechanism of LSDs

Despite the extensive spectroscopic studies of NOV1 and CAO1, the catalytic cycle of these Fe²⁺-dependent dioxygenases remains poorly understood. Elucidating the mechanism of LSDs and CCOs is of interest because their 4-histidine coordination sphere has not been reported in many other enzymes. Transient-state kinetic studies are one means to probe the mechanism. As proposed by McAndrew, a quinonoid intermediate is formed during the catalytic cycle of LSD (117). This intermediate should have a distinct spectroscopic signal relative to the un-activated stilbenoid (227). Further, nitro-stilbenoids such as 4-nitro-4'-hydroxystilbene may provide spectroscopic signals to facilitate the detection, characterization, and monitoring of catalytic intermediates. While LsdA was unable to cleave the 4-nitro-4'-hydroxystilbene, two of the eight LSD homologs of SYK-6, SYK6_YP_004834418.1 and SYK6_YP_004835929.1, possess this activity (Kuatsjah & Eltis, unpublished).

6.3 Stability of the type-II extradiol dioxygenases and its MCP

As presented in Chapter 2, the *in vitro* studies of LigZ revealed two characteristics of the system that might affect OH-DDVA catabolism *in vivo*: the O₂-lability of LigZ and the rapid non-enzymatic transformation of DCHM-HOPDA. At this time, it is clear to what degree either factor is an *in vitro* artifact as SYK-6 grows efficiently on DDVA as a sole carbon source (50). With respect to the adventitious oxidation of active site Fe²⁺ of LigZ, it is noted that the bacterial cytoplasm pro-

vides a reducing environment and the local effective concentration of O₂ inside the cell may also vary (228,229). Nevertheless, some extradiol dioxygenases that are oxidatively inactivated during catalytic turnover are reduced by a dedicated ferredoxin. This is exemplified by XylT of the TOL pathway, which maintains the ferrous iron of catechol-2,3-dioxygenase, XylE, in the reduced form (230). The DDVA pathway of SYK-6 does not apparently contain such a ferredoxin. However, in the absence of a specific ferredoxin, the dioxygenase may be reactivated by a non-specific electron transfer protein. Such a mechanism appears to account for the *in vivo* reactivation of BphC in *B. xenovorans* LB400 and *E. coli* (86).

The O₂-lability observed in LigZ is more severe than what was observed in related enzymes (1). For example, despite a comparable partition ratio between LigZ and LigAB towards OH-DDVA and protocatechuate, respectively, LigAB is not as sensitive towards exposure to oxygen in the absence of an organic substrate (103). Of particular interest to LigZ is the characterization of another “capless” extradiol dioxygenase, DesZ (105); particularly, on whether DesZ exhibit similar O₂-lability as LigZ. Further, neither LigZ nor DesZ has been structurally characterized.

The rapid, non-enzymatic transformation of DCHM-HOPDA could in principle result in a dead-end metabolite. To ensure efficient catabolism of DCHM-HOPDA, one could imagine some form of coordination between LigZ and LigY. This may be achieved through the formation of a complex between the two enzymes, or simply ensuring that LigZ is not rate-limiting in OH-DDVA catabolism. Alternatively, SYK-6 may harbor a mechanism to prevent or reverse the non-enzymatic transformation of DCHM-HOPDA. The latter could involve an enzyme that hydrolyzes the dead-end hemiacetal or lactone, analogous to what occurs in the catabolism of protocatechuate by the β-ketoadipate pathway (Figure 1.2).

6.4 Divergence in MCP hydrolysis

Through work described in Chapters 4 and 5, it is now established that MCP hydrolysis can be effected by serine- and Zn²⁺-dependent enzymes. Despite the body of work on both classes of enzymes, aspects of MCP hydrolysis remain unresolved. For example, the nature of ES^{red} is unclear and further evidence is required to substantiate the proposed mechanism. A higher resolution structure may help establish the protonation state and configuration of the ES^{red} intermediate. Another approach would be to investigate ES^{red} via NMR spectroscopy. However, this likely requires the synthesis of ¹³C-labelled material and a monomeric enzyme.

With respect to LigY in particular, the contribution of the metal ion to catalysis should be further probed. As noted in Chapter 5, an emerging theme in COG2159 amidohydrolases is the use of the metal ion to bind and polarize the ligand. In LigY, this role could be investigated from the perspective of the metal ion by substituting the spectroscopically silent Zn^{2+} ion with a spectroscopically active one, such as Co^{2+} . Co^{2+} has similar coordination chemistry and ionic radius as Zn^{2+} . Thus, this substitution often results in active enzymes (66). Indeed, Co^{2+} -substituted LigY has a comparable substrate specificity towards DCHM-HOPDA as the wild-type enzyme (Kuatsjah & Eltis, unpublished). Spectroscopic studies of Co^{2+} -substituted LigY may help discern the nature of substrate binding and the electronic contribution of the metal ion to catalysis. More specifically, Co^{2+} -LigY-ligand complexes may be trapped via rapid freeze-quench and then studied using EPR spectroscopy and XAS.

Other aspects of LigY function that merit future study include the role of the substrate's C4-carboxylate, the mechanism of water activation, and the catalytic roles of key residues such as Glu-282 and Tyr-190. The contribution of C4-carboxylate in HOPDA during catalysis remains obscure. One possibility is that it acts as an acid-base catalyst in a similar manner to Glu-217 in CDA (Figure 1.10). This hypothesis may be tested using a substrate analog such as 4-amide HOPDA. Further, should the compound not be hydrolyzed, it may bind in a manner closer to that of the substrate than does 4-Me HOPDA. This experiment is contingent upon the chemical synthesis of 5-amide DHB its cleavage by an extradiol dioxygenase. In the proposed mechanism of LigY, the hydroxyl nucleophile is generated in a substrate-assisted fashion (Figure 5.13). However, in the recent characterization of LigJ, that general base role was ascribed to Glu-284 (Figure 1.14). Indeed, the Glu-282 variants in LigY are catalytically inactive and the role of this residue in catalysis needs further elaboration. Future transient kinetic analyses could be aimed at evaluating the contribution of different active site residues towards catalysis, in particular ES^{red} formation. Finally, as noted in Chapter 5, Tyr-190 could not be ruled out as the nucleophile in LigY. Its role could be tested using a combination of chemical quench and MS analyses to detect a benzoylated enzyme adduct. This experiment would be similar to the detection of an acyl-enzyme intermediate in BphD and DxnB2 (129,150).

6.5 The development of biocatalysts for lignin valorization

As mentioned above, one motivation for the studies in this thesis is in providing a framework for the development of biocatalysts. Although a primary challenge in lignin valorization is to depolymerize lignin, there are increasing efforts to engineer bacteria to transform complex mixtures

of lignin-derived aromatic compounds to commodity chemicals in high atom yield (32). In this context, the enzymes described in this thesis may be introduced into microorganisms to augment their catabolic capabilities. For example, with the recent discovery of the DDVA importer (231), it might be possible to engineer other strains to degrade DDVA. Alternatively, LsdA lends itself to biocatalytic applications considering its stability and activity. For example, most industrial lignins are condensed and, unlike native lignins, contain stilbenoid linkages (119,120). LsdA may be used to cleave such structures, thereby functionalizing the lignin by introducing reactive aldehydes. For example, incubation of softwood kraft lignin with LsdA liberates vanillin (Kuatsjah & Eltis, unpublished). We are investigating this ability further, using NMR analyses of the lignin sample prior to and after enzymatic treatment to evaluate the extent and efficiency of stilbenoid cleavage.

Bibliography

1. Kuatsjah, E., Chen, H. M., Withers, S. G., and Eltis, L. D. (2017) Characterization of an Extradiol Dioxygenase Involved in the Catabolism of Lignin-derived Biphenyl. *FEBS Lett.* **591**, 1001-1009
2. Kuatsjah, E., Chan, A. C. K., Kobylarz, M. J., Murphy, M. E. P., and Eltis, L. D. (2017) The Bacterial *meta*-Cleavage Hydrolase LigY Belongs to the Amidohydrolase Superfamily, Not to the Alpha/Beta-hydrolase Superfamily. *J. Biol. Chem.* **292**, 18290-18302
3. Kuatsjah, E., Chan, A. C. K., Hurst, T. E., Snieckus, V., Murphy, M. E. P., and Eltis, L. D. (2018) Metal- and Serine-Dependent Meta-Cleavage Product Hydrolases Utilize Similar Nucleophile-Activation Strategies. *AcS Catal.* **8**, 11622-11632
4. Nerding, S., Kuatsjah, E., Hurst, T. E., Schlapp-Hackl, I., Kahlenberg, V., Wurst, K., Eltis, L. D., and Snieckus, V. (2018) Bacterial Catabolism of Biphenyls: Synthesis and Evaluation of Analogue. *ChemBioChem* **19**, 1771-1778
5. Cyranski, M. K. (2005) Energetic aspects of cyclic pi-electron delocalization: evaluation of the methods of estimating aromatic stabilization energies. *Chem Rev* **105**, 3773-3811
6. Bar-On, Y. M., Phillips, R., and Milo, R. (2018) The biomass distribution on Earth. *Proc Natl Acad Sci U S A* **115**, 6506-6511
7. Boerjan, W., Ralph, J., and Baucher, M. (2003) Lignin biosynthesis. *Annu Rev Plant Biol* **54**, 519-546
8. Dagley, S. (1975) A biochemical approach to some problems of environmental pollution. *Essays Biochem* **11**, 81-138
9. Faix, O. (1991) Classification of Lignins from Different Botanical Origins by Ft-Ir Spectroscopy. *Holzforschung* **45**, 21-27
10. Bugg, T. D., Ahmad, M., Hardiman, E. M., and Rahmankour, R. (2011) Pathways for degradation of lignin in bacteria and fungi. *Nat Prod Rep* **28**, 1883-1896
11. Ragauskas, A. J., Beckham, G. T., Biddy, M. J., Chandra, R., Chen, F., Davis, M. F., Davison, B. H., Dixon, R. A., Gilna, P., Keller, M., Langan, P., Naskar, A. K., Saddler, J. N., Tschaplinski, T. J., Tuskan, G. A., and Wyman, C. E. (2014) Lignin valorization: improving lignin processing in the biorefinery. *Science* **344**, 1246843
12. Sannigrahi, P., and Ragauskas, A. J. (2011) Characterization of fermentation residues from the production of bio-ethanol from lignocellulosic feedstocks. *J. Biobased Mat. Bioeng* **5**, 514-519
13. Cai, Y., Zhang, K., Kim, H., Hou, G., Zhang, X., Yang, H., Feng, H., Miller, L., Ralph, J., and Liu, C. J. (2016) Enhancing digestibility and ethanol yield of Populus wood via expression of an engineered monolignol 4-O-methyltransferase. *Nat Commun* **7**, 11989
14. Singh, R., Hu, J., Regner, M. R., Round, J. W., Ralph, J., Saddler, J. N., and Eltis, L. D. (2017) Enhanced delignification of steam-pretreated poplar by a bacterial laccase. *Sci Rep* **7**, 42121
15. Zhang, K., Bhuiya, M. W., Pazo, J. R., Miao, Y., Kim, H., Ralph, J., and Liu, C. J. (2012) An engineered monolignol 4-o-methyltransferase depresses lignin biosynthesis and confers novel metabolic capability in Arabidopsis. *Plant Cell* **24**, 3135-3152
16. Wilkerson, C. G., Mansfield, S. D., Lu, F., Withers, S., Park, J. Y., Karlen, S. D., Gonzales-Vigil, E., Padmakshan, D., Unda, F., Rencoret, J., and Ralph, J. (2014) Monolignol ferulate transferase introduces chemically labile linkages into the lignin backbone. *Science* **344**, 90-93
17. Falkowski, P. G., Fenchel, T., and Delong, E. F. (2008) The microbial engines that drive Earth's biogeochemical cycles. *Science* **320**, 1034-1039

18. Vaillancourt, F. H., Bolin, J. T., and Eltis, L. D. (2006) The ins and outs of ring-cleaving dioxygenases. *Crit. Rev. Biochem. Mol. Biol.* **41**, 241-267
19. Carmona, M., Zamarro, M. T., Blazquez, B., Durante-Rodriguez, G., Juarez, J. F., Valderrama, J. A., Barragan, M. J., Garcia, J. L., and Diaz, E. (2009) Anaerobic catabolism of aromatic compounds: a genetic and genomic view. *Microbiol Mol Biol Rev* **73**, 71-133
20. Dagley, S. (1978) Microbial catabolism, the carbon cycle and environmental pollution. *Naturwissenschaften* **65**, 85-95
21. Mason, J. R., and Cammack, R. (1992) The electron-transport proteins of hydroxylating bacterial dioxygenases. *Annu Rev Microbiol* **46**, 277-305
22. Palfey, B. A., and McDonald, C. A. (2010) Control of catalysis in flavin-dependent monooxygenases. *Arch Biochem Biophys* **493**, 26-36
23. Rather, L. J., Knapp, B., Haehnel, W., and Fuchs, G. (2010) Coenzyme A-dependent aerobic metabolism of benzoate via epoxide formation. *J Biol Chem* **285**, 20615-20624
24. Crowe, A. M., Casabon, I., Brown, K. L., Liu, J., Lian, J., Rogalski, J. C., Hurst, T. E., Snieckus, V., Foster, L. J., and Eltis, L. D. (2017) Catabolism of the Last Two Steroid Rings in *Mycobacterium tuberculosis* and Other Bacteria. *MBio* **8**
25. Harayama, S., and Rekik, M. (1989) Bacterial aromatic ring-cleavage enzymes are classified into two different gene families. *J Biol Chem* **264**, 15328-15333
26. Solomon, E. I., Brunold, T. C., Davis, M. I., Kemsley, J. N., Lee, S. K., Lehnert, N., Neese, F., Skulan, A. J., Yang, Y. S., and Zhou, J. (2000) Geometric and electronic structure/function correlations in non-heme iron enzymes. *Chem Rev* **100**, 235-350
27. Eltis, L. D., and Singh, R. (2018) Chapter 11 Biological Funneling as a Means of Transforming Lignin-derived Aromatic Compounds into Value-added Chemicals. in *Lignin Valorization: Emerging Approaches*, The Royal Society of Chemistry. pp 290-313
28. Yam, K. C., Van der Geize, R., and Eltis, L. D. (2010) Biology of *Rhodococcus*. (M., A. H. ed.). pp 133-169
29. Kamimura, N., Takahashi, K., Mori, K., Araki, T., Fujita, M., Higuchi, Y., and Masai, E. (2017) Bacterial catabolism of lignin-derived aromatics: New findings in a recent decade: Update on bacterial lignin catabolism. *Environ Microbiol Rep* **9**, 679-705
30. Patrauchan, M. A., Florizone, C., Dosanjh, M., Mohn, W. W., Davies, J., and Eltis, L. D. (2005) Catabolism of benzoate and phthalate in *Rhodococcus* sp. strain RHA1: redundancies and convergence. *J Bacteriol* **187**, 4050-4063
31. Chen, H. P., Chow, M., Liu, C. C., Lau, A., Liu, J., and Eltis, L. D. (2012) Vanillin catabolism in *Rhodococcus jostii* RHA1. *Appl Environ Microbiol* **78**, 586-588
32. Wang, X., Salvachua, D., Sanchez, I. N. V., Michener, W. E., Bratis, A. D., Dorgan, J. R., and Beckham, G. T. (2017) Propionic acid production from corn stover hydrolysate by *Propionibacterium acidipropionici*. *Biotechnol Biofuels* **10**, 200
33. Bugg, T. D., Ahmad, M., Hardiman, E. M., and Singh, R. (2011) The emerging role for bacteria in lignin degradation and bio-product formation. *Curr. Opin. Biotechnol.* **22**, 394-400
34. Kirk, T. K., and Farrell, R. L. (1987) Enzymatic "combustion": the microbial degradation of lignin. *Annu Rev Microbiol* **41**, 465-505
35. Wong, D. W. (2009) Structure and action mechanism of ligninolytic enzymes. *Appl Biochem Biotechnol* **157**, 174-209
36. Dey, S., Maiti, T. K., and Bhattacharyya, B. C. (1994) Production of some extracellular enzymes by a lignin peroxidase-producing brown rot fungus, *Polyporus ostreiformis*, and its comparative abilities for lignin degradation and dye decolorization. *Appl Environ Microbiol* **60**, 4216-4218

37. Vanden Wymelenberg, A., Gaskell, J., Mozuch, M., Sabat, G., Ralph, J., Skyba, O., Mansfield, S. D., Blanchette, R. A., Martinez, D., Grigoriev, I., Kersten, P. J., and Cullen, D. (2010) Comparative transcriptome and secretome analysis of wood decay fungi Postia placenta and Phanerochaete chrysosporium. *Appl Environ Microbiol* **76**, 3599-3610
38. Jackson, C. A., Couger, M. B., Prabhakaran, M., Ramachandriya, K. D., Canaan, P., and Fathepure, B. Z. (2017) Isolation and characterization of Rhizobium sp. strain YS-1r that degrades lignin in plant biomass. *J Appl Microbiol* **122**, 940-952
39. Wilhelm, R. C., Singh, R., Eltis, L. D., and Mohn, W. W. (2018) Bacterial and fungal contributions to delignification and lignocellulose degradation in forest soils with metagenomic and quantitative stable isotope probing. *bioRxiv*
40. Strachan, C. R., Singh, R., VanInsberghe, D., Ievdokymenko, K., Budwill, K., Mohn, W. W., Eltis, L. D., and Hallam, S. J. (2014) Metagenomic scaffolds enable combinatorial lignin transformation. *Proc Natl Acad Sci U S A* **111**, 10143-10148
41. Roberts, J. N., Singh, R., Grigg, J. C., Murphy, M. E., Bugg, T. D., and Eltis, L. D. (2011) Characterization of dye-decolorizing peroxidases from *Rhodococcus jostii* RHA1. *Biochemistry* **50**, 5108-5119
42. Brown, M. E., Barros, T., and Chang, M. C. (2012) Identification and characterization of a multifunctional dye peroxidase from a lignin-reactive bacterium. *ACS Chem Biol* **7**, 2074-2081
43. Ho, J. C. H., Pawar, S. V., Hallam, S. J., and Yadav, V. G. (2018) An Improved Whole-Cell Biosensor for the Discovery of Lignin-Transforming Enzymes in Functional Metagenomic Screens. *ACS Synth Biol* **7**, 392-398
44. Masai, E., Katayama, Y., and Fukuda, M. (2007) Genetic and biochemical investigations on bacterial catabolic pathways for lignin-derived aromatic compounds. *Biosci. Biotechnol. Biochem.* **71**, 1-15
45. Varman, A. M., He, L., Follenfant, R., Wu, W., Wemmer, S., Wrobel, S. A., Tang, Y. J., and Singh, S. (2016) Decoding how a soil bacterium extracts building blocks and metabolic energy from ligninolysis provides road map for lignin valorization. *Proc. Natl. Acad. Sci. U. S. A.* **113**, E5802-E5811
46. Zakzeski, J., Bruijnincx, P. C., Jongerius, A. L., and Weckhuysen, B. M. (2010) The catalytic valorization of lignin for the production of renewable chemicals. *Chem Rev* **110**, 3552-3599
47. Denef, V. J., Park, J., Tsoi, T. V., Rouillard, J. M., Zhang, H., Wibbenmeyer, J. A., Verstraete, W., Gulari, E., Hashsham, S. A., and Tiedje, J. M. (2004) Biphenyl and benzoate metabolism in a genomic context: outlining genome-wide metabolic networks in *Burkholderia xenovorans* LB400. *Appl Environ Microbiol* **70**, 4961-4970
48. Sonoki, T., Obi, T., Kubota, S., Higashi, M., Masai, E., and Katayama, Y. (2000) Coexistence of two different *o*-demethylation systems in lignin metabolism by *Sphingomonas paucimobilis* SYK-6: cloning and sequencing of the lignin biphenyl-specific *o*-demethylase (*ligX*) gene. *Appl. Environ. Microbiol.* **66**, 2125-2132
49. Yoshikata, T., Suzuki, K., Kamimura, N., Namiki, M., Hishiyama, S., Araki, T., Kasai, D., Otsuka, Y., Nakamura, M., Fukuda, M., Katayama, Y., and Masai, E. (2014) Three-Component O-Demethylase System Essential for Catabolism of a Lignin-Derived Biphenyl Compound in *Sphingobium* sp. Strain SYK-6. *Appl Environ Microbiol* **80**, 7142-7153
50. Peng, X., Egashira, T., Hanashiro, K., Masai, E., Nishikawa, S., Katayama, Y., Kimbara, K., and Fukuda, M. (1998) Cloning of a *Sphingomonas paucimobilis* SYK-6 gene encoding a novel oxygenase that cleaves lignin-related biphenyl and characterization of the enzyme. *Appl. Environ. Microbiol.* **64**, 2520-2527

51. Peng, X., Masai, E., Katayama, Y., and Fukuda, M. (1999) Characterization of the *meta*-Cleavage Compound Hydrolase Gene Involved in Degradation of the Lignin-related Biphenyl Structure by *Sphingomonas paucimobilis* SYK-6. *Appl. Environ. Microbiol.* **65**, 2789-2793
52. Peng, X., Masai, E., Kitayama, H., Harada, K., Katayama, Y., and Fukuda, M. (2002) Characterization of the 5-carboxyvanillate decarboxylase gene and its role in lignin-related biphenyl catabolism in *Sphingomonas paucimobilis* SYK-6. *Appl. Environ. Microbiol.* **68**, 4407-4415
53. Takahashi, K., Kamimura, N., Hishiyama, S., Hara, H., Kasai, D., Katayama, Y., Fukuda, M., Kajita, S., and Masai, E. (2014) Characterization of the catabolic pathway for a phenylcoumaran-type lignin-derived biaryl in *Sphingobium* sp. strain SYK-6. *Biodegradation* **25**, 735-745
54. Takahashi, K., Hirose, Y., Kamimura, N., Hishiyama, S., Hara, H., Araki, T., Kasai, D., Kajita, S., Katayama, Y., Fukuda, M., and Masai, E. (2015) Membrane-associated glucose-methanol-choline oxidoreductase family enzymes PhcC and PhcD are essential for enantioselective catabolism of dehydroniconiferyl alcohol. *Appl. Environ. Microbiol.* **81**, 8022-8036
55. Takahashi, K., Miyake, K., Hishiyama, S., Kamimura, N., and Masai, E. (2018) Two novel decarboxylase genes play a key role in the stereospecific catabolism of dehydroniconiferyl alcohol in *Sphingobium* sp. strain SYK-6. *Environ Microbiol* **20**, 1739-1750
56. Masai, E., Katayama, Y., Nishikawa, S., Yamasaki, M., Morohoshi, N., and Haraguchi, T. (1989) Detection and localization of a new enzyme catalyzing the beta-aryl ether cleavage in the soil bacterium (*Pseudomonas paucimobilis* SYK-6). *FEBS Lett* **249**, 348-352
57. Sato, Y., Moriuchi, H., Hishiyama, S., Otsuka, Y., Oshima, K., Kasai, D., Nakamura, M., Ohara, S., Katayama, Y., Fukuda, M., and Masai, E. (2009) Identification of three alcohol dehydrogenase genes involved in the stereospecific catabolism of arylglycerol-beta-aryl ether by *Sphingobium* sp. strain SYK-6. *Appl Environ Microbiol* **75**, 5195-5201
58. Pereira, J. H., Heins, R. A., Gall, D. L., McAndrew, R. P., Deng, K., Holland, K. C., Donohue, T. J., Noguera, D. R., Simmons, B. A., Sale, K. L., Ralph, J., and Adams, P. D. (2016) Structural and Biochemical Characterization of the Early and Late Enzymes in the Lignin beta-Aryl Ether Cleavage Pathway from *Sphingobium* sp. SYK-6. *J Biol Chem* **291**, 10228-10238
59. Masai, E., Ichimura, A., Sato, Y., Miyauchi, K., Katayama, Y., and Fukuda, M. (2003) Roles of the enantioselective glutathione S-transferases in cleavage of beta-aryl ether. *J Bacteriol* **185**, 1768-1775
60. Helmich, K. E., Pereira, J. H., Gall, D. L., Heins, R. A., McAndrew, R. P., Bingman, C., Deng, K., Holland, K. C., Noguera, D. R., Simmons, B. A., Sale, K. L., Ralph, J., Donohue, T. J., Adams, P. D., and Phillips, G. N., Jr. (2016) Structural Basis of Stereospecificity in the Bacterial Enzymatic Cleavage of beta-Aryl Ether Bonds in Lignin. *J Biol Chem* **291**, 5234-5246
61. Meux, E., Prosper, P., Masai, E., Mulliert, G., Dumarcay, S., Morel, M., Didierjean, C., Gelhaye, E., and Favier, F. (2012) *Sphingobium* sp. SYK-6 LigG involved in lignin degradation is structurally and biochemically related to the glutathione transferase omega class. *FEBS Lett* **586**, 3944-3950
62. Higuchi, Y., Aoki, S., Takenami, H., Kamimura, N., Takahashi, K., Hishiyama, S., Lancefield, C. S., Ojo, O. S., Katayama, Y., Westwood, N. J., and Masai, E. (2018) Bacterial Catabolism of beta-Hydroxypropiovanillone and beta-Hydroxypropiosyringone Produced in the Reductive Cleavage of Arylglycerol-beta-Aryl Ether in Lignin. *Appl Environ Microbiol* **84**
63. Fukuhara, Y., Kamimura, N., Nakajima, M., Hishiyama, S., Hara, H., Kasai, D., Tsuji, Y., Narita-Yamada, S., Nakamura, S., Katano, Y., Fujita, N., Katayama, Y., Fukuda, M., Kajita,

- S., and Masai, E. (2013) Discovery of pinoresinol reductase genes in sphingomonads. *Enzyme Microb Technol* **52**, 38-43
64. Habu, N., Samejima, M., Saburi, Y., and Yoshimoto, T. (1988) Purification and Some Properties of 2 C-Alpha-Dehydrogenases Oxidizing Dimeric Lignin Model Compounds from Pseudomonas Sp Tmy1009. *Agr Biol Chem Tokyo* **52**, 3073-3079
65. Kishi, K., Habu, N., Samejima, M., and Yoshimoto, T. (1991) Purification and Some Properties of the Enzyme Catalyzing the C-Gamma-Elimination of a Diarylpropane-Type Lignin Model from Pseudomonas-Paucimobilis Tmy1009. *Agr Biol Chem Tokyo* **55**, 1319-1323
66. Bertini, I. (1994) *Bioinorganic chemistry*, University Science Books, Mill Valley, Calif.
67. Siegbahn, P. E., and Haeffner, F. (2004) Mechanism for catechol ring-cleavage by non-heme iron extradiol dioxygenases. *J Am Chem Soc* **126**, 8919-8932
68. Kovaleva, E. G., and Lipscomb, J. D. (2008) Versatility of biological non-heme Fe(II) centers in oxygen activation reactions. *Nat Chem Biol* **4**, 186-193
69. Cannatelli, M. D., and Ragauskas, A. J. (2016) Conversion of lignin into value-added materials and chemicals via laccase-assisted copolymerization. *Appl Microbiol Biotechnol* **100**, 8685-8691
70. Wang, Y., Li, J., and Liu, A. (2017) Oxygen activation by mononuclear nonheme iron dioxygenases involved in the degradation of aromatics. *J Biol Inorg Chem* **22**, 395-405
71. Harrison, P. J., and Bugg, T. D. (2014) Enzymology of the carotenoid cleavage dioxygenases: reaction mechanisms, inhibition and biochemical roles. *Arch Biochem Biophys* **544**, 105-111
72. Ballou, D. P. (1999) *Metalloproteins*, Princeton University Press, Princeton, N.J.
73. Mascotti, M. L., Juri Ayub, M., Furnham, N., Thornton, J. M., and Laskowski, R. A. (2016) Chopping and Changing: the Evolution of the Flavin-dependent Monooxygenases. *J Mol Biol* **428**, 3131-3146
74. Dresen, C., Lin, L. Y., D'Angelo, I., Tocheva, E. I., Strynadka, N., and Eltis, L. D. (2010) A flavin-dependent monooxygenase from Mycobacterium tuberculosis involved in cholesterol catabolism. *J Biol Chem* **285**, 22264-22275
75. Fetzner, S. (2002) Oxygenases without requirement for cofactors or metal ions. *Appl Microbiol Biotechnol* **60**, 243-257
76. Kal, S., and Que, L. (2017) Dioxygen activation by nonheme iron enzymes with the 2-His-1-carboxylate facial triad that generate high-valent oxoiron oxidants. *J. Biol. Inorg. Chem.*
77. Pau, M. Y., Lipscomb, J. D., and Solomon, E. I. (2007) Substrate activation for O₂ reactions by oxidized metal centers in biology. *Proc Natl Acad Sci U S A* **104**, 18355-18362
78. Minor, W., Steczko, J., Stec, B., Otwinowski, Z., Bolin, J. T., Walter, R., and Axelrod, B. (1996) Crystal structure of soybean lipoxygenase L-1 at 1.4 Å resolution. *Biochemistry* **35**, 10687-10701
79. Carredano, E., Karlsson, A., Kauppi, B., Choudhury, D., Parales, R. E., Parales, J. V., Lee, K., Gibson, D. T., Eklund, H., and Ramaswamy, S. (2000) Substrate binding site of naphthalene 1,2-dioxygenase: functional implications of indole binding. *J Mol Biol* **296**, 701-712
80. Imbeault, N. Y., Powlowski, J. B., Colbert, C. L., Bolin, J. T., and Eltis, L. D. (2000) Steady-state kinetic characterization and crystallization of a polychlorinated biphenyl-transforming dioxygenase. *J Biol Chem* **275**, 12430-12437
81. Fitzpatrick, P. F. (1999) Tetrahydropterin-dependent amino acid hydroxylases. *Annu Rev Biochem* **68**, 355-381
82. Price, J. C., Barr, E. W., Tirupati, B., Bollinger, J. M., Jr., and Krebs, C. (2003) The first direct characterization of a high-valent iron intermediate in the reaction of an alpha-

- ketoglutarate-dependent dioxygenase: a high-spin FeIV complex in taurine/alpha-ketoglutarate dioxygenase (TauD) from Escherichia coli. *Biochemistry* **42**, 7497-7508
83. Vetting, M. W., and Ohlendorf, D. H. (2000) The 1.8 Å crystal structure of catechol 1,2-dioxygenase reveals a novel hydrophobic helical zipper as a subunit linker. *Structure* **8**, 429-440
84. Eltis, L. D., and Bolin, J. T. (1996) Evolutionary relationships among extradiol dioxygenases. *J Bacteriol* **178**, 5930-5937
85. Dunwell, J. M., Culham, A., Carter, C. E., Sosa-Aguirre, C. R., and Goodenough, P. W. (2001) Evolution of functional diversity in the cupin superfamily. *Trends Biochem Sci* **26**, 740-746
86. Vaillancourt, F. H., Labbe, G., Drouin, N. M., Fortin, P. D., and Eltis, L. D. (2002) The mechanism-based inactivation of 2,3-dihydroxybiphenyl 1,2-dioxygenase by catecholic substrates. *J Biol Chem* **277**, 2019-2027
87. Vaillancourt, F. H., Han, S., Fortin, P. D., Bolin, J. T., and Eltis, L. D. (1998) Molecular Basis for the Stabilization and Inhibition of 2, 3-Dihydroxybiphenyl 1,2-Dioxygenase by *t*-Butanol. *J. Biol. Chem.* **273**, 34887-34895
88. Kovaleva, E. G., and Lipscomb, J. D. (2007) Crystal structures of Fe²⁺ dioxygenase superoxo, alkylperoxo, and bound product intermediates. *Science* **316**, 453-457
89. Veldhuizen, E. J., Vaillancourt, F. H., Whiting, C. J., Hsiao, M. M., Gingras, G., Xiao, Y., Tanguay, R. M., Boukouvalas, J., and Eltis, L. D. (2005) Steady-state kinetics and inhibition of anaerobically purified human homogentisate 1,2-dioxygenase. *Biochem. J.* **386**, 305-314
90. Yang, Y., Liu, F., and Liu, A. (2018) Adapting to oxygen: 3-Hydroxyanthrinilate 3,4-dioxygenase employs loop dynamics to accommodate two substrates with disparate polarities. *J Biol Chem* **293**, 10415-10424
91. Fielding, A. J., Lipscomb, J. D., and Que, L., Jr. (2014) A two-electron-shell game: intermediates of the extradiol-cleaving catechol dioxygenases. *J. Biol. Inorg. Chem.* **19**, 491-504
92. Vaillancourt, F. H., Barbosa, C. J., Spiro, T. G., Bolin, J. T., Blades, M. W., Turner, R. F., and Eltis, L. D. (2002) Definitive evidence for monoanionic binding of 2,3-dihydroxybiphenyl to 2,3-dihydroxybiphenyl 1,2-dioxygenase from UV resonance Raman spectroscopy, UV/Vis absorption spectroscopy, and crystallography. *J Am Chem Soc* **124**, 2485-2496
93. Lipscomb, J. D. (2008) Mechanism of extradiol aromatic ring-cleaving dioxygenases. *Curr Opin Struct Biol* **18**, 644-649
94. Klecka, G. M., and Gibson, D. T. (1981) Inhibition of catechol 2,3-dioxygenase from *Pseudomonas putida* by 3-chlorocatechol. *Appl Environ Microbiol* **41**, 1159-1165
95. Bartels, I., Knackmuss, H. J., and Reineke, W. (1984) Suicide Inactivation of Catechol 2,3-Dioxygenase from *Pseudomonas putida* mt-2 by 3-Halocatechols. *Appl Environ Microbiol* **47**, 500-505
96. Cerdan, P., Wasserfallen, A., Rekik, M., Timmis, K. N., and Harayama, S. (1994) Substrate specificity of catechol 2,3-dioxygenase encoded by TOL plasmid pWW0 of *Pseudomonas putida* and its relationship to cell growth. *J. Bacteriol.* **176**, 6074-6081
97. Cerdan, P., Rekik, M., and Harayama, S. (1995) Substrate specificity differences between two catechol 2,3-dioxygenases encoded by the TOL and NAH plasmids from *Pseudomonas putida*. *Eur J Biochem* **229**, 113-118
98. Tropel, D., Meyer, C., Armengaud, J., and Jouanneau, Y. (2002) Ferredoxin-mediated reactivation of the chlorocatechol 2,3-dioxygenase from *Pseudomonas putida* GJ31. *Arch Microbiol* **177**, 345-351

99. Costas, M., Mehn, M. P., Jensen, M. P., and Que, L., Jr. (2004) Dioxygen activation at mononuclear nonheme iron active sites: enzymes, models, and intermediates. *Chem Rev* **104**, 939-986
100. Hori, K., Hashimoto, T., and Nozaki, M. (1973) Kinetic studies on the reaction mechanism of dioxygenases. *J Biochem* **74**, 375-384
101. Eltis, L. D., Hofmann, B., Hecht, H. J., Lunsdorf, H., and Timmis, K. N. (1993) Purification and crystallization of 2,3-dihydroxybiphenyl 1,2-dioxygenase. *J Biol Chem* **268**, 2727-2732
102. Sugimoto, K., Senda, M., Kasai, D., Fukuda, M., Masai, E., and Senda, T. (2014) Molecular mechanism of strict substrate specificity of an extradiol dioxygenase, DesB, derived from *Sphingobium* sp. SYK-6. *PLoS One* **9**, e92249
103. Barry, K. P., and Taylor, E. A. (2013) Characterizing the promiscuity of LigAB, a lignin catabolite degrading extradiol dioxygenase from *Sphingomonas paucimobilis* SYK-6. *Biochemistry* **52**, 6724-6736
104. Sugimoto, K., Senda, T., Aoshima, H., Masai, E., Fukuda, M., and Mitsui, Y. (1999) Crystal structure of an aromatic ring opening dioxygenase LigAB, a protocatechuate 4,5-dioxygenase, under aerobic conditions. *Structure* **7**, 953-965
105. Kasai, D., Masai, E., Miyauchi, K., Katayama, Y., and Fukuda, M. (2005) Characterization of the gallate dioxygenase gene: three distinct ring cleavage dioxygenases are involved in syringate degradation by *Sphingomonas paucimobilis* SYK-6. *J Bacteriol* **187**, 5067-5074
106. Peng, X., Masai, E., Kasai, D., Miyauchi, K., Katayama, Y., and Fukuda, M. (2005) A second 5-carboxyvanillate decarboxylase gene, *ligW2*, is important for lignin-related biphenyl catabolism in *Sphingomonas paucimobilis* SYK-6. *Appl. Environ. Microbiol.* **71**, 5014-5021
107. Kasai, D., Masai, E., Miyauchi, K., Katayama, Y., and Fukuda, M. (2004) Characterization of the 3-*o*-methylgallate dioxygenase gene and evidence of multiple 3-*o*-methylgallate catabolic pathways in *Sphingomonas paucimobilis* SYK-6. *J. Bacteriol.* **186**, 4951-4959
108. Barry, K. P., Ngu, A., Cohn, E. F., Cote, J. M., Burroughs, A. M., Gerbino, J. P., and Taylor, E. A. (2015) Exploring allosteric activation of LigAB from *Sphingobium* sp. strain SYK-6 through kinetics, mutagenesis and computational studies. *Arch. Biochem. Biophys.* **567**, 35-45
109. Walter, M. H., and Strack, D. (2011) Carotenoids and their cleavage products: Biosynthesis and functions. *Nat Prod Rep* **28**, 663-692
110. Nambara, E., and Marion-Poll, A. (2005) Abscisic acid biosynthesis and catabolism. *Annu Rev Plant Biol* **56**, 165-185
111. Krinsky, N. I., and Johnson, E. J. (2005) Carotenoid actions and their relation to health and disease. *Mol Aspects Med* **26**, 459-516
112. Sui, X., Kiser, P. D., Lintig, J., and Palczewski, K. (2013) Structural basis of carotenoid cleavage: from bacteria to mammals. *Arch Biochem Biophys* **539**, 203-213
113. Sui, X., Golczak, M., Zhang, J., Kleinberg, K. A., von Lintig, J., Palczewski, K., and Kiser, P. D. (2015) Utilization of Dioxygen by Carotenoid Cleavage Oxygenases. *J Biol Chem* **290**, 30212-30223
114. Sui, X., Weitz, A. C., Farquhar, E. R., Badiee, M., Banerjee, S., von Lintig, J., Tochtrop, G. P., Palczewski, K., Hendrich, M. P., and Kiser, P. D. (2017) Structure and Spectroscopy of Alkene-Cleaving Dioxygenases Containing an Atypically Coordinated Non-Heme Iron Center. *Biochemistry* **56**, 2836-2852
115. dela Sena, C., Riedl, K. M., Narayanasamy, S., Curley, R. W., Jr., Schwartz, S. J., and Harrison, E. H. (2014) The human enzyme that converts dietary provitamin A carotenoids to vitamin A is a dioxygenase. *J Biol Chem* **289**, 13661-13666
116. Kamoda, S., Habu, N., Samejima, M., and Yoshimoto, T. (1989) Purification and Some Properties of Lignostilbene-Alpha-Beta-Dioxygenase Responsible for the C-Alpha-C-Beta

- Cleavage of a Diarylpropane Type Lignin Model-Compound from Pseudomonas Sp Tmy1009. *Agr Biol Chem Tokyo* **53**, 2757-2761
117. McAndrew, R. P., Sathitsuksanoh, N., Mbughuni, M. M., Heins, R. A., Pereira, J. H., George, A., Sale, K. L., Fox, B. G., Simmons, B. A., and Adams, P. D. (2016) Structure and mechanism of NOV1, a resveratrol-cleaving dioxygenase. *Proc Natl Acad Sci U S A* **113**, 14324-14329
118. Kamoda, S., and Saburi, Y. (1993) Structural and enzymatical comparison of lignostilbene-alpha,beta-dioxygenase isozymes, I, II, and III, from Pseudomonas paucimobilis TMY1009. *Biosci Biotechnol Biochem* **57**, 931-934
119. Nunes, S., Danesi, F., Del Rio, D., and Silva, P. (2018) Resveratrol and inflammatory bowel disease: the evidence so far. *Nutr Res Rev* **31**, 85-97
120. Crestini, C., Lange, H., Sette, M., and Argyropoulos, D. S. (2017) On the structure of softwood kraft lignin. *Green Chem* **19**, 4104-4121
121. Kamoda, S., and Saburi, Y. (1993) Cloning, expression, and sequence analysis of a lignostilbene-alpha,beta-dioxygenase gene from Pseudomonas paucimobilis TMY1009. *Biosci Biotechnol Biochem* **57**, 926-930
122. Diaz-Sanchez, V., Estrada, A. F., Limon, M. C., Al-Babili, S., and Avalos, J. (2013) The oxygenase CAO-1 of Neurospora crassa is a resveratrol cleavage enzyme. *Eukaryot Cell* **12**, 1305-1314
123. Marasco, E. K., and Schmidt-Dannert, C. (2008) Identification of bacterial carotenoid cleavage dioxygenase homologues that cleave the interphenyl alpha,beta double bond of stilbene derivatives via a monooxygenase reaction. *Chembiochem* **9**, 1450-1461
124. Kamoda, S., and Saburi, Y. (1995) Cloning of a lignostilbene-alpha,beta-dioxygenase isozyme gene from Pseudomonas paucimobilis TMY1009. *Biosci Biotechnol Biochem* **59**, 1866-1868
125. Kamoda, S., Terada, T., and Saburi, Y. (1997) Purification and some properties of lignostilbene-alpha, beta-dioxygenase isozyme IV from Pseudomonas paucimobilis TMY1009. *Biosci Biotechnol Biochem* **61**, 1575-1576
126. Kamoda, S., Terada, T., and Saburi, Y. (2003) A common structure of substrate shared by lignostilbenedioxygenase isozymes from Sphingomonas paucimobilis TMY1009. *Biosci Biotechnol Biochem* **67**, 1394-1396
127. Han, S., Inoue, H., Terada, T., Kamoda, S., Saburi, Y., Sekimata, K., Saito, T., Kobayashi, M., Shinozaki, K., Yoshida, S., and Asami, T. (2002) Design and synthesis of lignostilbene-alpha,beta-dioxygenase inhibitors. *Bioorg Med Chem Lett* **12**, 1139-1142
128. Han, S. Y., Inoue, H., Terada, T., Kamoda, S., Saburi, Y., Sekimata, K., Saito, T., Kobayashi, M., Shinozaki, K., Yoshida, S., and Asami, T. (2003) N-benzylideneaniline and N-benzylaniline are potent inhibitors of lignostilbene-alpha,beta-dioxygenase, a key enzyme in oxidative cleavage of the central double bond of lignostilbene. *J Enzyme Inhib Med Chem* **18**, 279-283
129. Ruzzini, A. C., Ghosh, S., Horsman, G. P., Foster, L. J., Bolin, J. T., and Eltis, L. D. (2012) Identification of an Acyl-enzyme Intermediate in a Meta-cleavage Product Hydrolase Reveals the Versatility of the Catalytic Triad. *J Am. Chem. Soc.* **134**, 4615-4624
130. Lam, W. W., and Bugg, T. D. (1997) Purification, Characterization, and Stereochemical Analysis of a C-C Hydrolase: 2-Hydroxy-6-keto-nona-2,4-diene-1,9-dioic Acid 5,6-Hydrolase. *Biochemistry* **36**, 12242-12251
131. Horsman, G. P., Ke, J., Dai, S., Seah, S. Y., Bolin, J. T., and Eltis, L. D. (2006) Kinetic and Structural Insight into the Mechanism of BphD, a C-C Bond Hydrolase from the Biphenyl Degradation Pathway. *Biochemistry* **45**, 11071-11086

132. Seah, S. Y., Ke, J., Denis, G., Horsman, G. P., Fortin, P. D., Whiting, C. J., and Eltis, L. D. (2007) Characterization of a C-C bond hydrolase from *Sphingomonas wittichii* RW1 with novel specificities towards polychlorinated biphenyl metabolites. *J Bacteriol* **189**, 4038-4045
133. Seah, S. Y., Labbe, G., Nerding, S., Johnson, M. R., Snieckus, V., and Eltis, L. D. (2000) Identification of a serine hydrolase as a key determinant in the microbial degradation of polychlorinated biphenyls. *J Biol Chem* **275**, 15701-15708
134. Lack, N. A., Yam, K. C., Lowe, E. D., Horsman, G. P., Owen, R. L., Sim, E., and Eltis, L. D. (2010) Characterization of a carbon-carbon hydrolase from *Mycobacterium tuberculosis* involved in cholesterol metabolism. *J Biol Chem* **285**, 434-443
135. Ryan, A., Keany, S., Eleftheriadou, O., Ballet, R., Cheng, H. Y., and Sim, E. (2014) Mechanism-based inhibition of HsdA: a C-C bond hydrolase essential for survival of *Mycobacterium tuberculosis* in macrophage. *FEMS Microbiol Lett* **350**, 42-47
136. Van der Geize, R., Yam, K., Heuser, T., Wilbrink, M. H., Hara, H., Anderton, M. C., Sim, E., Dijkhuizen, L., Davies, J. E., Mohn, W. W., and Eltis, L. D. (2007) A gene cluster encoding cholesterol catabolism in a soil actinomycete provides insight into *Mycobacterium tuberculosis* survival in macrophages. *Proc Natl Acad Sci U S A* **104**, 1947-1952
137. Ollis, D. L., Cheah, E., Cygler, M., Dijkstra, B., Frolov, F., Franken, S. M., Harel, M., Remington, S. J., Silman, I., Schrag, J., Sussman, J. L., Verschueren, K. H. G., and Goldman, A. (1992) The alpha/beta hydrolase fold. *Protein Eng* **5**, 197-211
138. Rauwerdink, A., and Kazlauskas, R. J. (2015) How the Same Core Catalytic Machinery Catalyzes 17 Different Reactions: the Serine-Histidine-Aspartate Catalytic Triad of alpha/beta-Hydrolase Fold Enzymes. *AcS Catal* **5**, 6153-6176
139. Nardini, M., and Dijkstra, B. W. (1999) Alpha/beta hydrolase fold enzymes: the family keeps growing. *Curr Opin Struct Biol* **9**, 732-737
140. Gruber, K., Gartler, G., Krammer, B., Schwab, H., and Kratky, C. (2004) Reaction mechanism of hydroxynitrile lyases of the alpha/beta-hydrolase superfamily: the three-dimensional structure of the transient enzyme-substrate complex certifies the crucial role of LYS236. *J Biol Chem* **279**, 20501-20510
141. Fischer, F., Kunne, S., and Fetzner, S. (1999) Bacterial 2,4-dioxygenases: new members of the alpha/beta hydrolase-fold superfamily of enzymes functionally related to serine hydrolases. *J Bacteriol* **181**, 5725-5733
142. Holmquist, M. (2000) Alpha/Beta-hydrolase fold enzymes: structures, functions and mechanisms. *Curr Protein Pept Sci* **1**, 209-235
143. Li, B., Yang, G., Wu, L., and Feng, Y. (2012) Role of the NC-loop in catalytic activity and stability in lipase from *Fervidobacterium changbaicum*. *PLoS One* **7**, e46881
144. Grogan, G. (2005) Emergent Mechanistic Diversity of Enzyme-catalysed Beta-diketone Cleavage. *Biochem. J.* **388**, 721-730
145. Bateman, R. L., Bhanumoorthy, P., Witte, J. F., McClard, R. W., Grompe, M., and Timm, D. E. (2001) Mechanistic Inferences from the Crystal Structure of Fumarylacetoacetate Hydrolase with a Bound Phosphorus-based Inhibitor. *J. Biol. Chem.* **276**, 15284-15291
146. Crowe, A. M., Workman, S. D., Watanabe, N., Worrall, L. J., Strynadka, N. C. J., and Eltis, L. D. (2018) IpdaB, a Virulence Factor in *Mycobacterium tuberculosis*, Is a Cholesterol Ring-cleaving Hydrolase. *Proc. Natl. Acad. Sci. U. S. A.* **115**, E3378-E3387
147. Phillips, R. S. (2011) Structure, mechanism, and substrate specificity of kynureninase. *Biochim Biophys Acta* **1814**, 1481-1488
148. Henderson, I. M., and Bugg, T. D. (1997) Pre-Steady-State Kinetic Analysis of 2-Hydroxy-6-keto-nona-2,4-diene-1,9-dioic Acid 5,6-Hydrolase: Kinetic Evidence for Enol/Keto Tautomerization. *Biochemistry* **36**, 12252-12258

149. Horsman, G. P., Bhowmik, S., Seah, S. Y., Kumar, P., Bolin, J. T., and Eltis, L. D. (2007) The Tautomeric Half-reaction of BphD, a C-C Bond Hydrolase. Kinetic and Structural Evidence Supporting a Key Role for Histidine 265 of the Catalytic Triad. *J. Biol. Chem.* **282**, 19894-19904
150. Ruzzini, A. C., Bhowmik, S., Ghosh, S., Yam, K. C., Bolin, J. T., and Eltis, L. D. (2013) A Substrate-assisted Mechanism of Nucleophile Activation in a Ser-His-Asp Containing C-C Bond Hydrolase. *Biochemistry* **52**, 7428-7438
151. Li, J. J., Li, C., Blindauer, C. A., and Bugg, T. D. (2006) Evidence for a gem-diol reaction intermediate in bacterial C-C hydrolase enzymes BphD and MhpC from ¹³C NMR spectroscopy. *Biochemistry* **45**, 12461-12469
152. Ruzzini, A. C. (2013) *Investigating the catalytic mechanism of the meta-cleavage product hydrolases*. Doctor of Philosophy - PhD, University of British Columbia
153. Li, J. J., and Bugg, T. D. (2005) Stereochemistry of the reaction catalysed by 2-hydroxy-6-keto-6-phenyl-hexa-2,4-dienoic acid 5,6-hydrolase (BphD). *Chem Commun (Camb)*, 130-132
154. Holm, L., and Sander, C. (1997) An evolutionary treasure: unification of a broad set of amidohydrolases related to urease. *Proteins* **28**, 72-82
155. Bigley, A. N., Xu, C., Henderson, T. J., Harvey, S. P., and Raushel, F. M. (2013) Enzymatic neutralization of the chemical warfare agent VX: evolution of phosphotriesterase for phosphorothiolate hydrolysis. *J Am Chem Soc* **135**, 10426-10432
156. Wille, T., Neumaier, K., Koller, M., Ehinger, C., Aggarwal, N., Ashani, Y., Goldsmith, M., Sussman, J. L., Tawfik, D. S., Thiermann, H., and Worek, F. (2016) Single treatment of VX poisoned guinea pigs with the phosphotriesterase mutant C23AL: Intraosseous versus intravenous injection. *Toxicol Lett* **258**, 198-206
157. Schwarzenbacher, R., Canaves, J. M., Brinen, L. S., Dai, X., Deacon, A. M., Elsliger, M. A., Eshaghi, S., Floyd, R., Godzik, A., Grittini, C., Grztechnik, S. K., Guda, C., Jaroszewski, L., Karlak, C., Klock, H. E., Koesema, E., Kovarik, J. S., Kreusch, A., Kuhn, P., Lesley, S. A., McMullan, D., McPhillips, T. M., Miller, M. A., Miller, M. D., Morse, A., Moy, K., Ouyang, J., Robb, A., Rodrigues, K., Selby, T. L., Spraggon, G., Stevens, R. C., van den Bedem, H., Velasquez, J., Vincent, J., Wang, X., West, B., Wolf, G., Hodgson, K. O., Wooley, J., and Wilson, I. A. (2003) Crystal structure of uronate isomerase (TM0064) from *Thermotoga maritima* at 2.85 Å resolution. *Proteins* **53**, 142-145
158. Seibert, C. M., and Raushel, F. M. (2005) Structural and Catalytic Diversity Within the Amidohydrolase Superfamily. *Biochemistry* **44**, 6383-6391
159. Tatusov, R. L., Fedorova, N. D., Jackson, J. D., Jacobs, A. R., Kiryutin, B., Koonin, E. V., Krylov, D. M., Mazumder, R., Mekhedov, S. L., Nikolskaya, A. N., Rao, B. S., Smirnov, S., Sverdlov, A. V., Vasudevan, S., Wolf, Y. I., Yin, J. J., and Natale, D. A. (2003) The COG Database: An Updated Version Includes Eukaryotes. *BMC Bioinf.* **4**, 41
160. Finn, R. D., Coggill, P., Eberhardt, R. Y., Eddy, S. R., Mistry, J., Mitchell, A. L., Potter, S. C., Punta, M., Qureshi, M., Sangrador-Vegas, A., Salazar, G. A., Tate, J., and Bateman, A. (2016) The Pfam protein families database: towards a more sustainable future. *Nucleic Acids Res* **44**, D279-285
161. Manta, B., Raushel, F. M., and Himo, F. (2014) Reaction mechanism of zinc-dependent cytosine deaminase from *Escherichia coli*: a quantum-chemical study. *J Phys Chem B* **118**, 5644-5652
162. Hall, R. S., Fedorov, A. A., Xu, C., Fedorov, E. V., Almo, S. C., and Raushel, F. M. (2011) Three-dimensional structure and catalytic mechanism of cytosine deaminase. *Biochemistry* **50**, 5077-5085

163. Wilson, D. K., Rudolph, F. B., and Quiocco, F. A. (1991) Atomic structure of adenosine deaminase complexed with a transition-state analog: understanding catalysis and immunodeficiency mutations. *Science* **252**, 1278-1284
164. Hall, R. S. (2011) *Mechanistic studies and function discovery of mononuclear amidohydrolase enzymes*. Doctor of Philosophy, Texas A&M University
165. Manta, B., Raushel, F. M., and Himo, F. (2014) Reaction mechanism of zinc-dependent cytosine deaminase from *Escherichia coli*: a quantum-chemical study. *J. Phys. Chem. B* **118**, 5644-5652
166. Hobbs, M. E., Malashkevich, V., Williams, H. J., Xu, C., Sauder, J. M., Burley, S. K., Almo, S. C., and Raushel, F. M. (2012) Structure and catalytic mechanism of LigI: insight into the amidohydrolase enzymes of cog3618 and lignin degradation. *Biochemistry* **51**, 3497-3507
167. Martynowski, D., Eyobo, Y., Li, T., Yang, K., Liu, A., and Zhang, H. (2006) Crystal structure of alpha-amino-beta-carboxymuconate-epsilon-semialdehyde decarboxylase: insight into the active site and catalytic mechanism of a novel decarboxylation reaction. *Biochemistry* **45**, 10412-10421
168. Li, T., Huo, L., Pulley, C., and Liu, A. (2012) Decarboxylation mechanisms in biological system. *Bioorg Chem* **43**, 2-14
169. Li, T., Walker, A. L., Iwaki, H., Hasegawa, Y., and Liu, A. (2005) Kinetic and Spectroscopic Characterization of ACMSD from *Pseudomonas fluorescens* Reveals a Pentacoordinate Mononuclear Metallocofactor. *J. Am. Chem. Soc.* **127**, 12282-12290
170. Li, T., Iwaki, H., Fu, R., Hasegawa, Y., Zhang, H., and Liu, A. (2006) Alpha-amino-beta-carboxymuconic-epsilon-semialdehyde decarboxylase (ACMSD) is a new member of the amidohydrolase superfamily. *Biochemistry* **45**, 6628-6634
171. Xu, S., Li, W., Zhu, J., Wang, R., Li, Z., Xu, G. L., and Ding, J. (2013) Crystal Structures of Isoorotate Decarboxylases Reveal a Novel Catalytic Mechanism of 5-Carboxyl-Uracil Decarboxylation and Shed Light on the Search for DNA Decarboxylase. *Cell Res.* **23**, 1296-1309
172. Goto, M., Hayashi, H., Miyahara, I., Hirotsu, K., Yoshida, M., and Oikawa, T. (2006) Crystal Structures of Nonoxidative Zinc-dependent 2,6-Dihydroxybenzoate (Gamma-Resorcylate) Decarboxylase from *Rhizobium* sp. Strain MTP-10005. *J. Biol. Chem.* **281**, 34365-34373
173. Sheng, X., Patkovsky, Y., Vladimirova, A., Bonanno, J. B., Almo, S. C., Himo, F., and Raushel, F. M. (2018) Mechanism and Structure of gamma-Resorcylate Decarboxylase. *Biochemistry* **57**, 3167-3175
174. Snini, S. P., Tadrist, S., Laffitte, J., Jamin, E. L., Oswald, I. P., and Puel, O. (2014) The gene PatG involved in the biosynthesis pathway of patulin, a food-borne mycotoxin, encodes a 6-methylsalicylic acid decarboxylase. *Int J Food Microbiol* **171**, 77-83
175. Hogancamp, T. N., and Raushel, F. M. (2018) Functional Annotation of LigU as a 1,3-Allylic Isomerase during the Degradation of Lignin in the Protocatechuate 4,5-Cleavage Pathway from the Soil Bacterium *Sphingobium* sp. SYK-6. *Biochemistry* **57**, 2837-2845
176. Otani, H., Lee, Y. E., Casabon, I., and Eltis, L. D. (2014) Characterization of *p*-hydroxycinnamate catabolism in a soil Actinobacterium. *J. Bacteriol.* **196**, 4293-4303
177. Vladimirova, A., Patkovsky, Y., Fedorov, A. A., Bonanno, J. B., Fedorov, E. V., Toro, R., Hillerich, B., Seidel, R. D., Richards, N. G., Almo, S. C., and Raushel, F. M. (2016) Substrate Distortion and the Catalytic Reaction Mechanism of 5-Carboxyvanillate Decarboxylase. *J. Am. Chem. Soc.* **138**, 826-836
178. Vladimirova, A. V. (2015) *Enzymes in COG2159 of the Amidohydrolase Superfamily : Structure and Mechanism of 5-Carboxyvanillate Decarboxylase (LIGW)*. Doctor of Philosophy, Texas A & M University

179. Sheng, X., Zhu, W., Huddleston, J., Xiang, D. F., Raushel, F. M., Richards, N. G. J., and Himo, F. (2017) A Combined Experimental-Theoretical Study of the LigW-Catalyzed Decarboxylation of 5-Carboxyvanillate in the Metabolic Pathway for Lignin Degradation. *ACS Catal.* **7**, 4968-4974
180. Hogancamp, T. N., Mabanglo, M. F., and Raushel, F. M. (2018) Structure and Reaction Mechanism of the LigJ Hydratase: An Enzyme Critical for the Bacterial Degradation of Lignin in the Protocatechuate 4,5-Cleavage Pathway. *Biochemistry* **57**, 5841-5850
181. Huo, L., Davis, I., Chen, L., and Liu, A. (2013) The Power of Two: Arginine 51 and Arginine 239* from a Neighboring Subunit Are Essential for Catalysis in Alpha-amino-beta-carboxymuconate-epsilon-semialdehyde Decarboxylase. *J. Biol. Chem.* **288**, 30862-30871
182. Ausubel, F. M. (2002) *Short protocols in molecular biology : a compendium of methods from Current protocols in molecular biology*, 5th ed., Wiley, New York
183. Zabinski, R., Munck, E., Champion, P. M., and Wood, J. M. (1972) Kinetic and Mossbauer studies on the mechanism of protocatechuic acid 4,5-oxygenase. *Biochemistry* **11**, 3212-3219
184. Shiel, A. E., Weis, D., and Orians, K. J. (2012) Tracing cadmium, zinc and lead sources in bivalves from the coasts of western Canada and the USA using isotopes. *Geochim Cosmochim Ac* **76**, 175-190
185. Cornish-Bowden, A. (1995) *Analysis of Enzyme Kinetic Data*, Oxford University Press, Oxford, U. K.
186. Soltis, S. M., Cohen, A. E., Deacon, A., Eriksson, T., Gonzalez, A., McPhillips, S., Chui, H., Dunten, P., Hollenbeck, M., Mathews, I., Miller, M., Moorhead, P., Phizackerley, R. P., Smith, C., Song, J., van dem Bedem, H., Ellis, P., Kuhn, P., McPhillips, T., Sauter, N., Sharp, K., Tsbyba, I., and Wolf, G. (2008) New paradigm for macromolecular crystallography experiments at SSRL: automated crystal screening and remote data collection. *Acta Crystallogr D Biol Crystallogr* **64**, 1210-1221
187. McCoy, A. J., Grosse-Kunstleve, R. W., Adams, P. D., Winn, M. D., Storoni, L. C., and Read, R. J. (2007) Phaser Crystallographic Software. *J. Appl. Crystallogr.* **40**, 658-674
188. Adams, P. D., Afonine, P. V., Bunkoczi, G., Chen, V. B., Davis, I. W., Echols, N., Headd, J. J., Hung, L. W., Kapral, G. J., Grosse-Kunstleve, R. W., McCoy, A. J., Moriarty, N. W., Oeffner, R., Read, R. J., Richardson, D. C., Richardson, J. S., Terwilliger, T. C., and Zwart, P. H. (2010) PHENIX: a comprehensive Python-based system for macromolecular structure solution. *Acta Crystallogr., Sect. D: Biol. Crystallogr.* **66**, 213-221
189. Emsley, P., Lohkamp, B., Scott, W. G., and Cowtan, K. (2010) Features and Development of Coot. *Acta Crystallogr., Sect. D: Biol. Crystallogr.* **66**, 486-501
190. Afonine, P. V., Grosse-Kunstleve, R. W., Echols, N., Headd, J. J., Moriarty, N. W., Mustyakimov, M., Terwilliger, T. C., Urzhumtsev, A., Zwart, P. H., and Adams, P. D. (2012) Towards Automated Crystallographic Structure Refinement with Phenix.Refine. *Acta Crystallogr., Sect. D: Biol. Crystallogr.* **68**, 352-367
191. Winn, M. D., Ballard, C. C., Cowtan, K. D., Dodson, E. J., Emsley, P., Evans, P. R., Keegan, R. M., Krissinel, E. B., Leslie, A. G., McCoy, A., McNicholas, S. J., Murshudov, G. N., Pannu, N. S., Potterton, E. A., Powell, H. R., Read, R. J., Vagin, A., and Wilson, K. S. (2011) Overview of the CCP4 suite and current developments. *Acta Crystallogr. D Biol. Crystallogr.* **67**, 235-242
192. Battye, T. G., Kontogiannis, L., Johnson, O., Powell, H. R., and Leslie, A. G. (2011) iMOSFLM: a new graphical interface for diffraction-image processing with MOSFLM. *Acta Crystallogr. D Biol. Crystallogr.* **67**, 271-281
193. Holm, L., and Sander, C. (1995) Dali: a network tool for protein structure comparison. *Trends Biochem Sci* **20**, 478-480

194. Sui, X., Zhang, J., Golczak, M., Palczewski, K., and Kiser, P. D. (2016) Key Residues for Catalytic Function and Metal Coordination in a Carotenoid Cleavage Dioxygenase. *J Biol Chem* **291**, 19401-19412
195. Loewen, P. C., Switala, J., Wells, J. P., Huang, F., Zara, A. T., Allingham, J. S., and Loewen, M. C. (2018) Structure and function of a lignostilbene-alpha,beta-dioxygenase orthologue from *Pseudomonas brassicacearum*. *BMC Biochem* **19**, 8
196. Sekimoto, T., Matsuyama, T., Fukui, T., and Tanizawa, K. (1993) Evidence for lysine 80 as general base catalyst of leucine dehydrogenase. *J Biol Chem* **268**, 27039-27045
197. Vaillancourt, F. H., Barbosa, C. J., Spiro, T. G., Bolin, J. T., Blades, M. W., Turner, R. F., and Eltis, L. D. (2002) Definitive evidence for monoanionic binding of 2,3-dihydroxybiphenyl to 2,3-dihydroxybiphenyl 1,2-dioxygenase from UV resonance Raman spectroscopy, UV/Vis absorption spectroscopy, and crystallography. *J. Am. Chem. Soc.* **124**, 2485-2496
198. Dai, S., Vaillancourt, F. H., Maaroufi, H., Drouin, N. M., Neau, D. B., Snieckus, V., Bolin, J. T., and Eltis, L. D. (2002) Identification and analysis of a bottleneck in PCB biodegradation. *Nat. Struct. Biol.* **9**, 934-939
199. Dagley, S., Evans, W. C., and Ribbons, D. W. (1960) New pathways in the oxidative metabolism of aromatic compounds by microorganisms. *Nature* **188**, 560-566
200. Weller, M. G., and Weser, U. (1982) Ferric Nitritotriacetate - an Active-Center Analog of Pyrocatechase. *J. Am. Chem. Soc.* **104**, 3752-3754
201. Seah, S. Y., Labbe, G., Nerding, S., Johnson, M. R., Snieckus, V., and Eltis, L. D. (2000) Identification of a Serine Hydrolase as a Key Determinant in the Microbial Degradation of Polychlorinated Biphenyls. *J. Biol. Chem.* **275**, 15701-15708
202. Kuatsjah, E., Chen, H. M., Withers, S. G., and Eltis, L. D. (2017) Characterization of an extradiol dioxygenase involved in the catabolism of lignin-derived biphenyl. *FEBS Lett* **591**, 1001-1009
203. Van Duyne, G. D., Standaert, R. F., Karplus, P. A., Schreiber, S. L., and Clardy, J. (1993) Atomic structures of the human immunophilin FKBP-12 complexes with FK506 and rapamycin. *J. Mol. Biol.* **229**, 105-124
204. McCall, K. A., and Fierke, C. A. (2000) Colorimetric and fluorimetric assays to quantitate micromolar concentrations of transition metals. *Anal. Biochem.* **284**, 307-315
205. Touw, W. G., Baakman, C., Black, J., te Beek, T. A., Krieger, E., Joosten, R. P., and Vriend, G. (2015) A series of PDB-related databanks for everyday needs. *Nucleic Acids Res.* **43**, D364-368
206. Kabsch, W., and Sander, C. (1983) Dictionary of protein secondary structure: pattern recognition of hydrogen-bonded and geometrical features. *Biopolymers* **22**, 2577-2637
207. Vriend, G. (1990) WHAT IF: a molecular modeling and drug design program. *J. Mol. Graph.* **8**, 52-56, 29
208. Krissinel, E., and Henrick, K. (2007) Inference of macromolecular assemblies from crystalline state. *J. Mol. Biol.* **372**, 774-797
209. Dolinsky, T. J., Czodrowski, P., Li, H., Nielsen, J. E., Jensen, J. H., Klebe, G., and Baker, N. A. (2007) PDB2PQR: expanding and upgrading automated preparation of biomolecular structures for molecular simulations. *Nucleic Acids Res.* **35**, W522-525
210. Dolinsky, T. J., Nielsen, J. E., McCammon, J. A., and Baker, N. A. (2004) PDB2PQR: an automated pipeline for the setup of Poisson-Boltzmann electrostatics calculations. *Nucleic Acids Res.* **32**, W665-667
211. Baker, N. A., Sept, D., Joseph, S., Holst, M. J., and McCammon, J. A. (2001) Electrostatics of nanosystems: application to microtubules and the ribosome. *Proc. Natl. Acad. Sci. U. S. A.* **98**, 10037-10041

212. Celniker, G., Nimrod, G., Ashkenazy, H., Glaser, F., Martz, E., Mayrose, I., Pupko, T., and Ben-Tal, N. (2013) ConSurf: Using Evolutionary Data to Raise Testable Hypotheses about Protein Function. *Isr J Chem* **53**, 199-206
213. Goldenberg, O., Erez, E., Nimrod, G., and Ben-Tal, N. (2009) The ConSurf-DB: pre-calculated evolutionary conservation profiles of protein structures. *Nucleic Acids Res.* **37**, D323-327
214. Notredame, C., Higgins, D. G., and Heringa, J. (2000) T-Coffee: A novel method for fast and accurate multiple sequence alignment. *J. Mol. Biol.* **302**, 205-217
215. Pruitt, K. D., Tatusova, T., and Maglott, D. R. (2005) NCBI Reference Sequence (RefSeq): a curated non-redundant sequence database of genomes, transcripts and proteins. *Nucleic Acids Res.* **33**, D501-504
216. Bateman, A., Coin, L., Durbin, R., Finn, R. D., Hollich, V., Griffiths-Jones, S., Khanna, A., Marshall, M., Moxon, S., Sonnhammer, E. L., Studholme, D. J., Yeats, C., and Eddy, S. R. (2004) The Pfam protein families database. *Nucleic Acids Res.* **32**, D138-141
217. Hara, H., Masai, E., Katayama, Y., and Fukuda, M. (2000) The 4-Oxalomesaconate Hydratase Gene, Involved in the Protocatechuate 4,5-cleavage Pathway, Is Essential to Vanillate and Syringate Degradation in *Sphingomonas paucimobilis* SYK-6. *J. Bacteriol.* **182**, 6950-6957
218. Fowden, L., and Webb, J. A. (1955) Evidence for the occurrence of gamma-methylene-alpha-oxoglutaric acid in groundnut plants (*Arachis hypogaea*). *Biochem. J.* **59**, 228-234
219. Liu, X. X., and Wang, Y. (2015) Crystal structure and luminescent properties of [1-(biphenyl-4-yl)-1H-imidazole-kappaN³]di-chloridozinc. *Acta Crystallogr. E Crystallogr. Commun.* **71**, 272-274
220. Huo, L., Davis, I., Chen, L., and Liu, A. (2013) The power of two: arginine 51 and arginine 239* from a neighboring subunit are essential for catalysis in alpha-amino-beta-carboxymuconate-epsilon-semialdehyde decarboxylase. *J. Biol. Chem.* **288**, 30862-30871
221. Ruzzini, A. C., Horsman, G. P., and Eltis, L. D. (2012) The catalytic serine of meta-cleavage product hydrolases is activated differently for C-O bond cleavage than for C-C bond cleavage. *Biochemistry* **51**, 5831-5840
222. Cooper, B. F., Sideraki, V., Wilson, D. K., Dominguez, D. Y., Clark, S. W., Quiocho, F. A., and Rudolph, F. B. (1997) The role of divalent cations in structure and function of murine adenosine deaminase. *Protein Sci.* **6**, 1031-1037
223. Silverman, D. N., and Lindskog, S. (1988) The Catalytic Mechanism of Carbonic-Anhydrase - Implications of a Rate-Limiting Protolysis of Water. *Accounts Chem Res* **21**, 30-36
224. Cohen, A. E., Doukov, T., and Soltis, M. S. (2016) UV-Visible Absorption Spectroscopy Enhanced X-ray Crystallography at Synchrotron and X-ray Free Electron Laser Sources. *Protein Pept. Lett.* **23**, 283-290
225. Tekeste, T., and Vahrenkamp, H. (2006) "Inhibition" of the Enzyme Model TpPh,MeZn-OH by Diketo Compounds. *European Journal of Inorganic Chemistry* **2006**, 5158-5164
226. Watts, A. G., Damager, I., Amaya, M. L., Buschiazza, A., Alzari, P., Frasch, A. C., and Withers, S. G. (2003) *Trypanosoma cruzi* Trans-Sialidase Operates Through a Covalent Sialyl-enzyme Intermediate: Tyrosine Is the Catalytic Nucleophile. *J. Am. Chem. Soc.* **125**, 7532-7533
227. Raman, M. C., Johnson, K. A., Yard, B. A., Lowther, J., Carter, L. G., Naismith, J. H., and Campopiano, D. J. (2009) The external aldimine form of serine palmitoyltransferase: structural, kinetic, and spectroscopic analysis of the wild-type enzyme and HSAN1 mutant mimics. *J Biol Chem* **284**, 17328-17339
228. Arras, T., Schirawski, J., and Unden, G. (1998) Availability of O₂ as a substrate in the cytoplasm of bacteria under aerobic and microaerobic conditions. *J Bacteriol* **180**, 2133-2136

229. Stewart, E. J., Aslund, F., and Beckwith, J. (1998) Disulfide bond formation in the *Escherichia coli* cytoplasm: an in vivo role reversal for the thioredoxins. *EMBO J* **17**, 5543-5550
230. Polissi, A., and Harayama, S. (1993) In vivo reactivation of catechol 2,3-dioxygenase mediated by a chloroplast-type ferredoxin: a bacterial strategy to expand the substrate specificity of aromatic degradative pathways. *EMBO J* **12**, 3339-3347
231. Mori, K., Niinuma, K., Fujita, M., Kamimura, N., and Masai, E. (2018) DdvK, a novel major facilitator superfamily transporter essential for 5,5'-dehydروdivanillate uptake by *Sphingobium* sp. strain SYK-6. *Appl Environ Microbiol*

Appendices

Appendix A Sequences of the synthesized DNA

A.1 Lignostilbene- α , β -dioxygenase LsdA (locus tag: 1917171A)

ATGGCACACTTCCGCAAACCCGGGCTTAGTGGCACCCCTGCGTCCGCTGCGTATTGAA
GGCGACATTCTGGATATTGAAATCGAAGGCGAAGTTCCGCCGCAGCTGAACGGCACCTT
CATCGTGTCCACCCGGATGCACAGTTCCGCCGTTCGAAGATGACCAATTTCAT
GGCGATGGTATGGTTCCCTGTTCGTTCCATGATGGTAAAATTGACTTCGTACGCG
TATGCCCAAACCGATAAATGGAAAGTCGAACGTAAGCAGGCAAATCCCTGTTGGTGCT
TACCGCAACCGCTGACGGATGACCGTCAGTCAGGGCATGATTGCGGTACGCCAAC
ACGAATGTGATGGTCATGCGGGCAAACGTATGCCATGAAAGAAGACTCTCCGTGCCTG
ATCATGGATCCGCTGACCCTGGAAACGGAAGGCTACACCAACTTGACGGTAAACTGCAG
TCACAAACGTTCTGCGCGACCCGAAAATTGATCCGGTTACCGTAATCTGTGTGCGTT
GCCTATGGCGAAAAGGTCTGATGACCCTGGATATGGCTTACATTGAAATCAGCCCGACG
GGCAAACGTGAAAGAAATCCCCTCCAGAATCCGTATTACTGTATGATGCATGACTTT
GGTGTGACCGAAGATTATGCGGTCTCGCCGTGATGCCGCTGCTGAGCTCTGGGACCGT
CTGGAACAACGCCCTGCCGTTTCGGCTTGATACCACGCTGCCGTGCTATCTGGCATT
CTGCCCGTAACGGTGATGCCGTGACCTGCCGTGGTTAAAACCGGAATTGTTCGTT
GGTCATGTCATGAACGCATTAATGACGGCACGAAAGTCACATCGATATGCCGGTTCG
CGTAACAATAGCTCCGTTTCGACGTCCACGGTGCACCGTTGATCCGGTGGCCGGT
CAGGGTTCTGACCCGTTGGACGGTGGACATGGCATCTAACGGGATAGTTTGAAAAAA
ACCGAACGTCTGTTGATGCCCGGACGAAATTCCCGTATTGATGAACGCTATGCAACC
CGTGCTTACGCCATGGTGGATGCTGATCCTGGATACGGAAAAACCGTATGAAGCACCG
GGCGGTGCGTTTACGCCCTGACCAACACGCTGGCCACATTGATCTGGCTACCGTAAA
AGTTCCCTCATGGTGGCAGGCCCGCTTGCCTATTCAAGGAACCGTGGTTATCCCGCGT
TCGCCGGATGCACCGGAAGGTGACGGTTATGTGATCGCGCTGGTTGATGACCATGTCGCC
AATTACAGCGATCTGGCAATTTCGACGCTCAGCACGTGGATCAAGGTCCGATCGCACGC
GCTAAACTGCCGGTCTGATTGCCAAGGTCTGCACGGTAACGGGCGATGCCTCCCGC
CTGGCTGTCGCTGCCCTGA

A.2 DCHM-HOPDA hydrolase LigY (locus tag: SLG_07750)

ATGATTATCGACTGTCACGGTCACTTTGGCTCCGGTTGAAGTGTGGGCTTACAAAGCG
TCTCTGCTGGCTCATCGCGCTCGCACGGCCGTGGCGGTGTCAAAGTGACCGATGAACAG
ATTATCGCGGCCGCACATCACAAAGAAACGTGGCCGGATGGTCATATTGAAC TGCTGCAT
AACCACGGCACCGACATGCAGCTGATCAGCCCGTCCGTTCAAATGATGAAC TCTGCT
AAACC CGCGCGCGTGGTCATTGGTTCTGCGAAGAAGTGAATACCCTGATT CACCGTCAG
TGTACGCTGATTCCGGAAATGTTATCCC GGTTGCAGGTCTGCCGCAAGTCGCAGGTGAA
CCGATCGAAAATGTGTTCGCGGAAATGGATCGCTGC GTTCAATGGTTTAAAGGCTTC
CTGCTGAACCCGGATCCGTATGAAAATGGTGCAGAAGAAGCACC GCCGCTGGGTGACCGT
TATTGGTACCCGCTGTACGAAAAACTGTGCGA ACTGGATCTGCCGGCTCATATT CACGCG
ACCGGTAGTCAGTCCGAACGCAGCCGTATTCTCTGCATTTATAACGAAGAAACCATC
GCTACGTACAATCTGTGTACGAGCTCTGTTTGATGACTTCCGCAGCTGAAAGTCGTG
GTTTCCCATGGCGGTGGGCCATCCGTATCAGCTGGTCGTTGAATCACAATCGCGT
CGCAGTAAACACCTGTTCCGAACGCATGCCAAACTGTATTCGACACCGCCTGTAC
ACGGAAGGCGCACTCGTCTGCTGATTGAAACCGTGGGTCCGGAACGCTGCCTGTTGGC
TCAGAATGTCCGGGTGTTGGCTCGACCATCGATCCGGCTACGGGCAAACAGATGGACCAC
ATTGCGCCGTTCATCCAAAAATTGATTCCTGAGCGATGCCGATAAAAAACTGATCTTC
GAAGACAATGCCCGTAAAGTGTCAACCTGGAAGTCTGA

Appendix B Oligonucleotides used in this study

B.1 LsdA Primers

Oligonucleotide name	Nucleotide sequence	Restriction site
Cloning^a		
lsd-I fwd	GCTGAAC <u>ATATGG</u> CACACTTCCGCAAAC	NdeI
<i>lsd-I</i> rev tagless	CCC <u>CTCGAG</u> TCA <u>GGCAGG</u> CACAGCCAGGCCGG	XhoI
<i>lsd-I</i> rev tagged	CCC <u>AAGCTT</u> CGACT <u>GGAA</u> GTACAG <u>GGTCTCGG</u> CAGCGACAGCCAGGCCGG	HindIII
Mutagenesis^b		
F59H fwd	CGAAGATGACCA <u>TTTACA</u> ATGGCGATGGTATGG	
F59H rev	CCATACC <u>ATGCCATTG</u> TGAAATTGGTCATCTCG	
Y101F fwd	CTGTT <u>CGGTGC</u> TTTCGCAACCCGCTGAC	
Y101F rev	GTCAG <u>CGGGTTGC</u> AAAAGCACCGAACAG	
K134M fwd	CAA <u>ACTGTATGCCATG</u> ATGGAAGACTCTCCGTGCC	
K134M rev	GGC <u>ACGGAGAGTCTTCC</u> ATCATGGCATA <u>ACAGTTG</u>	
H218Q fwd	GTATT <u>ACTGTATGCAAG</u> ACTTGGTGTGACCGAAG	
H218Q rev	CTTC <u>GGTCACACCAAGTCTT</u> GCATCATACAGTAATAC	

^aIntroduced restriction site underlined

^bSubstituted oligonucleotide underlined

B.2 LigY Primers

Oligonucleotide name	Nucleotide sequence	Restriction site
<u>Cloning^a</u>		
<i>ligY</i> fwd	GCTGAACC <u>ATATGATTATCGACTGTCACGG</u>	NdeI
<i>ligY</i> rev tagless	TATTGT <u>CTCGAGTCAGACTTCCAGGTTGAACACT</u>	XhoI
<i>ligY</i> rev tagged	CCCA <u>AGCTTCGACTGGAAGTACAGGTTCTGACTTCCAGGTTGAACACTT</u>	HindIII
<i>ligW</i> fwd	GAAGGAGATATA <u>CATATGCGACTGATGCCACCGA</u>	
<i>ligW</i> rev	TGGTGGTG <u>CTCGAGTCAGGTGATGCGGAAGATGC</u>	
<i>pET41b</i> -linear fwd	CTCGAGCACCA <u>CCACCACC</u>	
<i>pET41b</i> -linear rev	ATGTATAT <u>CTCCTTCTTAAA</u>	
<u>Mutagenesis^b</u>		
S222A fwd	GAAAGTCGTGG <u>TTGCCCATGG</u>	
S222A rev	CCATGG <u>GGCAACCACGACTTTC</u>	
H223A fwd	GTCGTGG <u>TTCCGCTGGCGGTGG</u>	
H223A rev	CCAC <u>CGCCAGCGAAACCACGAC</u>	
H223Q fwd	CGTGG <u>TTCCAGGGCGGTGGCGC</u>	
H223Q rev	GCGCCAC <u>CGCCCTGGAAACCACG</u>	
R234K fwd	CGTATCAG <u>CTGGTAAATTGAATCACAATC</u>	
R234K rev	GATTGTGATT <u>CAAATTACCCAGCTGATACG</u>	
R234Q fwd	GTATCAG <u>CTGGTCAGTTGAATCACAATC</u>	
R234Q rev	GATTGTGATT <u>CAAU<u>CTGACCCAGCTGATAC</u></u>	
E282D fwd	GT <u>TTGGCTCAGATTGTCCGG</u>	
E282D rev	CCGGAC <u>AATCTGAGCCAAAC</u>	
E282Q fwd	GT <u>TTGGCTCAC<u>ATGTCCGG</u></u>	
E282Q rev	CCGGAC <u>AATTGTGAGCCAAAC</u>	
R72Q	5' P-GCTGAT <u>CAGCCCCG<u>CAGCCGTTCAAATGATG</u></u>	
Y190F	5' P-CAGTCCGAAC <u>GCAGCCC<u>GT<u>TTCTGCATTTATTAAAC</u></u></u>	

^aIntroduced restriction site underlined

^bSubstituted oligonucleotide underlined

Appendix C Fluorescence spectra of 5CVA

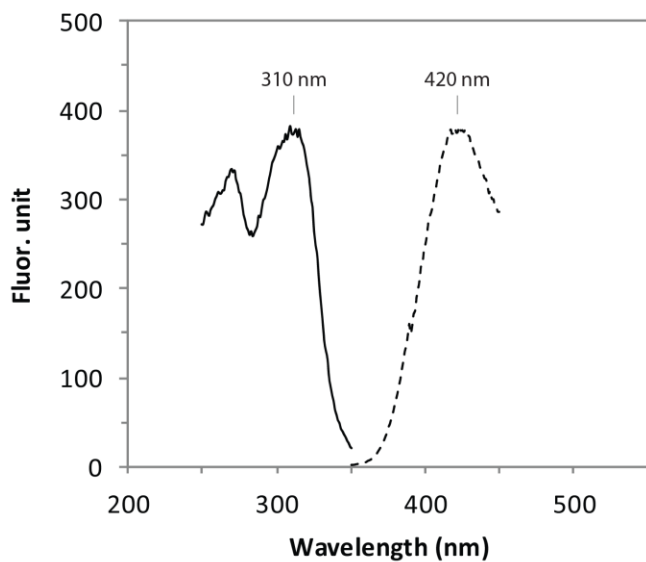


Figure 6.1. Fluorescence spectra of 5CVA.

Fluorescence excitation (solid, $\lambda_{\text{emission}}$ at 420 nm) and emission (dashed, $\lambda_{\text{excitation}}$ at 310 nm) spectra of $\sim 200 \mu\text{M}$ 5CVA in KPi ($I = 0.1$) pH 7.5.

Appendix D Additional publications not included in this thesis

Du, Y.L., Singh, R., Alkhalfaf, L.M., Kuatsjah, E., He, H.Y., Eltis, L.D., Ryan, K.S. (2016) A pyridoxal phosphate-dependent enzyme that oxidizes an unactivated carbon-carbon bond. *Nat. Chem. Biol.* **12**, 194-199

Hedges, J.B., Kuatsjah, E., Du, Y.L., Eltis, L.D., Ryan, K.S. (2018) Snapshots of the Catalytic Cycle of an O₂-Pyridoxal Phosphate-Dependent Hydroxylase. *ACS Chem. Biol.* **13**, 965-874.

Nerdinger, S., Kuatsjah E., Hurst, T.E., Schlapp-Hackl, I., Kahlenber, V., Wurst, K., Eltis, L.D., Snieckus, V. (2018) Bacterial Catabolism of Biphenyls: Synthesis and Evaluation of Analogues. *ChemBioChem* **19**, 1771-1778.